Spatial Organizing Principles of Cytokinesis Signaling

Spatial Organizing Principles of Cytokinesis Signaling

A dissertation presented

by

Phuong Anh Nguyen

to

The Committee on Higher Degrees in Chemical Biology

in partial fulfillment of the requirements

for the degree of

Doctor of Philosophy

in the subject of

Chemical Biology

Harvard University

Cambridge, Massachusetts

June 2015

Dissertation Advisor:
Professor Timothy J. Mitchison

Author:
Phuong Anh Nguyen

Spatial Organizing Principles of Cytokinesis Signaling

Abstract

Cytokinesis is the final step of cell division, in which the cytoplasm of one cell is physically divided into two. Animal cells integrate multiple positional cues from the mitotic spindle to decide where to position their cleavage plane. The unusually large egg cells from frogs face additional spatial organization challenges due to their large size compared to their mitotic spindle. How the spindle communicates to the cell cortex to precisely position the cleavage furrow at the cell midplane in these large cells is the focus of this dissertation.

Chapter One introduces how cells across all domains of life position their division site, and the spatial organizing principles and molecular mechanisms that have been established for animal cells. The unique challenges faced by very large cells are discussed using eggs from the frog *Xenopus laevis* as a model system, and the large microtubule asters that organize the cytoplasm in these cells during cytokinesis are described.

Chapter Two describes the development of a cell-free system using cytoplasmic extracts from *Xenopus* eggs to reconstitute signaling events from microtubules to the cell cortex that lead to cleavage furrow induction. This is the first time a biochemical extract system is reported for studying cytokinesis. The Chromosome Passenger Complex (CPC) is identified as the main furrow-inducing signal, which is delivered to the interaction zone between neighboring asters through a combined action of two kinesins, Kif4A and an embryonic paralog of Kif20A.

Chapter Three describes experiments using the cell-free system to elucidate what happens when two neighboring asters meet and how they maintain an interaction zone that serves as a clear mutual boundary where cytokinesis proteins can be accumulated. The

Prc1/Kif4A midzone module is identified as being essential for forming antiparallel microtubule overlaps that block further plus end growth, which both prevents microtubules from one aster from crossing into another and ensures that the majority of microtubules within a single aster grow radially outward.

Chapter Four describes experiments in both extracts and whole embryos that identify initial conditions for CPC recruitment to aster interactions, such as proximity of chromatin and optimal starting distance between aster centers.

Table of Contents

Acknowledgements

It has been a long and winding road. With many steep hills, fast declines, unexpected rocks, some of which turned out to be gold. I still remember when I joined his lab, Professor Tim Mitchison reassured me (or was it a warning?): “We will have *fin* and make some *bug* discoveries.” (No, those are not typos.) In retrospect, he was absolutely right. When we were in familiar waters, we cruised fast and effortless. But there were times we got stranded on land…and, well, those were deep learning experiences. About life on land–for creatures with fins… Both my scientific endeavor and my life were profoundly touched by many people on this journey, to whom I owe many thanks.

Professor Mitchison showed me for the first time how to image the large microtubule asters in Xenopus egg extract. I fell in love immediately with both the extract system and live microscopy. He continued to deepen my appreciation for this cell-like biochemical system through his own enthusiasm in trying to “understand the extract” by imaging various cytoplasmic components. His curiosity and sense of wonder about all processes that bring matter to life have always been highly contagious. I am grateful for his continuous support for my learning new technologies, even if those were beyond his own realm of expertise.

I was fortunate to have Dr. Christine Field as my unofficial second adviser. She not only brought in her expertise of cytokinesis and the actin cytoskeleton, but also provided the perspective of a female scientist, juggling her family life with her scientific life. It was a lot of fun to compare the extract structures and phenomena to those that she observed in whole frog eggs—it was like being detectives in a mystery novel. With each mystery solved, both of us felt a tinge of sadness. I will always cherish our bilayer experiments, lunches and theater outings together. I looked upon Prof. Mitchison and Dr. Field as my local parents.

Dr. Aaron Groen was the heart of our extract group. He was always on the lookout for his labmates’ well-being, both scientifically and emotionally. He cared deeply about people and their stories. His empathy extended not only to people, but also animals and even inanimate

objects, such as molecules. He had a deep knowledge of the literature of his field, a knack for constructing scientific stories, a super power for finding the last experiment to complete a story, and an unbridled enthusiasm for doing whatever was needed to finish that story. It was no surprise so many people loved collaborating with him—he was always ready to offer a solution, hope or just humor in the face of setbacks. He kept me going when I was ready to give up.

I got to know Keisuke Ishihara as a friend first, and as a labmate later. We shared an interest in collective behavior phenomena and a love for imaging, based on which I tried hard to recruit him to join the extract group. His ability to simplify complex phenomena and describe them in quantitative terms has always fascinated and inspired me. He always was a source of stability in the face of all the drama—always organized, responsible, and eager to discuss scientific ideas.

I had the opportunity work with Dr. Martin Loose thanks to Dr. Field, who coordinated that collaboration. Beyond teaching me how to make supported lipid bilayers, Dr. Loose also showed me how to structure a scientific story, ways to improve figures and to tell the story more succinctly.

I inherited the aster-aster interaction project from Dr. Martin Wühr's graduate work, who continued to support our group with his large egg expertise and mass spectrometry proteomics work. Dr. Yangzhong Tang supervised my rotation in the lab and taught me tissue culture, Dr. Edwin Tan taught me protein biochemistry when I first joined the lab, Dr. Chi-Kuo Hu discussed cytokinesis with me and taught me immunofluorescence and cloning.

I had the opportuniy to initiate collaborations with others in the lab: Dr. Margaret Coughlin, Dr. Nefeli Georgoulia, Dr. Alexandra Zidovska, Mariah Hanley. Kathy Buhl kept our lab well-supplied and functional. Many Mitchison lab members provided me scientific and emotional support: Dr. Yuyu Song, Dr. Kristin Krukenberg, Dr. Sophie Dumont, Dr. Lingyin Li, Dr. Ruomu Jiang, Dr. Hallie Kuhn, Dr, Zoltan Maliga, Dr. Paul Choi, Dr. Elvan Böke, Dr. Jui-Hsia Weng, Dr. Jade Shi, James Pelletier and Javier Pineda. Dr. Rebecca Ward helped with

manuscript revision. Collaborators at the Marine Biological Laboratory during the summer made our time together fun and memorable: Andrew Bridges, James Hazel, Molly Su, Dr. Amy Gladfelter, and Dr. Jesse Gatlin. Current and previous staff members at the Nikon Imaging Center at Harvard Medical School provided microscopy support: Dr. Jennifer Waters, Wendy Salmon, Lauren Alvarenga, Lara Petrak, Dr. Talley Lambert. Dr. Lynne Chang from Nikon provided microscopy support and the National Xenopus Resource provided animal care at the Marine Biological Laboratory.

I would like to thank my dissertation advisory and examination committee members: Dr. David Burgess, Dr. Gaudenz Danuser, Dr. Daniel Kahne, Dr. Randall King, and Dr. Marc Kirshner. My graduate program coordinators in Chemical Biology, Samantha Reed and Jason Millberg pushed me through the finish line. I deeply appreciate your patience.

Lastly, I would like to thank my family and friends, housemates and members of True Story Theater their continuous support, without which I could not have finished graduate school.

Chapter One

Introduction

Strategies for Positioning Cytokinesis

Cytokinesis is the final step of cell division: a process that physically splits dividing cells in two following chromosome segregation. Since the formulation of the cell theory in the mid-19th century, biologists have been fascinated by the question of how cells across all domains of life faithfully partition their genetic material and other cytoplasmic contents into daughter cells (reviewed in (Wilson, 1928)). More than a century later, we now know that both prokaryotes and eukaryotes employ actin and tubulin cytoskeletal structures during cell division: a mitotic apparatus for segregating chromosomes and a plasma-membrane associated cytokinesis apparatus for cleaving the cell into two (reviewed in (Balasubramanian et al., 2004; Busiek and Margolin, 2015)). Among eukaryotes, while the mechanisms by which the microtubule-based mitotic spindle segregates chromosomes are fairly conserved, diverse strategies have evolved to position the division site and to subsequently separate daughter cells. Failure to correctly position the division site leads to uneven partitioning of the genetic material and potentially cell death; in multicellular organisms, it also results in abnormal tissue growth and morphogenesis. Thus understanding the mechanisms of cytokinesis positioning allows us to develop therapeutics to induce cell death in unwanted organisms, to correct uncontrolled cell division during cancer, and to prevent abnormal tissue morphogenesis and differentiation during growth and development.

There are three major mechanisms involved in correct positioning of the division site: (1) active choice of a fixed division site using positive signals based on cell division history; (2) active choice of a dynamic division site using positive signals independent of history; and (3) inhibition of cell division at inappropriate locations using negative signals (Balasubramanian et al., 2004). In yeast and animal cells, the cytokinesis apparatus is the contractile ring assembled from F-actin and myosin, while in plant cells it is the phragmoplast consisting of microtubules, F-actin, and endoplasmic reticulum (ER) (Figure 1.1) (Barr and Grüneberg, 2007; Müller, 2012). The budding yeast (*Saccharomyces cerevisiae*) uses strategy #1 to place the

division site adjacent to the previous division site ('bud scar'), whereas the fission yeast (*Saccharomyces pombe*) uses both strategies #2 and #3 to place its contractile ring at the position specified by the pre-mitotic nucleus (Figure 1.1) (Oliferenko et al., 2009). Plants use strategy #2 and the pre-mitotic nucleus as a dynamic positional cue, similar to the fission yeast (Murata and Wada, 1991). In addition, plants employ a transient ring-like microtubule array termed the preprophase band (PPB) at the cortex to precisely mark the position of the nucleus. The PPB disassembles before formation of the mitotic spindle, leaving behind a cortical division site that later guides the placement of the phragmoplast and construction of a new cell wall ('cell plate') during cytokinesis (Figure 1.1) (Müller et al., 2009). Generally speaking, the position of the future division site in both fungi and plants is determined early on, before the cells enter mitosis.

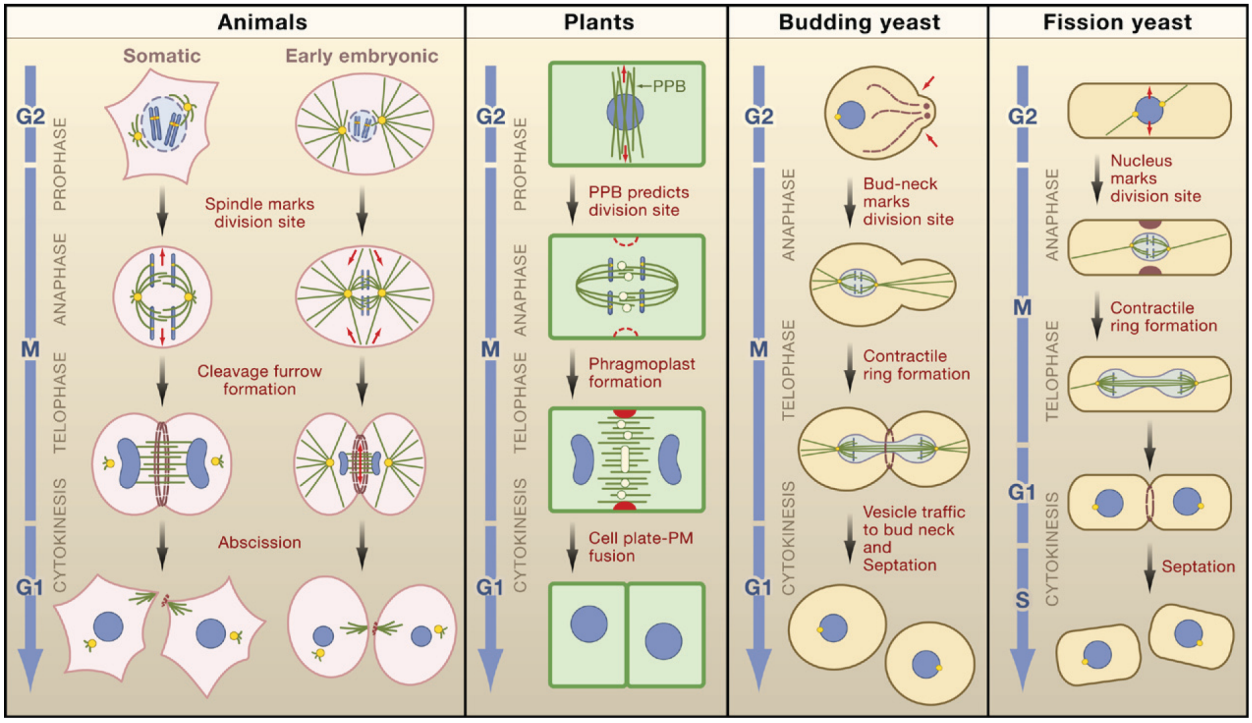

Figure 1.1: Cytokinesis in animals, plants, and yeast. The selection of the division site and cytokinesis relative to other key cell-cycle transitions is shown for animal cells, plants, and budding and fission yeast. Reprinted from (Barr and Grüneberg, 2007), with permission from Elsevier.

In contrast to yeast and plant cells, animal cells are not encased by a rigid cell wall and thus are able to migrate and change their shape within tissues. This lifestyle demands that animal cells employ flexible mechanisms for cleavage furrow positioning that facilitate error correction even in the relatively late stages of mitosis. Animal cells therefore use strategies #2 and #3 to determine the division plane and to position the actomyosin contractile ring at the cortex, integrating multiple spatial cues provided by the mitotic apparatus (reviewed in (von Dassow, 2009; Rappaport, 1996)).

This dissertation focuses on animal cells and how they specify their cytokinesis site. The focus will be on unusually large egg cells, exemplified by the frog egg. A priori, large egg cells might use a scaled-up version of the same cell division mechanisms used in somatic cells of the same organism, some variant of those mechanisms, or a completely different mechanism. The work described in this thesis, together with parallel effort from co-workers in our laboratory, has partly answered this question for the first time for frog eggs.

In the Introduction, I will first discuss the various positional cues provided by the mitotic apparatus in specifying the cleavage furrow and how their relative contribution could vary with cell size. I will then review the key molecular regulators of cytokinesis signaling and their roles in various animal model systems. Next, I will discuss the challenges of cleavage furrow positioning faced by very large cells, using eggs from the frog *Xenopus laevis* as a model system, and raise mechanistic questions regarding the spatial organization of cytokinesis signaling. Finally, I will outline the development of and the mechanistic insights gained from a cell-free system using *Xenopus* egg cytoplasm that reconstitutes the signaling processes involved in cleavage furrow specification.

Positional Cues from the Mitotic Apparatus in Animal Cytokinesis

Classical experiments in sea urchin eggs have established that the position of the mitotic apparatus determines the cleavage plane: when the spindle was displaced by

micromanipulation, the existing furrow regressed and a new furrow formed at the spindle midplane (Rappaport, 1985; Rappaport and Ebstein, 1965). Four spindle-derived spatial cues have been proposed to position the cleavage furrow in animal cells during anaphase (Burgess and Chang, 2005; Eggert et al., 2006). Positive cues lead to 'equatorial stimulation', while negative cues lead to 'polar relaxation' of the cortex (Figure 1.2). Positive cues for furrow induction include the midzone microtubules (Bement et al., 2005; Bonaccorsi et al., 1998; Bringmann and Hyman, 2005a; Cao and Wang, 1996), astral microtubules that reach the cortex at the cell midplane (Bringmann and Hyman, 2005b; Rappaport, 1961; Rappaport and Rappaport, 1985), and the chromosomes that load positive signals onto both midzone and astral microtubules at the cell midplane (Canman et al., 2003; Fuller et al., 2008; Hu et al., 2008). Negative cues from the astral microtubules that reach the cortex near the spindle poles are thought to locally inhibit cortical contractility (Hiramoto, 1990; White and Borisy, 1983).

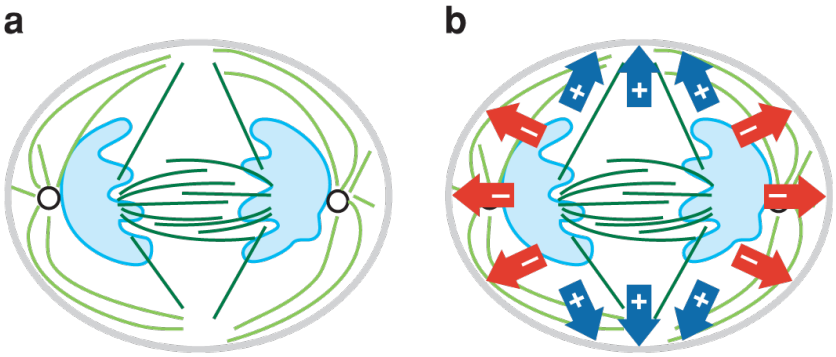

Figure 1.2: Organization of anaphase microtubule arrays and models for their roles in signaling to the cortex in animal cells. (**a**) In anaphase, astral microtubules (*light green*) emanate from the centrosomes (*circles*) and many of their plus ends reach the cortex. The midzone microtubule array (*dark green*) consists of bundled, overlapping microtubules that extend between the segregated chromatins (*light blue*). (**b**) Models of how anaphase microtubules signal to the cortex: equatorial stimulation signals (*blue arrows*) and polar relaxation signals (*red arrows*) are shown. Reprinted from (Eggert et al., 2006).

While the various models for cleavage plane positioning (equatorial stimulation vs. polar relaxation, midzone vs. asters) were once considered alternatives, we now believe that cells employ multiple overlapping signaling mechanisms, where no single positional cue is absolutely necessary. An animal cell will integrate information from all available signals to make a final decision about where to position the cleavage furrow. For example, in a classic experiment in sea urchin embryos, Rappaport induced a furrow between a pair of asters, where both chromosomes and midzone were absent (Rappaport, 1961). However, when faced with a decision whether to form a furrow between asters or at a midzone, *C. elegans* embryos pick the midzone as the dominant cue (Bringmann and Hyman, 2005b).

It has been proposed that the relative contribution from each positional cue varies depending on spindle-to-cell size ratio (von Dassow, 2009; Wang, 2001). Most somatic cells have a diameter of ~10-20 μm when rounded up during mitosis, and their metaphase spindle measures ~5-10 μm in length. This represents a 1:2 spindle-to-cell ratio. Spindle size does not scale with cell size infinitely, however. Wühr and colleagues have found an upper limit on spindle length (~60 μm) by measuring mitotic spindle lengths and cell sizes in early cleaving frog embryos (Wühr et al., 2008). Therefore, in large embryo cells, the larger the cell is, the smaller is its spindle-to-cell ratio (see Table 1.1).

Table 1.1: Estimates of spindle-to-cell size ratio for various animal cell model systems

Cell type	**Mitotic spindle length (μm)**	**Cell diameter (μm)**	**Spindle-to-cell ratio**
Somatic cell	5-10	10-20	1:2
C. elegans egg	25	50	1:2
Sea urchin egg	30	90	1:3
Zebrafish egg (*D. rerio*)	60	600	1:10
Frog egg (*X. laevis*)	60	1200	1:20
Sturgeon egg	?	4000	?

In small cells, the midzone and the chromosomes are thought to be the dominant furrow positioning cues. In large cells, where the spindle-to-cell size ratio is reduced, the asters' role becomes more important (von Dassow, 2009; Wang, 2001). Whether polar relaxation is a real phenomenon and its contribution towards furrow positioning is still unclear.

Key Molecular Regulators of Cytokinesis Signaling

Key proteins involved in cytokinesis have been previously identified by classical genetics and biochemistry, and more recently by chemical genetic and RNA interference (RNAi) screens (Echard et al., 2004; Eggert et al., 2004; Sönnichsen et al., 2005) as well as mass spectrometry-based proteomics (Skop et al., 2004). We now have an almost complete "parts list" (Eggert et al., 2006; Glotzer, 2005) and the challenge is to relate this list to biological mechanisms. For the scope of this dissertation, I am particularly interested in how some of these known proteins participate in the signaling processes between the mitotic apparatus and the cell cortex described above. Identifying the signals associated with the positive and negative positional cues, and the molecular mechanisms through which they are delivered and restricted to their target location, could explain why certain cues override others (e.g. midzone overrides asters (Bringmann and Hyman, 2005b)). It could also explain the cell size-dependent importance of each positional cue.

Figure 1.3 outlines an input-output model that I use to conceptualize and categorize candidate molecules for various roles in cytokinesis signaling. The output in this model is cleavage furrow induction at the cortex, the first step of which is thought to be activation of the small GTPase RhoA, a master organizer of the furrow (Bement et al., 2005; Drechsel et al., 1997; Jordan and Canman, 2012; Piekny et al., 2005; Zuo et al., 2014). The mechanism of RhoA activation is still not well understood. Several guanine nucleotide exchange factors (GEFs) are implicated in converting RhoA from its GDP-bound form to its active GTP-bound form (Figure 1.3; reviewed in (Jordan and Canman, 2012)). One protein that has emerged as

Figure 1.3: Molecular input-output model for cytokinesis signaling. *Output:* RhoA activation at the cell cortex that leads to actomyosin contractility. *Input:* positive signals that are associated with positive positional cues, i.e. midzone microtubules (MTs), astral MTs, and chromatin. The two putative signals we will consider here are the Chromosome Passenger Complex (CPC) and the Centralspindlin complex. *Spatial organizing mechanisms:* the overarching role of these mechanisms is to deliver the signals to a narrow band at the cleavage plane that reaches the cell cortex. Possible mechanisms: (a) directed transport towards MT plus ends, (b) recruitment to antiparallel microtubule overlaps, (c) lateral transfer from microtubules to microtubules that make contact through bending and/or buckling. Listed are the candidate microtubule associated proteins (MAPs) that we consider in this dissertation. Parts of the figure are adapted by permission from Macmillan Publishers Ltd: *Nature Cell Biology* (Fededa and Gerlich, 2012), © 2012.

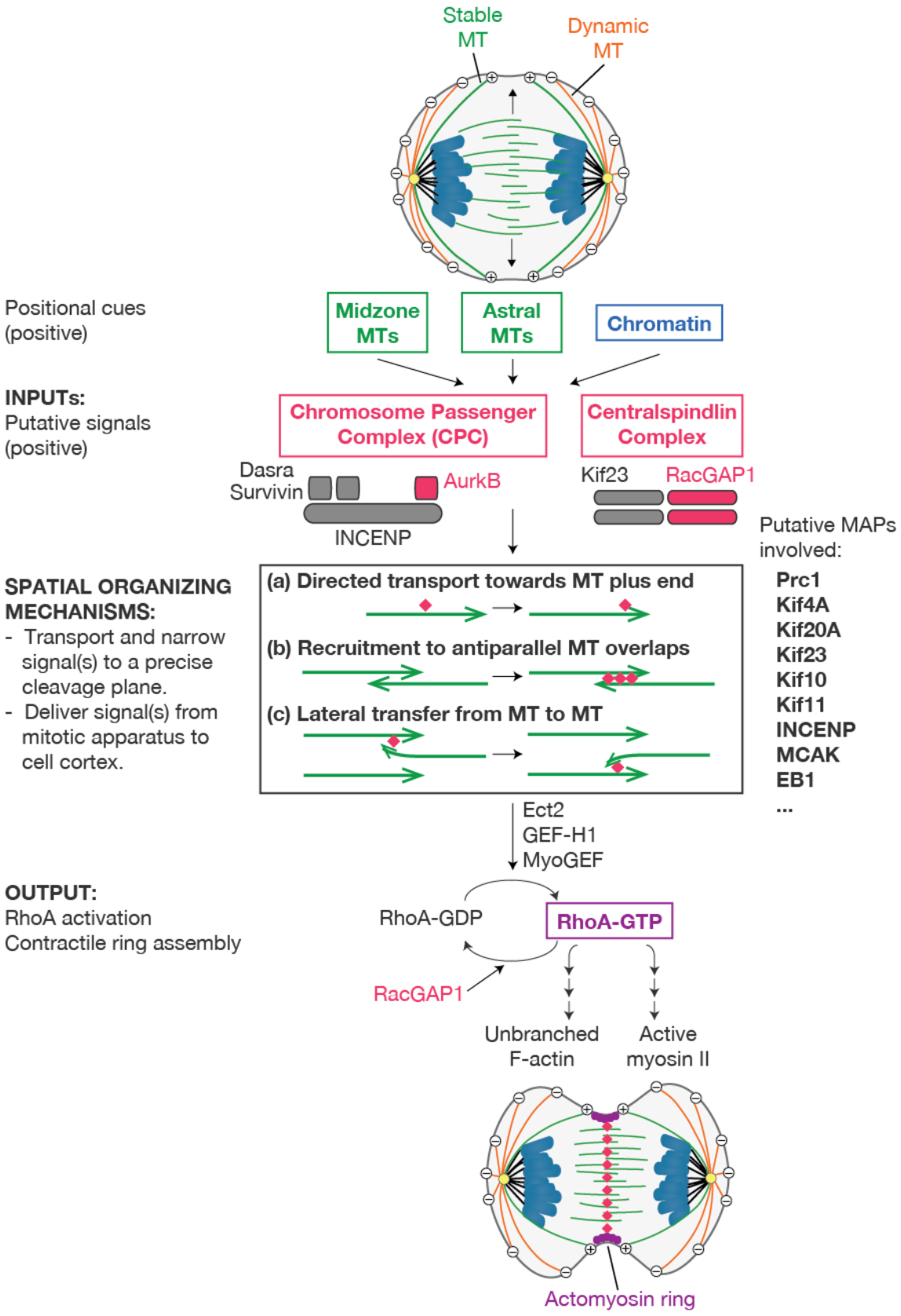

Figure 1.3 (Continued)

being crucial in many animal systems is Ect2, which is thought to be delivered to the cleavage plane by binding to the RacGAP1 subunit of the Centralspindlin complex (see below) (Kamijo et al., 2006; Loria et al., 2012; Nishimura and Yonemura, 2006; Wolfe et al., 2009; Yüce et al., 2005). The role of GTPase activating proteins (GAPs) that convert RhoA-GTP back to RhoA-GDP is even less understood. For example, RacGAP1 (or MgcRacGAP), a protein highly implicated in regulating RhoA activity, has in vitro GAP activity for other GTPases, but not for RhoA (reviewed in (Jordan and Canman, 2012)). Thus how its GAP activity regulates RhoA activity is still an active area of research.

For the inputs in this model, I am only considering putative signaling molecules associated with the positive positional cues, as molecular evidence for aster-mediated polar relaxation is still lacking. Two conserved signaling complexes have emerged as being critical for cleavage furrow induction: the Chromosome Passenger Complex (CPC; a 1:1:1:1 complex between INCENP, Aurora B kinase (AurkB), Dasra/Borealin and Survivin) and the Centralspindlin complex (a 2:2 complex between the plus end-directed kinesin MKLP1 (Kif23) and RacGAP1) (Figure 1.3) (Carmena et al., 2012; White and Glotzer, 2012). Both complexes can bind to microtubules and both localize to the spindle midzone after anaphase onset in somatic cells. The CPC can also bind to the chromosomes at the metaphase place (hence its name), and is therefore an attractive candidate for the positive signal associated with the chromosomes (Fuller et al., 2008). Centralspindlin received its name from its presumed essential role in assembly of the central spindle (another name for the midzone) (Mishima et al., 2002). The connection between Centralspindlin and RhoA activation has been much better studied due to its RacGAP1 subunit (see above). Less is known about the connection between CPC and RhoA regulation. In somatic cells undergoing drug-induced monopolar cytokinesis (Canman et al., 2003), AurkB but not Kif23 localizes to actin filaments in the gap region between the end of the polarized monopolar spindle and the plasma membrane (Hu et al., 2008). This

localization is dependent on the plus end-directed kinesin MKLP2 (or Kif20A), and is required for furrow propagation and completion in monopolar cytokinesis (Kitagawa et al., 2013).

The final component of this model is what connects the inputs to the output: spatial organizing mechanisms that make sure the positive signals are delivered to the right place (Figure 1.3). Specifically, the signaling molecule(s) must be transported to a narrow plane on midzone microtubule bundles in order to precisely specify the cleavage plane. Furthermore, they must somehow be delivered to the cell cortex to activate RhoA and induce furrow assembly. A priori, three main microtubule-mediated mechanisms of transport can be proposed: (a) directed transport towards microtubule plus ends by motors, (b) recruitment to antiparallel microtubule overlaps by microtubule crosslinkers, (c) lateral transfer from microtubules to microtubules that make contact through bending and/or buckling. A list of candidate microtubule associated proteins (MAPs) involved in processes is provided and the individual proteins will be introduced in subsequent chapters where it is appropriate.

Cytokinesis Signaling in Very Large Animal Cells

Eggs of the frog *Xenopus laevis* are among the largest fully cleaving cells (see Table 1.1) and face unique challenges in their cytoplasmic organization (reviewed in (Ishihara et al., 2014; Mitchison et al., 2012; Wühr et al., 2009)). One major challenge is: how does the relatively small mitotic apparatus, a 60 μm-long spindle (Wühr et al., 2008), specify the cytokinetic apparatus, a contractile ring with an initial radius of 600 μm (Figure 1.4A)? Unlike smaller somatic cells, these large embryonic cells cannot solely rely on the spindle midzone to position the division plane and to deliver cytokinesis signals to the cortex. Previously, Martin Wühr's work in the Mitchison lab established the importance of microtubule asters, huge radial arrays of microtubules that emanate from the spindle poles, in determining the cleavage plane (Figure 1.4, B and C) (Wühr et al., 2010).

Theories have proposed that in large cells, asters deliver factors by microtubule-based

transport to the equatorial cortex where they stimulate cleavage (Atilgan et al., 2012; Devore et al., 1989). Due to difficulty of imaging and molecular perturbation in large eggs, the precise identity of these signals and how they are transported on microtubules had been largely unknown. In order to circumvent the challenges of working with intact eggs, my co-workers and I have developed an egg extract-based system that for the first time reconstituted the full complexity of cytokinesis signaling events outside of a real cell (Nguyen, Groen et al., 2014). While an extract system has been available to study metaphase spindles for more than two decades (Sawin and Mitchison, 1991), the cytokinesis field had been waiting for a similar, biochemically tractable extract system to be reported. Chapter Two describes this cell-free system and addresses questions regarding signal identity and transport.

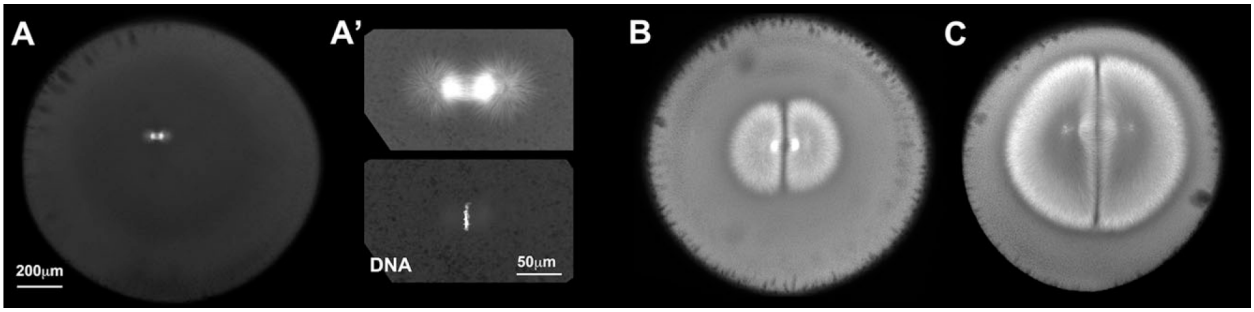

Figure 1.4: Growth and interaction of sister asters in the first two divisions in *X. laevis*. Fertilized eggs were fixed, stained for tubulin (A, A' upper, B, and C) and DNA (A' lower) as described (Wühr et al., 2010). The animal half of the egg was cut off and imaged from the cut surface, so the z-axis is parallel to the animal-vegetal axis of the zygote. (**A, A'**) Metaphase of first mitosis. Note the small mitotic spindle (~60 μm) compared to the large cell diameter (~1200 μm). Also note small asters in metaphase. (**B**) Anaphase–telophase of first mitosis. Note aster growth and formation of an interaction zone between sister asters at mid-cell. (C) later telophase. Note the dense, bushy appearance of microtubules at the aster periphery and low microtubule density in the interaction zone. Adapted from (Mitchison et al., 2012).

As described in Chapter Two, we found that cytokinesis signals were indeed localized to the interaction zone that forms where asters emanating from the spindle poles meet. We termed

this microtubule structure the aster-aster interaction zone (AAIZ). In order for the signaling molecules to be restricted to a precise, narrow plane that marks the putative cleavage furrow, the AAIZ structure must be established and maintained in such a way as to demarcate a clear intracellular boundary. This raises the question: what happens when two neighboring asters grow to touch each other?

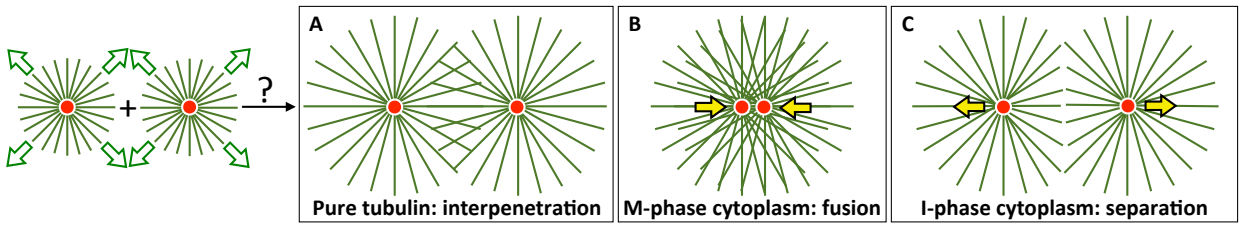

Figure 1.5: Consequences of aster-aster interaction depend on the system. Possible branching nucleation is omitted for simplicity. (**A**) In pure tubulin, plus ends simply grow past each other (Brinkley et al., 1981). (**B**) In metaphase (M-phase) extract prepared from unfertilized *Xenopus* eggs, asters (and spindles) that touch each other adhere, move together, and fuse. Movement is driven by dynein, which is thought to cross-bridge antiparallel microtubules (Gatlin et al., 2009). (**C**) In interphase (I-phase) in early embryos, growing asters interact to generate a zone of antiparallel overlap and low microtubule density at their mutual boundary, called an aster-aster interaction zone (AAIZ). The asters then tend to move apart, pulled by cytoplasmic dynein anchored in bulk cytoplasm (Wühr et al., 2010). A block to microtubule interpenetration during anaphase-telophase was also noted in a classic EM study in echinoderm embryos (Asnes and Schroeder, 1979). Adapted from (Mitchison et al., 2012).

Beyond cell division, this is a central question in spatial organization of any cell with two or more centrosomes, such as egg cells undergoing polyspermic fertilization or multinucleated syncytial cells (e.g. muscle myofibers, bone osteoclasts, placental synsytiotrophoblasts, fungal hyphae). Figure 1.5 shows three possibilities drawn from the literature, where the consequence of aster–aster interaction depends strongly on the system and cell cycle state. When asters grow from nearby centrosomes in pure tubulin, their microtubules simply interpenetrate (Figure

1.5A) (Brinkley et al., 1981). When two asters meet in mitotic Xenopus egg extract, they adhere, then move together and fuse due to dynein activity (Figure 1.5B) (Gatlin et al., 2009). When two asters meet during interphase in frog and fish embryos, their microtubules do not interpenetrate and the asters move apart (Figure 1.5C) (Wühr et al., 2010). Aster movement is again driven by dynein, but in this case the dynein is presumably anchored in the cytoplasm rather than to another microtubule, so it produces force in the opposite direction (reviewed in (Mitchison et al., 2012). The molecular mechanisms underlying the block to interpenetration had been unclear and are the focus of Chapter Three.

My investigations into the mechanisms regulating aster-aster interactions were highly confounded by the fact that not all interactions are equivalent in frog eggs. Unlike echinoderm embryos, frog embryos cannot form so-called 'Rappaport furrows'. In his famous toroidal cell experiment in echinoderm embryos, Rappaport observed that neighboring pairs of asters could induce furrows regardless of whether the asters arose from the poles of the same spindle ('sister' asters) or from juxtaposed poles of two different spindles ('non-sister' asters). The furrow between non-sister asters was recorded in history as the 'Rappaport furrow'. In polyspermic frog embryos, however, furrows are induced only where the AAIZs between sister asters, but not non-sister asters, reach the cortex after 1st mitosis (Figure 1.6, A-C) (Render and Elinson, 1986; Wakabayashi and Shinagawa, 2001). While AAIZs between both sister and non-sister asters are very similar in terms of microtubule morphology (Figure 1.6D), the fact that one induces furrows while the other does not suggests that they are different molecularly.

Chapter Four addresses this difference and reveals insights about the contributions from positional cues other than asters in directing cleavage furrow positioning.

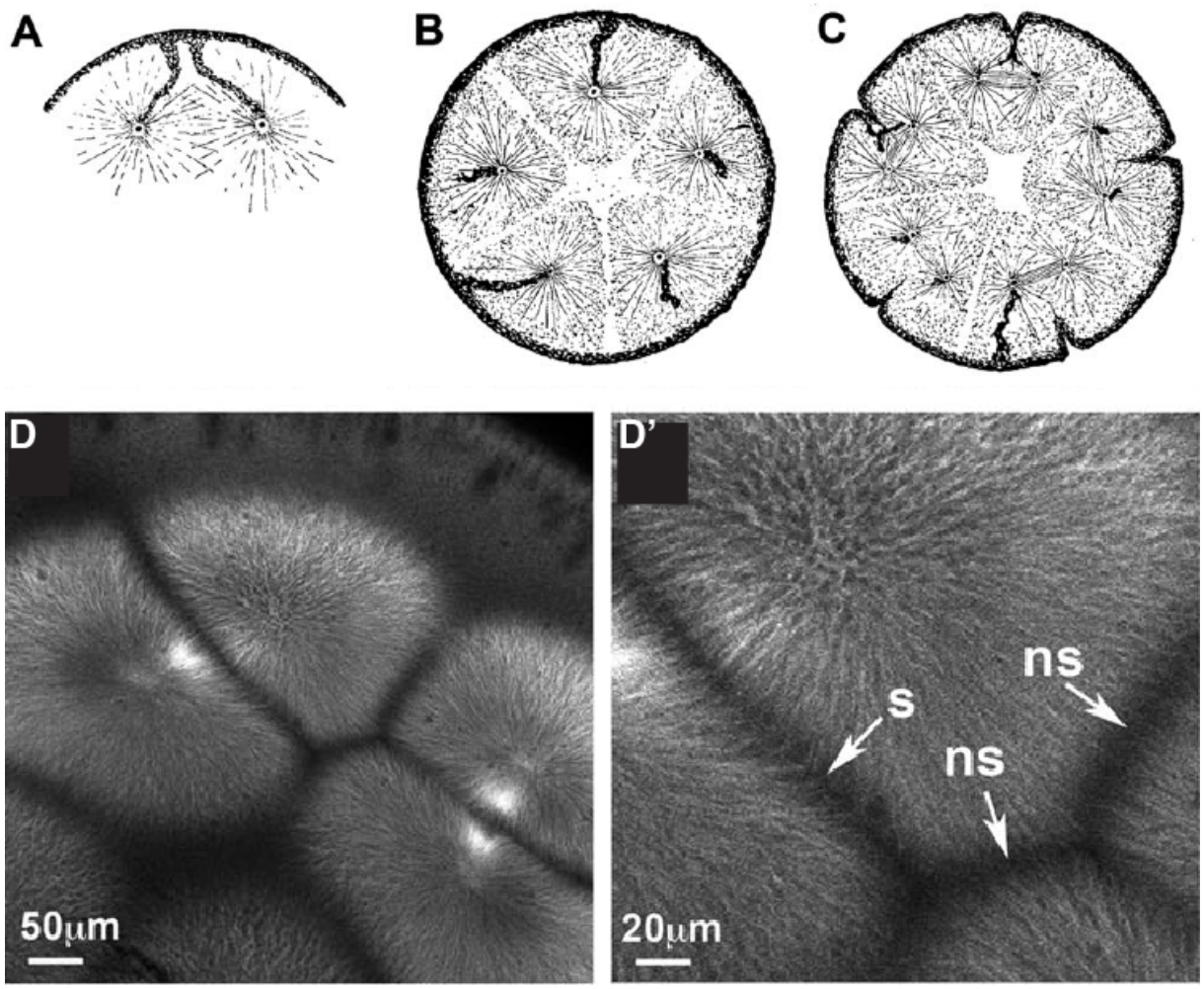

Figure 1.6: Interaction of non-sister asters following polyspermic fertilization in amphibian embryos. (**A-C**) Sequential stages from fertilization to 1st cleavage following forced polyspermy in the frog *R. fusca*. Images drawn from histological sections (Brachet, 1910). (**D**) Tubulin staining in fixed polyspermic *X, laevis* embryo. (**A**) Neighboring sperm asters move apart as they center within the egg. (**B**) Asters tend to space out regularly before 1st mitosis, dividing the cytoplasm into regularly spaced units. (**C**) Cleavage furrows are induced between sister asters at 1st cleavage in *R. fusca*, while zones between non-sisters do not. The same is true in *X. laevis* (Render and Elinson, 1986; Wakabayashi and Shinagawa, 2001). (**D, D'**) Forced polyspermy in *X. laevis* after anaphase of 1st mitosis but before furrow induction. Two pairs of sister asters can be recognized in **D** by the brighter bundles of microtubules at the center of the interaction zone where the metaphase spindle used to be. Note the sharply defined interaction zones between both sister and non-sister asters. **D'** is a higher mag. view from **D** where (s) denotes interaction zones between sister asters, and (ns) between non-sister asters. Adapted from (Mitchison et al., 2012).

Scope of Dissertation

To study the spatial organizing principles of cytokinesis signaling, my collaborators and I have developed a cell-free system that can reconstitutes these processes outside of a real cell (described in Chapter Two). This system has allowed us to address several mechanistic questions related to cleavage furrow positioning in the unusually large egg cells of the frog. Future studies are required to determine which of these mechanisms are conserved among all animal cells, and which are evolutionary adaptations specific to the large frog egg.

Questions addressed in Chapter Two:

1) What is the positive furrow signal delivered by the large asters to the cell cortex in frog eggs?
2) How is the furrow signal delivered to the equatorial plane and the cortex?

Questions addressed in Chapter Three:

1) How is the asters-aster interaction zone formed and maintained?
    a. How do asters recognize each other?
    b. How are they prevented from growing into each other and therefore maintain a clear boundary?
2) What is the microtubule dynamics at aster-aster interaction zones? Is there evidence for stabilization of microtubules?

Questions addressed in Chapter Four:

1) Why Rappaport furrows (i.e. induced by asters without midzone or chromatin between them) do not form in polyspermic frog embryos?
2) Under what conditions are aster-aster interaction zones sufficient to induce a cleavage furrow?
3) How do the other positional cues, such as the chromosomes, contribute towards furrow induction?

References

Asnes, C.F., and Schroeder, T.E. (1979). Cell cleavage. Ultrastructural evidence against equatorial stimulation by aster microtubules. Exp Cell Res *122*, 327–338.

Atilgan, E., Burgess, D., and Chang, F. (2012). Localization of cytokinesis factors to the future cell division site by microtubule-dependent transport. Cytoskeleton (Hoboken) *69*, 973–982.

Balasubramanian, M.K., Bi, E., and Glotzer, M. (2004). Comparative analysis of cytokinesis in budding yeast, fission yeast and animal cells. Curr Biol *14*, R806–R818.

Barr, F.A., and Grüneberg, U. (2007). Cytokinesis: placing and making the final cut. Cell *131*, 847–860.

Bement, W.M., Benink, H.A., and von Dassow, G. (2005). A microtubule-dependent zone of active RhoA during cleavage plane specification. J Cell Biol *170*, 91–101.

Bonaccorsi, S., Giansanti, M.G., and Gatti, M. (1998). Spindle self-organization and cytokinesis during male meiosis in asterless mutants of Drosophila melanogaster. J Cell Biol *142*, 751–761.

Brachet, A. (1910). La polyspermie expérimentale comme moyen d“analyse de la fe”condation. Development Genes and Evolution *30*, 261–303.

Bringmann, H., and Hyman, A.A. (2005a). A cytokinesis furrow is positioned by two consecutive signals. Nature *436*, 731–734.

Bringmann, H., and Hyman, A.A. (2005b). A cytokinesis furrow is positioned by two consecutive signals. Nat Cell Biol *436*, 731–734.

Brinkley, B.R., Cox, S.M., Pepper, D.A., Wible, L., Brenner, S.L., and Pardue, R.L. (1981). Tubulin assembly sites and the organization of cytoplasmic microtubules in cultured mammalian cells. J Cell Biol *90*, 554–562.

Burgess, D.R., and Chang, F. (2005). Site selection for the cleavage furrow at cytokinesis. Trends Cell Biol *15*, 156–162.

Busiek, K.K., and Margolin, W. (2015). Bacterial actin and tubulin homologs in cell growth and division. Curr Biol *25*, R243–R254.

Canman, J.C., Cameron, L.A., Maddox, P.S., Straight, A., Tirnauer, J.S., Mitchison, T.J., Fang, G., Kapoor, T.M., and Salmon, E.D. (2003). Determining the position of the cell division plane. Nature *424*, 1074–1078.

Cao, L.G., and Wang, Y.L. (1996). Signals from the spindle midzone are required for the stimulation of cytokinesis in cultured epithelial cells. Mol Biol Cell *7*, 225–232.

Carmena, M., Wheelock, M., Funabiki, H., and Earnshaw, W.C. (2012). The chromosomal passenger complex (CPC): from easy rider to the godfather of mitosis. Nat Rev Mol Cell Biol *13*, 789–803.

von Dassow, G. (2009). Concurrent cues for cytokinetic furrow induction in animal cells. Trends Cell Biol *19*, 165–173.

Devore, J.J., Conrad, G.W., and Rappaport, R. (1989). A model for astral stimulation of cytokinesis in animal cells. J Cell Biol *109*, 2225–2232.

Drechsel, D.N., Hyman, A.A., Hall, A., and Glotzer, M. (1997). A requirement for Rho and Cdc42 during cytokinesis in Xenopus embryos. Curr Biol *7*, 12–23.

Echard, A., Hickson, G.R.X., Foley, E., and O'Farrell, P.H. (2004). Terminal cytokinesis events uncovered after an RNAi screen. Curr Biol *14*, 1685–1693.

Eggert, U.S., Kiger, A.A., Richter, C., Perlman, Z.E., Perrimon, N., Mitchison, T.J., and Field, C.M. (2004). Parallel chemical genetic and genome-wide RNAi screens identify cytokinesis inhibitors and targets. PLoS Biol *2*, e379.

Eggert, U.S., Mitchison, T.J., and Field, C.M. (2006). Animal cytokinesis: from parts list to mechanisms. Annu Rev Biochem *75*, 543–566.

Fededa, J.P., and Gerlich, D.W. (2012). Molecular control of animal cell cytokinesis. Nat Cell Biol *14*, 440–447.

Fuller, B.G., Lampson, M.A., Foley, E.A., Rosasco-Nitcher, S., Le, K.V., Tobelmann, P., Brautigan, D.L., Stukenberg, P.T., and Kapoor, T.M. (2008). Midzone activation of aurora B in anaphase produces an intracellular phosphorylation gradient. Nature *453*, 1132.

Gatlin, J.C., Matov, A., Groen, A.C., Needleman, D.J., Maresca, T.J., Danuser, G., Mitchison, T.J., and Salmon, E.D. (2009). Spindle fusion requires dynein-mediated sliding of oppositely oriented microtubules. Curr Biol *19*, 287–296.

Glotzer, M. (2005). The molecular requirements for cytokinesis. Science *307*, 1735–1739.

Hiramoto, Y. (1990). Mechanical properties of the cortex before and during cleavage. Ann N Y Acad Sci *582*, 22–30.

Hu, C.-K., Coughlin, M., Field, C.M., and Mitchison, T.J. (2008). Cell polarization during monopolar cytokinesis. J Cell Biol *181*, 195–202.

Ishihara, K., Nguyen, P.A., Wühr, M., Groen, A.C., Field, C.M., and Mitchison, T.J. (2014). Organization of early frog embryos by chemical waves emanating from centrosomes. Philos. Trans. R. Soc. Lond., B, Biol. Sci. *369*.

Jordan, S.N., and Canman, J.C. (2012). Rho GTPases in animal cell cytokinesis: an occupation by the one percent. Cytoskeleton (Hoboken) *69*, 919–930.

Kamijo, K., Ohara, N., Abe, M., Uchimura, T., Hosoya, H., Lee, J.-S., and Miki, T. (2006). Dissecting the role of Rho-mediated signaling in contractile ring formation. Mol Biol Cell *17*, 43–55.

Kitagawa, M., Fung, S.Y.S., Onishi, N., Saya, H., and Lee, S.H. (2013). Targeting Aurora B to the equatorial cortex by MKlp2 is required for cytokinesis. PLoS ONE *8*, e64826.

Loria, A., Longhini, K.M., and Glotzer, M. (2012). The RhoGAP domain of CYK-4 has an essential role in RhoA activation. Curr Biol *22*, 213–219.

Mishima, M., Kaitna, S., and Glotzer, M. (2002). Central spindle assembly and cytokinesis require a kinesin-like protein/RhoGAP complex with microtubule bundling activity. Dev Cell *2*, 41–54.

Mitchison, T., Wühr, M., Nguyen, P., Ishihara, K., Groen, A., and Field, C.M. (2012). Growth, interaction, and positioning of microtubule asters in extremely large vertebrate embryo cells. Cytoskeleton (Hoboken) *69*, 738–750.

Murata, T., and Wada, M. (1991). Effects of centrifugation on preprophase-band formation in Adiantum protonemata. Planta *183*, 391–398.

Müller, S. (2012). Universal rules for division plane selection in plants. Protoplasma *249*, 239–253.

Müller, S., Wright, A.J., and Smith, L.G. (2009). Division plane control in plants: new players in the band. Trends Cell Biol *19*, 180–188.

Nguyen, P.A., Groen, A.C., Loose, M., Ishihara, K., Wühr, M., Field, C.M., and Mitchison, T.J. (2014). Spatial organization of cytokinesis signaling reconstituted in a cell-free system. Science *346*, 244–247.

Nishimura, Y., and Yonemura, S. (2006). Centralspindlin regulates ECT2 and RhoA accumulation at the equatorial cortex during cytokinesis. J Cell Sci *119*, 104–114.

Oliferenko, S., Chew, T.G., and Balasubramanian, M.K. (2009). Positioning cytokinesis. Genes Dev *23*, 660–674.

Piekny, A., Werner, M., and Glotzer, M. (2005). Cytokinesis: welcome to the Rho zone. Trends Cell Biol *15*, 651–658.

Rappaport, R. (1961). Experiments concerning the cleavage stimulus in sand dollar eggs. J Exp Zool *148*, 81–89.

Rappaport, R. (1985). Repeated furrow formation from a single mitotic apparatus in cylindrical sand dollar eggs. J Exp Zool *234*, 167–171.

Rappaport, R. (1996). Cytokinesis in animal cells (Cambridge; New York: Cambridge University Press).

Rappaport, R., and Ebstein, R.P. (1965). Duration of stimulus and latent periods preceding furrow formation in sand dollar eggs. J Exp Zool *158*, 373–382.

Rappaport, R., and Rappaport, B. (1985). Surface contractile activity associated with isolated asters in cylindrical sand dollar eggs. J Exp Zool *235*, 217–226.

Render, J.A., and Elinson, R.P. (1986). Axis determination in polyspermic Xenopus laevis eggs. Dev Biol *115*, 425–433.

Sawin, K.E., and Mitchison, T.J. (1991). Mitotic spindle assembly by two different pathways in vitro. J Cell Biol *112*, 925–940.

Skop, A.R., Liu, H., Yates, J., Meyer, B.J., and Heald, R. (2004). Dissection of the mammalian midbody proteome reveals conserved cytokinesis mechanisms. Science *305*, 61–66.

Sönnichsen, B., Koski, L.B., Walsh, A., Marschall, P., Neumann, B., Brehm, M., Alleaume, A.M., Artelt, J., Bettencourt, P., Cassin, E., et al. (2005). Full-genome RNAi profiling of early embryogenesis in Caenorhabditis elegans. Nature *434*, 462–469.

Wakabayashi, Y., and Shinagawa, A. (2001). Presence of a nucleus or nucleus-deriving factors is indispensable for the formation of the spindle, the diastema and the cleavage furrow in the blastomere of the Xenopus embryo. Dev Growth Differ *43*, 633–646.

Wang, Y.L. (2001). The mechanism of cytokinesis: reconsideration and reconciliation. Cell Struct. Funct. *26*, 633–638.

White, E.A., and Glotzer, M. (2012). Centralspindlin: at the heart of cytokinesis. Cytoskeleton (Hoboken) *69*, 882–892.

White, J.G., and Borisy, G.G. (1983). On the mechanisms of cytokinesis in animal cells. J Theor Biol *101*, 289–316.

Wilson, E.B. (1928). The cell in development and heredity (New York: The Macmillan Co.).

Wolfe, B.A., Takaki, T., Petronczki, M., and Glotzer, M. (2009). Polo-like kinase 1 directs assembly of the HsCyk-4 RhoGAP/Ect2 RhoGEF complex to initiate cleavage furrow formation. PLoS Biol *7*, e1000110.

Wühr, M., Chen, Y., Dumont, S., Groen, A.C., Needleman, D.J., Salic, A., and Mitchison, T.J. (2008). Evidence for an upper limit to mitotic spindle length. Curr Biol *18*, 1256–1261.

Wühr, M., Dumont, S., Groen, A.C., Needleman, D.J., and Mitchison, T.J. (2009). How does a millimeter-sized cell find its center? Cell Cycle *8*, 1115–1121.

Wühr, M., Tan, E.S., Parker, S.K., Detrich, H.W., and Mitchison, T.J. (2010). A model for cleavage plane determination in early amphibian and fish embryos. Curr Biol *20*, 2040–2045.

Yüce, O., Piekny, A., and Glotzer, M. (2005). An ECT2-centralspindlin complex regulates the localization and function of RhoA. J Cell Biol *170*, 571–582.

Zuo, Y., Oh, W., and Frost, J.A. (2014). Controlling the switches: Rho GTPase regulation during animal cell mitosis. Cell Signal *26*, 2998–3006.

Chapter Two

Cell-Free Reconstitution of Cytokinesis Signaling

Citation. This chapter was assembled with modifications from the final as well as earlier, longer versions of the following published manuscript:

Science **346***,* 244-247 (2014)

Spatial Organization of Cytokinesis Signaling Reconstituted in a Cell-Free System

Phuong A. Nguyen[1,2]†, Aaron C. Groen[1,2]†, Martin Loose[1], Keisuke Ishihara[1,2], Martin Wühr[1], Christine M. Field[1,2]‡, Timothy J. Mitchison[1,2]‡

[1]Department of Systems Biology, Harvard Medical School, Boston, MA 02115, USA.
[2]Marine Biological Laboratory, Woods Hole, MA 02543, USA.
† Co-first authors.
‡ Co-senior authors.

Contributions. This was a highly collaborative project and would have been impossible without the contribution from many excellent scientists. I feel very grateful to have been able to work with them.

Methods. Drs. Christine Field, Timothy Mitchison and I worked together to develop the interphase aster assembly assay starting in 2009. Initially, Drs. Field and Mitchison used demembranated sperm with attached centrosome to nucleate microtubule asters in calcium-activated Xenopus egg extract, then imaged the asters between uncoated or casein-coated glass coverslips. I introduced the use of PEG-passivated coverslips, which allowed for reproducible aster morphology, and reliable localization and inhibition of proteins or protein complexes that would otherwise adsorb to the uncoated glass surface. To circumvent the effect of sperm chromosomes on microtubule morphology, I initially used purified centrosomes as

microtubule nucleating centers. Later, Drs. Field and Mitchison introduced the Aurora A kinase-based artificial centrosome beads in the system. I also developed the conditions for imaging asters with TIRF microscopy (kappa-casein coating of bottom coverslip, PEG-coating of top coverslips, combined with dynein inhibition). Dr. Aaron Groen helped optimize the protocol for extract preparation with intact actin by modifying centrifugation conditions. Dr. Field introduced the use of fluorescently labeled Fab fragments coupled with target-specific antibodies to visualize certain proteins (e.g. Aurora kinase B, Kif23) in extract. This approach was later replaced by using directly labeled antibodies, whose labeling protocol was developed by Dr. Mitchison. We published these developments in the following methods paper:

Field, C.M., Nguyen, P.A., Ishihara, K., Groen, A.C., and Mitchison, T.J. (2014). Xenopus egg cytoplasm with intact actin. Meth Enzymol *540*, 399–415.

Dr. Martin Loose and I worked together to develop a supported lipid bilayer system that would be stable when combined with the Xenopus egg extract system; Dr. Field initiated and supervised this project. Dr. Loose came up with the initial lipid composition (70% PC, 29% PS, 1% $PI(4,5)P_2$) based on a previous publication, which Dr. Field and I later modified to support reproducible RhoA activation. Rotation student Himanish Basu helped optimize the buffer conditions for lipid bilayer assembly, and found that addition of sucrose was beneficial. I confirmed this finding and also found that increasing the salt concentration helped too. Dr. Field and I optimized glass cleaning procedures. We published these developments in the following methods paper:

Nguyen, P.A., Field, C.M., Groen, A.C., Mitchison, T.J., and Loose, M. (2015). Using supported bilayers to study the spatiotemporal organization of membrane-bound proteins. Methods Cell Biol *128*, 223–241.

Reagents. While Dr. Martin Wühr was building a mass spectrometry-based proteomic database of all proteins found in *Xenopus* eggs and embryos at various developmental stages, he pointed out Kif20AE as a kinesin highly abundant in early *Xenopus* development. I designed and ordered the affinity purified C-terminal peptide antibodies against *X. laevis* Kif23, Kif20A, and Kif20AE. The Kif23 and Kif20AE antibodies worked for immunofluorescence (in both extract and egg) and immunoblot, but less so for immunodepletion. Thus Dr. Groen proceeded to make antibodies against longer C-terminal fragments of these kinesins with the help of Dr. Edwin Tan. Dr. Groen also made the antibodies against *X. laevis* Aurora A kinase, which we initially received from Dr. Yixian Zheng. I inherited the *X. laevis* Kif4A antibodies from Dr. David Miyamoto, and when we ran out of the antibodies, I purified them from stored sera. Dr. Mitchison performed the on-column labeling of antibodies.

I made the baculovirus for Kif4A-GFP expression using an expression plasmid from Dr. Thomas Surrey, and purified the protein from Sf21 insect cells. I cloned and purified the GFP-PRC1E protein. Dr. Groen cloned and purified the RhoA-GTP reporter (mCherry-rGBD). I designed the DasraA constructs with the purpose of visualizing the CPC without using antibodies, and purchased the cDNA and the primers. Dr. Aaron Groen carried out the subcloning and purification of the GFP-DasraA protein.

Drs. Groen and Dr. Edwin Tan helped me with tubulin preparation from bovine brains, and labeling tubulin with fluorophores.

Experiments. I conducted all the experiments and analyses described in this chapter except for the following:

Dr. Groen and I designed the experiment testing the role of various kinesins in CPC recruitment and motility (Figure 2.6, A and B, and Figure S2.4). I had previously made the observation that Kif4A depletion leads to lack of CPC movement, so we proceeded to test the

role of other kinesins. Specifically, Dr. Groen acquired the data for Kif23, Kif20AE, Kif20A depletion, and Kif10, Kif11 inhibition.

Dr, Groen acquired the time-lapse sequence shown in Figures 2.2 and S2.1A. While I had previously acquired imaged many image sequences of aster-aster interactions, this sequence was particularly beautiful and showcased the resemblance to cytokinesis zones in dividing embryos the best. Dr. Groen also provided the data for Figure 2.6C.

Drs. Field and Mitchison performed the fertilization and immunofluorescence of *Xenopus* zygotes with advice from Dr. Wühr (Figures 2.3 and 2.5). Dr. Groen microinjected the zygotes with the Aurora B kinase inhibitor (Figure 2.5).

The supported lipid bilayer experiments (Figures 2.7 and 2.8) were two-person experiments. I worked with either Dr. Groen or Dr. Field. When working with Dr. Groen, I made the bilayer, he made the extract, I prepared the sample, and he and I imaged (data shown in Figure 2.8). When working with Dr. Field, I made the extract, she made the bilayer, and I prepared and imaged the sample. For the immunodepletion experiments shown in Figure 2.7C, either Dr. Groen or I carried out the depletion.

Keisuke Ishihara helped with setting up the lab at Woods Hole, moving and organizing reagents, frog maintenance, extract reagents and preparation, and critical reading of the manuscript.

Writing. I made all the figures, tables, and movies except for Figure 2.3 (by Dr. Mitchison and Field) and Figure 2.5 (by Dr. Field). Dr. Groen, Dr Mitchison and I wrote the manuscript with significant contributions from Drs. Loose and Field.

Supplemental materials. Materials and Methods, Supplementary Figures, Tables and Movies for this chapter can be found in Appendix I.

Abstract

During animal cell division, the cleavage furrow is positioned by microtubules that signal to the actin cortex, inducing cortical contraction at the cell midplane. Molecular genetics has revealed the key signaling molecules, but it has been difficult to assign precise spatiotemporal functions to them. Here, we developed a cell-free system to recapitulate cytokinesis signaling using cytoplasmic extract from *Xenopus* eggs. Microtubules grew out as asters from artificial centrosomes and met to organize antiparallel overlap zones. These zones blocked interpenetration of neighboring asters and recruited cytokinesis midzone proteins including the Chromosomal Passenger Complex (CPC) and Centralspindlin. The CPC was transported to overlap zones, which required two motor proteins, Kif4A and a Kif20A paralog. Using supported lipid bilayers to mimic the plasma membrane, we observed recruitment of cleavage furrow markers, including a RhoA-GTP reporter, at microtubule overlaps. This system opens further approaches to understanding the biophysics of cytokinesis signaling.

Introduction

Actomyosin-based cleavage furrows in animal cells are positioned by signals emanating from microtubule assemblies formed shortly after anaphase onset (Rappaport, 1996). In typical somatic cells, the signaling complexes Centralspindlin and CPC (Chromosomal Passenger Complex) accumulate at the center of a microtubule structure called the midzone (or central spindle), which forms in the space previously occupied by the mitotic spindle (Carmena et al., 2012; Glotzer, 2005; Mastronarde et al., 1993; White and Glotzer, 2012). It is unclear how the microtubules that position furrows are organized in much larger egg cells, and how they signal to the cortex (Mitchison et al., 2012; Wühr et al., 2009). We addressed these questions by developing a cell-free system to reconstitute the spatial signaling characteristic of cytokinesis in a large egg cell.

Results and Discussion

Cell-free system that reconstitutes cytokinesis signaling

Cytoplasmic extracts prepared from unfertilized *Xenopus laevis* eggs by centrifugal crushing contain undiluted cytosol and organelles, and have long provided a system for accurate reconstitution of meiosis-II spindles (Sawin and Mitchison, 1991). To extend this system to reconstitution of cytokinesis events, we prepared undiluted egg cytoplasm with intact actin (Field et al., 2014). We then added fluorescent probes and beads coated with an activating antibody to Aurora kinase A (AurkA), which mimic centrosomes without chromosomes attached (Tsai and Zheng, 2005). Extract was released from meiotic arrest by a Ca^{2+} pulse, which mimics fertilization, and immediately spread between two passivated coverslips to a ~10-15 μm thickness for imaging (Figure 2.1).

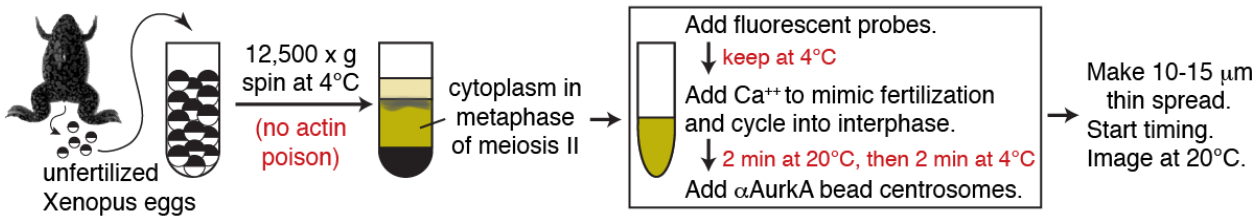

Figure 2.1: Workflow of interphase aster assembly assay in *Xenopus* egg cytoplasm. Undiluted cytoplasm with intact actin was prepared from *Xenopus* eggs (Field et al., 2014). Extract was supplemented with fluorescent probes and then released from meiotic arrest into interphase by calcium addition, which mimics fertilization. Beads coated with Aurora A kinase (AurkA) antibody that mimic centrosomes (Tsai and Zheng, 2005) were added, a thin extract layer was spread between PEG-passivated coverslips and immediately imaged.

A description of the cell cycle state of our extract system can be found in our recent methods paper (Field et al., 2014). Judging by immunoblots of proteins that report on Cdk1 phosphorylation status, some mitotic Cdk1 sites were lost as soon as 5 min after calcium addition, while others took up to 20 min to be lost. These findings are consistent with previous observations that different Cdk1 substrates are dephosphorylated at different rates following the fertilization-induced calcium pulse, which breaks the arrest at metaphase of meiosis II (cytostatic factor (CSF)-arrested state) (Lorca et al., 1993; Mochida and Hunt, 2007; Nishiyama et al., 2007; Rauh et al., 2005). We conclude that calcium addition caused the extract to begin to enter the interphase state within a few minutes, but that the full interphase state was not reached until approximately 20 min after calcium addition.

As the cell cycle progressed from metaphase to interphase, large microtubule asters grew out rapidly from each AurkA bead. Where the expanding edges of two neighboring asters met, antiparallel microtubule bundles formed in a boundary zone that we term the aster-aster interaction zone (AAIZ) (Figure 2.2, Figure S2.1A, and Movie S2.1). AAIZs started forming after about 15 min, and remained for at least 20 min (Figure S2.1B), so their assembly occurred in the full interphase state. In somatic cells, the CPC and Centralspindlin complexes are recruited

to the midplane in anaphase where they specify the division plane by activating the small GTPase RhoA at the cortex (Asiedu et al., 2008; Kamijo et al., 2006; Kitagawa et al., 2013; Nishimura and Yonemura, 2006; Wu et al., 2014; Yüce et al., 2005). We imaged endogenous complexes by adding labeled antibodies, and for the CPC confirmed localization with a GFP tagged DasraA subunit. CPC and the Kif23 subunit of Centralspindlin were recruited to the AAIZ in a 5-15 µm wide line bisecting the line between two AurkA beads (Figure 2.2, B and C; Figure S2.1, A and B). This is the first time co-recruitment of conserved cytokinesis midzone complexes has been observed in a cell-free system.

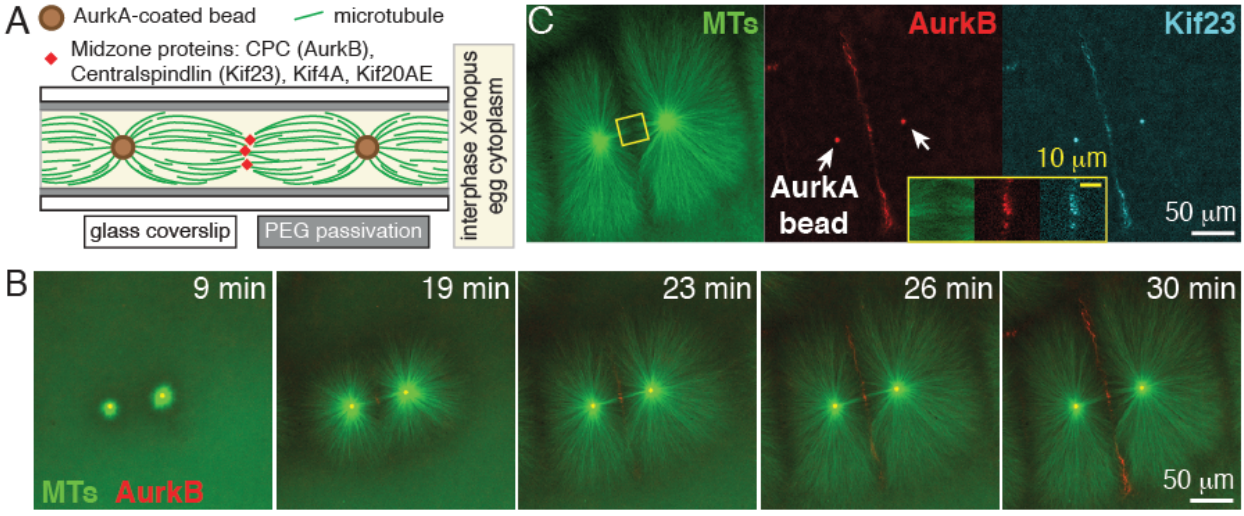

Figure 2.2: Aster outgrowth and interaction reconstituted in cell-free *Xenopus* egg cytoplasm. (A) Experimental setup. Cytoplasmic extract was sandwiched between two PEG-passivated glass coverslips. Microtubules (MTs) grow from Aurora kinase A (AurkA)-coated beads to form aster-aster interaction zones (AAIZs). **(B)** Widefield time-lapse sequence showing recruitment of Aurora kinase B (AurkB, *red*) to an AAIZ. MTs (*green*) were visualized with Alexa488-labeled tubulin and AurkB visualized with a specific Alexa647-labeled antibody. **(C)** Same AAIZ at 30 min (widefield) showing recruitment of AurkB (CPC subunit, *red*) and Kif23 (Centralspindlin subunit, *cyan*). Kif23 was visualized with a specific Alexa568-labeled antibody.

Visualization of cytokinesis structures in dividing *Xenopus* zygotes

The AAIZ formed in the cell-free extract was wider than a somatic cell midzone, and hundreds of microns long. To evaluate its physiological relevance, we imaged the same proteins in *Xenopus* zygotes fixed between mitosis and cytokinesis, which takes place at interphase in early embryonic cells (Figure 2.3) (Wühr et al., 2010). The 1st mitotic spindle was small compared to the egg (Figure 2.3B, Z1) (Wühr et al., 2008). As zygotes proceeded from metaphase to cleavage, asters from the two halves of the spindle grew, and a zone of antiparallel overlap formed between them (Mitchison et al., 2012). We found that the CPC and Centralspindlin were first recruited to the spindle midzone marked by a dense array of microtubules (Figure 2.3C, arrowheads in Z1 and Z2), and later spread to the less dense overlap zone between the asters (Figure 2.3C, arrows in Z2). As the asters grew further and the centrosomes moved apart, the overlap zone expanded radially, forming a plane ~10-30 μm wide that bisected the egg and appeared as a line in optical section (Figure 2.3C, Z3). The morphology of the midplane in zygotes, as defined by microtubule morphology and CPC/Centralspindlin localization, was strikingly similar to the AAIZ in extracts (Figure 2.2).

We propose that while the AAIZ is morphologically different, it is functionally equivalent to the central overlap in midzones in smaller cells. In each case the molecules that accumulate at this plane are thought to signal to the cell cortex and plasma membrane to induce a furrow (Argiros et al., 2012; Yabe et al., 2009). By forming a 10-30 μm thick disk whose radius also expands as the asters expand to fill the entire cytoplasm, the AAIZ serves as a structure that can deliver the cytokinesis signals from the spindle to the cortex at the rate of aster expansion (~15-30 μm/min) (Wühr et al., 2009), which is much faster than the rate of transport by diffusion alone (~5 μm/min) (Ishihara et al., 2014). Thus the AAIZ could be an evolutionary adaptation in very large cells to face spatial challenges arising from their size.

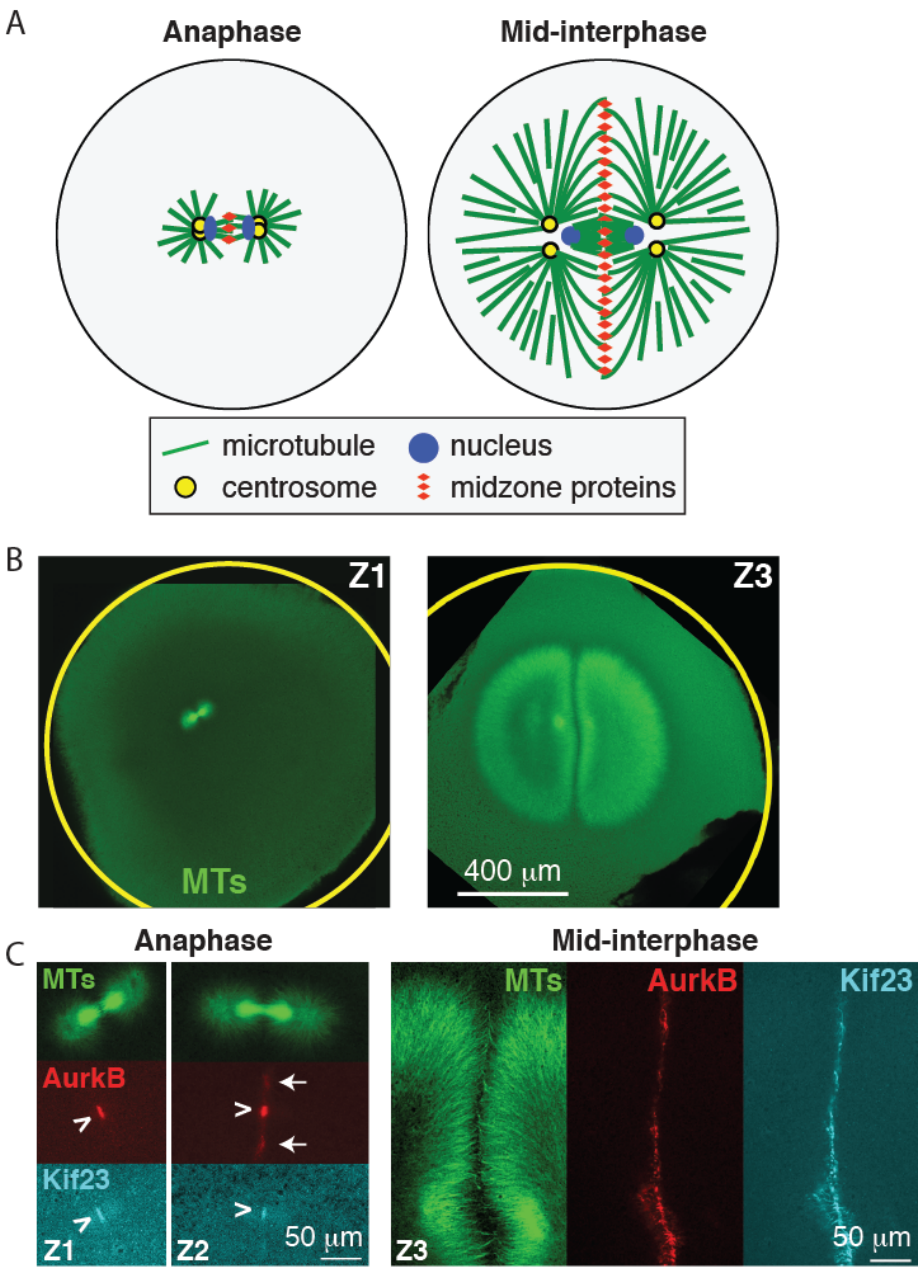

Figure 2.3: Visualization of cytokinesis structures in *Xenopus* zygotes. (A) Cartoons of microtubule structures formed in dividing *Xenopus* zygotes after metaphase exit, during anaphase (*left*) and mid-interphase (*right*). **(B,C)** Localization of MTs (*green*), AurkB (CPC subunit, *red*) and Kif23 (Centralspindlin subunit, *cyan*) in *Xenopus* zygotes fixed at consecutive stages of the first cell division (Z1-Z3) imaged by laser scanning confocal microscopy. Low-mag images show almost whole zygotes **(B)** and high-mag cropped images show detailed the morphology of cytokinesis structures **(C)**. Localization of AurkB and Kif23 to the spindle midzone (*arrowheads*) is distinct from localization to the aster-aster interaction zone (AAIZ) (*arrows* in Z2). [Figure by Timothy Mitchison and Christine Field]

Microtubule organization at the AAIZ requires Aurora B kinase activity

To measure microtubule orientation at the AAIZ we tracked GFP-tagged EB1, which binds to growing microtubule plus ends (Figure 2.4A, Figure S2.2, Movie S2.2) (Petry et al., 2013; Tirnauer and Bierer, 2000; Tirnauer et al., 2002). Microtubules grew outward radially within each aster. At the AAIZ, EB1 comets from both directions entered antiparallel bundles, where they usually disappeared (Figure 2.4A). We quantified the degree of interpenetration by categorizing EB1 comets based on their direction, and measuring the fraction of each population at different distances along the bead-bead axis (Figure S2.3; see Methods). The AAIZ was characterized by a sharp change in directionality over ~20 μm, indicating a localized block to interpenetration between the asters (Figure 2.4B).

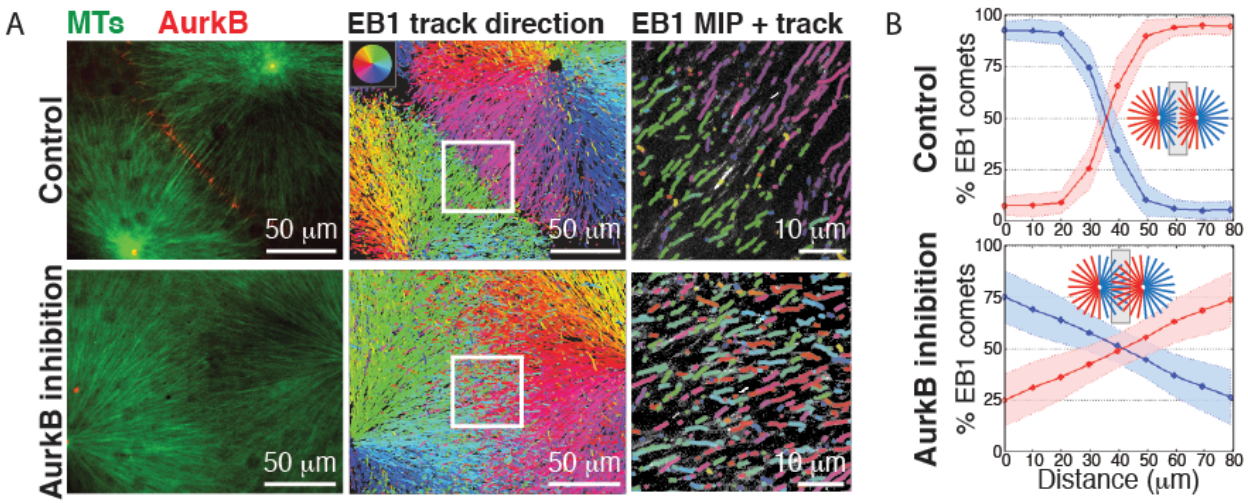

Figure 2.4: Microtubule organization at the AAIZ visualized with plus tip tracking in cell-free extract. (A) Quantification of microtubule orientation using EB1 tracking. *Left*: Spinning disc confocal images of control (*top*) and AurkB inhibited (*bottom*) AAIZs. MTs (*green*) were visualized with Alexa568-labeled tubulin and AurkB visualized with a specific Alexa647-labeled antibody. *Middle*: Map of EB1-GFP trajectories colored by their mean direction (over 2 min). *Right*: 4X zoom-up of square in middle panel with maximum intensity projection (MIP) of EB1 tracks (over 15 sec). **(B)** Spatial distribution of EB1 tracks at AAIZs classified by direction (shading indicates standard deviations determined from $n \geq 5$ zones). (See Figures S2.2, S2.3, and Methods for data analysis.)

Kinase activity of the Aurora B (AurkB) subunit of the CPC is required to establish midzone morphology and for furrow ingression (Argiros et al., 2012; Yabe et al., 2009). We confirmed this in *Xenopus* eggs by injecting the specific inhibitor ZM447439 into fertilized eggs either before or after metaphase of 1st mitosis. Cytokinesis was completely inhibited after early injections (50-55 min) and no furrows (2/10) or shallow, abortive cleavage was observed after late injections (8/10 embryos). Immunofluorescence of zygotes injected after metaphase (75-80 min) showed disruption in AAIZ formation and CPC recruitment (Figure 2.5). Control buffer injections had no effect (6/6 embryos), confirming the expected AurkB requirement (Argiros et al., 2012; Yabe et al., 2009).

AurkB inhibition blocked recruitment of the CPC in our cell free system (Figure 2.4A), and caused much deeper interpenetration of microtubules (Figure 2.4, A and B; Movie S2.3). Thus, AurkB activity was required to create a sharp boundary between asters. This is the first quantitative measurement of the role of AurkB in blocking microtubule interpenetration, which would be difficult to visualize in live cells. Our cell-free system allows us to separate the effects of AurkB inhibition on cytokinesis from other stages during mitosis, which is also difficult to achieve in live cells.

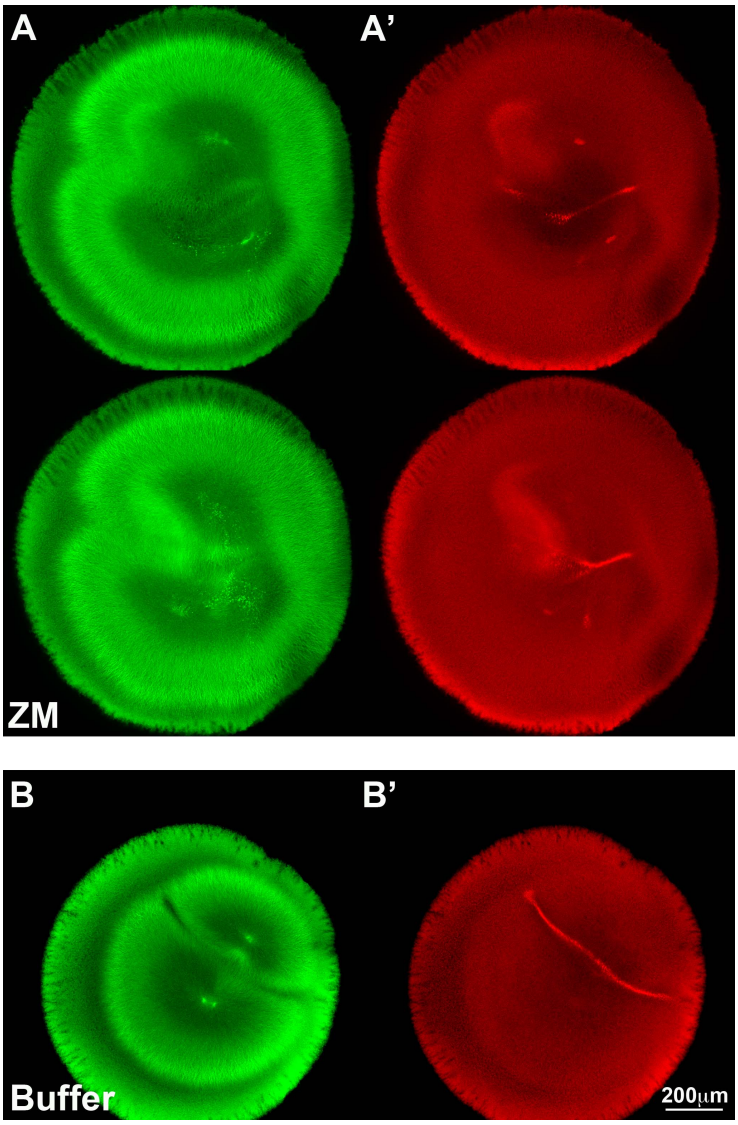

Figure 2.5: Aurora B kinase activity is required for organization of the aster-aster interaction zone (AAIZ) in *Xenopus* zygotes. Fertilized *Xenopus* eggs were injected with the Aurora kinase B specific inhibitor ZM447439 (10mM in buffer) or buffer alone after first mitosis and before first cytokinesis (75-80 minutes post fertilization), then fixed, stained for microtubules (green) and AurkB (red), and imaged by confocal microscopy. Similar images were obtained in three biological repeats. **(A, A')** Zygote injected with ZM447439 at 78 min and fixed at 130 min. Two focal planes are shown. Note disruption of antiparallel microtubule organization and CPC recruitment between the growing asters. Aster growth was not affected. **(B, B')** Zygote injected with control buffer at 73 min and fixed at 110 min. Antiparallel microtubule organization and CPC recruitment were not affected. Note buffer injection could move or distort the asters, however organization of the AAIZ with AurkB in zone was maintained. [Figure by Christine Field]

Recruitment and directed transport of CPC requires Kif20AE and Kif4A

Next we wondered how the CPC is recruited to the AAIZ and how its localization is restricted to a narrow band (~5-15 μm wide). The CPC is proposed to be transported to the center of midzones along microtubules by a kinesin molecular motor (Grüneberg et al., 2004; Kitagawa et al., 2013), but transport has not been observed directly (Atilgan et al., 2012). Five plus-end directed kinesins involved in cell division are candidates for CPC transport (Cross and McAinsh, 2014): Kif4A, Kif10 (also called CenpE), Kif11 (Eg5), Kif20A (Mklp2/Rabkinesin-6) and Kif23 (Mklp1, a subunit of Centralspindlin*). Xenopus* eggs also contain an unusual kinesin 41% identical to Kif20A by sequence (Wühr et al., 2014). This is likely to be an embryo-specific paralog, and we propose the name KIF20Aembryonic, abbreviated KIF20AE.

We tested the roles of these motor proteins in our system by immunodepletion or inhibition (Figure 2.6, A and B). Small molecule inhibition of Kif10 and Kif11, and depletion of somatic Kif20A and Kif23, had no effect on antiparallel microtubule bundling in the AAIZ or on CPC localization (Figure 2.6, A and B, Figures S2.4 and S2.5). Depletion of Kif4A did not block CPC accumulation or assembly of antiparallel bundles, but increased the width of the CPC-positive zone; adding back recombinant Kif4A rescued this phenotype (Figures 2.6A and S2.5). Depletion of Kif20AE completely blocked CPC accumulation and disorganized the AAIZ (Figure 2.6A). Thus Kif20AE is absolutely required for CPC recruitment in eggs, presumably mirroring the Kif20A requirement in somatic cells (Grüneberg et al., 2004; Kitagawa et al., 2013), and Kif4A plays some role in focusing it.

Figure 2.6: Kinesin-dependent recruitment and motility of the CPC.

(**A**) Representative spinning disc confocal images of microtubules (MTs) and AurkB at AAIZs after kinesin immunodepletions, as labeled above. MTs were visualized with Alexa568-labeled tubulin and AurkB visualized with a specific Alexa647-labeled antibody. (**B**) Summary of kinesin perturbations using drug inhibition (inh) or immunodepletion (dep). (**C** and **D**) Localization of Kif20AE and Kif4A at AAIZs. MTs (*green*) were visualized with Alexa488- (**C**) or Alexa568-labeled (**D**) tubulin, AurkB (*red*) with a specific Alexa647-labeled antibody, Kif20AE (*cyan*) with a specific Alexa568-labeled antibody, and Kif4A (*cyan*) with a Kif4A-GFP fusion protein. (**E**) Kymographs of CPC dynamics on individual microtubule bundles in AAIZs. AurkB was visualized with a specific Alexa647-labeled antibody. (**F**) CPC velocity as a function of distance from the center of the AAIZ [error bars are standard deviations determined from $n \geq 3$ microtubule bundles (see Methods)].

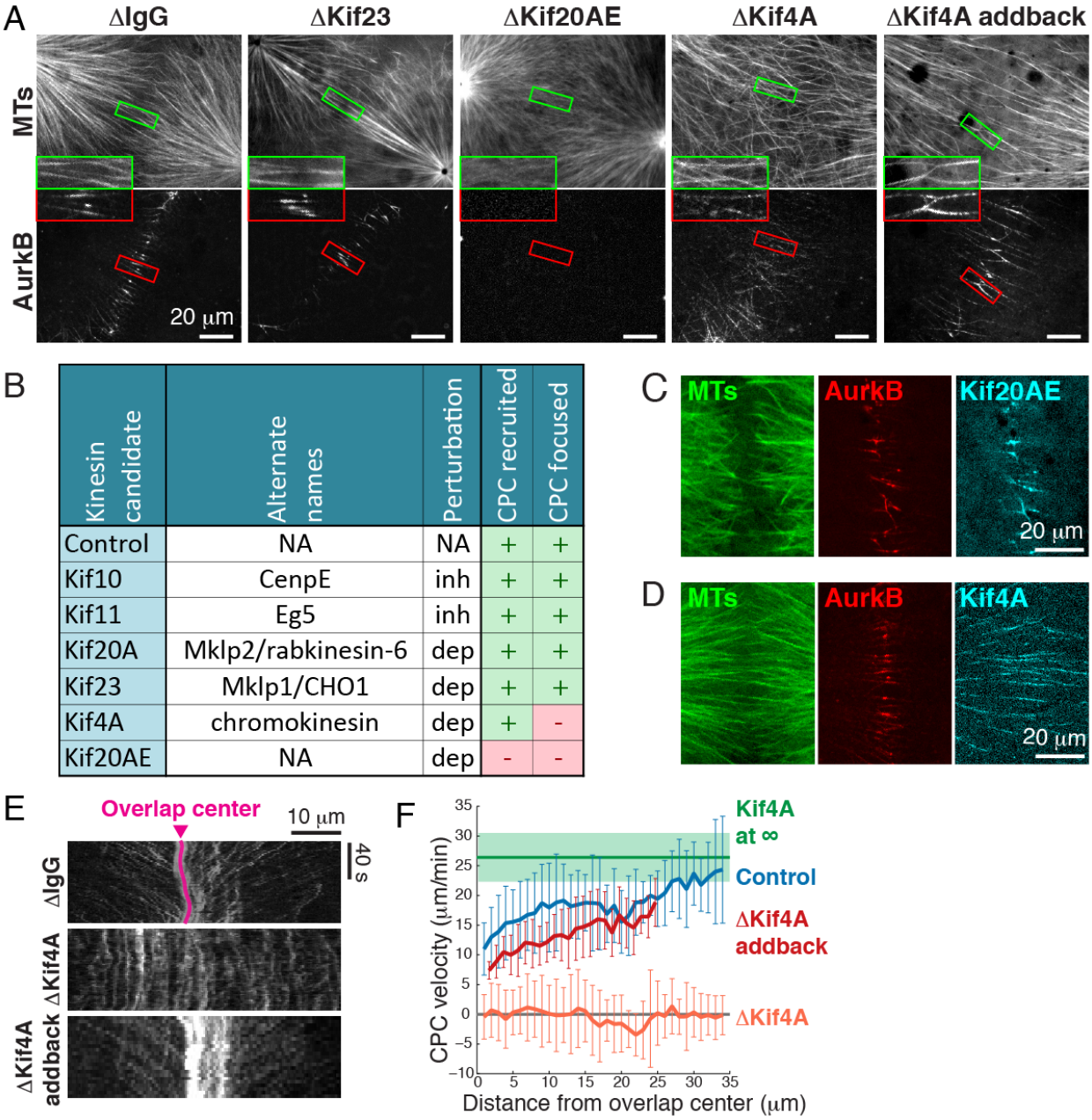

Kinesin candidate	Alternate names	Perturbation	CPC recruited	CPC focused
Control	NA	NA	+	+
Kif10	CenpE	inh	+	+
Kif11	Eg5	inh	+	+
Kif20A	Mklp2/rabkinesin-6	dep	+	+
Kif23	Mklp1/CHO1	dep	+	+
Kif4A	chromokinesin	dep	+	-
Kif20AE	NA	dep	-	-

Figure 2.6 (Continued)

Microtubule bundles in the AAIZ localized Kif20AE (Figure 2.6C), Kif4A (Figure 2.6C), and an embryonic paralog of PRC1 (PRC1E, an antiparallel microtubule crosslinker and Kif4A's binding partner; Figure S2.1C), all of which have been shown to bind the CPC in pull-down experiments (Bieling et al., 2010; Grüneberg et al., 2004; Mitchison et al., 2013; Ozlü et al., 2010). Time-lapse imaging showed that CPC clusters moved to the center of the overlap zone at a rate of 10-25 μm/min, slowing as they reached the center (Figure 2.6, E and F, Figure S2.6, Movie S2.4). Tubulin speckle imaging showed sliding of microtubules away from the overlap center at <5 μm/min (Figure S2.7, Movies S2.6 to S2.8). Thus the observed CPC movement represents transport towards plus ends. The maximal transport rate was close to that of Kif4A in an isolated aster not part of an AAIZ (26.4 ± 4.1 μm/min [mean ± SD, *n* = 34 tracked Kif4A particles]) (Figure 2.6F, green line, Figure S2.8) (see Methods). Kif4A depletion blocked CPC movement, and addback of recombinant Kif4A rescued it (Figure 2.6, E and F, Figure S2.9, Movie S2.5). Moving CPC and Kif4A partially co-localized by live imaging (Figure S2.10). Thus, the CPC is targeted to the AAIZ and transported to a narrow band by the combined action of Kif20AE and Kif4A. Transport probably slows as CPC engages binding sites in the AAIZ.

Model for CPC Recruitment and Transport at AAIZs

The simplest model that is consistent with our data is one in which the CPC is targeted to regions of antiparallel overlap by interaction with Kif20AE; once recruited there, it is transported to the center of the overlap region by interaction with Kif4A. In this model Kif4A acts as a transport motor, at least over a limited region. Kif20AE could act as a transport motor, or in some other way. For example it could serve as a recognition element for antiparallel overlapping microtubules that lacks transport activity, and instead promotes targeting of CPC to the overlap by diffusion and trapping. It could also act as an allosteric activator of the CPC without microtubule binding activity. Its somatic homolog Kif20A has been shown to possess microtubule-stimulated ATPase activity, but has not been shown to possess transport motor

activity (Neef et al., 2003). Our reasons for proposing the simple model are listed below. We note that our data do not exclude less direct roles for either kinesin, where the kinesin need not directly interact with the CPC. For example, Kif4A could act to somehow modify the microtubule tracks in the overlap zone to promote transport of CPC by some other kinesin, for example Kif20AE. It is difficult, in general, to rule out indirect actions in a complex system. Pure protein reconstitution is required to fully address the function of the two kinesins in CPC targeting.

The following observations from the depletion/addback experiments lead us to propose the two-kinesin mechanism above for CPC transport:

1. Kif20AE depletion leads to complete block of CPC recruitment to antiparallel microtubule overlaps (Figure 2.6A).
2. Kif4A depletion does not lead to block of CPC or Kif20AE recruitment (Figure 2.6A), but only blocks transport of CPC within antiparallel microtubule overlaps (Figure 2.6, E and F).
3. The localizations of Kif20AE and Kif4A are distinct: Kif20AE co-localized with the CPC in the center (Figure 2.6C), while Kif4A localized more broadly on antiparallel microtubule overlaps (Figure 2.6D). This suggests that the CPC-Kif20AE complex could be a cargo of the Kif4A transport motor.

We hypothesize that a two-kinesin mechanism is required to ensure precise localization of the CPC to the cleavage plane in egg cells where the spatial scale is very large, and antiparallel overlaps are much wider (up to tens of μms) than in small somatic cells (2-3μm) (Bieling et al., 2010; Kurasawa et al., 2004). Further experiments are required to better define the spatial extent of antiparallel overlaps, and the factors that determine the extent of Kif4A and CPC localization relative to these overlaps.

Cytokinesis signaling from microtubules to the cortex

We next tested if the AAIZs in the cell-free system can signal to the cortex. To mimic the cell membrane, we prepared supported lipid bilayers on glass coverslips using lipids

characteristic of the inner leaflet of animal cell plasma membranes, including phosphatidylinositol (PI) and phosphatidylinositol 4,5-bisphosphate [PI(4,5)P_2] (Lee et al., 2010; Loose et al., 2008; Nguyen et al., 2015). Protein recruitment was imaged using total internal reflection fluorescence (TIRF) microscopy (Figure 2.7).

The small GTPase RhoA is thought to be the master organizer of the furrow by positively regulating actomyosin contractility (Benink and Bement, 2005; Jordan and Canman, 2012; Piekny et al., 2005). To localize active, GTP-bound RhoA we added an mCherry-tagged RhoA binding fragment of Rhotekin (mCherry-rGBD) (Benink and Bement, 2005). Using PEG-passivated coverslips (as per Figure 2.2A), we saw no recruitment of RhoA-GTP. Using lipid bilayers (as per Figure 2.7A), the RhoA-GTP reporter was enriched at the bilayer under AAIZs that recruited CPC and Centralspindlin (Figures 2.7B and S2.11). Inhibition of AurkB or depletion of Kif20AE completely blocked AAIZ assembly and CPC localization as expected (Argiros et al., 2012; Grüneberg et al., 2004; Yabe et al., 2009), and also blocked localized RhoA-GTP enrichment (Figure 2.7, B and C). Kif4A depletion resulted in broadening of both CPC and RhoA-GTP zones (Figure 2.7C).

Figure 2.7: Spatially localized recruitment of GTP-bound RhoA on model plasma membranes. (**A**) Drawing of experimental setup. Cytoplasmic extract was incubated on a lipid bilayer-coated glass coverlip. The lipid composition was 60% PC, 30% PS, 10% PI, and 0-1% PI(4,5)P_2 (see Methods). (**B** and **C**) Localization of a probe for RhoA-GTP (mCherry-rGBD; *cyan*) (Benink and Bement, 2005) and AurkB (*red*) at lipid bilayers proximal to AAIZs. MTs (*green*) were visualized with Alexa488-labeled tubulin and AurkB with a specific Alexa647-labeled antibody. TIRF images from 3 × 3 to 5 × 5 adjacent fields were corrected for uneven illumination and stitched (see Methods). (**B**) Representative images of control and AurkB inhibition. (**C**) Representative images of kinesin immunodepletions, as labeled above. Scale bar, 200 mm.

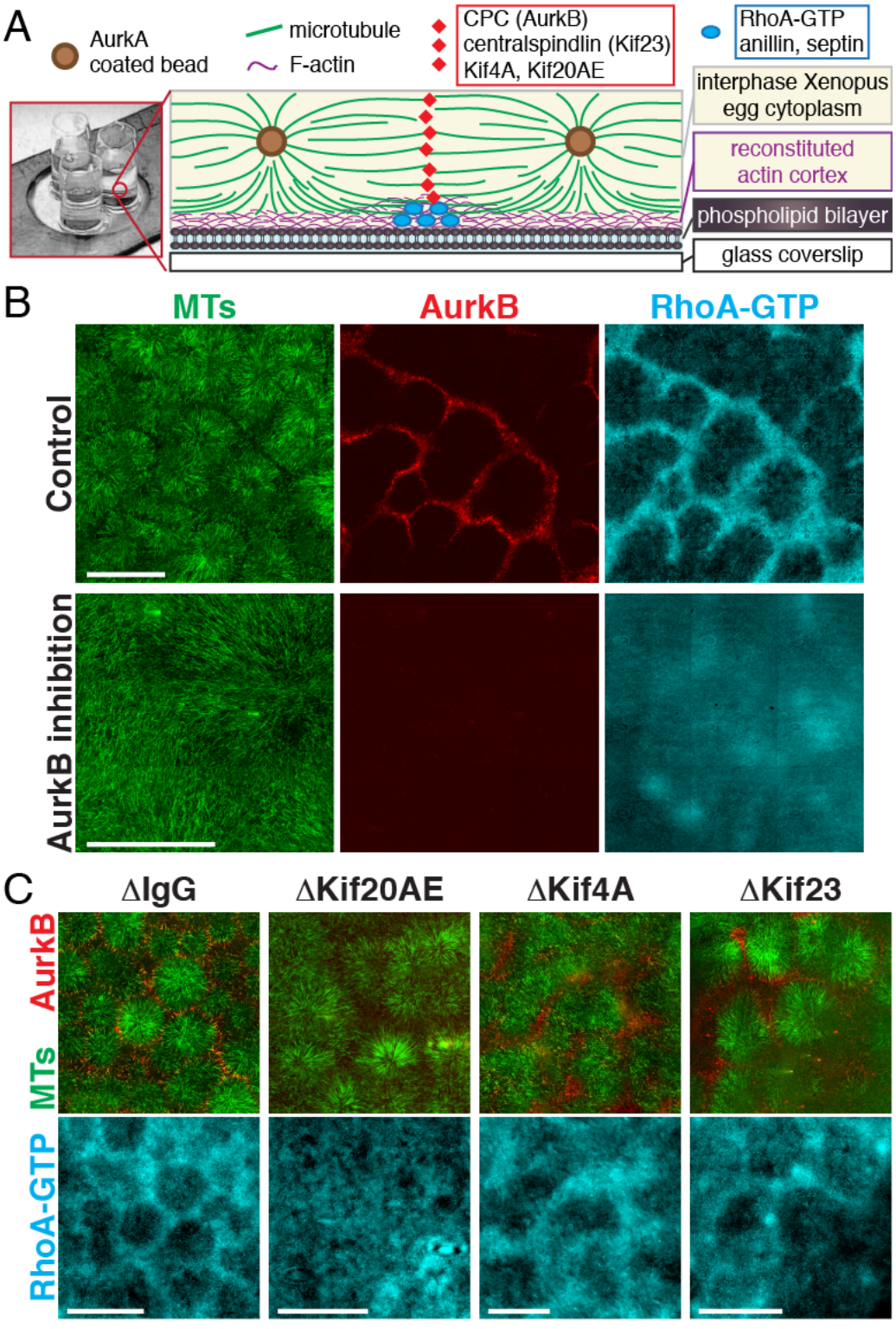

Figure 2.7 (Continued)

Depletion of Kif23, a subunit of the Centralspindlin complex, did not block AAIZ assembly (Figure 2.6A) or RhoA-GTP recruitment (Figure 2.7C). RhoA activation in the absence of Kif23 (or Mklp1) is consistent with previous observations that a furrow still ingresses, albeit fails to complete and thus later regresses, when Kif23 is knocked down in *C. elegans* embryos (Powers et al., 1998; Raich et al., 1998) or human somatic cells (Yüce et al., 2005). One caveat in our depletion experiment is that we only depleted Kif23, the motor component of Centralspindlin. We do not know whether its binding partner, the Rho GTPase activating protein RacGAP1, is still present in our system after Kif23 depletion, and whether its activity could contribute towards the localized RhoA activation we observed.

More surprising was the lack of detectable difference in AAIZ morphology in the absence of Kif23: neither antiparallel microtubule overlap formation nor CPC recruitment was affected. Studies in *C. elegans* embryos found that knocking down either Centralspindlin subunit, Kif23 (or ZEN-4) or RacGAP1 (or CYK-4) blocked the formation of a midzone (Jantsch-Plunger et al., 2000; Raich et al., 1998), leading to a popular model of midzone assembly where Centralspindlin plays a crucial role in microtubule bundling (Glotzer, 2009; Mishima et al., 2002; 2004). In human somatic cells, however, midzones can still form and recruit the CPC in the absence of Centralspindlin (Zhu et al., 2005). In the same study, when INCENP (a CPC subunit) was knocked down, Kif23 was no detected at the midzone (Zhu et al., 2005), consistent with our findings. Thus the dispensability of Kif23 in our system likely reflects functional redundancy among midzone factors.

Overall, we conclude that a CPC-positive AAIZ can locally activate RhoA in our system, although we cannot distinguish whether localized AurkB phosphorylation of cytokinetic factors or some specific organization of microtubules at the AAIZ is required for furrow signaling.

Recruitment and organization of cortical cleavage furrow proteins

Cytokinesis signaling from microtubules leads to the reorganization of the actin cortex

and recruitment of cleavage furrow proteins to form a contractile ring. To probe cortical organization in our system we visualized F-actin using Lifeact-GFP (Figure 2.8) (Riedl et al., 2008). F-actin was enriched at the lipid bilayer under CPC-positive AAIZs, while microtubules were depleted (Figure 2.8, A and B). Above the cortical layer, F-actin organized into branched networks that showed only partial alignment with the microtubules (Figure 2.8C). At the cortical layer, F-actin organized into long, uniformly spaced cables that aligned radially with microtubule asters (Figure 2.8, left). Where asters interacted, F-actin cables ran parallel to the overlapping microtubule bundles, forming a continuous array of cables between the two asters (Figure 2.8, middle). Where CPC and RhoA-GTP were recruited and microtubule density was lower, we observed increase in actin polymer density, most likely due to local nucleation and assembly (Movie S2.9). The spacing between actin cables was 1.3 ± 0.5 μm (SD; n = 140), comparable to actin-containing contractile bands on the cortex of live frog eggs (Danilchik et al., 2006). This organization was microtubule-dependent (Figure 2.8D, right). The furrow-selective actin bundling protein Anillin (Straight et al., 2005) co-localized with F-actin cables throughout the cortex, but not in the cytoplasm above the cortex (Figure 2.8C), and was enriched under AAIZs along with its binding partner septin complex (Figure 2.8E, Movie S2.10).

We suspect that our system reconstitutes a pre-cytokinesis state where the CPC-positive overlap zones signal to the cortex to position the cleavage furrow. The orientation of actin cables we observe in our system likely represents a configuration of actin bundles at early anaphase in live cells, and not the contractile ring itself. The alignment of cortical actin cables orthogonal to the putative cleavage plane is consistent with observations using fluorescently labeled actin filaments in somatic cells (Oegema et al., 2000). It has been proposed that actin filaments undergo reorganization at the cleavage site from an orthogonal alignment to a parallel one along the cleavage plane as cells proceed from anaphase to cytokinesis (Fishkind and Wang, 1993; Noguchi and Mabuchi, 2001; Opas and Sołtyńska, 1978).

Figure 2.8: Recruitment and organization of cortical cleavage furrow proteins.
Experimental setup was as per Figure 2.7A. (**A**) F-actin (TIRF image). Note the enrichment proximal to the CPC at AAIZs. Microtubules (*green*) were visualized with Alexa568-labeled tubulin, AurkB (*red*) with a specific Alexa647-labeled antibody, and F-actin (*cyan*) with Lifeact-GFP (Riedl et al., 2008). (**B**) Intensity line scans across the AAIZ [boxed in (**A**)] show enrichment of AurkB and F-actin; a.u., arbitrary units. (**C**) XZ slices of three-dimensional reconstructions using spinning disc confocal microscopy, showing the organization of the microtubules, F-actin, and Anillin (*left*). XY slices of microtubules and F-actin at the plane marked by an arrow (*right*). Microtubules (*green*) were visualized with Alexa647-labeled tubulin, and F-actin (*cyan*) with Lifeact-GFP, and Anillin (*magenta*) with a specific Alexa568-labeled antibody. (**D**) TIRF images of microtubules and F-actin at aster center (*left*) and an AAIZ (*middle*). The right panel shows a nocodazole-treated sample. (**E**) Anillin and septin on a bilayer (TIRF image) colocalize with the CPC at the AAIZ. AurkB (*red*), Anillin (*magenta*), and septin (*yellow*) were each visualized with a specific antibody labeled with Alexa488, Alexa568, and Alexa647, respectively.

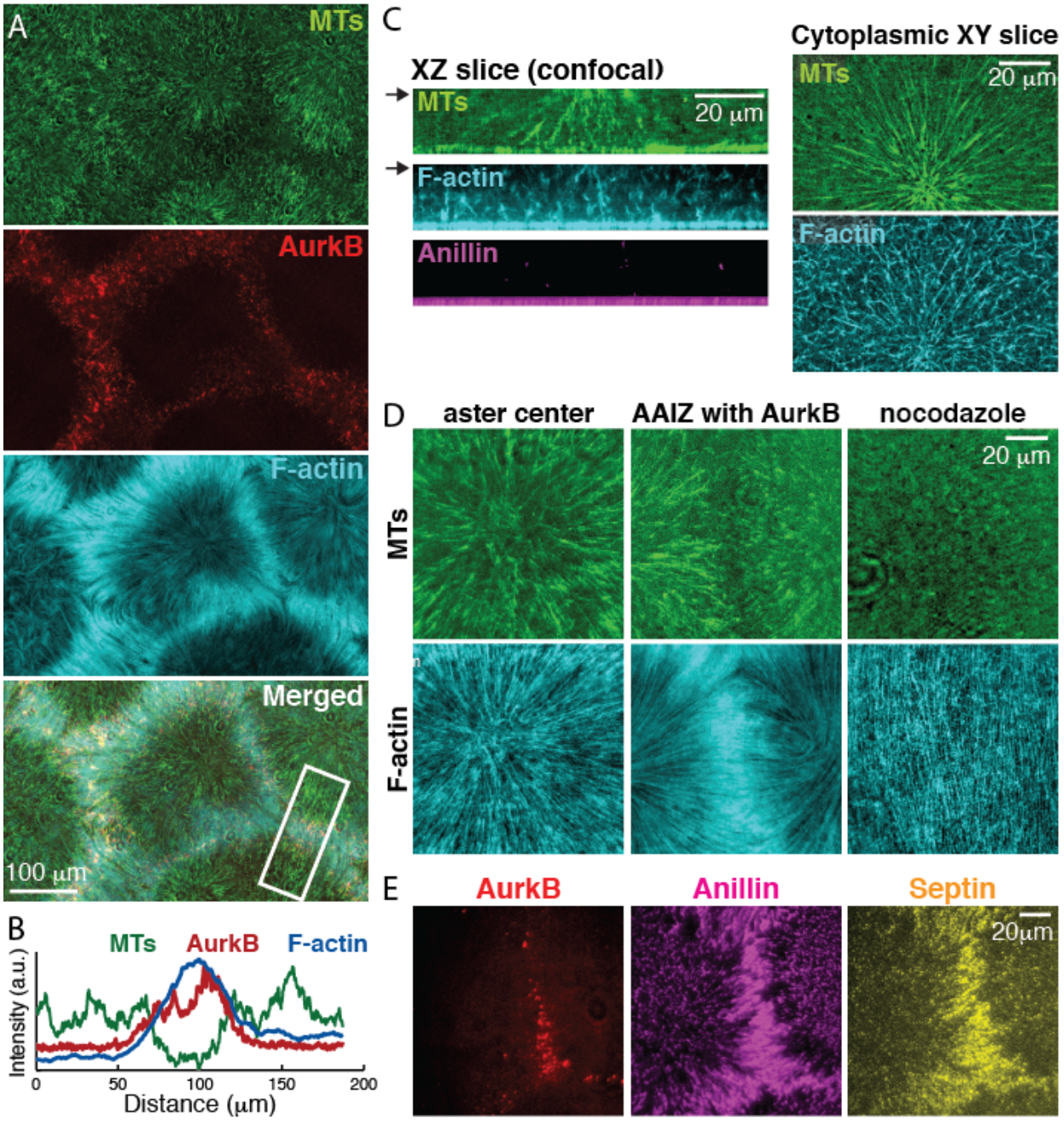

Figure 2.8 (Continued)

Summary

Summarizing, we have developed a cell-free system that recapitulates the hallmarks of spatially organized signaling characteristic of egg cytokinesis. Midzone proteins were recruited to the overlap zone between microtubule asters in egg extract, where they signaled to a nearby lipid bilayer to locally activate the RhoA pathway. Our system confirmed known mechanisms of spatially organized signaling, for example the Aurora B kinase activity requirement for cleavage furrow induction, and revealed new mechanistic aspects that were difficult to observe in living cells, notably transport of the CPC along microtubules towards the midzone in a process requiring two kinesins. Our data favor a model in which Kif4A is a transport motor for the CPC, and Kif20AE is required for it to bind microtubules, though not necessarily as a transporter. Future pure protein reconstitution experiments are required to conclusively determine the mechanism of CPC transport and the exact roles of these two kinesins.

Two factors facilitated imaging approaches in the cell-free system: the large spatial scale of the AAIZ (~20 μm) and its long time duration (>20 minutes). Both reflect the pre-cytokinesis organization of the large egg cell. By comparison, the microtubule overlap in somatic cell midzones is ~2-3 μm wide and lasts only ~3 minutes before being compressed by the furrow (*21*). Future studies will take advantage of these features and the experimental flexibility of an extract system to probe biophysical mechanisms involved in cytokinesis.

Acknowledgements

We thank Ryoma Ohi for the generous gift of Aurora B antibody and David Burgess for the Lifeact-GFP construct and protein; Edwin Tan for initiating Kif20A and Kif23 antibody projects and help with tubulin preparation; David Miyamoto for initiating the Xklp1/Kif4 antibody project; Himanish Basu for contributing towards optimization of the supported lipid bilayer preparation. We thank Jennifer Waters, Lara Petrak, Lauren Piedmont and the Nikon Imaging Center at Harvard Medical School (HMS) for microscopy support; Lynne Chang, Nikon and the Marine Biological Laboratory (MBL) for use of laser scanning confocal and TIRF microscopes; the NXR at MBL for *Xenopus* animals and care. We also thank Calixto Saenz and the Microfluidics Core Facility at HMS for use of their plasma etcher for coverslip cleaning, and Stephen Harrison's lab for providing Sf21 insect cells. This work was supported by NIH grant GM39565 (T.J.M.); MBL fellowships from the Evans Foundation, MBL Associates, and the Colwin Fund (T.J.M. and C.M.F.); HFSP fellowship LT000466/2012-L (M.L.); and NIH grant GM103785 (M.W.).

Supplemental materials

Supplementary content includes Materials and Methods, Figures S2.1 to S2.12, Tables S2.1 to S2.2, Movies S2.1 to S2.10, and References.

References

Argiros, H., Henson, L., Holguin, C., Foe, V., and Shuster, C.B. (2012). Centralspindlin and chromosomal passenger complex behavior during normal and Rappaport furrow specification in echinoderm embryos. Cytoskeleton (Hoboken) *69*, 840–853.

Asiedu, M., Wu, D., Matsumura, F., and Wei, Q. (2008). Phosphorylation of MyoGEF on Thr-574 by Plk1 promotes MyoGEF localization to the central spindle. J Biol Chem *283*, 28392–28400.

Atilgan, E., Burgess, D., and Chang, F. (2012). Localization of cytokinesis factors to the future cell division site by microtubule-dependent transport. Cytoskeleton (Hoboken) *69*, 973–982.

Benink, H.A., and Bement, W.M. (2005). Concentric zones of active RhoA and Cdc42 around single cell wounds. J Cell Biol *168*, 429–439.

Bieling, P., Telley, I.A., and Surrey, T. (2010). A Minimal Midzone Protein Module Controls Formation and Length of Antiparallel Microtubule Overlaps. Cell *142*, 420–432.

Carmena, M., Wheelock, M., Funabiki, H., and Earnshaw, W.C. (2012). The chromosomal passenger complex (CPC): from easy rider to the godfather of mitosis. Nat Rev Mol Cell Biol *13*, 789–803.

Cross, R.A., and McAinsh, A. (2014). Prime movers: the mechanochemistry of mitotic kinesins. Nat Rev Mol Cell Biol *15*, 257–271.

Danilchik, M.V., Brown, E.E., and Riegert, K. (2006). Intrinsic chiral properties of the Xenopus egg cortex: an early indicator of left-right asymmetry? Development *133*, 4517–4526.

Field, C.M., Nguyen, P.A., Ishihara, K., Groen, A.C., and Mitchison, T.J. (2014). Xenopus egg cytoplasm with intact actin. Meth Enzymol *540*, 399–415.

Fishkind, D.J., and Wang, Y.L. (1993). Orientation and three-dimensional organization of actin filaments in dividing cultured cells. J Cell Biol *123*, 837–848.

Glotzer, M. (2005). The molecular requirements for cytokinesis. Science *307*, 1735–1739.

Glotzer, M. (2009). The 3Ms of central spindle assembly: microtubules, motors and MAPs. Nat Rev Mol Cell Biol *10*, 9–20.

Grüneberg, U., Neef, R., Honda, R., Nigg, E.A., and Barr, F.A. (2004). Relocation of Aurora B from centromeres to the central spindle at the metaphase to anaphase transition requires MKlp2. J Cell Biol *166*, 167–172.

Ishihara, K., Nguyen, P.A., Wühr, M., Groen, A.C., Field, C.M., and Mitchison, T.J. (2014). Organization of early frog embryos by chemical waves emanating from centrosomes. Philos. Trans. R. Soc. Lond., B, Biol. Sci. *369*.

Jantsch-Plunger, V., Gönczy, P., Romano, A., Schnabel, H., Hamill, D., Schnabel, R., Hyman, A.A., and Glotzer, M. (2000). CYK-4: A Rho family gtpase activating protein (GAP) required for central spindle formation and cytokinesis. J Cell Biol *149*, 1391–1404.

Jordan, S.N., and Canman, J.C. (2012). Rho GTPases in animal cell cytokinesis: an occupation by the one percent. Cytoskeleton (Hoboken) *69*, 919–930.

Kamijo, K., Ohara, N., Abe, M., Uchimura, T., Hosoya, H., Lee, J.-S., and Miki, T. (2006). Dissecting the role of Rho-mediated signaling in contractile ring formation. Mol Biol Cell *17*, 43–55.

Kitagawa, M., Fung, S.Y.S., Onishi, N., Saya, H., and Lee, S.H. (2013). Targeting Aurora B to the equatorial cortex by MKlp2 is required for cytokinesis. PLoS ONE *8*, e64826.

Kurasawa, Y., Earnshaw, W.C., Mochizuki, Y., Dohmae, N., and Todokoro, K. (2004). Essential roles of KIF4 and its binding partner PRC1 in organized central spindle midzone formation. Embo J *23*, 3237–3248.

Lee, K., Gallop, J.L., Rambani, K., and Kirschner, M.W. (2010). Self-assembly of filopodia-like structures on supported lipid bilayers. Science *329*, 1341–1345.

Loose, M., Fischer-Friedrich, E., Ries, J., Kruse, K., and Schwille, P. (2008). Spatial regulators for bacterial cell division self-organize into surface waves in vitro. Science *320*, 789–792.

Lorca, T., Cruzalegui, F.H., Fesquet, D., Cavadore, J.C., Méry, J., Means, A., and Dorée, M. (1993). Calmodulin-dependent protein kinase II mediates inactivation of MPF and CSF upon fertilization of Xenopus eggs. Nature *366*, 270–273.

Mastronarde, D.N., McDonald, K.L., Ding, R., and McIntosh, J.R. (1993). Interpolar spindle microtubules in PTK cells. J Cell Biol *123*, 1475–1489.

Mishima, M., Kaitna, S., and Glotzer, M. (2002). Central spindle assembly and cytokinesis require a kinesin-like protein/RhoGAP complex with microtubule bundling activity. Dev Cell *2*, 41–54.

Mishima, M., Pavicic, V., Grüneberg, U., Nigg, E.A., and Glotzer, M. (2004). Cell cycle regulation of central spindle assembly. Nature *430*, 908–913.

Mitchison, T.J., Nguyen, P., Coughlin, M., and Groen, A.C. (2013). Self-organization of stabilized microtubules by both spindle and midzone mechanisms in Xenopus egg cytosol. Mol Biol Cell *24*, 1559–1573.

Mitchison, T., Wühr, M., Nguyen, P., Ishihara, K., Groen, A., and Field, C.M. (2012). Growth, interaction, and positioning of microtubule asters in extremely large vertebrate embryo cells. Cytoskeleton (Hoboken) *69*, 738–750.

Mochida, S., and Hunt, T. (2007). Calcineurin is required to release Xenopus egg extracts from meiotic M phase. Nature *449*, 336–340.

Neef, R., Preisinger, C., Sutcliffe, J., Kopajtich, R., Nigg, E.A., Mayer, T.U., and Barr, F.A. (2003). Phosphorylation of mitotic kinesin-like protein 2 by polo-like kinase 1 is required for cytokinesis. J Cell Biol *162*, 863–875.

Nguyen, P.A., Field, C.M., Groen, A.C., Mitchison, T.J., and Loose, M. (2015). Using supported bilayers to study the spatiotemporal organization of membrane-bound proteins. Methods Cell Biol *128*, 223–241.

Nishimura, Y., and Yonemura, S. (2006). Centralspindlin regulates ECT2 and RhoA accumulation at the equatorial cortex during cytokinesis. J Cell Sci *119*, 104–114.

Nishiyama, T., Yoshizaki, N., Kishimoto, T., and Ohsumi, K. (2007). Transient activation of calcineurin is essential to initiate embryonic development in Xenopus laevis. Nature *449*, 341–345.

Noguchi, T., and Mabuchi, I. (2001). Reorganization of actin cytoskeleton at the growing end of the cleavage furrow of Xenopus egg during cytokinesis. J Cell Sci *114*, 401–412.

Oegema, K., Savoian, M.S., Mitchison, T.J., and Field, C.M. (2000). Functional analysis of a human homologue of the Drosophila actin binding protein anillin suggests a role in cytokinesis. J Cell Biol *150*, 539–552.

Opas, J., and Sołtyńska, M.S. (1978). Reorganization of the cortical layer during cytokinesis in mouse blastomeres. Exp Cell Res *113*, 208–211.

Ozlü, N., Monigatti, F., Renard, B.Y., Field, C.M., Steen, H., Mitchison, T.J., and Steen, J.J. (2010). Binding partner switching on microtubules and aurora-B in the mitosis to cytokinesis transition. Mol Cell Proteomics *9*, 336–350.

Petry, S., Groen, A.C., Ishihara, K., Mitchison, T.J., and Vale, R.D. (2013). Branching microtubule nucleation in Xenopus egg extracts mediated by augmin and TPX2. Cell *152*, 768–777.

Piekny, A., Werner, M., and Glotzer, M. (2005). Cytokinesis: welcome to the Rho zone. Trends Cell Biol *15*, 651–658.

Powers, J., Bossinger, O., Rose, D., Strome, S., and Saxton, W. (1998). A nematode kinesin required for cleavage furrow advancement. Curr Biol *8*, 1133–1136.

Raich, W.B., Moran, A.N., Rothman, J.H., and Hardin, J. (1998). Cytokinesis and midzone microtubule organization in Caenorhabditis elegans require the kinesin-like protein ZEN-4. Mol Biol Cell *9*, 2037–2049.

Rappaport, R. (1996). Cytokinesis in animal cells (Cambridge; New York: Cambridge University Press).

Rauh, N.R., Schmidt, A., Bormann, J., Nigg, E.A., and Mayer, T.U. (2005). Calcium triggers exit from meiosis II by targeting the APC/C inhibitor XErp1 for degradation. Nature *437*, 1048–1052.

Riedl, J., Crevenna, A.H., Kessenbrock, K., Yu, J.H., Neukirchen, D., Bista, M., Bradke, F., Jenne, D., Holak, T.A., Werb, Z., et al. (2008). Lifeact: a versatile marker to visualize F-actin. Nat Methods *5*, 605–607.

Sawin, K.E., and Mitchison, T.J. (1991). Mitotic spindle assembly by two different pathways in vitro. J Cell Biol *112*, 925–940.

Straight, A.F., Field, C.M., and Mitchison, T.J. (2005). Anillin binds nonmuscle myosin II and regulates the contractile ring. Mol Biol Cell *16*, 193–201.

Tirnauer, J.S., and Bierer, B.E. (2000). EB1 proteins regulate microtubule dynamics, cell polarity, and chromosome stability. J Cell Biol *149*, 761–766.

Tirnauer, J.S., Grego, S., Salmon, E.D., and Mitchison, T.J. (2002). EB1-microtubule interactions in Xenopus egg extracts: role of EB1 in microtubule stabilization and mechanisms of targeting to microtubules. Mol Biol Cell *13*, 3614–3626.

Tsai, M.-Y., and Zheng, Y. (2005). Aurora A kinase-coated beads function as microtubule-organizing centers and enhance RanGTP-induced spindle assembly. Curr Biol *15*, 2156–2163.

White, E.A., and Glotzer, M. (2012). Centralspindlin: at the heart of cytokinesis. Cytoskeleton (Hoboken) *69*, 882–892.

Wu, D., Asiedu, M., Matsumura, F., and Wei, Q. (2014). Phosphorylation of myosin II-interacting guanine nucleotide exchange factor (MyoGEF) at threonine 544 by aurora B kinase promotes the binding of polo-like kinase 1 to MyoGEF. J Biol Chem *289*, 7142–7150.

Wühr, M., Chen, Y., Dumont, S., Groen, A.C., Needleman, D.J., Salic, A., and Mitchison, T.J. (2008). Evidence for an upper limit to mitotic spindle length. Curr Biol *18*, 1256–1261.

Wühr, M., Dumont, S., Groen, A.C., Needleman, D.J., and Mitchison, T.J. (2009). How does a millimeter-sized cell find its center? Cell Cycle *8*, 1115–1121.

Wühr, M., Freeman, R.M., Presler, M., Horb, M.E., Peshkin, L., Gygi, S.P., and Kirschner, M.W. (2014). Deep proteomics of the Xenopus laevis egg using an mRNA-derived reference database. Curr Biol *24*, 1467–1475.

Wühr, M., Tan, E.S., Parker, S.K., Detrich, H.W., and Mitchison, T.J. (2010). A model for cleavage plane determination in early amphibian and fish embryos. Curr Biol *20*, 2040–2045.

Yabe, T., Ge, X., Lindeman, R., Nair, S., Runke, G., Mullins, M.C., and Pelegri, F. (2009). The maternal-effect gene cellular island encodes aurora B kinase and is essential for furrow formation in the early zebrafish embryo. PLoS Genet *5*, e1000518.

Yüce, O., Piekny, A., and Glotzer, M. (2005). An ECT2-centralspindlin complex regulates the localization and function of RhoA. J Cell Biol *170*, 571–582.

Zhu, C., Bossy-Wetzel, E., and Jiang, W. (2005). Recruitment of MKLP1 to the spindle midzone/midbody by INCENP is essential for midbody formation and completion of cytokinesis in human cells. Biochem J *389*, 373–381.

Chapter Three

Regulation of Microtubule Orientation Within and Between Large Asters

Citation. With minor modifications to standardize the format, this chapter was reproduced in its entirety from the following manuscript under review:

The Prc1/Kif4A Module Controls Microtubule Orientation Within and Between Large Embryo Asters

Phuong A. Nguyen[1,2], Christine M. Field[1,2], Timothy J. Mitchison[1,2]

[1]Department of Systems Biology, Harvard Medical School, Boston, MA 02115, USA.
[2]Marine Biological Laboratory, Woods Hole, MA 02543, USA.

Contributions.

Experiments. I conducted all the experiments described in this chapter except for the following: Dr. Christine Field performed the fertilization and immunofluorescence experiments on whole Xenopus eggs. Dr. Timothy Mitchison labeled the antibodies for immunofluorescence.

Reagents. I cloned the Prc1 and Prc1E constructs and purified the proteins. I purified all proteins (Kif4A, Prc1, Prc1E constructs, EB1-GFP, tubulin) except for GFP-DasraA and EB1-mCherry (kindly provided by Dr. Aaron Groen). I made the Prc1 antibody, designed and purchased the Prc1E peptide antibody, and affinity purified some Kif4A and Kif23 antibodies. Dr. Groen made the AurkA and Kif23 antibodies, and Dr. David Miyamoto made the Kif4A antibodies.

Writing. I made all the figures and wrote the manuscript with help from Dr. Groen during the initial stages and Dr. Mitchison at the final stages (see Acknowledgements).

Supplemental materials. Materials and Methods, Supplementary Figures, Tables and Movies for this chapter can be found in Appendix I.

Abstract

In dividing cells, signalling complexes that induce cleavage furrows are transported by plus end-directed kinesins. Anaphase microtubules must, therefore, orient with their plus end towards the cell midplane. In very large embryo cells, furrow-inducing complexes are positioned by large microtubule asters that form a distinct aster-aster interaction zone (AAIZ) with anti-parallel overlaps at the cell midplane. The AAIZ is known to block interpenetration of microtubules from the two asters, but the molecular basis of this block is unknown. Here we investigated the role of the Prc1/Kif4A module, which organises cytokinesis microtubules in many systems. Using a cell-free system derived from *Xenopus laevis* eggs, we showed that growth of plus ends slows down and terminates preferentially in AAIZs. Both the slowdown and the block to interpenetration depended on Prc1 and Kif4A. Unexpectedly, Prc1 and Kif4A were also required for radial order of large asters growing in isolation. Our findings describe in unprecedented detail how the conserved Prc1/Kif4A module regulates microtubule overlap interactions in a dividing cell. They also reveal a novel function of this module, eliminating inappropriate anti-parallel overlaps to control microtubule orientation.

Introduction

Symmetric cell division requires precise positioning of the cleavage furrow at the midplane of a cell. Animal somatic cells typically initiate furrowing within 5 minutes of anaphase onset; during this time microtubules assemble into a bipolar array called the cytokinesis midzone or central spindle, which fills the space in the cell centre left by the separating chromosomes (Glotzer, 2009). The plus end directed kinesin-family motors Kif23 (MKLP1) and Kif20A (MKLP2) recruit the furrow-stimulating factors RacGAP1 (which is in the Centralspindlin complex with Kif23) and the chromosome passenger complex (CPC, which binds Kif20A) to the cell midplane along midzone microtubules (Grüneberg et al., 2004; Mishima et al., 2002). RacGAP1 and the CPC then signal locally to the equatorial cortex to position the furrow (Argiros et al., 2012; Canman et al., 2008; Jantsch-Plunger et al., 2000; Lewellyn et al., 2011; Yüce et al., 2005). Centralspindlin has also been implicated in anti-parallel bundling in midzones (Mishima et al., 2002; 2004). In addition, astral microtubules may inhibit furrow formation at the poles in some systems (Tse et al., 2011; White and Borisy, 1983).

The orientation of midzone microtubules plays a central role in cleavage plane positioning. Recruitment of RacGAP1 and CPC to the midplane depends on uniform orientation of microtubules in each half of the cell, with limited anti-parallel overlap at the midplane (Euteneuer and McIntosh, 1980). When midzone microtubules are forced to adopt a monopolar orientation, RacGAP1 and CPC accumulate on one side of the cell, resulting in highly asymmetric, incomplete cleavage (Canman et al., 2003; Hu et al., 2008; Shrestha et al., 2012). How midzone microtubules are orientated is unclear, but the conserved Prc1/Kif4A module is known to play an important role in controlling the anti-parallel overlap at the midplane (Kurasawa et al., 2004). These proteins interact dynamically but do not form a stable complex (Zhu and Jiang, 2005). Prc1 (a member of the Ase1/MAP65 family of microtubule crosslinkers) promotes anti-parallel bundling (Gaillard et al., 2008; Jiang et al., 1998; Kapitein et al., 2008;

Loïodice et al., 2005; Mollinari et al., 2002; Subramanian et al., 2010; Yamashita et al., 2005), while Kif4A (a member of the Kinesin-4 family of plus end directed motors with plus end polymerization-inhibiting activity) antagonizes growth of midzone plus ends (Bringmann et al., 2004; Hu et al., 2011; Sekine et al., 1994). Together, they can generate anti-parallel overlaps of defined length in a pure protein system (Bieling et al., 2010).

In the very large cells of early frog and fish embryos, the mitotic spindle is small compared to the cell (Mitchison et al., 2012; Wühr et al., 2009). Large microtubule asters grow out from centrosomes at the spindle poles at anaphase onset, and it takes many minutes for them to reach the cortex to initiate furrowing. As the asters grow, the centrosomes and nuclei at their centres move away from the midplane of the cell under the influence of dynein (Wühr et al., 2010). What happens at the midplane is unclear. In tubulin immunofluorescence images of dividing frog embryos fixed between anaphase and furrow initiation, a darker region is observed where the two asters meet, which we termed the 'aster-aster interaction zone' (AAIZ) (Mitchison et al., 2012; Wühr et al., 2009; 2010). Microtubules from each aster appear not to cross the AAIZ. Wühr and colleagues (2010) proposed that this zone served to limit microtubule length, and thus generate length asymmetries that promote dynein-mediated centrosome movement (Wühr et al., 2010).

We recently reconstituted growth and interaction of large interphase asters in a cell-free system derived from *Xenopus laevis* eggs, and showed that when pairs of growing asters meet, they recognize each other and assemble an AAIZ that recruits many of the same kinesins and furrow stimulating factors as cytokinesis midzones in somatic cells (Nguyen, Groen et al., 2014). Tracking of growing microtubule plus ends using a fluorescently labelled end binding protein EB1 revealed a block to interpenetration of microtubules at the shared boundary between asters (Nguyen, Groen et al., 2014). This block was shown to depend on activity of the Aurora B kinase (AurkB) subunit of the CPC (Argiros et al., 2012; Nguyen, Groen et al., 2014; Yabe et al., 2009). How AurkB and other factors locally regulate microtubule dynamics to generate the AAIZ

is unclear, however, as are the more fundamental questions of how the two asters recognize each other and how they stay separate. The cell-free system also revealed that aster growth occurs mainly by nucleation of microtubules at the expanding aster periphery (Ishihara et al., 2014). This raised another question: how is radial order of the aster maintained when most nucleation occurs away from the centrosome? Is microtubule direction controlled by oriented nucleation sites and parallel bundling with pre-existing microtubules, or are other mechanisms involved?

Here, we show that the Prc1/Kif4A module plays a key role in aster-aster recognition and organisation of an AAIZ by regulating anti-parallel overlaps. We provide a detailed analysis of microtubule dynamics at AAIZs regulated by a combined action of Prc1, Kif4A, and AurkB. Unexpectedly, we found that Prc1 and Kif4A also work together to enforce radial order in expanding single asters through removing anti-parallel overlaps. Although this function within asters appears opposite to their function in promoting overlaps between asters, we show that conceptually similar molecular activities are involved in each case. Thus, the Prc1/Kif4A module plays a central role in controlling microtubule orientation within, as well as between, large embryo asters. These findings extend our understanding of the biology of the Prc1/Kif4A module to new aspects of cell division biology, and reveal interesting adaptations of conserved microtubule organising mechanisms that allow scaling to very large cells.

Results

Prc1E and Kif4A localization in an egg extract system

We recently described a cell-free system that reconstituted spatial organisation of cytokinesis signalling molecules in *Xenopus* egg extracts (Field et al., 2014; Mitchison et al., 2012; Nguyen, Groen et al., 2014). *Xenopus* Kif4A, also called Xklp1, is present in eggs at ~100 nM (Wühr et al., 2014). An embryonic isoform of Prc1 that we will call Prc1E is present in eggs at ~63 nM (Nguyen, Groen et al., 2014; Wühr et al., 2014). We were unable to detect somatic Prc1 by either immunoblotting with an isoform specific antibody or mass spectrometry (Gache et al., 2010; Wühr et al., 2014). To localize Prc1E and Kif4A in the extract system we added fluorescently tagged recombinant proteins (Figure S3.1a), using <20% the concentration of endogenous proteins to minimize perturbation.

Aurora A kinase (AurkA)-coated beads were used as centrosome-mimics to nucleate microtubules (Tsai and Zheng, 2005), and the aster assembly reaction was spread to a layer ~10-15 μm thick between polyethylene glycol (PEG)-coated coverslips and imaged by confocal microscopy (Figure 3.1a and Movie S3.1). Both the Prc1E and Kif4A probes were recruited to microtubules and localized throughout asters. When AAIZs formed between asters, Prc1E was weakly enriched, while Kif4A strongly enriched, at anti-parallel bundles between the asters (Figure 3.1a, ~17 min). The proteins co-localized on some microtubule bundles, consistent with functioning together, but their overall distribution differed, consistent with their not forming a stable complex (Zhu and Jiang, 2005). To quantify microtubule morphology and Prc1E/Kif4A recruitment over time, we generated kymograph plots along the line connecting the two aster centres (Figure 3.1a'). These plots confirmed Prc1E and Kif4A recruitment to anti-parallel bundles between the asters. Both were recruited at the same time, and Kif4A was always more enriched in the AAIZ. Unexpectedly, we also observed bright streaks of Prc1E and Kif4A at the free edges of growing asters that have not yet formed an AAIZ (Figure 3.1a, zoom-ups).

Figure 3.1: Localization of Prc1E and Kif4A in *Xenopus laevis* egg extracts.
Confocal **(a)** and widefield **(b)** time-lapse sequence of asters nucleated from AurkA beads, visualizing: microtubules (Alexa647-tubulin), mCherry-Prc1E, and either Kif4A-GFP **(a)** (Movie S3.1) or the chromosome passenger complex (CPC) using a GFP-DasraA subunit **(b)** (Movie S3.2). **(a'** and **b')** Quantification of AAIZ formation: mean fluorescence intensities along a 30 μm wide line (cyan box in **a** and **b**) were plotted over time.

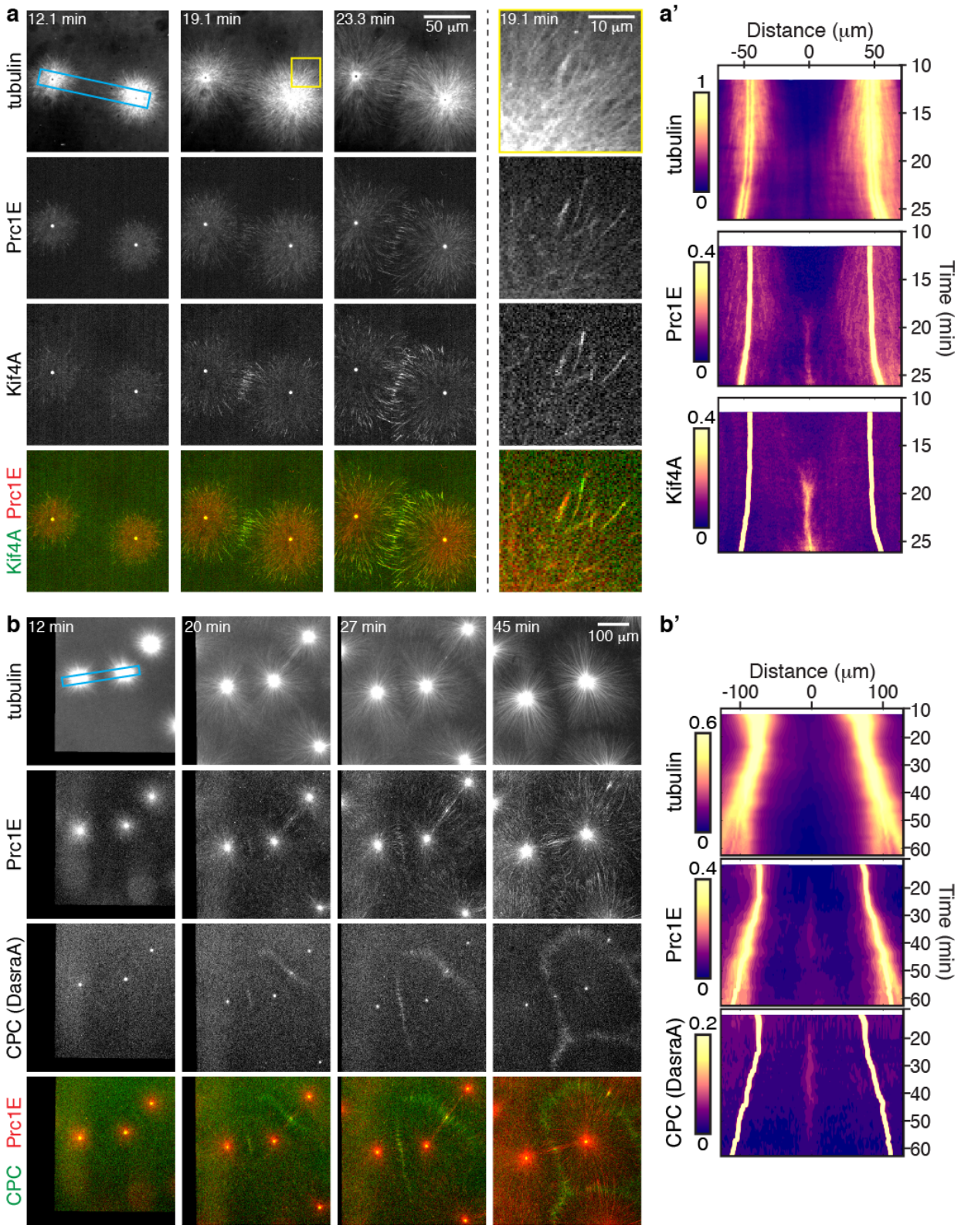

Figure 3.1 (Continued)

We also co-localized the CPC with Prc1E, using a GFP tagged DasraA subunit of the CPC (Figure 3.1b and Movie S3.2). Unlike Prc1E and Kif4A, the CPC exclusively localized to a narrow region at AAIZs, and also to the AurkA beads (Figure 3.1b). This observation was quantified using kymograph plots (Figure 3.1b'). No CPC localization was observed at free edges of growing asters.

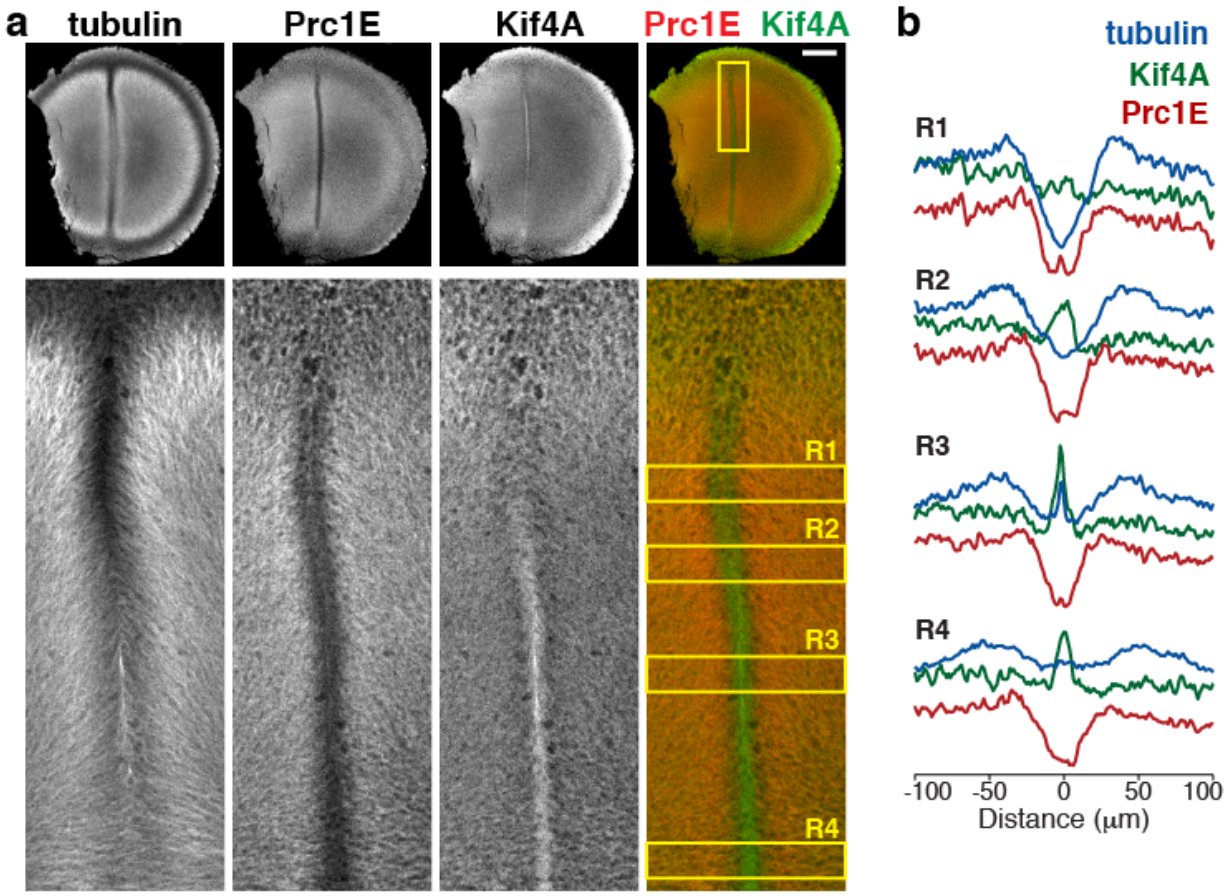

Figure 3.2: Localization of Prc1E and Kif4A in dividing *Xenopus laevis* zygotes.
(a) Immunofluorescence staining for tubulin, Prc1E and Kif4A in *Xenopus* zygotes fixed after anaphase of 1st mitosis at 100 min after fertilization. **(b)** Fluorescence profile plots along the transects R1-R4. Scale bars, 200 μm.

To observe Prc1E and Kif4A localizations *in vivo,* we probed fixed *Xenopus* zygotes by immunofluorescence (Figure 3.2). After anaphase of 1st mitosis, microtubule asters grew out from the spindle poles to fill the entire cytoplasm. Where the AAIZ formed between the asters at the egg midplane, a region of lower microtubule density was observed (Mitchison et al., 2012; Wühr et al., 2009; 2010). Both Prc1E and Kif4A localized to the entire aster. While Kif4A was highly enriched at the AAIZ nearer the centre of the egg, Prc1E was not. Prc1E appeared depleted from the AAIZ, except for a narrow zone nearer the periphery, where the asters only recently began to overlap. The overlap region of cytokinesis midzones in somatic cells exclude antibodies (Saxton and McIntosh, 1987), so the relative lack of Prc1E signal in the AAIZ could be either physiological or due to antibody exclusion.

Plus end dynamics in AAIZs

Live imaging is not feasible in opaque *Xenopus* eggs. Therefore, we used the extract system to investigate plus end dynamics in AAIZs, with the goal of understanding how microtubules from one aster are prevented from growing into the neighbouring aster. Figure 3.3a shows EB1 trajectories colour-coded by the orientation of microtubule growth (Movie S3.3) (Applegate et al., 2011; Matov et al., 2010; Nguyen, Groen et al., 2014). More than 90% of the growing microtubules within each aster were oriented with their plus ends pointing radially away from the nucleating site, and orientation switched abruptly over ~30 μm in the AAIZ (Figure 3.3a', red area). The position of the AAIZ midline was defined as the line where microtubules were growing equally in both directions.

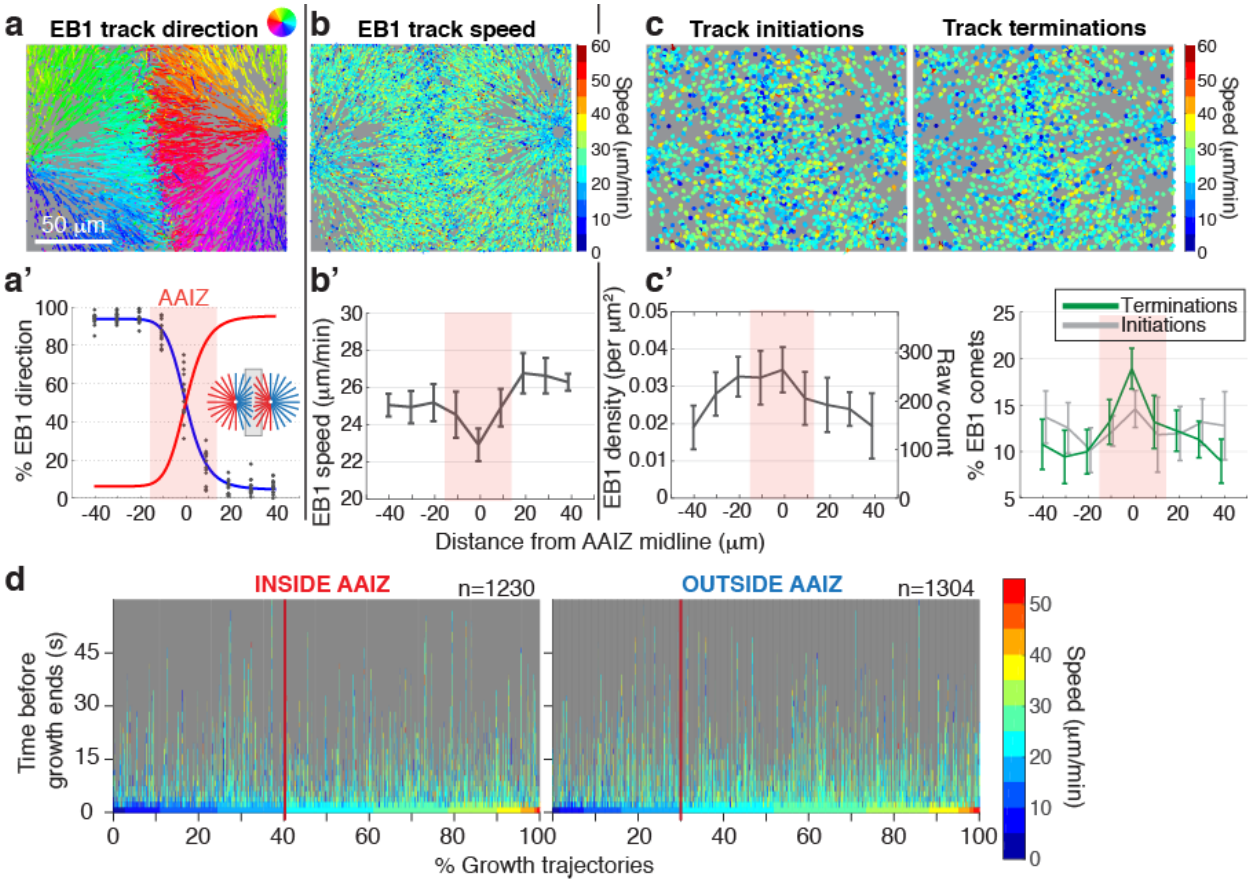

Figure 3.3: Plus end dynamics at AAIZs.

(a, b) Growth trajectories of microtubule plus ends coloured by their mean direction **(a)** or instantaneous velocity **(b)**. Trajectories were visualized by imaging and tracking the plus tip binding protein EB1-eGFP over 2 minutes at 1.5 sec intervals (Movie S3.3). Red-shaded region defines a 30 µm-wide AAIZ area. **(c)** Locations of growth initiations (*left*) and terminations (*right*) coloured by instantaneous growth velocity. Spatial distributions of **(a')** growth trajectories at AAIZs classified by direction (*grey dots*: fraction of EB1 comets moving from left to right, *blue curve*: sigmoidal fit to grey dots, *red curve*: sigmoidal fit to fraction of EB1 comets moving in opposite direction), **(b')** mean instantaneous growth rates (mean ± SEM), **(c')** EB1 comet density (*left*) and fractions of EB1 comets that are growth initiation/terminations (*right*) (mean ± SD), *n* = 12 neighbouring ROIs (see Methods for data analysis). **(d)** Straightened growth tracks color-coded by instantaneous velocity, and rank ordered by termination velocity measured during last 3 sec of growth. Tracks terminating inside (*left*) or outside (*right*) AAIZ. Red line demarcates tracks with termination velocity less than 20 µm/min from those with higher termination velocity.

Figure 3.3b shows EB1 comet trajectories colour-coded by velocity in the same AAIZ and Figure 3.3b' shows mean EB1 velocity as a function of distance from the AAIZ midline. EB1 comets tended to slow down as they entered the centre of the AAIZ. Mean growth rates in one experiment were 25.8 ± 9.9 μm/min (± SD, n = 13632 comets) outside the AAIZ and 22.9 ± 11.0 μm/min (± SD, n = 3172 comets) inside it, representing an 11% reduction (the two rate distributions were statistically significantly different, $P < 10^{-45}$ from KS test). Other experiments showed qualitatively similar slowdowns (11.3 ± 2.3% reduction, mean ± SD, n = 5 AAIZs, $P <$ 0.001 from one-sample t-test).

We located the initiation and termination of microtubule growth trajectories (Figure 3.3c). Initiations corresponded to microtubule nucleations or rescues, while terminations corresponded to catastrophes or pauses. We also measured the EB1 comet density as a function of distance from the AAIZ midline (Figure 3.3c', left), and determined the fraction of comets that were track initiations or terminations (Figure 3.3c', right). From the analysis of multiple representative AAIZs, we observed no particular spatial regulation of either EB1 comet density (10 ± 39% reduction, mean ± SD from n = 5 AAIZs, P = 0.59 from one-sample t-test) or frequency of initiation events (15 ± 33% increase, P = 0.37). However, we saw a consistent increase in the frequency of termination events near the AAIZ midline (86 ± 33% increase, P = 0.004). Thus, plus ends tended to slow down and terminate more within AAIZs than elsewhere in asters.

To determine if slowdown in AAIZs correlated with termination there, we extracted many EB1 trajectories for microtubules where growth terminated inside an AAIZ vs. outside, colour-coded the trajectory by instantaneous growth velocity, then rank ordered by velocity in the last 3 sec of growth (Figure 3.3d). Considering microtubules that stopped growing outside AAIZs, we noted an approximately equal spread of terminal velocities at the end of the growth interval. Considering microtubules that stopped growing inside, we noted more microtubules that slowed down before they stopped growing. We also observed a higher positive correlation between growth rates and growth lifetimes inside AAIZs than outside (Supplementary Note 3.1 and

Figure S3.2). Combined with the preceding data, we conclude that microtubules tend to slow down, then stop growing, inside AAIZs.

The Prc1/Kif4A module blocks interpenetration at AAIZs

To test the role of Kif23, Kif4A and Prc1E at AAIZs, we depleted each protein to less than 5% of its initial abundance, as judged by immunoblots (Figures 3.4 and S3.1b-d). We observed no obvious effect on nucleation from AurkA beads or on microtubule polymerization rates. Kif23, Kif4A and Prc1E did not significantly co-immunoprecipitate by immunoblot or mass spectrometry (not shown), so we could independently measure the effect of depletions on localization of the other factors as well as on AAIZ dynamics. Although Prc1E and Kif4A do not form a stable complex in egg extract, they do interact while bound to microtubules (Bieling et al., 2010; Zhu and Jiang, 2005), and phosphorylation of Kif4A by the AurkB subunit of the CPC may increase their interaction (Nunes Bastos et al., 2013).

Depletion of Kif23 did not have any detectable effect on AAIZ organisation, as measured by plus end interpenetration (Figure 3.4b). Depletion of either Kif4A or Prc1E caused strong perturbation of AAIZs (Figure S3a). Specifically, microtubules from each aster started to grow into the neighbouring aster (Figure 3.4c, d). There was still a gradual switch in microtubule orientation, but this might simply reflect distance from the nearest nucleating site. Prc1E depletion resulted in profound disorganisation of the AAIZ, with effects including inhibition of anti-parallel microtubule bundling, and a complete block to localization of Kif4A (Figure S3.3b, c) or the CPC (AurkB, INCENP, or DasraA; not shown). Kif4A depletion caused a less profound disorganisation: anti-parallel microtubule bundles were still observed, and these bundles localized Prc1E (Figure S3.3d) and other midzone markers such as the CPC (Nguyen, Groen et al., 2014). CPC localization, however, was dispersed and no directional movement of CPC was observed on bundles in the absence of Kif4A (Nguyen, Groen et al., 2014), consistent with siRNA experiments in mammalian cells (Hu et al., 2011; Kurasawa et al., 2004).

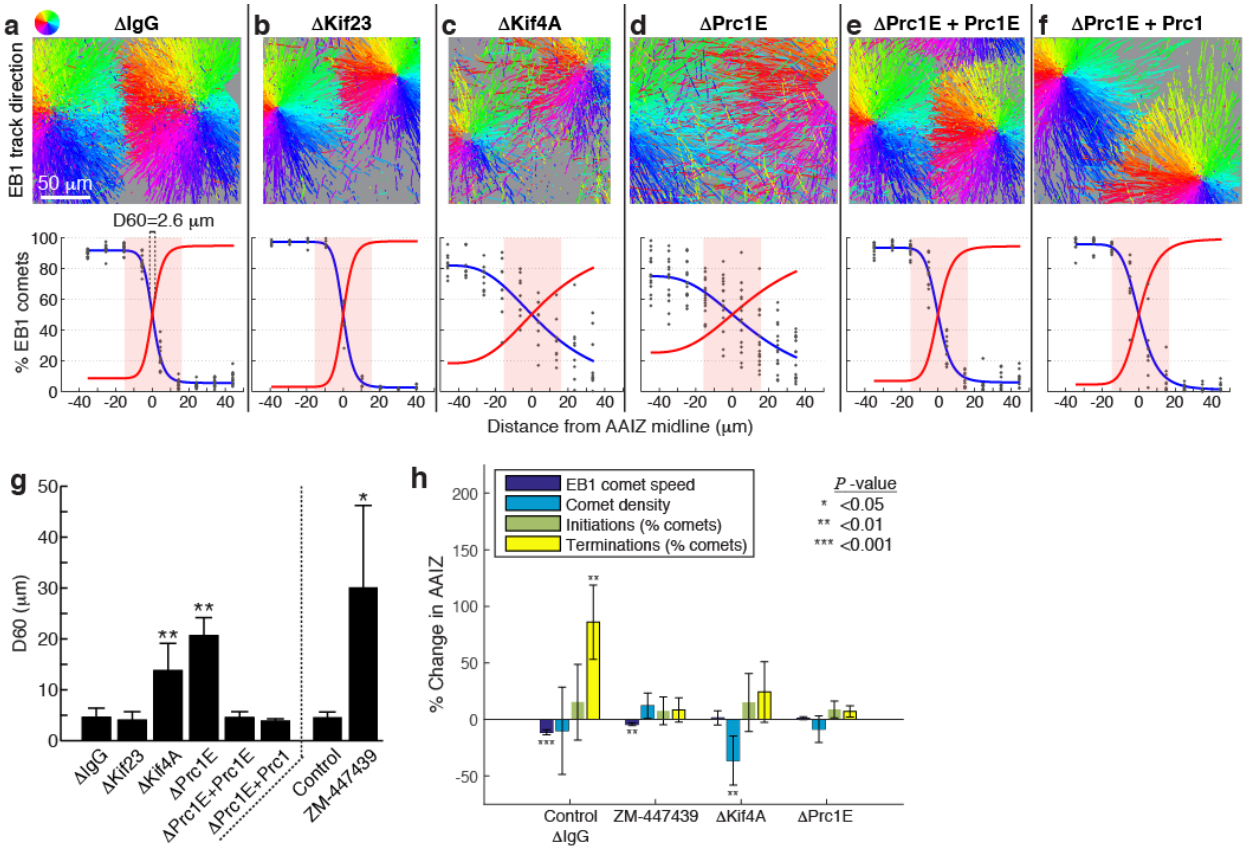

Figure 3.4: The Prc1/Kif4A module and AurkB activity are required for block of interpenetration at AAIZs.

(a-f) Analyses of microtubule growth directions as per Fig. 2a. Immunodepletion conditions as labelled above: control IgG **(a)**, Kif23 **(b)**, Kif4A **(c)**, Prc1E **(d)**, Prc1E depletion with addback of embryonic Prc1E **(e)**, Prc1E depletion with addback of somatic Prc1 **(f)**. **(g)** The D60 parameter, a metric for the degree of interpenetration, was defined as the difference between the interpolated distances where the red and blue curves crossed 60% (see panel **a**). Plot of mean D60 values (± SD) measured for each treatment ($n \geq 3$ AAIZs each). The last two bars (control and AurkB inhibition with 100 μM ZM-447439) were obtained from data reported in ref. (Nguyen, Groen et al., 2014). Welch's *t*-test analyses, compared with IgG control. **(h)** Difference in dynamics measurements (as per Figure 3.3b, c) for tracks ending inside vs. outside AAIZ under each treatment, expressed as % change of measurements inside compared to those outside. Mean ± SD, $n \geq 3$ AAIZs each condition. One-sample *t*-test analyses, null hypothesis of no change. *$P < 0.05$, **$P < 0.01$, ***$P < 0.001$).

Both Kif4A and Prc1E depletion phenotypes were rescued by adding back the appropriate recombinant purified proteins, either as a GFP fusion or unlabelled protein (Figures 3.4e and S3.1b, c). This confirms both the specificity of the immunodepletion and the functional attributes of the protein probes. The effect of Prc1E depletion was also fully rescued, to the extent we could assay, by adding back the somatic isoform of the Prc1 protein (Figure 3.4f).

The effects of depletions and addbacks are quantified in Figure 3.4g by the D60 parameter, a metric of the depth of growing plus end interpenetration at the aster-aster boundary. This plot includes the effects of small molecule inhibition (ZM-447439) of the AurkB subunit of the CPC, which we previously showed to block AAIZ formation (Nguyen, Groen et al., 2014). Anti-parallel bundles recruiting both Kif4A and Prc1E still formed at aster-aster boundaries when AurkB was inhibited (Figure S3.3e). However, they did not effectively block interpenetration, since the D60 parameter was increased to a similar extent when AurkB was inhibited as when Prc1E or Kif4A was depleted. Collectively, these data suggest that block of interpenetration at AAIZs require a combined action of Prc1 (represented here by its embryonic isoform Prc1E), Kif4A, and AurkB.

Next we quantified the effect of AurkB inhibition and Kif4A or Prc1E depletion on microtubule dynamics using the methods described in Figure 3.3. Figure 3.4h shows the difference between dynamics measurements of microtubule growth tracks ending inside vs. outside the ~30 μm AAIZ area (defined in Figure 3.3). Since the absolute values of dynamics measurements varied from experiment to experiment under the same condition, we used the values measured outside the AAIZ as the reference for each experiment. Differences were then expressed as % change of values measured inside the AAIZ compared to those measured outside, which was more consistent from experiment to experiment. *P*-values are therefore reported for inside-outside AAIZ differences under a particular condition, and not for comparison between conditions. More than 3 AAIZs were analysed for each condition.

For control AAIZs, there was a statistically significant decrease in growth rate (11.3 ± 2.3%, SD) and increase in growth termination frequency (86 ± 33%, SD), as per Figure 3.3. The increase in termination frequency disappeared when Kif4A or Prc1E was depleted, or AurkB was inhibited. The decrease in growth rate was eliminated when Kif4A or Prc1E was depleted, however, it was still present to a slight but statistically significant degree when AurkB was inhibited (4.3 ± 1.2%, SD). Note that while growth rate differences inside vs. outside AAIZs were proportionately smaller than termination differences, the standard deviation in growth rates was much smaller, so differences were as, or more, significant. Correlation between growth slowdown inside AAIZs and growth termination there was reduced when AurkB was inhibited, and completely lost when either Kif4A or Prc1E was depleted (see Supplementary Note 3.1, Figures S3.2 and S3.4).

Microtubules stop growing within anti-parallel microtubule overlaps formed by Prc1E and Kif4A at AAIZs

To determine how the Prc1/Kif4A module blocks aster interpenetration, we used high resolution TIRF microscopy to image microtubules, EB1 and Prc1E at AAIZs (Figure 3.5a). We then coloured EB1 tracks based on their direction and overlaid them on top of Prc1E images (Figure 3.5a, right, and Movie S4). We found that most microtubules that encountered and/or joined an anti-parallel overlap marked by Prc1E stopped growing. In contrast, when Kif4A was depleted, many microtubules that encountered Prc1E-marked anti-parallel overlaps continued growing beyond the overlap, leading to extensive interpenetration (Figure 3.5b and Movie S5). Although anti-parallel overlaps localizing both Prc1E and Kif4A still formed when AurkB was inhibited, these overlaps were less efficient at stopping microtubule growth, also resulting in interpenetration (not shown). These data suggest that neighbouring asters recognize each other via anti-parallel microtubule overlaps formed by Prc1E (or Prc1 in somatic cells). In the

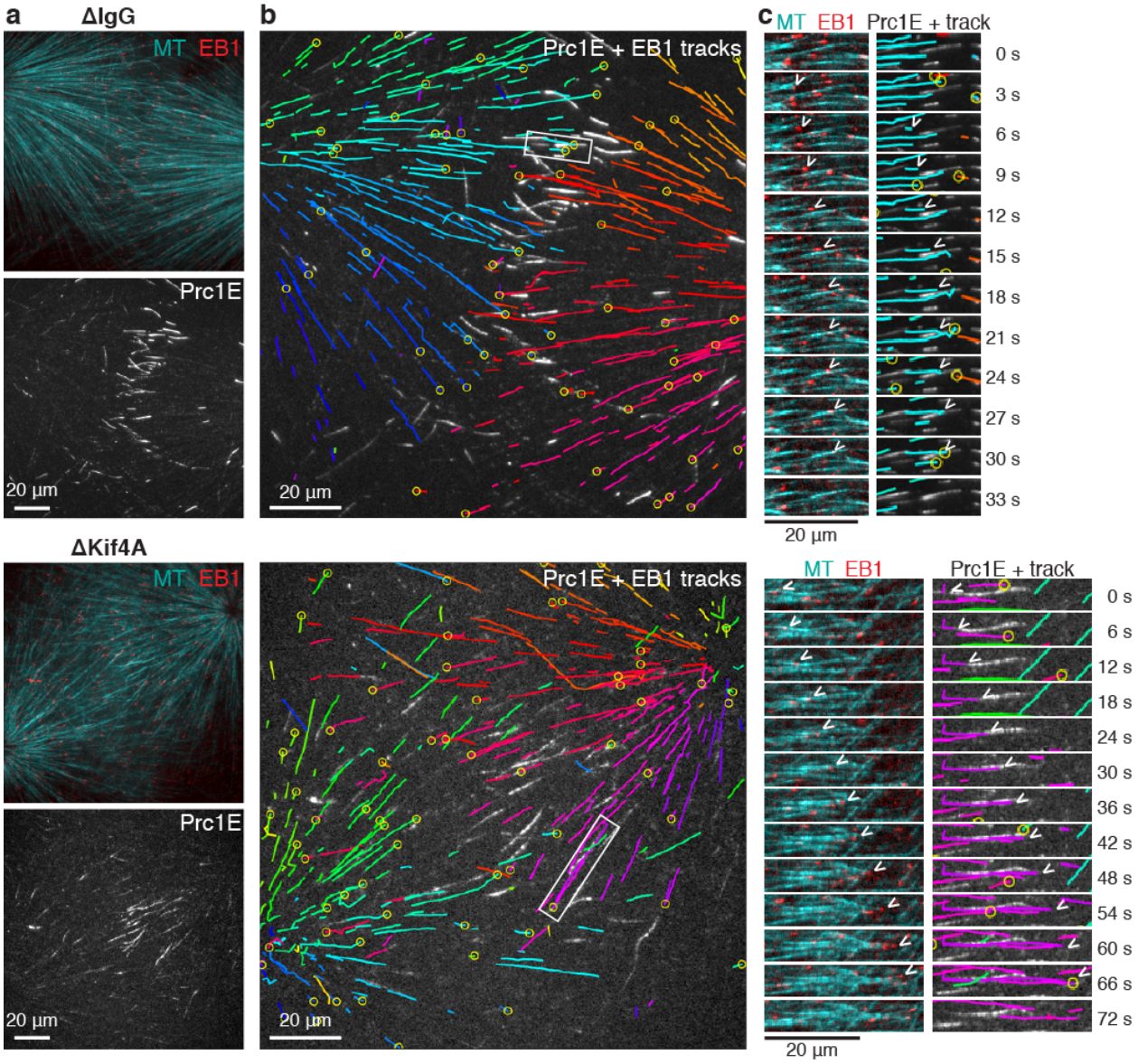

Figure 3.5: The Kif4A/Prc1E module inhibits microtubule growth within anti-parallel overlaps at AAIZs. (a) TIRF images of microtubules (Alexa647-tubulin, *cyan*), EB1-GFP (*red*), and mCherry-Prc1E (*grey*) at AAIZs formed in mock depleted and Kif4A depleted extracts. **(b)** Overlay of Prc1E image and direction-coloured EB1 tracks corresponding to each detected EB1 comet in a single frame. Yellow circles indicate track terminations (Movies S4 and S5). **(c)** Example behaviours of microtubule plus ends before they stop growing, shown as time-lapse montages of the boxed areas in **b**.

presence of Kif4A that gets recruited to the overlaps, microtubules encountering overlaps are prevented from further growth. This growth termination effect is enhanced by AurkB activity.

The Prc1/Kif4A module enforces radial order within large asters

In the course of measuring the effects of Prc1E and Kif4A depletion on AAIZs, we noticed that the morphology of isolated growing asters was also strongly perturbed. In isolated asters assembled in extracts depleted of either Prc1E or Kif4A, microtubules initially grew radially from the AurkA bead to a radius of ~40 μm. Microtubules continued to assemble at the periphery, but instead of forming a well-organised aster, they appeared disorganised at larger radii. This effect was not observed when AurkB was inhibited.

To quantify radial order in asters, we measured the directions of EB1 comet trajectories within a quadrant of an isolated aster with its centre at the top left corner (Figure 3.6a-e). We generated radial order heat maps by plotting radial order parameters (*R*) calculated from the distribution of angular deviations of EB1 trajectories from the radial direction (Figure 3.6a'-e'; see Methods). We also plotted radial order parameters against the distance from the aster centre at the AurkA bead (Figure 3.6f; see Methods). Radial order may be inaccurately measured at small radii (<10 μm) due to growth in the Z plane close to the bead, so the initial rise in these plots probably does not represent low order near the bead.

Mock depleted asters maintained high radial order out to the largest radius measured with our camera (~150-200 μm), with a slight decrease at large radii. Depletion of Kif4A or Prc1E strongly disrupted radial order: limited order was maintained within ~40 μm radius, presumably due to frequent re-nucleation of straight microtubules from the AurkA bead. Radial order was progressively lost as radius increased, though growth direction never completely randomized. Both depletion phenotypes could be rescued by adding back appropriate recombinant proteins (Figure 3.6d, e; data not shown for Kif4A addback). As with AAIZ formation, both the embryonic and somatic isoforms of Prc1 were able to rescue radial order.

Similar results were obtained using an alternative method of quantifying radial order (Figure S3.5). We conclude from these data that Kif4A and Prc1 (either embryonic or somatic) are necessary to maintain radial order within large asters as they expand.

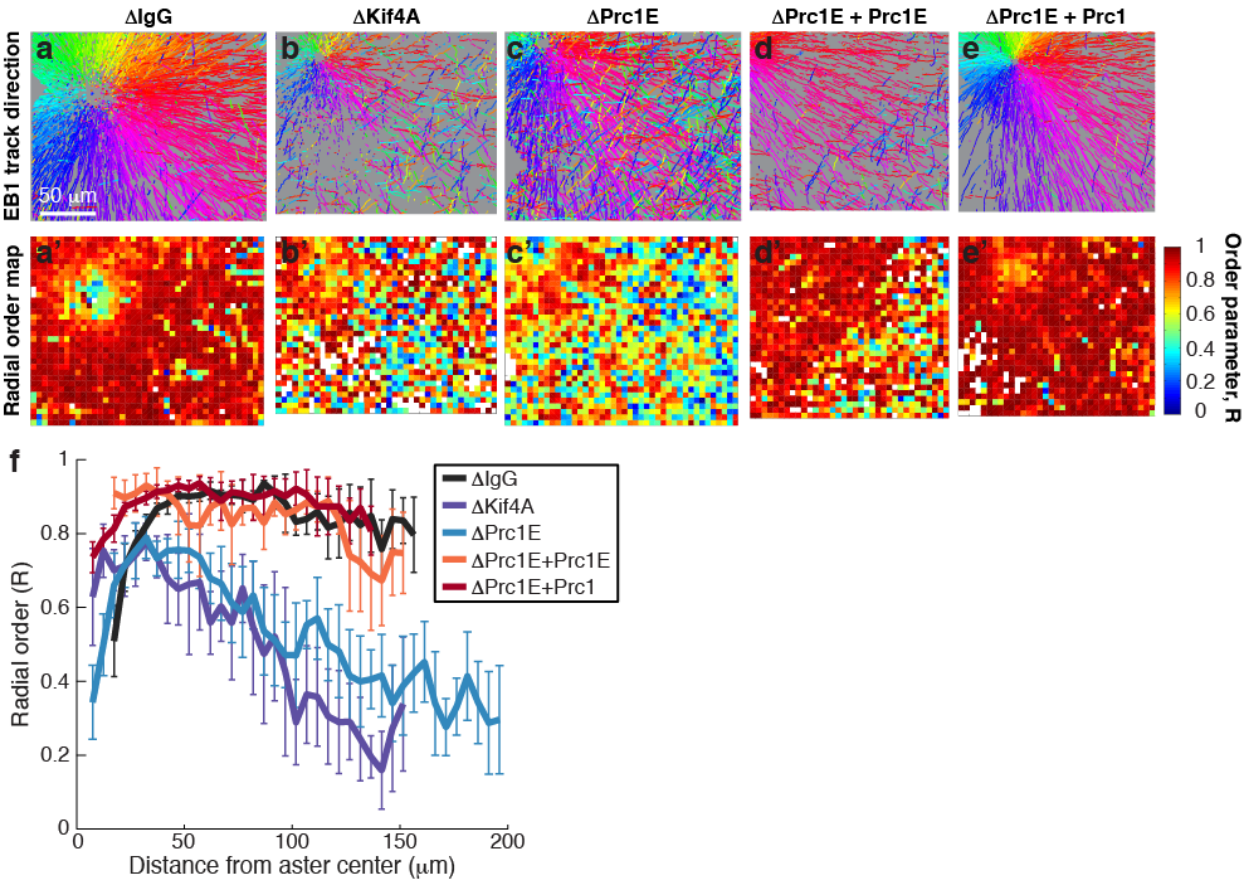

Figure 3.6: The Kif4A/Prc1 module enforces radial order within large microtubule asters. **(a-e)** Growth trajectories of microtubule plus ends coloured by their mean directions within isolated asters. Methods similar to Fig. 2a. Immunodepletion conditions as labelled above: control IgG **(a)**, Kif4A **(b)**, Prc1E **(c)**, Prc1E depletion with addback of embryonic Prc1E **(d)**, Prc1E depletion with addback of somatic Prc1 **(e)**. **(a'-e')** Radial order heat maps showing the local radial order quantified by the *R* parameter; each square cell measures 5x5 μm^2 (see Methods). Warmer colours represent higher radial order. **(f)** Order parameter *R* as a function of distance from the aster centre for the five asters shown above. Error bars are standard deviations (see Methods for analysis).

Regulation of anti-parallel microtubule overlaps by Prc1E and Kif4A

To better understand how Kif4A and Prc1E enforce radial order, we analysed representative regions of 2- or 3-colour movies of tubulin, Kif4A, Prc1E or EB1 within growing asters, seeking examples where we could interpret the dynamics (Figure 3.7). In general, Kif4A and Prc1E localized to a subset of microtubules bundles within the growing aster, and tubulin imaging suggested that these included at least one anti-parallel interaction. We know from EB1 tracking (Figure 3.3a) that ~3-10% of microtubules in control asters grow in the wrong direction (i.e. deviating by >±90° from the radial direction). This presumably occurs because nucleation away from the centrosome, which dominates in large asters (Ishihara et al., 2014), tends to randomize growth direction, while bundling interactions tend to line up microtubules either parallel or anti-parallel.

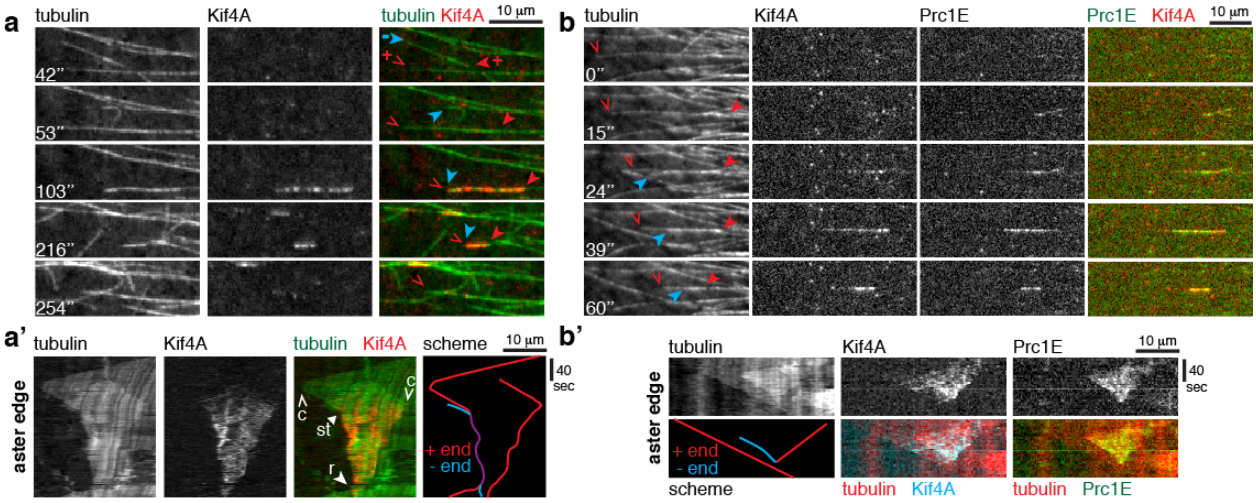

Figure 3.7: The Kif4A/Prc1E module eliminates anti-parallel overlaps within growing asters. (a,b) Examples of anti-parallel microtubule overlap formation and elimination at the edge of growing asters imaged with TIRF microscopy (Movies S3.6 and S3.7). Proteins visualized: Alexa647-tubulin and Kif4A-GFP **(a)**; Alexa647-tubulin, Kif4A-GFP, and mCherry-Prc1E **(b)**. Arrowheads indicate: plus ends (*red*), minus ends (*cyan*), microtubule growing out radially from aster (*empty*), microtubule growing in opposite direction (*full*). **(a',b')** Kymographs of examples above along the radially growing microtubule. Events indicated: catastrophe (c), stabilization (st), rescue (r).

In the example in Figure 3.7a (Movie S6), a microtubule initially grows at 33 μm/min from right to left at the edge of an expanding aster (empty arrowhead; 'MT1'). At 44 sec, an anti-parallel microtubule (full arrowhead; 'MT2') makes contact and bundles. Presumably, the anti-parallel crosslinking activity of Prc1E helps promote this bundling. We followed the overlap formation and microtubule dynamics using a kymograph along MT1 (Figure 3.7a'). MT1 slows down to 7.6 μm/min before it catastrophes and starts shrinking at 14 μm/min (55 sec). Formation of the overlap can be observed on the tubulin kymograph as an expanding bright patch. On the right, lengthening of the overlap (13 μm/min) can be attributed to growth of MT2 and/or anti-parallel sliding. Overlap extension is accompanied by recruitment of Kif4A, during which MT2 stops growing and starts depolymerizing within the bundle at 5.8 μm/min (86 sec). At this point, the shrinking rate of MT1 is reduced to 3.1 μm/min (101 sec). Eventually when the overlap shrinks from a maximum length of 19 μm to 1.9 μm (241 sec), the localization of Kif4A is diminished and MT1 rescues at a 40 μm/min growth rate.

It is unusual to find an example as clear as that shown in Figure 3.7a due to the high microtubule density in asters and the presence of more than two microtubules in most bundles, but we believe this sequence is representative, based on EB1 tracking and Kif4A localization. Figure 3.7b shows another example of anti-parallel overlap formation and turnover where both Kif4A and Prc1E were localized (Movie S7). Examples like this suggest that Prc1E is an accurate marker of anti-parallel overlaps, and that the bright streaks of Prc1E seen in Figure 3.1a mark microtubule bundles that contain at least one microtubule in the anti-parallel orientation.

Discussion

Figure 3.8 summarizes a model we propose for how control of antiparallel overlaps by the Prc1/Kif4 module (Figure 3.8a) gives rise to both radial order within a single aster and block of interpenetration between neighbouring asters (Figure 3.8b). In our egg extract system, Prc1 is required for bundling of antiparallel microtubules and recruitment of Kif4A and other cytokinesis factors to the overlaps (Figures 3.5, 3.7b, and S3.3), consistent with previous studies (Kurasawa et al., 2004; Mollinari et al., 2005; Subramanian et al., 2010). Microtubules within the overlap are prevented from further growing by Kif4A (Figures 3.5 and 3.7), consistent with Kif4A's function in inhibiting microtubule dynamics (Bieling et al., 2010; Bringmann et al., 2004; Hu et al., 2011; Nunes Bastos et al., 2013). Surprisingly, we found that in our system the Prc1/Kif4 overlaps underwent dynamic shrinking (Figure 3.7). Previous reconstitution studies using pure proteins reported only growing or stabilized, but not shrinking, microtubule overlaps formed in the presence of Prc1 and Kif4A (Bieling et al., 2010; Nunes Bastos et al., 2013). This suggests that in our system in addition to microtubule stabilization by Kif4A, anti-parallel sliding and/or microtubule depolymerisation are also involved in controlling the length of anti-parallel overlaps. Both depletion of Kif4A and inhibition of AurkB reduced the rate of overlap shrinkage, but did not completely eliminate it (not shown). Prc1 is known to bind to and target other cytokinesis factors to the midzones (Grüneberg et al., 2006; Kurasawa et al., 2004; Neef et al., 2007), whose roles in overlap shrinkage could be explored in future studies.

In large asters, most microtubules are nucleated away from the centrosome (Ishihara et al., 2014), which raises the question: how is radial order maintained? Oriented nucleation and/or parallel bundling are probably important, but evidently insufficient. Here we showed that the Prc1/Kif4A module is required for enforcing radial order (Figure 3.6), presumably by capturing and eliminating microtubules growing in the wrong direction (Figure 3.7). Whether or not Prc1 could bundle two anti-parallel microtubules depends on the contact angle between them (Dixit

and Cyr, 2004; Portran et al., 2013; Tulin et al., 2012). In our system, we observed that contact angles <~30° tended to result in bundling by Prc1 (e.g. Figure 3.7a), whereas angles >~30° tended to lead to crossovers (data not shown, but concept illustrated in Figure 3.8a). Therefore, the denser the microtubule array is, the higher is the probability of a stray microtubule being captured within an antiparallel overlap as the probability of encounters at a bundling contact angle is higher. Activity of Prc1/Kif4A within a large aster results in a small positive correlation between microtubule growth rate and growth lifetime (Figure S3.2). This is consistent with Kif4A's known function in reducing growth rate (Bieling et al., 2010; Bringmann et al., 2004; Nunes Bastos et al., 2013) and in increasing the frequency of pauses (Nunes Bastos et al., 2013).

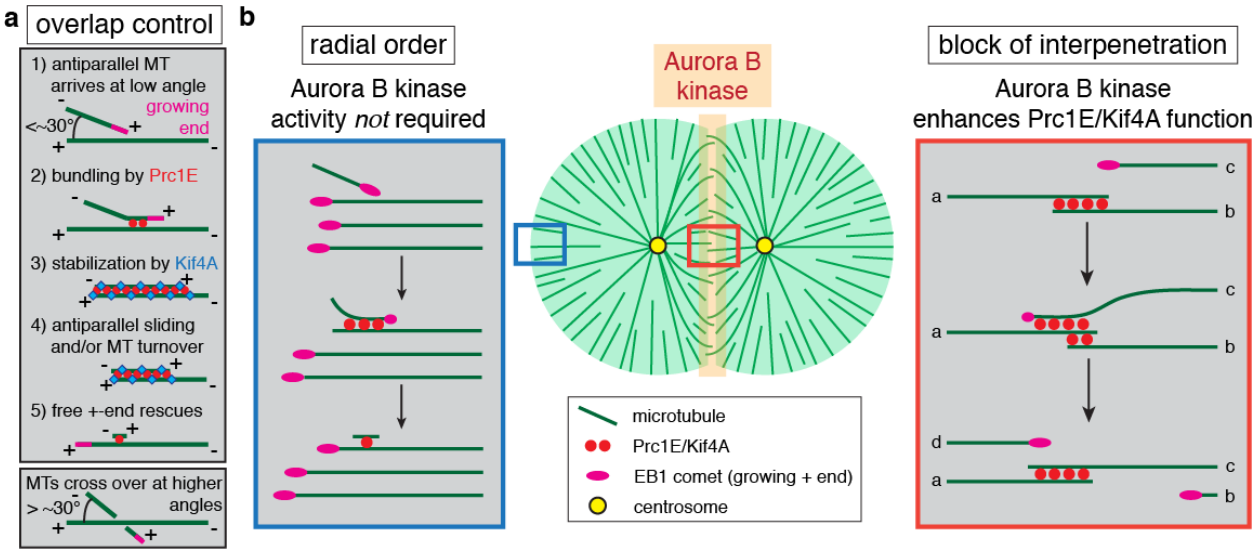

Figure 3.8: The Prc1/Kif4A module controls microtubule orientation within and between large asters. (a) Model of anti-parallel overlap control mediated by the Prc1E/Kif4A module. **(b)** Model of radial order and block to interpenetration at AAIZ through growth inhibition of anti-parallel microtubules and elimination of anti-parallel overlaps.

At AAIZs a similar mechanism of overlap control operates (Figure 3.8b). In this case, however, Prc1/Kif4A-coated bundles contain more than two microtubules and the antiparallel

overlaps persist longer, as new microtubules constantly join the bundle from both sides (Figure 3.5). Within the AAIZs, Kif4A and Prc1 lead to a decrease in growth rates, suggesting an increase in Kif4A activity due to an increase in Prc1 recruitment to anti-parallel bundles, an effect that is enhanced by Aurora B kinase activity (Figure 3.4h). AurkB activity also increases the correlation between growth rates and lifetimes (Figure S3.2), consistent with previous findings that phosphorylation of Kif4A by AurkB enhances its activity and binding affinity for Prc1 (Nunes Bastos et al., 2013).

Kif4A has been shown to be essential for normal cleavage and germ plasm organisation in *Xenopus* zygotes (Robb et al., 1996; Vernos et al., 1995). Those studies did not investigate interphase microtubule organisation in detail, but the findings are consistent with extensive disorganisation of interphase asters without Kif4A. A role for Prc1 in enforcing unidirectional microtubule organisation is new to our knowledge. Members of the conserved Ase1/MAP65/Prc1 family are thought to recognize anti-parallel microtubule overlaps in most eukaryotes, and are generally thought to promote formation of anti-parallel bundles during cell division (Bratman and Chang, 2008; Duellberg et al., 2013; Subramanian and Kapoor, 2012). Outside of cytokinesis, these proteins have known roles in organisation of the microtubule minus ends in interphase fission yeast cells (Sawin and Tran, 2006), as well as crosslinking of the cortical microtubule array, a scaffold for cell wall synthesis, in interphase plant cells (Paredez et al., 2006; Van Damme et al., 2004). A recent study suggested a role for Prc1 and Kif4A in marking and measuring single microtubules in human cells undergoing monopolar cytokinesis (Subramanian et al., 2013). We suspect additional roles of this interesting protein family remain to be discovered.

Acknowledgements

I am indebted to Aaron Groen for his generosity in providing the GFP-DasraA protein, antibodies against Aurora A kinase and Kif23 kinase, and helping me draft the initial manuscript. His support and enthusiasm were invaluable. We also thank Edwin Tan for initiating the Kif23 antibody project and help with tubulin preparation; David Miyamoto for initiating the Xklp1/Kif4A antibody project. Keisuke Ishihara and Martin Loose introduced us to the PLL-PEG coverslip passivation. We thank Jennifer Waters, Lara Petrak, Lauren Piedmont and the Nikon Imaging Center at Harvard Medical School (HMS) for microscopy support; Lynne Chang, Nikon and the Marine Biological Laboratory (MBL) for use of laser scanning confocal and TIRF microscopes; the NXR at MBL for *Xenopus* animals and care. We also thank Calixto Saenz and the Microfluidics Core Facility at HMS for use of their plasma etcher for coverslip cleaning, and Stephen Harrison's lab for providing Sf21 insect cells. Keisuke Ishihara, Mariah Hanley, James Pelletier, and Javier Pineda provided very helpful feedback on the manuscript. This work was supported by NIH grant GM39565 (T.J.M.); MBL fellowships from the Evans Foundation, MBL Associates, and the Colwin Fund (T.J.M. and C.M.F.).

Supplemental materials

Supplementary content includes Materials and Methods, Supplementary Note 3.1, Figures S3.1 to S3.5, Table S3.1, Movies S3.1 to S3.7, and References.

References

Applegate, K.T., Besson, S., Matov, A., Bagonis, M.H., Jaqaman, K., and Danuser, G. (2011). plusTipTracker: Quantitative image analysis software for the measurement of microtubule dynamics. J Struct Biol *176*, 168–184.

Argiros, H., Henson, L., Holguin, C., Foe, V., and Shuster, C.B. (2012). Centralspindlin and chromosomal passenger complex behavior during normal and Rappaport furrow specification in echinoderm embryos. Cytoskeleton (Hoboken) *69*, 840–853.

Bieling, P., Telley, I.A., and Surrey, T. (2010). A Minimal Midzone Protein Module Controls Formation and Length of Antiparallel Microtubule Overlaps. Cell *142*, 420–432.

Bratman, S.V., and Chang, F. (2008). Mechanisms for maintaining microtubule bundles. Trends Cell Biol *18*, 580–586.

Bringmann, H., Skiniotis, G., Spilker, A., Kandels-Lewis, S., Vernos, I., and Surrey, T. (2004). A kinesin-like motor inhibits microtubule dynamic instability. Science *303*, 1519–1522.

Canman, J.C., Cameron, L.A., Maddox, P.S., Straight, A., Tirnauer, J.S., Mitchison, T.J., Fang, G., Kapoor, T.M., and Salmon, E.D. (2003). Determining the position of the cell division plane. Nature *424*, 1074–1078.

Canman, J.C., Lewellyn, L., Laband, K., Smerdon, S.J., Desai, A., Bowerman, B., and Oegema, K. (2008). Inhibition of Rac by the GAP activity of centralspindlin is essential for cytokinesis. Science *322*, 1543–1546.

Dixit, R., and Cyr, R. (2004). Encounters between dynamic cortical microtubules promote ordering of the cortical array through angle-dependent modifications of microtubule behavior. Plant Cell *16*, 3274–3284.

Duellberg, C., Fourniol, F.J., Maurer, S.P., Roostalu, J., and Surrey, T. (2013). End-binding proteins and Ase1/PRC1 define local functionality of structurally distinct parts of the microtubule cytoskeleton. Trends Cell Biol *23*, 54–63.

Euteneuer, U., and McIntosh, J.R. (1980). Polarity of midbody and phragmoplast microtubules. J Cell Biol *87*, 509–515.

Field, C.M., Nguyen, P.A., Ishihara, K., Groen, A.C., and Mitchison, T.J. (2014). Xenopus egg cytoplasm with intact actin. Meth Enzymol *540*, 399–415.

Gache, V., Waridel, P., Winter, C., Juhem, A., Schroeder, M., Shevchenko, A., and Popov, A.V. (2010). Xenopus meiotic microtubule-associated interactome. PLoS ONE *5*, e9248.

Gaillard, J., Neumann, E., Van Damme, D., Stoppin-Mellet, V., Ebel, C., Barbier, E., Geelen, D., and Vantard, M. (2008). Two microtubule-associated proteins of Arabidopsis MAP65s promote antiparallel microtubule bundling. Mol Biol Cell *19*, 4534–4544.

Glotzer, M. (2009). The 3Ms of central spindle assembly: microtubules, motors and MAPs. Nat Rev Mol Cell Biol *10*, 9–20.

Grüneberg, U., Neef, R., Honda, R., Nigg, E.A., and Barr, F.A. (2004). Relocation of Aurora B from centromeres to the central spindle at the metaphase to anaphase transition requires MKlp2. J Cell Biol *166*, 167–172.

Grüneberg, U., Neef, R., Li, X., Chan, E.H.Y., Chalamalasetty, R.B., Nigg, E.A., and Barr, F.A. (2006). KIF14 and citron kinase act together to promote efficient cytokinesis. J Cell Biol *172*, 363–372.

Hu, C.-K., Coughlin, M., Field, C.M., and Mitchison, T.J. (2008). Cell polarization during monopolar cytokinesis. J Cell Biol *181*, 195–202.

Hu, C.-K., Coughlin, M., Field, C.M., and Mitchison, T.J. (2011). KIF4 regulates midzone length during cytokinesis. Curr Biol *21*, 815–824.

Ishihara, K., Nguyen, P.A., Groen, A.C., Field, C.M., and Mitchison, T.J. (2014). Microtubule nucleation remote from centrosomes may explain how asters span large cells. Proc Natl Acad Sci USA *111*, 17715–17722.

Jantsch-Plunger, V., Gönczy, P., Romano, A., Schnabel, H., Hamill, D., Schnabel, R., Hyman, A.A., and Glotzer, M. (2000). CYK-4: A Rho family gtpase activating protein (GAP) required for central spindle formation and cytokinesis. J Cell Biol *149*, 1391–1404.

Jiang, W., Jimenez, G., Wells, N.J., Hope, T.J., Wahl, G.M., Hunter, T., and Fukunaga, R. (1998). PRC1: a human mitotic spindle-associated CDK substrate protein required for cytokinesis. Mol Cell *2*, 877–885.

Kapitein, L.C., Janson, M.E., van den Wildenberg, S.M.J.L., Hoogenraad, C.C., Schmidt, C.F., and Peterman, E.J.G. (2008). Microtubule-driven multimerization recruits ase1p onto overlapping microtubules. Curr Biol *18*, 1713–1717.

Kurasawa, Y., Earnshaw, W.C., Mochizuki, Y., Dohmae, N., and Todokoro, K. (2004). Essential roles of KIF4 and its binding partner PRC1 in organized central spindle midzone formation. Embo J *23*, 3237–3248.

Lewellyn, L., Carvalho, A., Desai, A., Maddox, A.S., and Oegema, K. (2011). The chromosomal passenger complex and centralspindlin independently contribute to contractile ring assembly. J Cell Biol *193*, 155–169.

Loïodice, I., Staub, J., Setty, T.G., Nguyen, N.-P.T., Paoletti, A., and Tran, P.T. (2005). Ase1p organizes antiparallel microtubule arrays during interphase and mitosis in fission yeast. Mol Biol Cell *16*, 1756–1768.

Matov, A., Applegate, K., Kumar, P., Thoma, C., Krek, W., Danuser, G., and Wittmann, T. (2010). Analysis of microtubule dynamic instability using a plus-end growth marker. Nat Methods.

Mishima, M., Kaitna, S., and Glotzer, M. (2002). Central spindle assembly and cytokinesis require a kinesin-like protein/RhoGAP complex with microtubule bundling activity. Dev Cell *2*, 41–54.

Mishima, M., Pavicic, V., Grüneberg, U., Nigg, E.A., and Glotzer, M. (2004). Cell cycle regulation of central spindle assembly. Nature *430*, 908–913.

Mitchison, T., Wühr, M., Nguyen, P., Ishihara, K., Groen, A., and Field, C.M. (2012). Growth, interaction, and positioning of microtubule asters in extremely large vertebrate embryo cells. Cytoskeleton (Hoboken) *69*, 738–750.

Mollinari, C., Kleman, J.-P., Jiang, W., Schoehn, G., Hunter, T., and Margolis, R.L. (2002). PRC1 is a microtubule binding and bundling protein essential to maintain the mitotic spindle midzone. J Cell Biol *157*, 1175–1186.

Mollinari, C., Kleman, J.-P., Saoudi, Y., Jablonski, S.A., Perard, J., Yen, T.J., and Margolis, R.L. (2005). Ablation of PRC1 by small interfering RNA demonstrates that cytokinetic abscission requires a central spindle bundle in mammalian cells, whereas completion of furrowing does not. Mol Biol Cell *16*, 1043–1055.

Neef, R., Grüneberg, U., Kopajtich, R., Li, X., Nigg, E.A., Sillje, H., and Barr, F.A. (2007). Choice of Plk1 docking partners during mitosis and cytokinesis is controlled by the activation state of Cdk1. Nat Cell Biol *9*, 436–444.

Nguyen, P.A., Groen, A.C., Loose, M., Ishihara, K., Wühr, M., Field, C.M., and Mitchison, T.J. (2014). Spatial organization of cytokinesis signaling reconstituted in a cell-free system. Science *346*, 244–247.

Nunes Bastos, R., Gandhi, S.R., Baron, R.D., Grüneberg, U., Nigg, E.A., and Barr, F.A. (2013). Aurora B suppresses microtubule dynamics and limits central spindle size by locally activating KIF4A. J Cell Biol *202*, 605–621.

Paredez, A.R., Somerville, C.R., and Ehrhardt, D.W. (2006). Visualization of cellulose synthase demonstrates functional association with microtubules. Science *312*, 1491–1495.

Portran, D., Zoccoler, M., Gaillard, J., Stoppin-Mellet, V., Neumann, E., Arnal, I., Martiel, J.L., and Vantard, M. (2013). MAP65/Ase1 promote microtubule flexibility. Mol Biol Cell *24*, 1964–1973.

Robb, D.L., Heasman, J., Raats, J., and Wylie, C. (1996). A kinesin-like protein is required for germ plasm aggregation in Xenopus. Cell *87*, 823–831.

Sawin, K.E., and Tran, P.T. (2006). Cytoplasmic microtubule organization in fission yeast. Yeast *23*, 1001–1014.

Saxton, W.M., and McIntosh, J.R. (1987). Interzone microtubule behavior in late anaphase and telophase spindles. J Cell Biol *105*, 875–886.

Sekine, Y., Okada, Y., Noda, Y., Kondo, S., Aizawa, H., Takemura, R., and Hirokawa, N. (1994). A novel microtubule-based motor protein (KIF4) for organelle transports, whose expression is regulated developmentally. J Cell Biol *127*, 187–201.

Shrestha, S., Wilmeth, L.J., Eyer, J., and Shuster, C.B. (2012). PRC1 controls spindle polarization and recruitment of cytokinetic factors during monopolar cytokinesis. Mol Biol Cell *23*, 1196–1207.

Subramanian, R., and Kapoor, T.M. (2012). Building complexity: insights into self-organized assembly of microtubule-based architectures. Dev Cell *23*, 874–885.

Subramanian, R., Ti, S.-C., Tan, L., Darst, S.A., and Kapoor, T.M. (2013). Marking and measuring single microtubules by PRC1 and kinesin-4. Cell *154*, 377–390.

Subramanian, R., Wilson, U.E.M., Arthur, C.P., Bick, M.J., Campbell, E.A., Darst, S.A., Milligan, R.A., and Kapoor, T.M. (2010). Insights into antiparallel microtubule crosslinking by PRC1, a conserved nonmotor microtubule binding protein. Cell *142*, 433–443.

Tsai, M.-Y., and Zheng, Y. (2005). Aurora A kinase-coated beads function as microtubule-organizing centers and enhance RanGTP-induced spindle assembly. Curr Biol *15*, 2156–2163.

Tse, Y.C., Piekny, A., and Glotzer, M. (2011). Anillin promotes astral microtubule-directed cortical myosin polarization. Mol Biol Cell *22*, 3165–3175.

Tulin, A., McClerklin, S., Huang, Y., and Dixit, R. (2012). Single-Molecule Analysis of the Microtubule Cross-Linking Protein MAP65-1 Reveals a Molecular Mechanism for Contact-Angle-Dependent Microtubule Bundling. Biophys J *102*, 802–809.

Van Damme, D., Van Poucke, K., Boutant, E., Ritzenthaler, C., Inzé, D., and Geelen, D. (2004). In vivo dynamics and differential microtubule-binding activities of MAP65 proteins. Plant Physiol. *136*, 3956–3967.

Vernos, I., Raats, J., Hirano, T., Heasman, J., Karsenti, E., and Wylie, C. (1995). Xklp1, a chromosomal Xenopus kinesin-like protein essential for spindle organization and chromosome positioning. Cell *81*, 117–127.

White, J.G., and Borisy, G.G. (1983). On the mechanisms of cytokinesis in animal cells. J Theor Biol *101*, 289–316.

Wühr, M., Dumont, S., Groen, A.C., Needleman, D.J., and Mitchison, T.J. (2009). How does a millimeter-sized cell find its center? Cell Cycle *8*, 1115–1121.

Wühr, M., Freeman, R.M., Presler, M., Horb, M.E., Peshkin, L., Gygi, S.P., and Kirschner, M.W. (2014). Deep proteomics of the Xenopus laevis egg using an mRNA-derived reference database. Curr Biol *24*, 1467–1475.

Wühr, M., Tan, E.S., Parker, S.K., Detrich, H.W., and Mitchison, T.J. (2010). A model for cleavage plane determination in early amphibian and fish embryos. Curr Biol *20*, 2040–2045.

Yabe, T., Ge, X., Lindeman, R., Nair, S., Runke, G., Mullins, M.C., and Pelegri, F. (2009). The maternal-effect gene cellular island encodes aurora B kinase and is essential for furrow formation in the early zebrafish embryo. PLoS Genet *5*, e1000518.

Yamashita, A., Sato, M., Fujita, A., Yamamoto, M., and Toda, T. (2005). The roles of fission yeast ase1 in mitotic cell division, meiotic nuclear oscillation, and cytokinesis checkpoint signaling. Mol Biol Cell *16*, 1378–1395.

Yüce, O., Piekny, A., and Glotzer, M. (2005). An ECT2-centralspindlin complex regulates the localization and function of RhoA. J Cell Biol *170*, 571–582.

Zhu, C., and Jiang, W. (2005). Cell cycle-dependent translocation of PRC1 on the spindle by Kif4 is essential for midzone formation and cytokinesis. Proc Natl Acad Sci USA *102*, 343–348.

Chapter Four

Positional Cues for Cytokinesis Signaling in Large Cells

Citation. Parts of this chapter were taken with modifications from the following manuscript in revision:

Spindle to Cortex Communication in Cleaving, Polyspermic Xenopus Eggs

Christine M. Field[1,2], Aaron C. Groen[1,2], Phuong A. Nguyen[1,2], Timothy J. Mitchison[1,2]

[1]Department of Systems Biology, Harvard Medical School, Boston, MA 02115, USA.
[2]Marine Biological Laboratory, Woods Hole, MA 02543, USA.

Contributions. This was another highly collaborative project where observations made over many years in either whole Xenopus eggs or the extract system complemented each other and generated ideas for further experiments.

Experiments. Dr. Christine Field performed the polyspermic fertilization and immunofluorescence of polyspermic Xenopus eggs, and made the observation that CPC was recruited to sister aster-aster interaction zones (AAIZs), but not to non-sister ones. I made the initial observation of aster polarization in the presence of chromatin in Xenopus egg extract, and performed the experiment testing the role of Aurora B kinase in chromatin-induced polarization. One factor that allowed for these observations was the use of PEG-passivated coverslips, which I introduced in the extract system, as both localization and inhibition experiments were previously unreliable due to the tendency of the AurkB complex to adsorb to the uncoated glass surface. Drs. Field and Timothy Mitchison repeated the aster polarization experiments for statistics. I hypothesized that apart from the presence of chromatin, sister and non-sister zones differed in the distance that initially separated the aster centers, and therefore conducted and analyzed the experiment testing the effect of inter-aster distance on CPC recruitment AAIZs in extract. The results were consistent with Dr. Field's data that CPC was recruited to both sister

and non-sister interaction zones in highly polyspermic Xenopus eggs. Dr. Aaron Groen performed the experiment testing the effects of agents stimulating microtubule-mediated cytokinesis signaling on CPC recruitment to AAIZs in extract. (I had prior performed a preliminary experiment with MCAK antibody addition, where I observed enhanced CPC recruitment to AAIZs. This observation along with the literature inspired Dr. Groen to try out various microtubule stabilizing agents.) Dr. Groen designed and performed the microinjection experiments of Xenopus zygotes with these same agents, while Dr. Field carried out the fertilization, fixation, staining, and imaging of the embryos.

Writing. Drs. Field and Mitchison wrote the manuscript with contributions from Dr. Groen and myself. I only included select figures from the manuscript in this chapter, emphasizing the extract-based investigation of the question: what positional cues are employed by large cells to specify their cleavage plane? Figures 4.1 and 4.8 were created by Dr. Mitchison; Figures 4.2, 4.3 and 4.7 by Dr. Field; Figures 4.6 by Dr. Groen; and Figures 4.4 and 4.5 by myself.

Abstract[1]

In animal cells, mitotic spindles specify cleavage planes using various positional cues to communicate their position and orientation to the cell cortex. In early embryo cells, microtubule asters that grow out from the spindle poles during anaphase form an interaction zone where they meet, and this zone specifies the cleavage plane. The role of the chromatin and the spindle midzone is unclear in these cells. Polyspermic fertilization provides a natural experiment where aster pairs from the same spindle (sister asters) have chromatin and midzone between them, while asters pairs from different spindles (non-sisters) do not. In frogs, only sister aster pairs induce furrows. We found that only sister asters recruited two conserved furrow-inducing signaling complexes, the Chromosome Passenger Complex (CPC) and Centralspindlin, to the plane between them. This explains why only sister pairs induce furrows. We then used a cytokinesis egg extract system to investigate the factors that influenced CPC recruitment to microtubule bundles. We found that proximity to chromatin, optimal starting distance between asters, and microtubule stabilization all favored CPC recruitment. We propose a model in which proximity to chromatin biases initial CPC recruitment to bundles between asters from the same spindle. Next, a positive feedback between CPC recruitment and microtubule stabilization promotes lateral growth of a plane containing CPC-positive microtubule bundles out to the cortex to position the furrow.

[1] Modified from the manuscript.
[2] Reproduced from the manuscript with minor modifications.

Introduction[2]

Cleavage furrows in early metazoan embryos typically ingress on a plane defined by the metaphase plate of the mitotic spindle. How spatial information encoding the position and orientation of the spindle is transmitted to the cortex to position the furrow is unclear. In eggs, cleavage planes are induced between pairs of microtubule asters that grow out from centrosomes at the two poles of a mitotic spindle, and spindle position is communicated in part by the geometric relationship between these asters. The furrow is induced at the border between the asters at the time they reach the cortex (Rappaport, 1996). In *Xenopus laevis*, where the egg is large (~1.2mm) compared to the 1st mitotic spindle (~60µm), it takes many minutes for microtubule asters to grow out to touch the cortex after anaphase onset, and the distance between the cortex and the centrosomes at the time of furrow initiation is very large on a molecular scale (Mitchison et al., 2012). Thus, a spatially robust mechanism is required to transmit information on spindle position and orientation to the cortex.

A classic approach to the problem of how spindles communicate to the cortex in early embryos has been to ask: can any pair of microtubule asters induce a furrow between them, or must some special conditions be met? Polyspermic fertilization in frogs provides a natural experiment where different types of aster pairs can be generated in a single egg. When polyspermic *Rana* eggs entered anaphase, furrows were induced between pairs of asters that grew out from the same mitotic spindle, which we will call “sister asters”. They were *not* induced between pairs of asters that grew out from different spindles, which we will call “non-sister asters” (Brachet, 1910; Herlant, 1911). This classic observation, which was later confirmed in *Xenopus laevis* eggs (Render and Elinson, 1986), is diagrammed in Figure 4.1. One interpretation of these data is that the presence of chromatin and/or spindle midzone between aster pairs is necessary for them to induce a furrow. Consistent with a positive signal from

[2] Reproduced from the manuscript with minor modifications.

chromatin to the cortex, cells forced to undergo monopolar cytokinesis induced cleavage furrows only on the side of the cell nearest to chromatin (Canman et al., 2003; Hu et al., 2008).

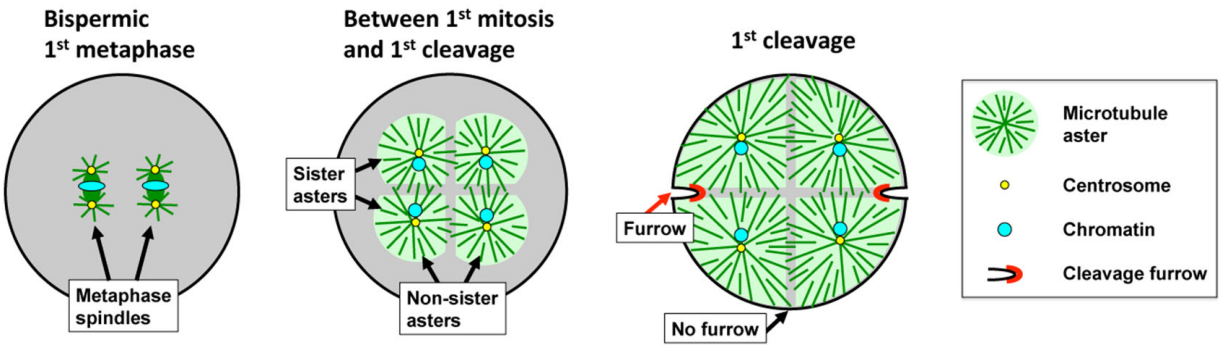

Figure 4.1: Cleavage pattern in a bispermic frog egg.

Metaphase spindles in Xenopus are ~50-60µm long in a 1.2mm egg. After anaphase onset the small asters at the spindle poles grow steadily until they fill the cell. Asters from the two poles of the same spindle (sister pairs) contact each other shortly after anaphase onset at the plane previously occupied by the metaphase plate. Asters from the poles of two different spindles (non-sister pairs) contact each other later. In both cases, aster growth halts where the asters contact each other, and a zone of lower microtubule density is observed at the aster-aster interaction zone (AAIZ) (grey shading). When asters grow to touch the cortex, furrows initiate between sister aster pairs, but not between non-sister pairs. Adapted from (Brachet, 1910; Mitchison et al., 2012; Snook et al., 2011; Wühr et al., 2009). [Figure by Timothy Mitchison]

A requirement for chromatin for furrow induction is not universal. In a famous experiment using micro-manipulated echinoderm eggs, Rappaport showed that furrows were induced between non-sister aster pairs as well as between sisters (Rappaport, 1961; 1996). This experiment proved that aster pairs did not have to grow out from the same spindle to induce a furrow between them, and therefore chromatin or spindle midzone was not required for furrow induction. The discrepancy with the polyspermic frog egg observations has not been explained. The Rappaport experiment was recently re-investigated in echinoderm eggs using molecular markers (Argiros et al., 2012). Here, we re-investigate cleavage following polyspermic

fertilization in the frog *Xenopus laevis*, focusing on a cell-free cytokinesis system that allows us to separate the contributions from various positional cues (Nguyen, Groen et al., 2014).

Cleavage furrow induction depends on two conserved signaling complexes that bind to microtubules: the Chromosome Passenger Complex (CPC; a 1:1:1:1 complex between INCENP, Aurora B kinase (AurkB), Dasra (CDCA8 or 9) and Survivin (BIRC5) (Carmena et al., 2012)) and Centralspindlin (a 2:2 complex between MKLP1 (Kif23) and RacGAP1 (White and Glotzer, 2012)). In somatic cells these complexes localize to midzone microtubule bundles after anaphase onset. In *Xenopus* eggs they initially also localize to the midzone, then spread to a plane that bisects the cell at the location previously occupied by the metaphase plate, but extends all the way to the cortex (Nguyen, Groen et al., 2014). Where one or both of these complexes touch the cortex, they induce cleavage furrows by locally activating the RhoA pathway. The furrow then ingresses along the plane defined by the signaling complexes (Eggert et al., 2006; Glotzer, 2005). While both CPC and Centralspindlin are implicated in cleavage furrow induction in all animal cells, their relative roles may vary. Centralspindlin was implicated as the main furrow-inducing molecule in some systems, with the CPC serving as its positive regulator (White and Glotzer, 2012). In *C. elegans*, both complexes were argued to contribute independently to furrow induction (Lewellyn et al., 2011). In a cell free system derived from *Xenopus* eggs, CPC activity, but not the Kif23 subunit of Centralspindlin, was required for local activation of RhoA on a model plasma membrane (Nguyen, Groen et al., 2014), suggesting the CPC plays a more important role in furrow specification in *Xenopus* eggs. Here, we will focus mainly of the role of the CPC in spindle to cortex communication because of its central role in *Xenopus* eggs.

The mechanisms by which the CPC is recruited to microtubule bundles during cytokinesis are complex and poorly understood. The INCENP subunit has direct microtubule binding sites (Carmena et al., 2012), and two kinesins, Kif4A and Kif20A, are also involved in CPC targeting (Grüneberg et al., 2004; Nguyen, Groen et al., 2014; Nunes Bastos et al., 2013).

CPC binds to chromatin during metaphase, which led Earnshaw and colleagues to propose that it is transported to spindle microtubules by chromatin at anaphase onset (Cooke et al., 1987). Currently, it is thought more likely that chromatin spatially bias CPC recruitment to microtubules by mechanisms that involve kinase activity gradients (Fuller et al., 2008). Microtubule binding activates the kinase activity of CPC, probably by promoting trans-phosphorylation of the AurkB and INCENP subunits (Kelly et al., 2007). Once activated, Aurora B kinase activity is thought to promote microtubule polymerization and stabilization. Several mechanisms may be involved, including CPC regulation of Kif4A (Nunes Bastos et al., 2013), KifC1 (MCAK) (Ohi et al., 2004), Stathmin (Kelly et al., 2007), and EB1 family members (Ferreira et al., 2013; Zimniak et al., 2009). Positive feedback between AurkB activity and microtubule stabilization has been proposed during assembly of cytokinesis midzones in somatic cells (Hu et al., 2008; Nunes Bastos et al., 2013) and meiosis-II spindles in eggs (Tseng et al., 2010).

Here, we re-investigated the origin of the cleavage pattern in polyspermic frog eggs by imaging the CPC and microtubules in both dividing frog eggs and the cell-free cytokinesis extract system. Our data partly solve a classic puzzle in fertilization biology, and suggest a mechanism by which information on spindle position is transmitted from the spindle at the center of the egg to the cortex to position the cleavage furrow.

Results

Visualization of aster pairs in fixed monospermic eggs[3]

To investigate the normal situation we fixed monospermic eggs after 1st mitosis and before or during 1st cleavage, and stained for microtubules and cytokinesis signaling complexes using fluorescently labeled antibodies: anti-Aurora B kinase (AurkB) for CPC and anti-Kif23 for Centralspindlin. Figure 4.2A shows an egg fixed shortly before cleavage onset. The sister asters

[3] Reproduced from the manuscript with modifications. Experiments performed by Dr. Christine Field.

Figure 4.2: Localization of furrow-inducing complexes in polyspermic eggs. Eggs were fixed between 1st mitosis and 1st cleavage, stained for AurkB (a subunit of the CPC) and Kif23 (a subunit of Centralspindlin) and imaged by confocal microscopy. Cyan double-headed arrows illustrate sister aster pairs. (**A**) Normal, monospermic egg. Note plane of CPC- and Centralspindlin-positive microtubule bundles between sister asters. (**B**) Bispermic egg fixed a few minutes after anaphase onset. The asters have just started to grow. A CPC-positive disc is evident at the plane previously occupied by the metaphase plate, where sister asters recently met. Centralspindlin recruitment is less evident (cyan single arrow in Kif23 image). (**C**) Bispermic egg fixed midway between anaphase and cleavage. Interaction zones between sister and non-sister asters were evident in the tubulin image. Note a brighter tuft of microtubules that connects the sister pair to the upper left, in register with the centrosomes. This midzone-like morphological marker reveals the previous position of the spindle, and was used to identify sister aster pairs in microtubule images. CPC and Centralspindlin have been recruited to the interaction zone between sister asters, but not to the zone between non-sister asters. (**D**) Egg with 4 sperm fixed early in cleavage. Cleavage has initiated near the animal pole (not shown). This image shows a focal plane near the equator, where 3 aster pairs are visible. Furrowing had not yet occurred in this focal plane, but asters had grown all the way to the cortex. Note selective recruitment of CPC and Centralspindlin to zones between sister asters. [Figure by Christine Field]

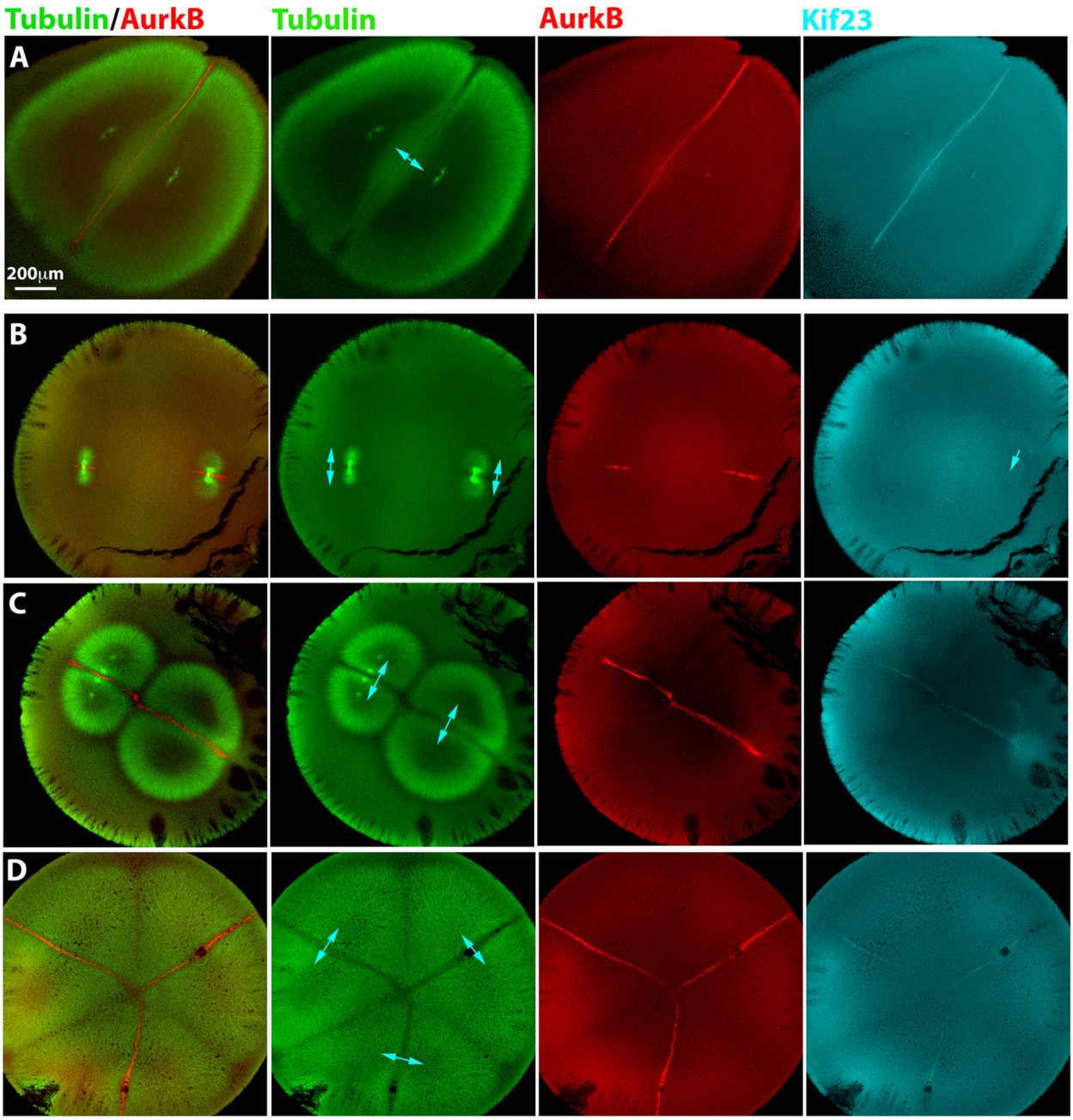

Figure 4.2 (Continued)

are dome-shaped, and a planar interaction zone of lower microtubule density forms where they meet at mid-cell. CPC was dramatically enriched at this interaction zone. Centralspindlin was also enriched at the interaction zone, though the staining was dimmer and the enrichment less dramatic. CPC was probed with either anti-AurkB or anti-INCENP (not shown); Kif23 was probed with two independent antibodies (not shown). In all cases, Kif23 staining was always fainter than CPC staining. This intensity difference possibly reflects the lower concentration in eggs of Kif23 (~20nM) compared to the CPC (~150nM) (Wühr et al., 2014).

Localization of cytokinesis signaling complexes in polyspermic eggs[4]

We induced polyspermic fertilization of *Xenopus laevis* eggs using sodium iodide treatment and followed eggs by time-lapse microscopy. As previously reported (Render and Elinson, 1986), polyspermic eggs were identified in time-lapse movies by concentration of cortical pigment into patches over centrosomes and nuclei starting ~50 min after fertilization, late in interphase before 1st mitosis. We confirmed that only one furrow was induced per sperm when 1-4 sperm entered the egg, and the furrow only cleaved between sister aster pairs, as diagrammed for a bispermic egg in Figure 4.1. Highly polyspermic eggs formed many furrows that fused and regressed unpredictably, making them difficult to analyze.

In polyspermic eggs fixed in late anaphase of 1st mitosis we observed well-separated anaphase spindles that were indistinguishable from those seen in monospermic eggs. Figure 4.2B shows a bispermic example. At this stage the asters had grown sufficiently that sister pairs had contacted each other at the center of each anaphase spindle, but not yet sufficiently for non-sister asters to contact each other. AurkB localized strongly to microtubule bundles on a plane bisecting each spindle, and extended outwards to an extent that depended on aster radius. Kif23 was only faintly localized at this stage, indicated by the blue arrow in Figure 4.2B.

[4] Reproduced from the manuscript with modifications. Experiments performed by Dr. Christine Field.

In polyspermic eggs fixed later in the interval between 1st mitosis and 1st cleavage we observed interactions between both sister and non-sister aster pairs (tubulin staining in Figure 4.2, C and D). A distinct zone of reduced microtubule density was evident for both types of aster-aster interaction. In most cases the zone of lower microtubule density at the boundary between the asters was more distinct for zones formed between sister asters (see tubulin panels in Figure 4.2, C and D). We used microtubule morphology to determine which aster pairs were sisters vs. non-sisters. A pair of opposed microtubule tufts with increased density compared to the rest of the aster, resembling a cytokinesis midzone in somatic cells, connected sister aster pairs at the position previously occupied by the spindle. An example of these tufts is seen connecting the upper left aster pair in Figure 4.2C. Using this criterion, we indicate sister pairs in Figure 4.2 using double headed blue arrows. Note that the midzone-like tuft of microtubules connecting sister asters was only present in a few focal planes in a confocal stack, and may not be evident in the image planes shown. Midzone-like microtubules tufts were no longer visible in eggs where cleavage had initiated, but in those eggs we could often infer which asters were sisters by the location of nuclei, which stained with AurkB at this stage, as in Figure 4.2A.

In eggs fertilized with 2-4 sperm we reproducibly observed CPC and Centralspindlin localizing to microtubule interaction zones formed between sister asters, but not to zones formed between non-sister asters (Figure 4.2, C and D). This observation was highly reproducible for eggs fertilized with 2-4 sperm; we observed no exceptions to this rule in more than 40 examples of polyspermic eggs. The difference was essentially binary; the CPC staining intensity was strongly elevated over the local background value in zones between sister asters, and was approximately the same as the local background in the zone between non-sister asters. We also investigated localization of another conserved cytokinesis midzone protein, Kif4A, in polyspermic eggs. This kinesin has been implicated in blocking growth of midzone microtubule plus ends, and also in targeting the CPC (Bieling et al., 2010; Hu et al., 2011;

Nguyen, Groen et al., 2014). We observed enrichment of Kif4A on microtubule bundles in the interaction plane between sister asters, but not between non-sister asters (Figure 4.3). Thus, Kif4A is recruited in a manner similar to CPC and Centralspindlin, implying that microtubule bundles between sister asters resemble somatic cell midzones in their biochemistry, while bundles between non-sister asters do not.

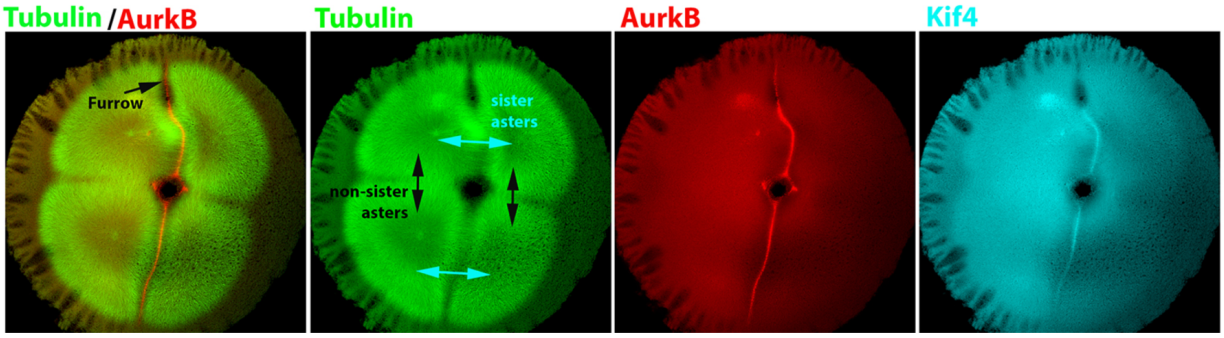

Figure 4.3: Kif4A co-localizes with Aurora B kinase in sister zones.
An example of a bispermic egg fixed at early cleavage (furrow is ingressing from above the plane of focus). Note that Kif4A co-localizes with AurkB and does not localize to interaction zones between non-sister asters. [Figure by Christine Field]

Kinase activity of the AurkB subunit of the CPC is required for furrow induction in *Xenopus* (Nguyen, Groen et al., 2014), and both CPC and Centralspindlin are required for furrowing in many systems (Eggert et al., 2006; Glotzer, 2005). Thus, the difference in recruitment of CPC and Centralspindlin presumably explains why sister aster pairs induce furrows between them, and non-sister aster pairs do not (Figure 4.1). This observation immediately begs the question: what controls differential recruitment of cytokinesis signaling complexes to interaction zones formed between sister vs. non-sister aster pairs?

We speculate that sister and non-sister zones are distinguished by three factors:

1) sister asters initially have a spindle midzone between them while non-sister asters do not;
2) sister asters have chromatins between them while non-sister asters do not;

3) sister asters start with their centers close to each other (pole-to-pole distance of the mitotic spindle, which is ~60 μm (Wühr et al., 2008)) while non-sister asters start with their centers far apart (~600 μm in Figure 4.2B).

To test the effect these different factors have on CPC recruitment, we turned to a recently reported *Xenopus* egg extract cytokinesis system. This system reconstitutes both recruitment of CPC to microtubule bundles between asters and also down-stream cytokinesis signaling events when placed on artificial lipid bilayers (Nguyen, Groen et al., 2014). Since we are not yet able to create midzones from mitotic spindles in our extract system, we could not test the contribution from the midzone (1). Therefore, we only focused on the proximity of chromatin (2) and the starting distance between aster centers (3).

Proximity to chromatin promotes CPC recruitment in egg extracts[5]

Multiple experiments have suggested that chromatin can provide a spatial bias to CPC recruitment to microtubules (Canman et al., 2003; Fuller et al., 2008; Hu et al., 2008). To test if proximity to chromatin influences CPC recruitment in *Xenopus* eggs, we modified the extract system by using permeabilized *Xenopus* sperm with attached centrosomes to nucleate asters. As isolated sperm asters grew, we noted they reproducibly became polarized with longer, more bushy microtubules on the side furthest from the chromatin, and shorter, more bundled microtubules on the side closest to chromatin (Figure 4.4A). The CPC was recruited preferentially to the aster periphery on the chromatin side, where microtubules were shorter and more bundled (Figure 4.4A). Both the length and angle of the CPC-positive arc increased as asters expanded, suggesting lateral spreading of the CPC along the aster circumference. Asters grew radially on both CPC-positive and negative sides, though more slowly on the CPC-positive side.

[5] Partially reproduced from the manuscript. Here I describe experiments that I performed, which were later repeated with modifications by Drs. Christine Field and Timothy Mitchison for statistics reported in the manuscript.

Figure 4.4: Chromatin spatially biases CPC recruitment in monopolar sperm asters in *Xenopus* egg extract, which requires Aurora B kinase activity. Microtubule asters were assembled by adding permeabilized sperm nuclei with attached centrosome to calcium activated egg extract. Microtubules (MTs, Alexa488-tubulin, *green*) and CPC (probed with Alexa647-anti-AurkB antibody, *red*). Note that the AurkB antibody also stains chromatin. Widefield time-lapse image sequences were collected in parallel from the same extract preparation. The last panel of each row is a 3x magnification of the boxed region. (**A**) Control sperm asters. Note polarized microtubule distribution and formation of an arc of CPC-positive bundles on the periphery of each isolated aster on the same side as the chromatin. (**B**) Control aster nucleated from centrosome without chromatin attached (*white box*). Note lower microtubule density than in sperm asters. (**C)** Sperm asters with AurkB inhibition (100 μM ZM447439). Note loss of both polarization and CPC localization to aster periphery in both **B** and **C**. Scale bars, 100 μm.

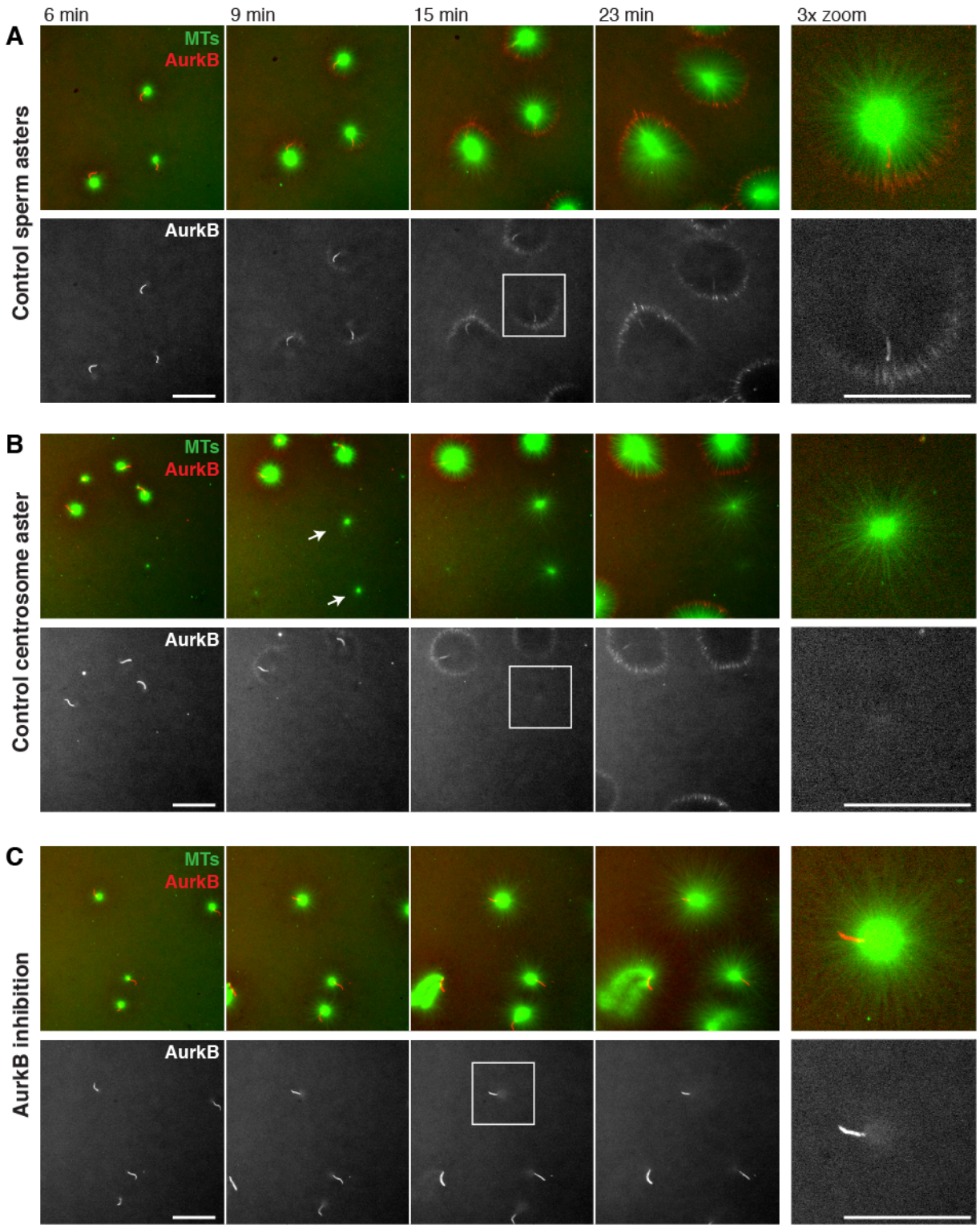

Figure 4.4 (Continued)

Aster polarization required chromatin and AurkB activity[6]

Our sperm preparations contained free centrosomes (i.e. not associated with chromatin). These nucleated asters that were radially symmetric and did not recruit CPC to their periphery unless they interacted with a neighboring aster (white arrows in Figure 4.4B). Similar observations were made using Aurora A kinase (AurkA)-based artificial centrosome beads (Tsai and Zheng, 2005) to nucleate asters, which were radially symmetric and did not recruit CPC to their periphery unless they interacted with a nearby aster (Figures 4.5 and 4.6) and (Ishihara et al., 2014; Nguyen, Groen et al., 2014). Thus, chromatin is required for polarized CPC recruitment to asters in the extract system.

Addition of the AurkB inhibitor ZM447439 blocked CPC recruitment to the sperm aster periphery in extract, and also blocked aster polarization (Figure 4.4C). This is consistent with previous reports that AurkB activity is required for CPC recruitment to microtubule asters in Hela cells and egg extract (Hu et al., 2008; Nguyen, Groen et al., 2014). Collectively, our data suggest that chromatin locally activates Aurora B kinase activity leading to its localization to the periphery of asters proximal to chromatin.

Starting distance between asters influences CPC recruitment[7]

To investigate the effect of initial distance between aster nucleating centers independent of the effect of chromatin, we used beads coated with an activating antibody to AurkA (Tsai and Zheng, 2005). Large asters grew out from the beads, and where they met, CPC-positive AAIZs formed (Nguyen, Groen et al., 2014). Here, we analyzed many fields at low magnification and noted that only a subset of aster-aster interactions recruited CPC (Figure 4.5A).

---

[6] Reproduced from the manuscript with modifications. Here I describe experiments that I performed.

[7] Reproduced from the manuscript. I conducted these experiments and analyses.

Figure 4.5: Initial distance between nucleating sites influences CPC recruitment.
Asters were assembled in interphase egg extracts containing fluorescent probes for tubulin (Alexa488-tubulin) and the CPC (Alexa647-labeled anti-AurkB), and beads coated with anti-AurkA as artificial centrosomes. Bead pairs were identified based on whether their asters interacted at the end of the movie. The distance between the bead pairs was measured at the start of the movie, and whether or not a CPC-positive zone formed between beads was scored upon initial aster-aster contact. (**A**) Example images from a widefield time-lapse sequence. Arrowheads indicate typical bead pairs. Yellow and blue show examples where AurkB-positive zones did not form between beads, magenta shows examples where AurkB-positive zones did form. Note that the yellow arrowheads are close together (n = 2), blue arrowheads further apart (n = 7), and magenta arrowheads are separated by an intermediate distance (n = 15). (**B**). Histogram of initial bead separations plotted separately for bead pairs where an AurkB-positive zone did (blue bars; n = 39), or did not (red bars; n = 30), form upon aster-aster contact. Initial distances were pooled for multiple fields imaged in parallel in two independent experiments (n = 6 fields total). Note the initial separation distance was uni-modal for bead pairs where a CPC-positive zone did form. The distribution was much more spread out, and possibly bimodal, for bead pairs where a CPC-positive zone did not form.

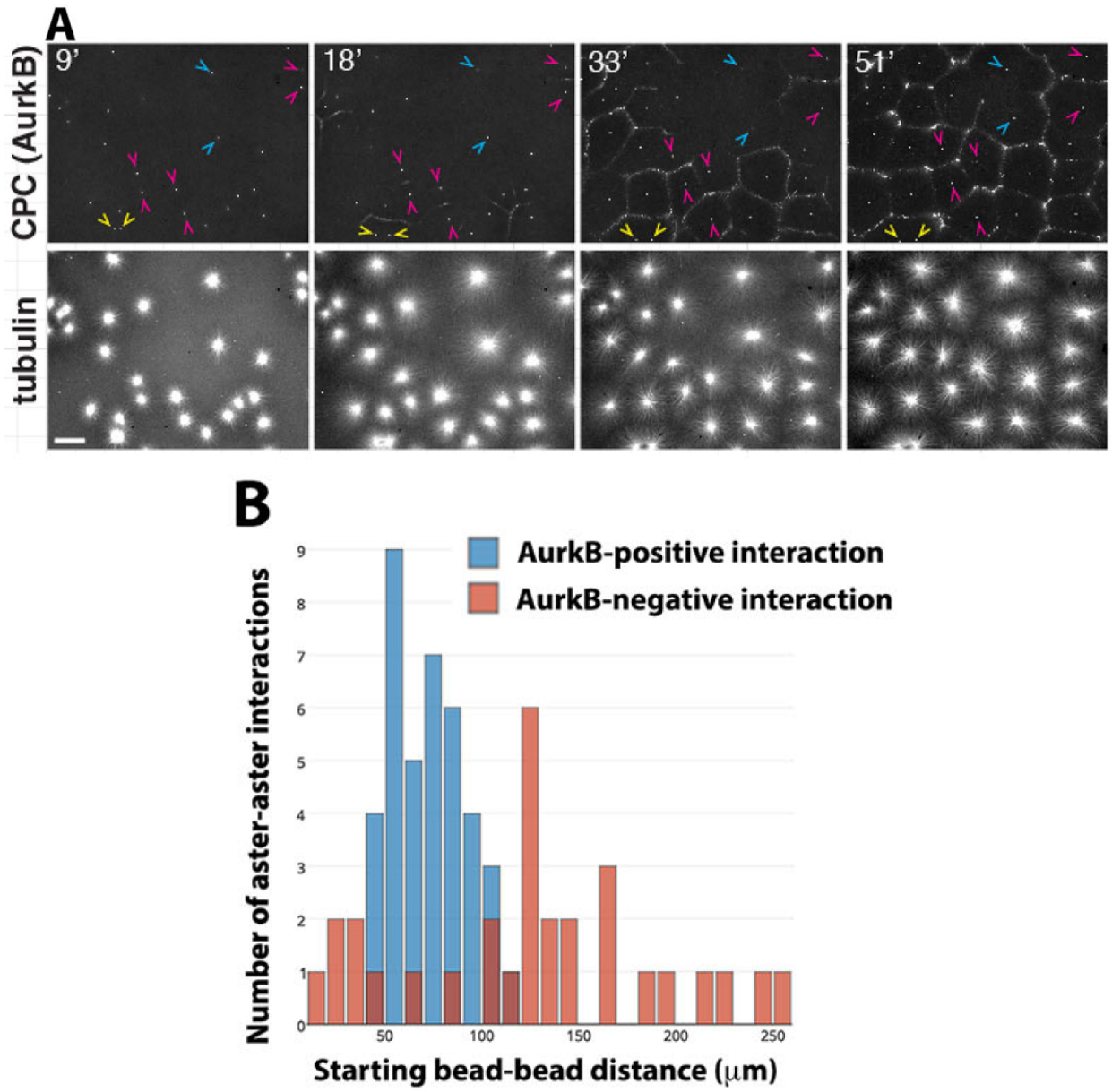

Figure 4.5 (Continued)

By analyzing pairwise interactions between beads we determined that the initial distance between beads correlated with whether they did, or did not, generate a CPC-positive zone between them. Bead pairs that started very close (yellow arrowheads in Figure 4.5A) or very far apart (blue arrowheads) usually failed to induce a CPC-positive zone between them upon aster-aster contact. Zones that were initially CPC-negative but then recruited CPC via a lateral spreading mechanism from neighboring CPC-zones were scored as CPC-negative.
Using this strategy, we counted 15/24 CPC-positive zones and 9/24 CPC-negative zones in a representative experiment shown in Figure 4.5A. Figure 4.5B shows a histogram where image sequences were collected from multiple positions using an automated stage. The X-axis is the initial bead-to-bead distance, and separate histograms are plotted for bead pairs that did, or did not, recruit CPC to a zone between them by the end of the movie. Note that CPC recruitment tended to fail at very short, and very long, initial distances. Initial separation distance is obligatorily coupled to the time when asters meet in this experiment. Thus, we cannot distinguish whether the preference for an intermediate initial distance is due to an optimal distance or an optimal time after initiating the reaction.

Forced activation of the CPC and microtubule stabilization increases CPC recruitment[8]

The extract experiments above showed that both proximity to chromatin and anti-parallel overlaps formed at some optimal initial distance between nucleating centers could trigger recruitment of the CPC to microtubule bundles. Once recruited, the CPC-positive zone was stable, and often spread laterally—either along the circumference of a sperm aster or an AAIZ. CPC recruitment to both the periphery of sperm asters (Figure 4.4) and AAIZs (Nguyen, Groen et al., 2014) required Aurrora B kinase activity. Both the binary nature of CPC recruitment to sister vs. non-sister zone and the lateral spreading phenomenon suggest that some positive feedback loop regulates CPC recruitment. In Xenopus extracts, the CPC can be activated by

[8] Modified from the manuscript. Experiments performed by Dr. Aaron Groen.

binding to microtubules (Tseng et al., 2010). Thus we proceeded to test if there was a relationship between microtubule stabilization and CPC activation and recruitment (Figure 4.6).

To test for a causal relationship between CPC activation and CPC recruitment to AAIZs, we made an activating antibody (IgG) to INCENP, copying a design of Funabiki and colleagues that was shown to activate Aurora B kinase activity by cross-linking the CPC (Kelly et al., 2007). To test if increasing microtubule stability (and density) promoted CPC recruitment to AAIZs, we used an inhibitory IgG to the catastrophe factor MCAK (Kif2C), which is a potent microtubule destabilizing factor in frog eggs (Walczak et al., 1996). To nucleate and stabilize microtubules by a different mechanism, we used used taxol at a low concentration (0.5 μM).

By eye, formation of CPC-positive AAIZs was enhanced by activating the CPC or stabilizing microtubules, as evidenced by more CPC-positive zones per field, and in some cases earlier formation of those zones (Figure 4.6, A and B). In some sequences, the CPC-positive state appeared to spread laterally from the initial point of microtubule interaction, suggesting the possibility of positive feedback regulation. To quantify CPC recruitment we made movies of multiple fields at low magnification, and quantified the total length of CPC-positive zones per field divided by the number of nucleating beads in that field. Normalization to bead density corrects for greater potential zone length in fields containing more beads. These data confirmed that forced CPC activation, or microtubule stabilization by two means, stimulated formation of CPC-positive interaction zones between asters (Figure 4.6C).

We confirmed the relevance of these findings in intact eggs by microinjecting these agents (activating anti-INCENP, inhibitory anti-MCAK, and taxol). In all cases, both ectopic CPC recruitment to microtubule arrays and ectopic furrowing were observed (not shown). Thus, CPC recruitment to aster microtubules is regulated in a similar manner in both intact eggs and egg extracts. In both cases, CPC recruitment is stimulated by both CPC activation and microtubule stabilization.

Figure 4.6: Forced activation of the CPC and microtubule stabilization promotes CPC recruitment.

Interphase egg extracts containing fluorescent probes for tubulin and the CPC (directly labeled anti-AurkB) and AurkA-based artificial centrosome beads. (**A**) Representative images from time-lapse sequences collected in parallel from the same extract preparation. Note more CPC-positive zones were formed between nucleating sites in extracts treated with activating IgG to INCENP, taxol and inhibitory IgG to MCAK than in control. Once formed, CPC-positive zones were stable for the duration of experiments under all conditions except MCAK inhibition, where they formed early relative to control, but then decayed. (**B**) Higher magnification image sequences of the regions shown by red boxes in **A**. Regions were chosen to highlight the establishment and growth of CPC-positive zones between nucleating sites. Note the zone from control and taxol treated extracts grows laterally after it initiates. CPC-positive zones formed earlier when the CPC was activated or microtubules were stabilized. (**C**) Quantification of CPC-positive zone formation from multiple image fields. At each time point the length of CPC-positive zones in a field was measured, and divided by the number of nucleating beads in the field. Note that CPC stimulation (anti-INCENP), taxol and MCAK inhibition all stimulated the rate and extent of CPC-positive zone formation. The last time point was omitted from the MCAK inhibition experiment since CPC-positive zones were unstable under this condition. [Figure by Aaron Groen]

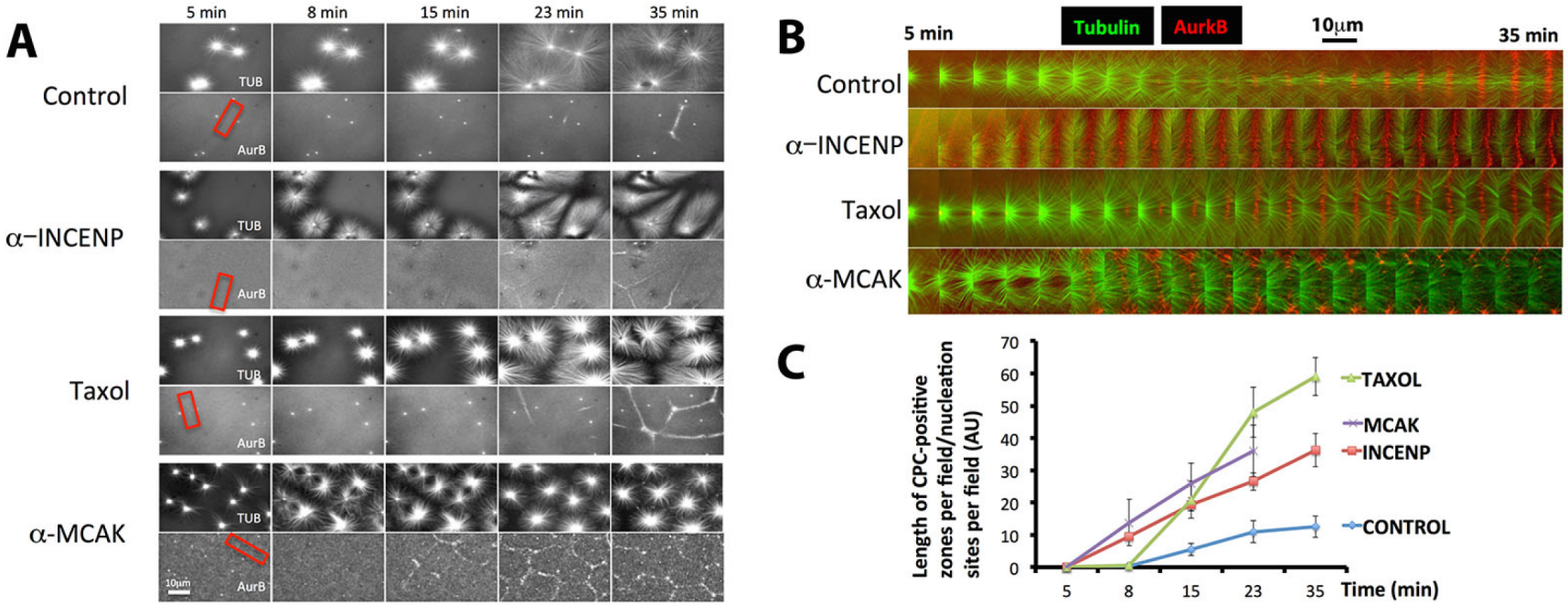

Figure 4.6 (Continued)

Forced recruitment of CPC to zones between non-sister asters[9]

Using the egg extract system, we identified the following factors in CPC recruitment (and hence cleavage plane specification potentially): (1) proximity of chromatin, (2) initial distance between aster nucleating centers, (3) CPC activation, and (4) microtubule stabilization. The ultimate test for the relevance of these factors in intact eggs is whether we can force recruitment of CPC to interaction zones formed between non-sister asters, which are normally CPC-negative (Figure 4.2, C and D), by varying these factors.

Highly polyspermic eggs provide a natural experiment where all asters start close together, and close to chromatin and/or spindle midzones, due to the general crowding of the egg. In these cases we observed CPC-positive interaction zones between asters that were clearly non-sisters (yellow arrows in Figure 4.7A). This is consistent with the fact that one or all of the conditions above explain why non-sister aster pairs recruited CPC between them in highly polyspermic eggs, although they did not in eggs containing 2-4 sperm.

We next asked if forced activation of CPC could force CPC recruitment to non-sister zones in eggs containing 2-4 sperm. We injected the activating anti-INCENP into polyspermic eggs, and fixed them before 1st cleavage. We observed CPC recruitment to zones formed between sister- and non-sister aster pairs with similar intensity (Figure 4.7, B and C). An image of un-injected bispermic embryo fixed at a similar stage is included for comparison (Figure 4.7D). Thus, artificial activation of the CPC forces its recruitment to interaction zones between non-sister asters, which are normally CPC negative.

[9] Modified from the manuscript. Experiments performed by Dr. Christine Field and Dr. Aaron Groen.

Figure 4.7: High sperm density and forced CPC activation can recruit the CPC to interaction zones between non-sister asters in polyspermic Xenopus eggs.

(**A**) Highly polyspermic egg fixed early in cleavage. The region presented at higher magnification shows a single aster with CPC-positive zones at the junction with several neighboring asters (yellow arrows). None of these are zones with its sister aster, which is in a different Z plane. (**B** and **C**) An activating anti-INCENP IgG was injected into polyspermic eggs 60-70 min post fertilization, after 1st mitosis. (**B**) Bispermic egg fixed at 90 min post fertilization. Note recruitment of CPC at similar levels to the interaction zones between sister and non-sister asters. Sister asters are indicated by blue double-headed arrows. CPC recruitment between non-sister asters is highlighted by yellow arrowheads. Note: Aster morphology has been slightly distorted by the injection. (**C**) Bispermic egg fixed 98 min post-fertilization. CPC is again recruited to interaction zones between non-sister asters. Same labeling convention as in **A**.
(**C**) Uninjected bispermic egg fixed at the same stage as **B** shown for comparison. CPC is not recruited between non-sister asters. [Figure by Christine Field]

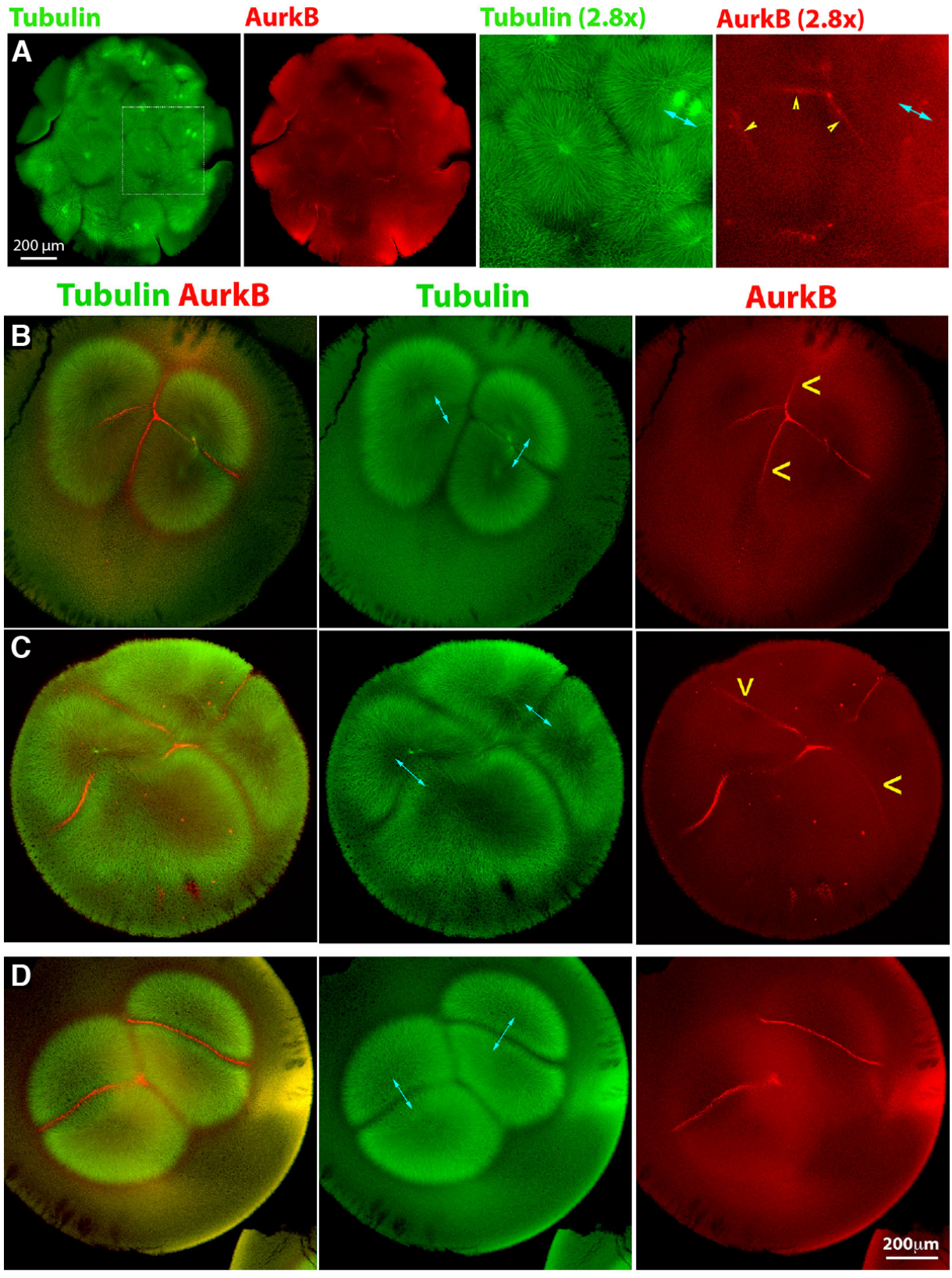

Figure 4.7 (Continued)

Discussion[10]

Figure 4.8 summarizes our results along with a mechanistic interpretation. We illustrate the arrangement of asters in a bi-spermic egg midway between 1st anaphase and cleavage, as per Figure 4.1. It has long been known in frog eggs that sister aster pairs, which are identified by the chromatin and spindle midzone position, induce furrows between them when they reach the cortex, while non-sister aster pairs do not (Brachet, 1910; Herlant, 1911). We showed that this is because the cytokinesis signaling complexes CPC and Centralspindlin are recruited to the interaction zones that form between sister asters, and not to the zones between non-sisters (Figure 4.2). We then explored the factors that determine this difference. Using a combination of egg extract and whole egg experiments, we identified four positive influences on CPC recruitment: proximity to chromatin (Figure 4.4), optimal starting distance between asters (Figure 4.5), microtubule stabilization (Figure 4.6), and forced CPC activation (Figure 4.6).

In Figure 4.8 we propose a conceptual separation between *initial conditions* that positively influence CPC recruitment to an aster-aster interaction zone (proximity to DNA and starting distance) and a *core feedback loop*, based on microtubule stabilization, CPC recruitment and activation, that maintains the CPC-positive state once it has initiated, and promotes its lateral growth. As cited in the Introduction, positive feedback in CPC recruitment has been proposed before, and multiple mechanisms may be involved, including spatial gradients of kinase activity, kinesin-mediated transport, microtubule bundling and microtubule stabilization. Here, we showed that forced activation of the CPC stimulated assembly of ectopic CPC-positive microtubule arrays (anti-INCENP injection in egg; not shown) and that forced microtubule stabilization promoted CPC recruitment (Figure 4.6), consistent with a feedback

[10] Reproduced from manuscript with minor modifications.

loop. Non-sister aster pairs, which never meet the initial conditions, never become CPC-positive at their shared boundary, do not initiate the feedback loop, and therefore do not induce furrows.

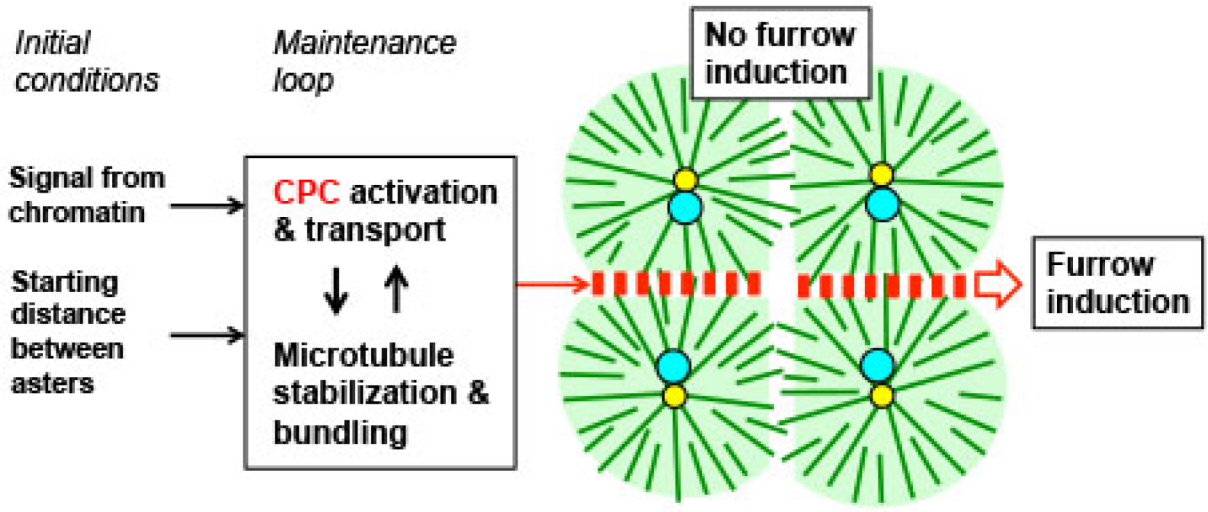

Figure 4.8: Model illustrating results and hypothetical underlying mechanisms.
The image illustrates the situation in a bispermic egg between 1st anaphase and 1st cleavage, similar to the cartoon in Figure 4.1 and the experimental examples in Figures 4.2C and 4.7D. Color-coding and orientation of sister and non-sister aster pairs are as Figure 4.1, red boxes indicate CPC and Centralspindlin complexes. The text boxes linked by arrows are factors we identified that control CPC recruitment and activation. We hypothesize that locally acting signals from chromatin (Figure 4.4) and the starting distance between asters (Figure 4.5) together provide an initial bias that promotes CPC recruitment between sister asters, and are lacking between non-sister asters. We further hypothesize that CPC activation/recruitment (Figures 4.6 and 4.7) and microtubule bundling/stabilization (Figure 4.6) together constitute a positive feedback loop that promotes CPC retention on microtubule bundles, and lateral spreading of CPC-positive bundles. These positive feedbacks allow a CPC-positive interaction zone to grow radially from the site previously occupied by the metaphase plate all the way to the cortex while retaining its CPC-positive state. [Figure by Timothy Mitchison]

By separating initial conditions from the feedback loop in Figure 4.8 we seek to explain how a zone between two sister asters remains CPC-positive, even when its cortex proximal

regions are hundreds of μm from the nearest chromatin. We propose that the positive feedback loop indicated in Figure 4.8 gives rise to a memory effect so that a transient influence from chromatin and starting distance (and possibly spindle midzone) can give rise to a long-lived, CPC-positive disc that grows out to reach the cortex. Alternatively, continued transport of CPC from chromatin to the aster periphery could be required to maintain the CPC-positive zone. Given the huge distances involved, and the dynamics of CPC-positive zone in egg extract (Figures 4.4 and 4.6), we consider a memory effect more likely. Our model does not precisely account for how the CPC-positive zone spreads outwards as the asters grow. Spreading might involve spatial gradients of AurkB kinase activity and/or bending fluctuations of microtubules. By initiating at the site previously occupied by the metaphase plate, and spreading outwards as a plane orthogonal to aster microtubules, the CPC-positive zone transmits information on spindle position and orientation to the cortex to correctly position the furrow. Understanding how this spreading occurs is a key question for future studies.

Why are Rappaport furrows induced between non-sister aster pairs in echinoderm eggs but not frog eggs? The different spatial scale is likely to be one factor; egg diameter is ~1200μm in frog compared to ~100μm in typical echinoderms. The difference between sister- and non-sister aster pairs appeared to break down in highly polyspermic frog eggs (Figure 4.7A), where the spatial scale becomes comparable to echinoderms. Starting distance between asters appears to be important in both systems. Rappaport noted that asters which started closer together were more likely to induce furrows (Rappaport, 1969), and we found an optimal range of starting distances in egg extract (Figure 4.4). CPC localization data shows both similarities and differences between systems. In sea urchin eggs Shuster and colleagues observed recruitment of the CPC to microtubule bundles between sister asters, but not between non-sisters (Argiros et al., 2012), which is similar to our data (Figure 4.2). They also proposed proximity to chromatin as a positive influence on CPC recruitment. However, the CPC-positive disc did not obviously extend all the way to the cortex in sea urchin eggs, as it does in frog.

Centralspindlin-positive bundles did extend to the cortex in sea urchin, suggesting a more central role for that complex in furrow induction in that system. Based on comparisons between frog eggs, echinoderm eggs, and mammalian tissue culture cells, we speculate that the molecular mechanisms proposed in Figure 4.8 are conserved, but the ability of the positive feedback loop to retain a memory of initial conditions provided by positional cues, and to propagate the CPC-positive state hundreds of microns from chromatin to the cortex, are special adaptations that allow spindle to cortex communication in huge egg cells.

Materials and methods[11]

Whole egg fertilization, injection and staining for imaging

Xenopus eggs were collected, fertilized, de-jellied and injected using standard methods (Sive et al., 2000). See also http://wiki.xenbase.org/xenwiki/index.php/Protocols. Polyspermic fertilization was induced with sodium iodide using a modification of a reported procedure (Render and Elinson, 1986). Eggs were extruded into MMR (100mM NaCl, 2mM KCl, 1mM $MgCl_2$, 2mM $CaCl_2$, 0.1mM EDTA and 10mM Hepes-KOH pH 7.8) quickly rinsed with a small volume of 20mM NaI in 0.1x MMR, then partially drained. 1/3rd of a testis per 5 cm dish of eggs, was homogenized in 0.75 ml of 1x MMR, and added to the eggs. After 90 sec to allow sperm attachment, the dish was flooded with 20mM NaI in 0.1x MMR. After ~20min eggs were de-jellied with 2% cysteine and transferred to 0.1x MMR for imaging and fixation.

For immunofluorescence de-jellied eggs in 0.1x MMR were fixed by transferring to 90% methanol, 50mM EGTA. After 24 hours of gentle agitation at RT eggs were transferred to 100% methanol and moved to 4°C where they can be stored for months. To probe with antibodies eggs were re-hydrated through a series of methanol-TBS mixtures (75%, 50%, 25% methanol,

[11] Reproduced from the manuscipt.

15 min each with gentle agitation) and finally transferred to TBS (50mM Tris pH 7.5, 150 mM NaCl). They were then hemisected and bleached overnight in a hydrogen peroxide/formamide mixture. Directly labeled antibodies were used at approximately the following concentrations: Alexa488-tubulin (1-2µg/mL), Alexa647-AurB kinase (0.5µg/mL), Alexa568-Kif23 (1-2µg/mL). See methods section in (Nguyen, Groen et al., 2014) for full protocol and more information on antibodies.

Light Microscopy for fixed embryos

Fixed Xenopus embryos were imaged with a laser scanning confocal microscopes at two locations. The Nikon Imaging Center at Harvard Medical School. A 10X dry and a 20X multi-immersion objective (Nikon) was used on a Nikon Ti-E inverted microscope with a Nikon A1R point scanning confocal head, driven by NIS-Elements image acquisition software. Also at MBL using a Zeiss 780 LSM (laser scanning confocal) on an inverted Observer Z1 microscope with a motorized stage driven by ZEN software, 10x dry objective.

Extract experiments

Actin-intact CSF-arrested Xenopus extract from unfertilized eggs was prepared as described, kept on ice, and used within 8hrs (Field et al., 2014). Fluorescence probes were prepared and used as described in (Nguyen, Groen et al., 2014). General methods for imaging microtubules in the egg extract system have been described (Desai et al., 1999; Maresca and Heald, 2006).

To initiate microtuble aster growth, extract containing fluorescent probes was converted to interphase by addition of $CaCl_2$ to 0.4mM, incubated at 20°C for 3 minutes, and transferred to ice. Calcium addition mimics fertilization and releases CSF arrest (Field et al., 2014). Two methods were used to nucleate microtubule asters: either AurkA coated magnetic beads (Nguyen, Groen et al., 2014; Tsai and Zheng, 2005) or permeablized Xenopus sperm (Murray,

1991) were added, and the reaction was spread between two coverslips that had been passivated by coating with polylysine-PEG (PLL(20)-g{3.5}-PEG(2): SuSOS Chemicals). We used a simplified method for this coating. Coverslips were dipped in 70% ethanol, flamed, cooled and placed onto a droplet of 100 µg/ml polylysine-PEG in 10 mM Hepes, pH 7.4 on Parafilm for 15-30 min. They were then washed twice with water for 5 min each and dried with a jet of nitrogen and used the same day.

Reactions were imaged by widefield fluorescence at 20°C, using a 10x or 20x Plan Apo 1.4 NA objective lens (Nikon) on an upright Nikon Eclipse 90i microscope equipped with a Prior Lumen 200 metal arc lamp, a Prior ProScan III motorized XY stage, a Hamamatsu ORCA-ER cooled CCD camera, and driven by Metamorph image acquisition software (Molecular Devices, CA).

Starting distance experiments

Interphase asters were nucleated using AurkA beads in extract containing Alexa488-labeled tubulin and Alexa647-labeled anti-AurkB IgG. The extract was assembled between PEG-coated coverslips. Two-color time-lapse sequences were taken of multiple image fields in parallel at 1.5 min intervals, starting from ~7-9 min of assembly reaction. Bead pairs were identified from the last frame of the tubulin movie (at ~50-55 min), based on whether their asters interacted. For each pair, the initial distance between the beads was measured from the first frame of the AurkB movie (at 9 min).The time of initial contact between each aster within a pair was estimated from the tubulin movie, and an interaction was scored based on the AurkB movie using the following criteria: 1) Was AurkB recruited to the zone within the next 4 frames (i.e. 6 minutes)? 2) Was AurkB recruited without lateral spreading from a neighboring zone? Zones satisfying both criteria were scored as AurkB -positive. Zones not satisfying criterion 1 were scored as AurkB -negative, even though they might acquire AurkB via lateral spreading at a later time point. Zones satisfying criterion 1 but not criterion 2 (i.e. they acquired AurkB via

lateral spreading from a neighboring zone) were scored as ambiguous and omitted from further analysis.

Acknowledgements

This work was supported by NIH grant GM39565 (T.J.M.), MBL fellowships from the Evans Foundation, MBL Associates, and the Colwin Fund (T.J.M. and C.M.F.). Authors thank the Nikon Imaging Center at Harvard Medical School for microscopy support; and the National Xenopus Resource at MBL for Xenopus animals and care. We also thank Martin Wühr for intellectual support and critical reading of the manuscript. Keisuke Ishihara and James Pelletier for critical reading of the manuscript.

References

Argiros, H., Henson, L., Holguin, C., Foe, V., and Shuster, C.B. (2012). Centralspindlin and chromosomal passenger complex behavior during normal and Rappaport furrow specification in echinoderm embryos. Cytoskeleton (Hoboken) *69*, 840–853.

Bieling, P., Telley, I.A., and Surrey, T. (2010). A Minimal Midzone Protein Module Controls Formation and Length of Antiparallel Microtubule Overlaps. Cell *142*, 420–432.

Brachet, A. (1910). La polyspermie expérimentale comme moyen d“analyse de la fe”condation. Development Genes and Evolution *30*, 261–303.

Canman, J.C., Cameron, L.A., Maddox, P.S., Straight, A., Tirnauer, J.S., Mitchison, T.J., Fang, G., Kapoor, T.M., and Salmon, E.D. (2003). Determining the position of the cell division plane. Nature *424*, 1074–1078.

Carmena, M., Wheelock, M., Funabiki, H., and Earnshaw, W.C. (2012). The chromosomal passenger complex (CPC): from easy rider to the godfather of mitosis. Nat Rev Mol Cell Biol *13*, 789–803.

Cooke, C.A., Heck, M.M., and Earnshaw, W.C. (1987). The inner centromere protein (INCENP) antigens: movement from inner centromere to midbody during mitosis. J Cell Biol *105*, 2053–2067.

Desai, A., Verma, S., Mitchison, T.J., and Walczak, C.E. (1999). Kin I kinesins are microtubule-destabilizing enzymes. Cell *96*, 69–78.

Eggert, U.S., Mitchison, T.J., and Field, C.M. (2006). Animal cytokinesis: from parts list to mechanisms. Annu Rev Biochem *75*, 543–566.

Ferreira, J.G., Pereira, A.J., Akhmanova, A., and Maiato, H. (2013). Aurora B spatially regulates EB3 phosphorylation to coordinate daughter cell adhesion with cytokinesis. J Cell Biol *201*, 709–724.

Field, C.M., Nguyen, P.A., Ishihara, K., Groen, A.C., and Mitchison, T.J. (2014). Xenopus egg cytoplasm with intact actin. Meth Enzymol *540*, 399–415.

Fuller, B.G., Lampson, M.A., Foley, E.A., Rosasco-Nitcher, S., Le, K.V., Tobelmann, P., Brautigan, D.L., Stukenberg, P.T., and Kapoor, T.M. (2008). Midzone activation of aurora B in anaphase produces an intracellular phosphorylation gradient. Nature *453*, 1132.

Glotzer, M. (2005). The molecular requirements for cytokinesis. Science *307*, 1735–1739.

Grüneberg, U., Neef, R., Honda, R., Nigg, E.A., and Barr, F.A. (2004). Relocation of Aurora B from centromeres to the central spindle at the metaphase to anaphase transition requires MKlp2. J Cell Biol *166*, 167–172.

Herlant, M. (1911). Recherches sur les oeufs di-et-trispermiques de grenouille. Arch Biol *26*, 103–336.

Hu, C.-K., Coughlin, M., Field, C.M., and Mitchison, T.J. (2008). Cell polarization during monopolar cytokinesis. J Cell Biol *181*, 195–202.

Hu, C.-K., Coughlin, M., Field, C.M., and Mitchison, T.J. (2011). KIF4 regulates midzone length during cytokinesis. Curr Biol *21*, 815–824.

Ishihara, K., Nguyen, P.A., Groen, A.C., Field, C.M., and Mitchison, T.J. (2014). Microtubule nucleation remote from centrosomes may explain how asters span large cells. Proc Natl Acad Sci USA *111*, 17715–17722.

Kelly, A.E., Sampath, S.C., Maniar, T.A., Woo, E.M., Chait, B.T., and Funabiki, H. (2007). Chromosomal enrichment and activation of the aurora B pathway are coupled to spatially regulate spindle assembly. Dev Cell *12*, 31–43.

Lewellyn, L., Carvalho, A., Desai, A., Maddox, A.S., and Oegema, K. (2011). The chromosomal passenger complex and centralspindlin independently contribute to contractile ring assembly. J Cell Biol *193*, 155–169.

Maresca, T.J., and Heald, R. (2006). Methods for studying spindle assembly and chromosome condensation in Xenopus egg extracts. Methods Mol Biol *322*, 459–474.

Mitchison, T., Wühr, M., Nguyen, P., Ishihara, K., Groen, A., and Field, C.M. (2012). Growth, interaction, and positioning of microtubule asters in extremely large vertebrate embryo cells. Cytoskeleton (Hoboken) *69*, 738–750.

Murray, A.W. (1991). Cell cycle extracts. Methods Cell Biol *36*, 581–605.

Nguyen, P.A., Groen, A.C., Loose, M., Ishihara, K., Wühr, M., Field, C.M., and Mitchison, T.J. (2014). Spatial organization of cytokinesis signaling reconstituted in a cell-free system. Science *346*, 244–247.

Nunes Bastos, R., Gandhi, S.R., Baron, R.D., Grüneberg, U., Nigg, E.A., and Barr, F.A. (2013). Aurora B suppresses microtubule dynamics and limits central spindle size by locally activating KIF4A. J Cell Biol *202*, 605–621.

Ohi, R., Sapra, T., Howard, J., and Mitchison, T.J. (2004). Differentiation of cytoplasmic and meiotic spindle assembly MCAK functions by Aurora B-dependent phosphorylation. Mol Biol Cell *15*, 2895–2906.

Rappaport, R. (1961). Experiments concerning the cleavage stimulus in sand dollar eggs. J Exp Zool *148*, 81–89.

Rappaport, R. (1969). Aster-equatorial surface relations and furrow establishment. J Exp Zool *171*, 59–68.

Rappaport, R. (1996). Cytokinesis in animal cells (Cambridge; New York: Cambridge University Press).

Render, J.A., and Elinson, R.P. (1986). Axis determination in polyspermic Xenopus laevis eggs. Dev Biol *115*, 425–433.

Sive, H.L., Grainger, R.M., and harland, R.M. (2000). Early development of *Xenopus laevis*: a laboratory manual

(Cold Spring Harbor, NY: Cold Spring Harbor Laboratory Press).

Snook, R.R., Hosken, D.J., and Karr, T.L. (2011). The biology and evolution of polyspermy: insights from cellular and functional studies of sperm and centrosomal behavior in the fertilized egg. Reproduction *142*, 779–792.

Tsai, M.-Y., and Zheng, Y. (2005). Aurora A kinase-coated beads function as microtubule-organizing centers and enhance RanGTP-induced spindle assembly. Curr Biol *15*, 2156–2163.

Tseng, B.S., Tan, L., Kapoor, T.M., and Funabiki, H. (2010). Dual detection of chromosomes and microtubules by the chromosomal passenger complex drives spindle assembly. Dev Cell *18*, 903–912.

Walczak, C.E., Mitchison, T.J., and Desai, A. (1996). XKCM1: a Xenopus kinesin-related protein that regulates microtubule dynamics during mitotic spindle assembly. Cell *84*, 37–47.

White, E.A., and Glotzer, M. (2012). Centralspindlin: at the heart of cytokinesis. Cytoskeleton (Hoboken) *69*, 882–892.

Wühr, M., Chen, Y., Dumont, S., Groen, A.C., Needleman, D.J., Salic, A., and Mitchison, T.J. (2008). Evidence for an upper limit to mitotic spindle length. Curr Biol *18*, 1256–1261.

Wühr, M., Freeman, R.M., Presler, M., Horb, M.E., Peshkin, L., Gygi, S.P., and Kirschner, M.W. (2014). Deep proteomics of the Xenopus laevis egg using an mRNA-derived reference database. Curr Biol *24*, 1467–1475.

Wühr, M., Mitchison, T.J., and Field, C.M. (2009). Size and speed go hand in hand in cytokinesis. Cell *137*, 798–800.

Zimniak, T., Stengl, K., Mechtler, K., and Westermann, S. (2009). Phosphoregulation of the budding yeast EB1 homologue Bim1p by Aurora/Ipl1p. J Cell Biol *186*, 379–391.

Chapter Five

Conclusions and Future Directions

This dissertation sought to understand the spatial organizing principles and molecular mechanisms that allow unusually large embryonic cells to precisely position their cleavage furrow to their midplane. Eggs from the frog *Xenopus laevis* served as the model system, as they are among the largest fully cleaving cells (Table 1.1). In these large cells, the mitotic spindle measures 1/20th of the cell diameter, which raises the question: how does such a small spindle communicate its position to the distant cell cortex to position the cleavage furrow exactly to the plane that would bisect the spindle?

Previous graduate work in the Mitchison lab by Martin Wühr had established the importance of interphase aster, an unusually large radial array of microtubules growing from a centrosome, in spatially organizing the egg cytoplasm and determining the cleavage plane (Mitchison et al., 2012; Wühr et al., 2008; 2009; 2010). In particular, it was proposed that asters growing from the spindle poles mark the putative cleavage plane where they meet each other and form a specialized microtubule structure, which we have termed the 'aster-aster interaction zone' (AAIZ). The work described in this dissertation followed up on these phenomenological observations to elucidate the underlying molecular mechanisms.

Whole frog eggs are difficult to study at a molecular level. Their interior cannot be imaged live using fluorescence microscopy, because they are filled with light scatter yolk particles and pigment granules. It is difficult to perform molecular perturbation on them: microinjected small molecules, especially if they are hydrophobic like taxol, cannot diffuse too far in the cytoplasm before being captured by yolk or lipid particles; morpholino knockdown in immature occytes is possible, but extremely technically challenging (Wylie and Heasman, 1997). In order to circumvent these difficulties, my colleagues and I developed a cell-free biochemical system using undiluted cytoplasmic extracts from unfertilized eggs that reconstituted cytokinesis signaling events on top of a coverslip (Chapter Two). Using this system, we were able to address several unanswered mechanistic questions about cleavage furrow specification in the large frog eggs (see Abstract for a summary of findings by chapter).

Aster-aster interaction zone: the primary positional cue for cytokinesis in large cells

As expected from its hypothesized role in cleavage furrow specification, we were able to localize all the key spindle midzone proteins against which we had antibodies to the AAIZ in dividing eggs: the Chromosome Passenger Complex (CPC; Figures 2.2, 4.2, 4.3, and 4.7), the Centralspindlin complex (Figures 2.2 and 4.2), Kif4A (Figures 3.2 and 4.3), and an embryonic paralog of Prc1 (Prc1E; Figure 3.2). All these localizations were observed on AAIZs assembled in the extract system between asters nucleated from Aurora A kinase-based artificial centrosome beads (Figures 2.2, 2.6, and 3.1). This result suggested that asters alone have the potential to specify a cleavage plane in the absence of either the spindle midzone or chromatins. The cell-free assay also allowed us to localize other proteins for which we only had purified fluorescent probes but not antibodies.

To confirm that AAIZs assembled in extract were able to signal to the cortex to initiate the assembly of a cleavage furrow, we layered the extract on top of a supported lipid bilayer with a composition that mimicked the inner leaflet of the plasma membrane (Figure 2.7). We found that CPC-positive AAIZs were able to locally activate RhoA, to induce F-actin assembly, and to recruit other cortical cleavage furrow proteins, such as anillin and septin (Figure 2.8).

Interestingly, neither AAIZ assembly nor RhoA activation was significantly affected when the Kif23 subunit of the Centralspindlin complex was depleted (Figure 2.7). This suggests that in our system, the microtubule-bound CPC is the positive signal that is delivered to the cell cortex to induce a cleavage furrow and that Centralspindlin (or at least Kif23) is dispensable. Future studies need to investigate whether RacGAP1 was co-depleted with Kif23 in our system, and if not, whether it has a role in localized RhoA activation. A recent study from the Glotzer lab proposes that Aurora B kinase (a CPC subunit) promotes cytokinesis by inducing oligomerization of Centralspindlin through phosphorylating Kif23, and that furrow is induced in *C. elegans* embryos where these oligomers associate with the plasma membrane (Basant et al.,

2015). Unfortunately, the findings in our system are not consistent with this model at all—which could be due to differences in animal cell systems.

Preliminary experiments delivering beads coated with antibodies against either Aurora B kinase or INCENP (CPC subunits) in extract to the lipid bilayer did not show local RhoA activation (unpublished data). Therefore, we are still unable to distinguish whether Aurora B activity at the cortex or the CPC-positive microtubule structure is required for furrow induction.

Based on these findings, some might argue that the AAIZ is just the spindle midzone in large cells and there is nothing new or special about it. However, I believe it is a structure distinct from both the midzone and the astral microtubules that reach the equatorial plane depicted in textbooks (Figure 1.1, the 'Animals' panel on the left, and Figure 1.2). Unlike the astral microtubules, the AAIZ contains antiparallel microtubule bundles. And unlike the midzone, the AAIZ does not require a pre-existing spindle for its assembly, and microtubule density is lower in the AAIZ than in the interior of the participating asters. Therefore, I think the AAIZ should be considered as a distinct microtubule structure and a 4th positive positional cue (next to the chromatin, midzone, and astral microtubules) that operates in larger cells.

Chromatin and starting distance between asters: secondary positional cues

My initial investigations into the molecular mechanisms establishing AAIZs using centrosomes attached to permeabilized sperm as nucleating centers were confounded by the fact that not all AAIZs were equivalent. To remove the Aurora B-dependent aster polarization effect associated with the sperm chromatin, I conducted experiments with either purified centrosomes or the Aurora A kinase beads. The beads were easier to work with because they were bigger and had autofluorescence, therefore it was easier to locate the asters early in the assembly reaction. When Aurora B kinase was inhibited, most AAIZs between beads were disrupted: microtubules interpenetrated and CPC was not localized (Figure 2.4). However, some AAIZs were still observed in terms of microtubule morphology: both reduced microtubule density

and lack interpenetration (unpublished data). The AAIZs formed under Aurora B inhibition did not localize the CPC, however, which reminded me of the non-sister zones in polyspermic eggs. In fact, the common property between the AAIZs formed under Aurora B inhibition was that they formed between asters with large initial inter-center distance.

These observations prompted us to test the effect of chromatin on CPC recruitment to isolated asters (Figure 4.4) and the effect of starting distance between aster centers on CPC recruitment to AAIZs (Figure 4.5). We concluded that proximity of the chromatin biased CPC recruitment onto microtubules even when they were not participating in an aster-aster interaction, and that in the absence of the chromatin, CPC was recruited to AAIZs between asters with an optimal starting distance. Since sister asters in polyspermic eggs both have chromatins between them and start close to each other (about the length of the spindle, i.e. 60 μm, which falls within the optimal range found in extract [~45-110 μm]) (Figure 4.2), we proposed that these two initial conditions allow them to recruit CPC to the interaction zone (Figure 4.8). Non-sister asters, however, do not have chromatin between them and start much father apart (~600 μm); therefore, according to our model, they do not recruit the CPC.

Block to microtubule interpenetration at AAIZs requires antiparallel overlaps and microtubule stabilization

In Chapter Three, I asked how neighboring asters recognized each other and how they were prevented from interpenetrating. In order to simplify analysis, I only reported AAIZs that were assembled between asters with a starting distance that fell under the optimal distance range. However, when I depleted either Prc1E or Kif4A, I observed only interpenetrating AAIZs regardless of starting distance (Figure 3.4 and unpublished data). As discussed above, when I inhibited Aurora B kinase, AAIZs formed between asters that started from farther apart did not interpenetrate, albeit they did not localize the CPC. They did localize Prc1E and Kif4A, however, although the localization was more disperse than what is seen in control AAIZs that also localize

the CPC (unpublished data). I also found that the somatic paralog of Prc1 could rescue normal AAIZ formation when Prc1E was depleted. From these data, I conclude that block to interpenetration at AAIZs requires antiparallel overlaps mediated by either form of Prc1, and the block to interpenetration is not a phenomenon specific to the embryonic Prc1E protein.

Careful analysis of microtubule dynamics inside and outside an AAIZ revealed that plus ends tended to slow down before they stopped growing within AAIZs. This behavior was dependent on Prc1 and Kif4A, and Aurora B kinase activity enhanced it (Figure 3.3). This provides evidence for microtubule stabilization at AAIZs, probably mediated by Kif4A activity (Bieling et al., 2010; Bringmann et al., 2004; Nunes Bastos et al., 2013). Preliminary analyses of microtubule dynamics in AAIZs assembled in extract that resemble non-sister zones also reveal reduced growth rate and increased rate of growth termination within these CPC-negative, but Prc1 and Kif4A positive, zones (unpublished data). From these results, I conclude that block to interpenetration also requires microtubule stabilization. To obtain more conclusive evidence for microtubule stabilization, photobleaching or photoactivation experiments need to be conducted in the future.

Why extract AAIZs resembling non-sister zones in embryos do not require Aurora B kinase activity for blocking interpenetration is an interesting question. It is possible that the increased initial distance between asters allows them to become very bushy and more disorganized at their peripheries, which in turn allows for formation of more Prc1E and Kif4A-coated antiparallel overlaps. This zone of overlaps again acts like a microtubule sink, preventing asters from growing into each other. Controlling initial distance between aster nucleating centers by micropatterning combined with computation modeling would be useful tools to explore the distance-dependent microtubule dynamics at AAIZs.

Positive feedback between microtubule stabilization and CPC recruitment/activation

We found that AAIZs that recruit CPC in extracts likely have stabilized microtubules, based on the observation that plus ends tend to slow down before they stop growing in AAIZs (Figure 3.3). This effect was more pronounced when Aurora B kinase was active, likely due to Aurora B regulation of Kif4A (Figure 3.4) (Nunes Bastos et al., 2013). We also found that treating extract with microtubule stabilizing agents led to increased CPC recruitment (Figure 4.6). From these observations we propose that there is a positive feedback loop between microtubule stabilization and CPC recruitment (Figure 4.8). We speculate that this loop serves to maintain the CPC-positive status of an interaction zone once it satisfies the initial conditions (proximity to chromatin or spindle midzone, and/or optimal starting distance), which could explain the binary nature of CPC recruitment to sister vs. non-sister aster interaction zones (Figure 4.2).

Another molecular evidence for the feedback loop is the finding that Kif4A transports the CPC towards microtubule plus ends within the antiparallel bundles at the AAIZ (Figure 2.6), and we already mentioned that Kif4A activity is enhanced by Aurora B phosphorylation (Nunes Bastos et al., 2013). An embryonic paralog of Kif20A (or Mklp2) is also involved in CPC localization, as expected from studies in somatic cells (Grüneberg et al., 2004; Kitagawa et al., 2013). We believe it is responsible for either targeting the CPC to antiparallel overlaps or activating Aurora B within the complex in an allosteric manner, which then allows for CPC binding to microtubule via INCENP.

The positive feedback is likely necessary for efficient transport of the CPC from its initial docking site at the spindle midzone and the nearly aster interaction zones all the way to the cell cortex. Future studies could address whether this transport is purely recruitment-based or whether there is a lateral transfer mechanism orthogonal to microtubules (Figure 1.3).

Radial order within large microtubule asters also requires the Prc1/Kif4A module

While investigating the role of the Prc1/Kif4A midzone module on AAIZs, I also discovered that they are necessary to maintain uniform radial microtubule orientation. Figure 3.8 describes the model for how antiparallel microtubule overlap control allows Prc1 and Kif4A to control microtubule orientation both within and between large asters. This role of Prc1 and Kif4A in maintaining radial order is likely a mechanism found in only large cells where microtubule asters expand via nucleation away from the centrosome (Ishihara et al., 2014), a process that would otherwise randomize microtubule orientation within an aster as it expands.

Why are there embryonic paralogs of cytokinesis proteins?

During our investigations of the molecular mechanism underlying AAIZ formation, we encountered several proteins that had a second paralog in Xenopus, which was only expressed during early embryonic development. Furthermore, phylogenetic analyses of these proteins revealed that the gene duplication was only present in species with large fully cleaving eggs (e.g. frogs and fish), but not in species with either small eggs or large eggs that do not cleave fully (unpublished data). Two of these proteins were discussed in this dissertation: Kif20A and Prc1. We are in the process of systematically finding all the proteins that satisfy the two criteria above. It would be an intellectually stimulating adventure to explore how these proteins have been evolved to adapt to the special challenges faced by very large cells.

References

Basant, A., Lekomtsev, S., Tse, Y.C., Zhang, D., Longhini, K.M., Petronczki, M., and Glotzer, M. (2015). Aurora B kinase promotes cytokinesis by inducing centralspindlin oligomers that associate with the plasma membrane. Dev Cell *33*, 204–215.

Bieling, P., Telley, I.A., and Surrey, T. (2010). A Minimal Midzone Protein Module Controls Formation and Length of Antiparallel Microtubule Overlaps. Cell *142*, 420–432.

Bringmann, H., Skiniotis, G., Spilker, A., Kandels-Lewis, S., Vernos, I., and Surrey, T. (2004). A kinesin-like motor inhibits microtubule dynamic instability. Science *303*, 1519–1522.

Grüneberg, U., Neef, R., Honda, R., Nigg, E.A., and Barr, F.A. (2004). Relocation of Aurora B from centromeres to the central spindle at the metaphase to anaphase transition requires MKlp2. J Cell Biol *166*, 167–172.

Ishihara, K., Nguyen, P.A., Groen, A.C., Field, C.M., and Mitchison, T.J. (2014). Microtubule nucleation remote from centrosomes may explain how asters span large cells. Proc Natl Acad Sci USA *111*, 17715–17722.

Kitagawa, M., Fung, S.Y.S., Onishi, N., Saya, H., and Lee, S.H. (2013). Targeting Aurora B to the equatorial cortex by MKlp2 is required for cytokinesis. PLoS ONE *8*, e64826.

Mitchison, T., Wühr, M., Nguyen, P., Ishihara, K., Groen, A., and Field, C.M. (2012). Growth, interaction, and positioning of microtubule asters in extremely large vertebrate embryo cells. Cytoskeleton (Hoboken) *69*, 738–750.

Nunes Bastos, R., Gandhi, S.R., Baron, R.D., Grüneberg, U., Nigg, E.A., and Barr, F.A. (2013). Aurora B suppresses microtubule dynamics and limits central spindle size by locally activating KIF4A. J Cell Biol *202*, 605–621.

Wühr, M., Chen, Y., Dumont, S., Groen, A.C., Needleman, D.J., Salic, A., and Mitchison, T.J. (2008). Evidence for an upper limit to mitotic spindle length. Curr Biol *18*, 1256–1261.

Wühr, M., Dumont, S., Groen, A.C., Needleman, D.J., and Mitchison, T.J. (2009). How does a millimeter-sized cell find its center? Cell Cycle *8*, 1115–1121.

Wühr, M., Tan, E.S., Parker, S.K., Detrich, H.W., and Mitchison, T.J. (2010). A model for cleavage plane determination in early amphibian and fish embryos. Curr Biol *20*, 2040–2045.

Wylie, C.C., and Heasman, J. (1997). What my mother told me: Examining the roles of maternal gene products in a vertebrate. Trends Cell Biol *7*, 459–462.

Appendix I

Supplemental Materials for Chapter Two: Cell-Free Reconstitution of Cytokinesis Signaling

Supplementary contents include Materials and Methods, Figures S2.1 to S2.12, Tables S2.1 to S2.2, Movies S2.1 to S2.10, and References.

Materials and Methods

Antibodies

Antibodies were raised in rabbits to GFP-fused *X. laevis* Aurora kinase A (full-length), Kif20A (C-terminal 359 amino acids), and Kif23 (C-terminal 309 amino acids), as well as GST-fused Kif20AE (C-terminal 190 amino acids). Antisera were first depleted of GFP or GST antibodies, then antibodies were affinity purified using the respective fusion protein. For antibodies against Aurora kinase A, antisera were depleted against Aurora kinase B to ensure that the purified antibody was specific to Aurora kinase A and did not perturb kinase activity. DNA for fusion constructs was purchased (GenScript, NJ) and subcloned with Gibson cloning.

Affinity purified C-terminal peptide (CTP) antibodies (rabbit) were produced against *X. laevis* Kif23 (C-EMRAGSNLGPGYEHHVVSKRRRP) and Kif20AE (C-KRTTSKSQEKPEEVSGTSRKRPLLSRR) (NeoBioLab, MA).

Antibodies (rabbit) generated to MBP-fused C-terminal 316 amino acids of *X. laevis* Kif4A (or Xklp1; construct kindly provided by Isabelle Vernos [ICREA, Spain]) were affinity purified (depleted of MBP antibodies). Antibodies (rabbit) generated to GST fused to the N-terminal 100 amino acids of *X. laevis* Aurora kinase B were kindly provided by Ryoma Ohi (Vanderbilt University, TN). See Table S2.1 for sequence information on the proteins studied in this paper.

Antibodies against anillin (Straight et al., 2005) and septin 7 (Oegema et al., 2000) were from previous studies. Tubulin antibodies (Sigma #T6074) were purchased.

Antibodies were labeled on column with Alexa-488, Alexa-568, or Alexa-647 dyes (Life Technologies, NY) as previously described (Groen et al., 2014).

Protein Expression Plasmid Constructs

The following constructs were received as kind gifts: Lifeact-GFP construct (Riedl et al., 2008) from David Burgess (Boston College, MA), human EB1-GFP construct from Kevin Slep (UNC Chapel Hill, NC), *X. laevis* Kif4A-GFP construct (aka Xklp1-GFP) in pFastBac1 baculovirus expression vector (Bieling et al., 2010) from Thomas Surrey (London Research Institute, UK).

The Rho GTPase-binding domain (rGBD) of mouse Rhotekin (amino acids 7-82) was subcloned into pGEX-4T-1 bacterial expression vector with an N-terminal 6xHis-mCherry tag, replacing the GST tag between EcoN1/Not1 restriction sites, creating mCherry-rGBD. The Rhotekin fragment (rGBD) specifically binds to active, GTP-bound RhoA (Bement et al., 2005; Benink and Bement, 2005). Mouse Rhotekin cDNA was a gift from William Bement (University of Wisconsin–Madison, WI).

The *X. laevis* DasraA cDNA (IRBHp990G0393D, Source Bioscience, UK) was subcloned into pGEX-4T-1 with an N-terminal 6xHis-eGFP tag, creating GFP-DasraA.

The *X. laevis* PRC1embryonic (PRC1E) cDNA (codon optimized for *E. coli* and insect cell expression; GenScript, NJ) was subcloned into pET-28b bacterial expression vector with an N-terminal Strep-tag (WSHPQFEK) followed by an eGFP tag, creating GFP-PRC1E. This is an embryonic paralog of the PRC1 protein in *Xenopus* that we called 'PRC1L' in a previous publication (Mitchison et al., 2013).

All subcloning was performed with Gibson cloning. See Table S2.1 for sequence information on the *Xenopus* proteins studied in this paper.

Protein Expression and Purification

EB1-GFP-His, His-mCherry-rGBD (Rho GTPase binding domain), His-GFP-DasraA were conventionally purified from *E. coli* (Rosetta2(DE3)pLysS). Purification of EB1-GFP-His was previously described (Petry et al., 2013). Briefly, expressing cells were lysed by sonication

in ice-cold lysis buffer A (50mM NaPi, pH 7.7, 500mM NaCl, 0.1mM $MgCl_2$, 1% Triton X-100, 1mM dithiothreitol [DTT], 1mM phenylmethylsulfonyl fluoride [PMSF]). Clarified lysates were batch-incubated for 1.5 hr at 4°C with HisPur Cobalt resin (~2 mL/L of culture; Thermo Scientific, MA). After elution in lysis buffer containing 300mM imidazole, proteins were gel filtered using a Superdex 75 10/300 GL column (GE Healthcare, MA) equilibrated with 10mM K-HEPES, pH 7.7, 150mM KCl, 1mM DTT. Proteins were supplemented with 10% (w/v) sucrose and flash-frozen in liquid nitrogen for storage at −80°C. Coomassie-stained gels are shown for mCherry-rGBD and GFP-DasraA in Figure S2.12.

Strep-GFP-PRC1E was expressed in *E. coli* (Rosetta2(DE3)pLysS) after induction with 0.5mM IPTG for 3-4 hrs at 18°C. Expressing cells were lysed by sonication in ice-cold lysis buffer B (50mM NaPi, pH 7.7, 400mM NaCl, 3mM EDTA, 10mM β-mercaptoethanol, Halt Protease Inhibitor Cocktail [Thermo Scientific, MA], 1mg/mL lysozyme, 10µg/mL DNase). Clarified lysates were loaded onto a Strep-Tactin column (IBA GmbH, Germany). After protein binding, column was washed with buffer C (50mM NaPi, 400mM NaCl, 3mM EDTA, 50mM arginine, 50mM glutamate, pH 7.7), then with buffer D (10mM K-Hepes, pH 7.7, 500mM KCl). Protein was eluted with buffer D containing 2.5mM desthiobiotin (Sigma #D1411), supplemented with 1mM DTT and 20% (w/v) sucrose, and flash-frozen in liquid nitrogen for storage at −80°C. Coomassie-stained gels are shown for GFP-PRC1E in Figure S2.12.

Kif4A-GFP-His was purified from Sf21 insect cells as previously described (Bieling et al., 2010) with the following modification: after elution from the HisPur Cobalt column, the protein was gel filtered using a Superose 6 10/300 GL column (GE Healthcare, MA) equilibrated with 10mM K-Hepes, pH 7.7, 500mM KCl, 1mM $MgCl_2$, 0.2mM ATP, 1mM DTT. Protein was supplemented with 20% (w/v) sucrose, and flash-frozen in liquid nitrogen for storage at −80°C.

Tubulin was purified from bovine brain and labeled with X-rhodamine, Alexa488, Alexa568, or Alexa647 dyes (Life Technologies, NY) as previously described (Groen et al., 2014). Purified Lifeact-GFP was a kind gift from David Burgess (Boston College, MA).

Protein concentrations were determined by Bradford assay with BSA standards, and refer to dimers for tubulin and monomers for all the other proteins. See Table S2.1 for sequence information on the *Xenopus* proteins studied in this paper.

Preparation of *Xenopus* Egg Cytoplasm with Intact Actin

Metaphase arrested *Xenopus* egg extracts with intact actin were prepared as described (Field et al., 2014). Briefly, eggs were dejellyed and processed at 16°C, and immediately crushed at ~12,500xg for 15 min at 4°C. The cytoplasmic layer was isolated, supplemented with protease inhibitors (leupeptin, pepstatin chymostatin; Sigma) and 50mM sucrose, and immediately stored at 4°C. Egg quality varied from frog to frog, thus batches of eggs from different female frogs were processed separately and the corresponding extracts were never pooled. Extracts from each batch were assayed for actin contractility (Field et al., 2014) and AAIZ formation between glass coverslips (see below). Only extracts that exhibited strong actin contractility, assembled dense microtubule asters, and formed robust AAIZs, were selected for further experiments.

Aster Assembly Assay Between Glass Coverslips (see Figures 2.1 and 2.2A)

For each experiment, ~50µL of extract was supplemented with fluorescent probes (directly labeled tubulin, directly labeled antibodies, GFP-tagged proteins). Extract was treated with 0.4mM $CaCl_2$ and incubated at 20°C for 2 min to mimic fertilization and induce metaphase-to-interphase transition (referred to as activated extract). Activated extract was incubated on ice for 2 min to depolymerize microtubule and F-actin polymers. Then extract was supplemented with Aurora A antibody-coupled Protein A Dynabeads (Life Technologies, NY) which served as artificial centrosomes (Tsai and Zheng, 2005), and placed between two PEG-passivated glass coverslips (~10-15µm deep, or ~5µL extract for a 18mm X 18mm glass coverslip prep; see workflow in Figure 2.1). Coverslips were passivated with silane-PEG as described (Field et al.,

2014). Aster assembly reactions were monitored with a widefield or spinning disc confocal microscope at 20°C.

For TIRF imaging, extract was placed between a PEG-passivated and a kappa-casein coated coverslip. Kappa-casein (Sigma #C0406) coating minimized the adsorption of many microtubule-interacting proteins on the glass, while it still allowed microtubules to track along the coated surface (Field et al., 2014).

For visualization, fluorescent probes were used at the following concentrations: 250nM Alexa488-, 568- or 647-tubulin, 40nM EB1-GFP, 10nM Kif4A-GFP, 20nM GFP-PRC1E, 20nM GFP-DasraA, and 0.1-1 μg/mL Alexa674-IgG against AurkB to visualize the CPC, Alexa568-IgG against a Kif23-CTP to visualize the Centralspindlin complex, Alexa568-IgG against a Ki20AE-CTP to visualize Kif20AE.

Aster Assembly Assay on Lipid Bilayer Coated Coverslips (see Figure 2.7A)

Supported lipid bilayers (SLBs) were prepared in a reaction chamber consisting of a plastic ring glued on plasma-cleaned glass coverslips as previously described (Loose and Schwille, 2009; Loose et al., 2008) with modifications in lipid compositions (Lee et al., 2010). Small unilamellar vesicles (SUVs) were prepared by sonication from porcine brain PC, porcine brain PS, and porcine liver PI (Avanti Polar Lipids, AL) at the molar ratio of 0.6/0.3/0.1 and 5mM total lipid concentration in high salt extract buffer XB (10mM K-Hepes, pH 7.7, 300mM KCl, 1mM $MgCl_2$, 0.1mM $CaCl_2$, 50mM sucrose). The SUV suspension was diluted to 1mM, added to the reaction chamber, and vesicle fusion was induced by adding 0.1mM $CaCl_2$. After 30-60 min incubation at 42°C, lipid bilayers were extensively washed with extract buffer XB (10mM K-Hepes, pH 7.7, 100mM KCl, 1mM $MgCl_2$, 0.1mM $CaCl_2$, 50mM sucrose), and stored at 4°C till experiment.

Note that *Xenopus* egg extracts made on different days varied in their ability to promote actin polymerization at the cortical layer, and we found that adding porcine brain $PI(4,5)P_2$

(Avanti Polar Lipids, AL) up to 1% of the total lipid mixture was sometimes necessary to observe actin enrichment at the AAIZs. We routinely prepared SLBs containing 0%, 0.1%, and 0.5% $PI(4,5)P_2$ for each extract and assayed for cortical actin morphology (alignment along microtubule asters and enrichment at AAIZs) at the beginning of each experiment to determine which $PI(4,5)P_2$ concentration to use for that particular extract.

For each experiment, 60µL of extract was treated with 0.4mM $CaCl_2$ and incubated at 20°C for 10 min, then returned to ice for 2 min. Bilayers were washed 2 times with 20µL extract each, and finally 20µL extract containing fluorescent probes and AurkA beads was layered on top of the bilayer. Aster assembly reactions were monitored with an inverted TIRF or spinning disc confocal microscope at 20°C.

For visualization, fluorescent probes were used at the following concentrations: 250nM Alexa488-, Alexa568-, or Alexa647-tubulin, 140nM mCherry-rGBD to visualize RhoA-GTP, 140nM Lifeact-GFP to visualize F-actin, and 0.1-1µg/mL Alexa488- or Alexa647-IgG against AurkB to visualize the CPC, Alexa568-IgG against a Kif23-CTP to visualize Centralspindlin, Alexa568-IgG against Anillin to visualize Anillin, and Alexa647-IgG against septin 7 to visualize the septin complex.

Immunodepletions, Protein Addback, and Drug Inhibitions

(related to Figures 2.4, 2.6, 2.7, 2.8D, S2.4, S2.5, and S2.9)

Kif4A, Kif23, Kif20A, and Kif20AE were depleted using 2 rounds of 20µg of IgG (raised against their C-terminal tail) conjugated to 50µL Protein A Dynabeads (Life Technologies, NY) for 50µL of extracts. Depletions using beads coated with random rabbit IgG served as controls. Depletions were confirmed by Western blots (Figure S2.5) and loss of localization of labeled antibodies against the depleted proteins in the aster assembly assay. Kif4A depletion phenotype was rescued by adding back 100nM Kif4A-GFP.

For drug inhibition experiments, 100μM ZM447439 (Aurora B kinase inhibitor; Tocris Bioscience, MN), 100μM STLC (S-trityl-l-cysteine; Eg5 inhibitor; Sigma), 100μM GSK-923295 (CenpE inhibitor; MedChem Express, NJ), or 100μM nocodazole (microtubule depolymerizer; Sigma) was added to calcium activated extracts, and samples were prepared and imaged as described above.

All immunodepletion and drug inhibition experiments were performed with $n \geq 3$ biological repeats, using extracts prepared from eggs produced by different female frogs.

Light Microscopy

Widefield images were obtained using a 20X Plan Apo 1.4 NA objective lens (Nikon) on an upright Nikon Eclipse 90i microscope equipped with a Prior Lumen 200 metal arc lamp, a Prior ProScan III motorized XY stage, a Hamamatsu ORCA-ER cooled CCD camera, and driven by Metamorph image acquisition software (Molecular Devices, CA).

Spinning disc confocal images were obtained using a 40X oil Plan Apo 1.30 NA objective lens (Nikon) on an upright Nikon Eclipse E800 microscope equipped with a Melles Griot Krypton/Argon ion laser (488nm, 568nm, 647nm), a Yokogawa CSU-10 spinning disc (Perkin Elmer, MA), a Hamamatsu ORCA-ER cooled CCD camera, and driven by Metamorph.

Confocal Z-stack images were obtained at the Nikon Imaging Center at Harvard Medical School using a 60X oil Plan Apo 1.49 NA objective lens (Nikon) on a confocal Nikon Ti motorized inverted microscope equipped with a Yokogawa CSU-X1 spinning disc (Spectral Applied Research Aurora Borealis modification), Perfect focus, a Prior Proscan II motorized stage, a Spectral Applied Research LMM-5 laser merge module (Ex:Em 488:480/40, 561:620/60, 642:700/75) with AOTF controlled solid state lasers, a Hamamatsu ORCA-AG cooled CCD camera, and driven by Metamorph.

Fixed *Xenopus* embryos were imaged with a laser scanning confocal microscope at the Nikon Imaging Center at Harvard Medical School. A 10X dry and a 20X multi-immersion

objective (Nikon) was used on a Nikon Ti-E inverted microscope with a Nikon A1R point scanning confocal head, driven by NIS-Elements image acquisition software.

TIRF images were obtained using a 60X Apo TIRF 1.49 NA objective lens (Nikon) on a Nikon Ti-E motorized inverted microscope equipped with a Nikon motorized TIRF illuminator, Perfect focus, a Prior Proscan II motorized stage, Agilent MLC400B laser launch (488nm, 561nm, 647nm), an Andor DU-897 EM-CCD camera driven by NIS-Elements image acquisition software. One such setup was used at the Nikon Imaging Center at Harvard Medical School and one at the Marine Biological Laboratory at Woods Hole.

Microtubule Plus Tip Tracking: Image Acquisition, Processing and Analysis (see Figures S2.2 and 2.4A)

Extract was supplemented with 250nM Alexa568-tubulin, 40nM EB1-GFP, and 1μg/mL Alexa647-IgG against AurkB to visualize the CPC. Asters were assembled between PEG-passivated glass coverslips as described above, simultaneously for samples treated with 100μM ZM447439 (AurkB specific inhibitor) and control buffer. Multiple AAIZs were imaged between 20 and 50 minutes of the assembly reaction at 20°C, alternating between control and treatment conditions. A spinning disc confocal microscope with a 40x oil objective (NA = 1.30) was used to acquire images with 2x2 binning. Time-lapse image sequences were acquired of EB1-GFP with 1.5 sec intervals for a total duration of 2 min. Images of tubulin and AurkB were acquired at the beginning and end of each sequence.

To correct for the flow of cytoplasm between the passivated coverslips, EB1 image sequences were registered using the *StackReg* ImageJ plugin with rigid body transformation (Thévenaz et al., 1998). The *plusTipTracker* Matlab software was used to perform automated detection and frame-to-frame linking of EB1 to obtain growth tracks (see Table S2.2 for parameters) (Applegate et al., 2011; Matov et al., 2010). Here we were only interested in the direction of microtubule plus tip growth, not its dynamics, thus we disabled the software's ability

to infer plus tip shrinkage events by restricting the 'maximum gap length' to 2 frames. This setting still allowed for inferred forward gaps due to potential error in comet detection, but minimized the number of inferred backward gaps. The frame-to-frame XY coordinates of each tracked comet were extracted from the software's output for further analysis in Matlab.

Tracks were filtered out and excluded from analysis based on the following criteria:

a) Mean intensity of detected particles within a single track is above 99th percentile of the intensity distribution of all detected particles. This is to filter out tracks associated with centrosome beads, bright aggregates and hot pixels that are not stationary because of image registration.
b) Tracks with lifetime longer than 1 min. This is to filter out tracks associated with less bright hot pixels.
c) Tracks with lifetime longer than 20 sec and with mean speed lower than 10μm/min. This is to filter out tracks associated with less bright hot pixels.

Tracks were plotted and colored according to their mean direction.

Aster-Aster Interpenetration Analysis (see Figures S2.3 and 2.4B)

All EB1 comets detected over the time-lapse sequence of 2 min were divided into two populations based on their direction with respect to the axis defined by the interaction zone: 0-180° (blue) and 180-360° (red). This was an approximation for which aster the microtubule originated from. Rectangular regions of interest (ROIs) with a length of 90μm and width of 10μm that were perpendicular to and bisected by the interaction zone were drawn across the image space. Each ROI was divided into 9 square bins with 10μm edges. For each ROI, the fraction of blue/red comets were calculated for each bin and plotted against distance along the length of the ROI (roughly corresponding to the bead-to-bead axis). The plots were visually inspected and outlying data were removed. Data from 50+ ROIs from 5+ interaction zones were pooled and the mean values of all fractions and their standard deviations were determined for each bin, and

plotted as a function of distance. The complementary red/blue fractions were also calculated and plotted against distance (Figure S2.3). Mean blue/red fractions are plotted as a blue solid line, and the complementary mean red/blue fractions as a red solid line in Figure 2.4B, where shaded areas represent standard deviations.

Velocity Measurements for CPC Movement (see Figures S2.6, S2.9, and 2.6, E and F)

Extract was supplemented with 250nM Alexa568-tubulin and 1μg/mL Alexa647-IgG against AurkB to visualize the CPC. Asters were assembled between PEG-passivated glass coverslips as described above and AAIZs were imaged between 20 and 50 minutes of the assembly reaction at 20°C. A spinning disc confocal microscope with a 40x oil objective (NA = 1.30) was used to acquire images with 2x2 binning. Time-lapse image sequences were acquired of the CPC at the AAIZ with 1.43 sec intervals for a total duration of 1.5-3 min. The most representative image sequences were selected for analysis.

To correct for the flow of cytoplasm between the passivated coverslips, CPC image sequences were registered using the *StackReg* ImageJ plugin with rigid body transformation. A segmented line (3 pixels wide) was manually drawn over the CPC-positive microtubule bundles in each image frame in ImageJ (Figure S2.6A), and kymographs were generated to show the frame-to-frame fluorescence intensities along these lines (Figure S2.6B).

For each kymograph, individual tracks of CPC clusters were marked with a segmented line in ImageJ, and coordinates of the tracks were imported into Matlab for further analysis (Figure S2,6C, Step 1). The position of the CPC cluster was interpolated for each time point ($d_i(t_i)$), and the instantaneous velocity of the CPC cluster was estimated as:

$$v_i(t_i) = \frac{\Delta d_i}{\Delta t_i} = \frac{d_i - d_{i-1}}{t_i - t_{i-1}}$$ (Figure S2.6C, Step 2).

The distance between the CPC cluster and the CPC-bright midpoint was determined for each time point ($D_i(t_i)$) (Figure S2.6C, Step 3), and v_i was plotted against D_i for each track

(Figure S2.6C, Step 4). Data from 3+ kymographs were pooled and binned along the D_i axis by 1μm intervals, and the mean CPC velocity with standard deviation was calculated for each interval (Figure S2.6C, Step 5). Mean CPC velocities are plotted against distance as solid lines in Figure 2.6F, where error bars represent standard deviations.

The same analysis was performed for AAIZs assembled with extracts where Kif4A was depleted (Figure S2.9, A to C) and where Kif4A depletion was followed by addback of 100nM recombinant Kif4A-GFP (Figure S2.9, D to F).

Velocity Measurements for CPC-Independent Kif4A Movement (see Figure S2.8)

Extract was supplemented with 250nM Alexa647-tubulin and 3nM Kif4A-GFP. Asters were assembled between a PEG-passivated glass coverslip and a partially passivated coverslip coated with kappa-casein (Field et al., 2014; Groen et al., 2014), which allows microtubules to track along the kappa-casein-coated side of the coverslip sandwich. A growing aster edge was imaged at 20 min of aster assembly reaction at 20°C. A TIRF microscope with a 60x TIRF objective (NA = 1.49) was used to acquire a two-color time-lapse sequence with 2.1 sec intervals (Figure S2.8A).

We observed that at the edges of expanding asters, Kif4A loaded onto antiparallel microtubule overlaps that transiently formed between radially outwards growing microtubules and isolated microtubules that grew in the opposite direction (Figure S2.8A). These antiparallel overlaps recruited PRC1E, the binding partner of Kif4A that preferentially crosslinks antiparallel microtubules, but not the CPC. Kymographs along microtubules that formed these overlaps allowed us to visualize Kif4A movement in the absence of recruited CPC (Figure S2.8B). After correcting for microtubule sliding from tubulin images, we obtained a mean velocity of 26.4±4.1 μm/min (mean±SD) from *n* = 34 tracked Kif4A particles (Figure S2.8C). This was the maximal Kif4A velocity we observed in our extract system on interphase asters, as within AAIZs Kif4A slowed down. The reason we observe Kif4A movement in situ at ~half the velocity of that seen

with pure protein is unclear (Bieling et al., 2010). One possibility is that other microtubule-associated proteins (MAPs) bound to microtubules slowed movement.

Co-localization of Moving Kif4A and Moving CPC (see Figure S2.10)

Extract was supplemented with 250nM Alexa568-tubulin, 0.1µg/mL Alexa674-IgG against AurkB, and 3nM Kif4A-GFP. Asters were assembled between a PEG-passivated glass coverslip and a partially passivated coverslip coated with kappa-casein. AAIZs were imaged at 50 min of aster assembly reaction at 20°C. A TIRF microscope with a 60x TIRF objective (NA = 1.49) with an additional magnification using a 1.5 optovar was used to acquire a two-color time-lapse sequence with 2.73 sec intervals. Kymographs along antiparallel microtubules bundles were created as described above (Figure S2.10).

Tubulin Speckle Imaging (see Figure S2.7)

Asters were assembled between two PEG-passivated glass coverslips, and AAIZs were imaged with either a 100X oil objective with 2x2 binning on a widefield microscope (Figure S2.7A) or a 60X oil objective with 2x2 binning on a spinning disc confocal microscope (Figure S2.7B). Extract was supplemented with 250nM X-rhodamine-tubulin and 40nM EB1-GFP for the widefield sample, and 1nM Alexa647-tubulin for the confocal sample. Kymographs along the microtubule bundles were created as described above.

TIRF Image Background Correction and Stitching

(related to Figure 2.7, B and C, Figures 2.8A and S2.11)

The *Scan Large Image* function of the NIS Elements image acquisition software was used to acquire 5x5 to 7x7 adjacent areas with 15% overlap. We refer to the small image captured of one area as a 'tile.' To correct for the dark grid in the large stitched image due to uneven illumination across the image area, a median image was obtained from all individual

tiles and normalized to the range 0-1 to obtain a correction image. All individual tiles were then divided by the correction image. The background corrected tiles were stitched into a large image using the *Grid/Collection stitching* ImageJ plugin. Regions of interest were cropped for display. All image processing was done in ImageJ.

3D Reconstructions of Z Stacks (related to Figure 2.8C)

Confocal Z stack images of asters assembled on top of a supported lipid bilayer were obtained using an inverted spinning disc microscope with a 60x objective (1.49 NA): 80 z-sections were acquired at 0.25-μm intervals. 3D reconstruction was performed with *Volume Viewer* ImageJ plugin.

Immunofluorescence of Fixed *Xenopus* Zygotes (see Figures 2.3 and 2.5)

Embryos were fixed and stained as previously described (Becker and Gard, 2006; Wühr et al., 2010). Briefly, embryos were fixed in 50mM EGTA, pH 6.8, 10% H_2O, 90% methanol for 24 hrs at room temperature with gentle shaking. Prior to staining, embryos were rehydrated in a series of steps—25%, 50% 75%, 100% TBS (50 mM Tris, pH 7.5, 150 mM NaCl) /Methanol—and then hemisected in TBS on an agarose cushion using a small piece of razor blade. Embryos were bleached overnight in a solution of 1% H_2O_2, 5% formamide, 0.5x SSC (75mM NaCl and 8mM sodium citrate, pH 7). Embryos were incubated with directly labeled antibodies for at least 24 hrs at 4° C with very gentle shaking. Antibodies were diluted into TBSN (10mM Tris-HCl, pH 7.4, 155mM NaCl, 0.1% Igepal CA-630) + 1% BSA + 2% FCS + 0.1% Azide. After antibody incubation, embryos were washed in TBSN for at least 48 hrs (with several buffer changes), then washed 1X in TBS and 2X in methanol for 20 min each. Embryos were cleared in Murray Clear solution (benzyl benzoate, part benzyl alcohol 2:1) and mounted in metal slides (1.2mm thick) with a hole in the center. The hole was closed on the bottom with a Parafilm-attached coverslip.

Directly labeled antibodies were used at approximately the following concentrations: Alexa488-tubulin (1-2µg/mL), Alexa647-AurB kinase (0.5µg/mL), Alexa568-Kif23 (1-2µg/mL), Alexa568-anillin (1-2µg/mL).

Aurora Kinase B Inhibition in *Xenopus* Zygotes (see Figure 2.5)

Eggs were fertilized, dejellyed with 2% cysteine in MMR (110mM NaCl, 2mM KCl, 1mM $MgCl_2$, 2mM $CaCl_2$, 2mM $NaHCO_3$, 5mM K-Hepes, pH 7.8), and microinjected with ZM447439 (Aurora B kinase inhibitor) before or after metaphase of 1st mitosis (either 50-55 or 75-80 minutes post fertilization). For injections, eggs were placed in Petri dishes, with mesh attached to the bottom, containing 5% Ficoll in 0.1X MMR. Eggs were injected with calibrated needles using an air-pressure microinjector (Narishige). Needles (~1.2mm initial diameter) were pulled with a Micropipette Puller (Sutter Instrument Company) and calibrated to inject 10nL of sample (Sive et al., 2010a). Briefly, the tips of needles were broken with a pair of forceps under a dissection microscope and the time of the injection pulse was varied until the desired injection volume was reached (Sive et al., 2010b). ZM447439 (10mM) was dissolved in 10mM glycine (pH 7); control buffer injections were done with 10mM glycine (pH 7).

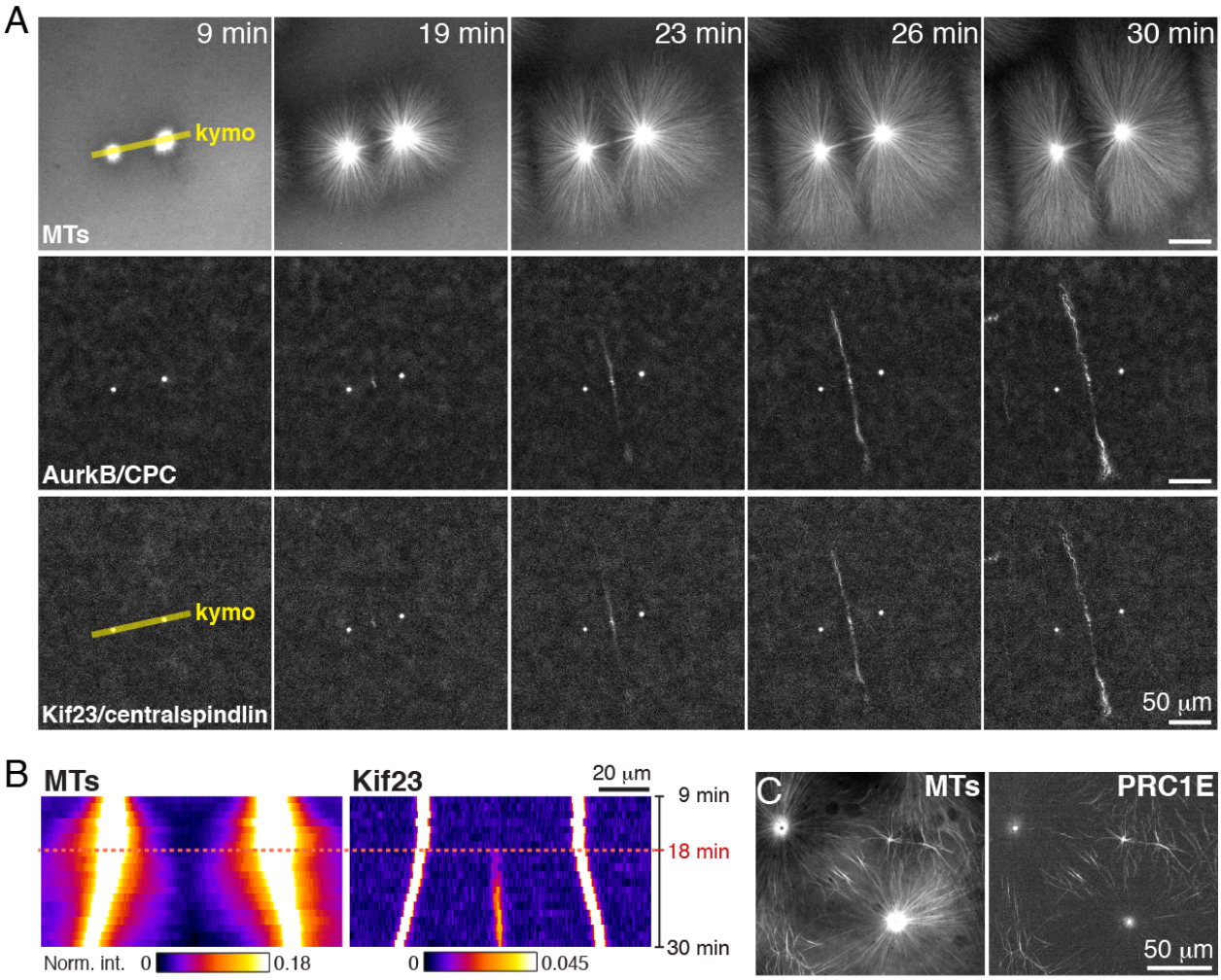

Figure S2.1: Related to Figure 2.2. Aster outgrowth and interaction reconstituted in cell-free *Xenopus* egg cytoplasm.

(A) Widefield time-lapse sequence showing recruitment of AurkB (CPC subunit) and Kif23 (Centralspindlin subunit) to an aster-aster interaction zone (AAIZ).

(B) Kymographs along the bead-bead axis (yellow lines in **(A)**) showing aster growth and interaction (MTs, left) and recruitment of Kif23 where asters interact (right, from 18 min). Similar profiles were obtained for AurkB recruitment.

(C) Spinning disc confocal image of AAIZs at 30min with the embryonic paralog of PRC1 localized (GFP-PRC1E).

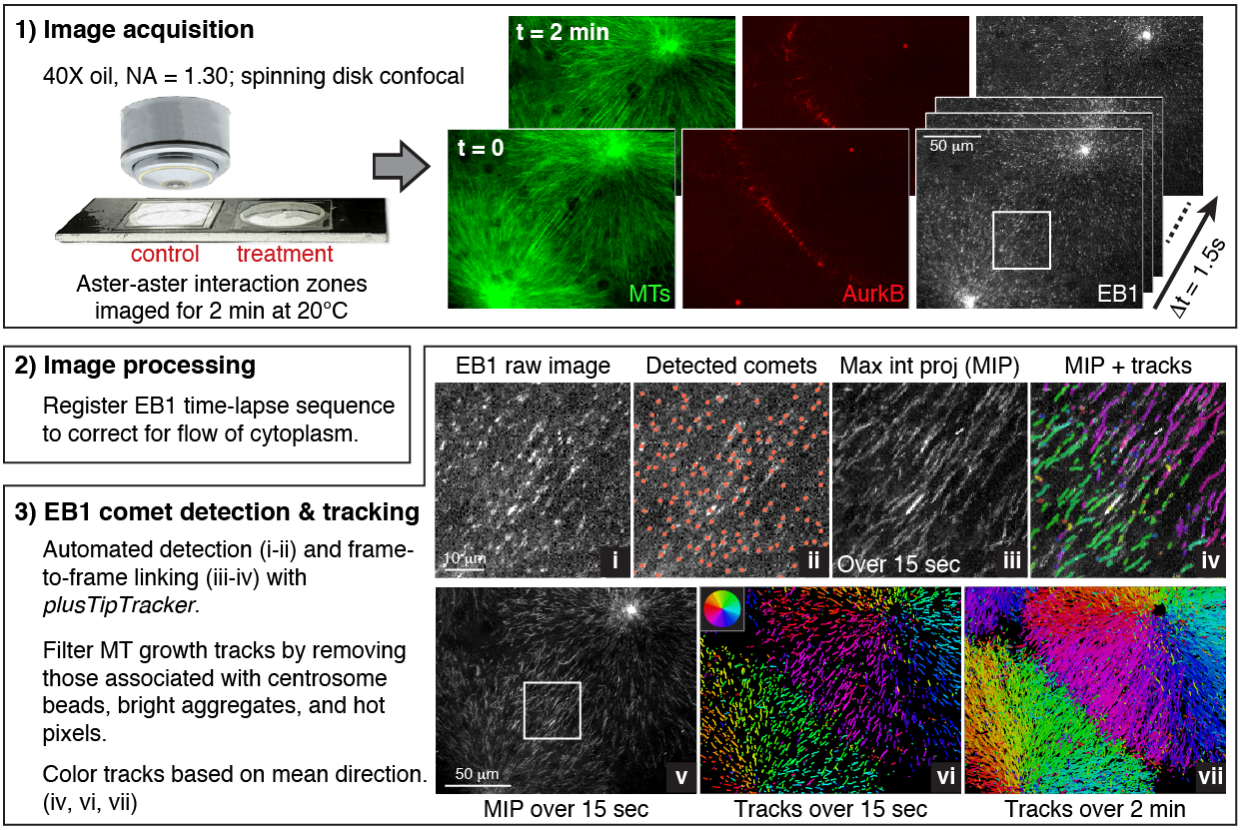

Figure S2.2: Related to Figure 2.4A. Microtubule plus tip tracking using EB1-GFP protein.

(1) Asters were assembled between PEG-passivated coverslips, simultaneously for control and treatment samples (e.g. AurkB inhibition). Multiple AAIZs were imaged between 20 and 50 min of the assembly reaction, alternating between control and treatment conditions, using a spinning disc confocal microscope with a 40x oil objective. Time-lapse sequences were acquired of EB1-GFP with 1.5 sec intervals for a total duration of 2 min. Images of tubulin and AurkB were acquired at the beginning and end of each sequence.

(2) Flow of cytoplasm was corrected by registering EB1 image sequences using the *StackReg* ImageJ plugin.

(3) The *plusTipTracker* Matlab software was used to perform automated detection and frame-to-frame linking of EB1 to obtain growth tracks (see Table S2.2 for parameters) (Applegate et al., 2011; Matov et al., 2010). False tracks associated with bright centrosome beads, protein aggregates, and hot pixels in the camera were removed. Tracks were plotted and colored according to their mean direction. Top row images are zoomed up views of area marked by white square in EB1 image in **Step 1**. See Methods section "Microtubule Plus Tip Tracking: Image Acquisition, Processing and Analysis" for more detailed description.

(analysis continued from MT plus tip tracking, Figure S2.2)

4) Interpenetration analysis for a single aster-aster interaction zone (AAIZ)

a. Divide comets (summed over 2 min) into two populations based on direction.
b. Divide space into binned rectangular ROIs perpendicular to interaction zone.
c. Determine population fractions. (Example data for ROI6)

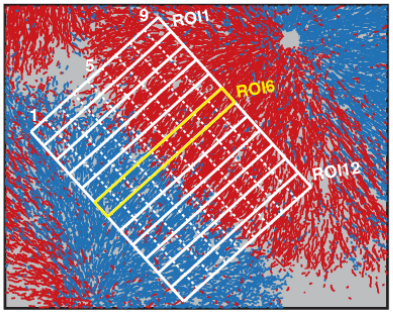

Bin No.	Number of EB1 comets			
	Total	Blue	Red	% Blue
1	265	240	25	90.6
2	279	250	29	89.6
3	308	278	30	90.3
4	351	281	70	80.1
5	282	41	241	14.5
6	268	10	258	3.7
7	255	30	225	11.8
8	265	22	243	8.3
9	301	6	295	2.0

d. Plot population fractions over distance for all ROIs.
e. Remove outlier ROIs (1 & 2).

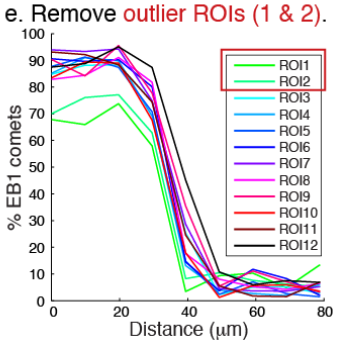

5) Interpenetration analysis for multiple AAIZs

Control (n = 52 ROIs from 6 zones) **AurkB inhibition** (n = 55 ROIs from 5 zones)

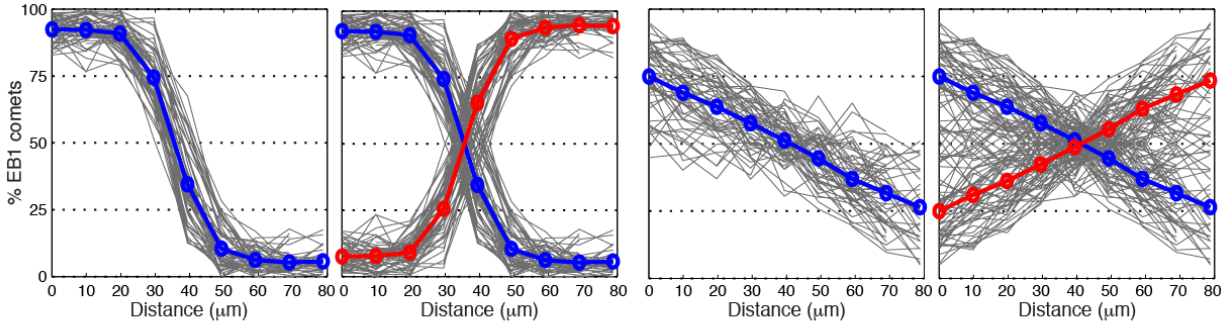

Gray lines -- population fraction data associated with each ROI.
Blue line -- mean fraction of "blue" comets.
Red line -- mean fraction of "red" comets, corresponding to (1 - Blue Fraction).

Same data are displayed in Figure 1F with standard deviation represented by shaded area.

Figure S2.3: Related to Figure 2.4AB Aster-aster interpenetration analysis based on tracked microtubule plus ends.

See Methods section "Aster-Aster Interpenetration Analysis" for description.

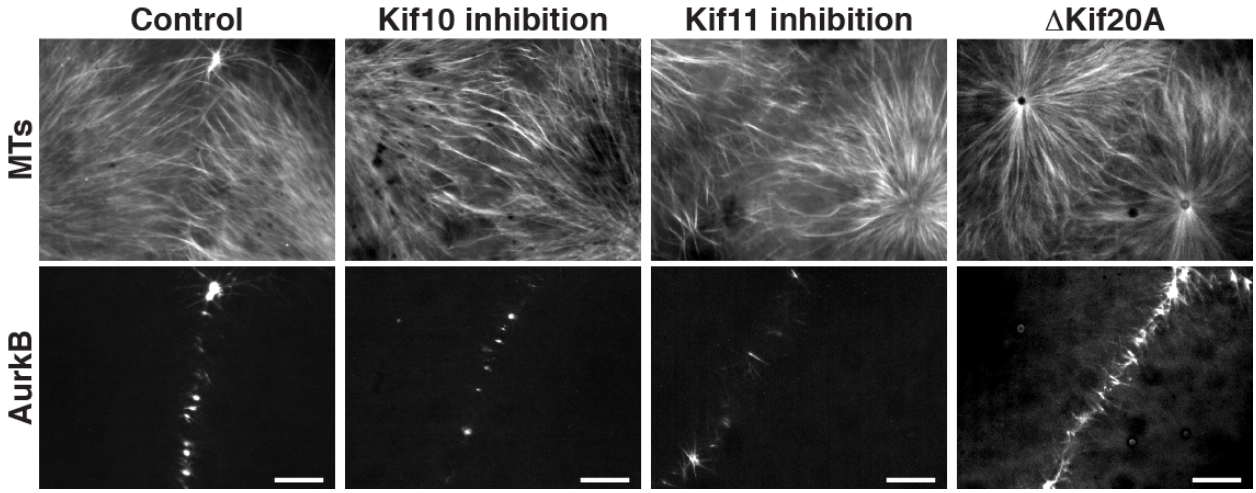

Figure S2.4: Related to Figure 2.6, A and B. Small molecule inhibition and immunodepletion of kinesin candidates that had no effect on AAIZ formation and CPC localization.

Asters were assembled between PEG-passivated coverslips, and AAIZs were imaged after 30 min. Representative spinning disc confocal images of MTs and AurkB at AAIZs after treatment with DMSO control, 100μM GSK-923295 (a Kif10/CenpE inhibitor; experiments with mitotic spindles in egg extracts and *Xenopus* tissue culture cells confirmed expected activity of this compound, i.e. displacement of mitotic chromosomes from the metaphase plate (Gudimchuk et al., 2013)), 100μM STLC (S-trityl-l-cysteine, a Kif11/Eg5 inhibitor (Groen et al., 2008)), or depletion of the somatic Kif20A motor, as labeled above. Representative control depletion with random IgG is shown in Figure 2.6A. Scale bar, 20 μm.

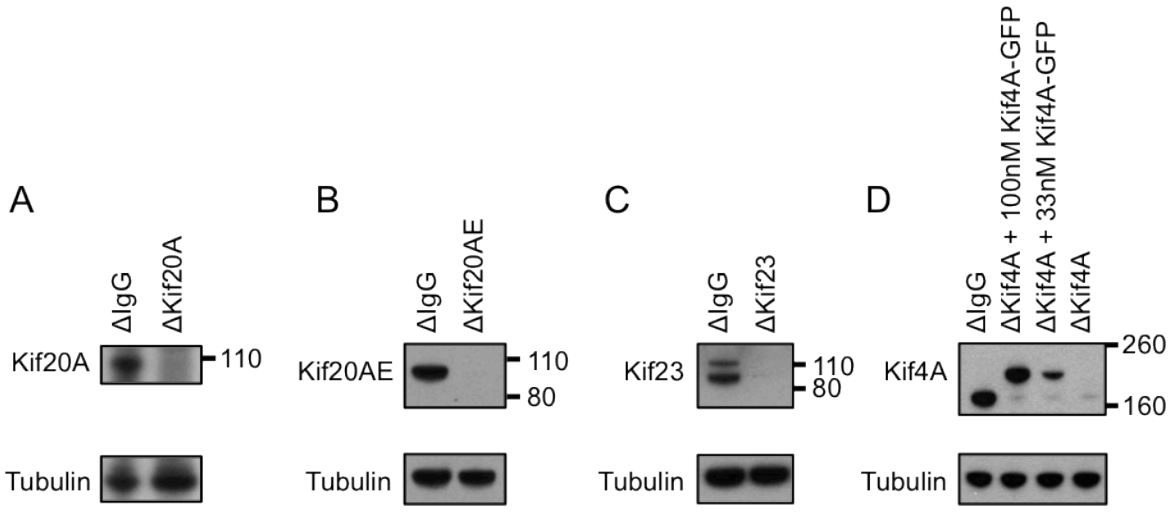

Figure S2.5: Related to Figure 2.6, A and B. Immunoblots showing immunodepletion of *Xenopus laevis* kinesin candidates.

(A) Kif20A (Mklp2 or Rabkinesin-6, ~101 kD).

(B) Kif20AE (~88 kD), an embryonic paralog of Kif20A in *Xenopus*.

(C) Kif23 (Mklp1, a subunit of Centralspindlin complex, ~90 kD).

(D) Kif4A (~139 kD) depletion was rescued by adding back 100nM recombinant Kif4A-GFP (~168 kD).

Figure S2.6: Related to Figure 2.6F. Measuring velocity of directed CPC movement on the antiparallel microtubule overlaps at the aster-aster interaction zones (AAIZs).

(**A**) Spinning disc confocal image of CPC visualized with Alexa647-labeled antibody against AurkB at an AAIZ at the beginning of a time-lapse sequence *(top)*. Segmented lines for kymographs are overlaid in yellow *(bottom)*.

(**B**) Kymographs generated from the time-lapse (total duration of 170 sec with 1.43 sec intervals) corresponding to lines (a-e) in (A).

(**C**) Procedure for obtaining CPC velocity as a function of distance from the CPC bright midpoint. See Methods section "Velocity Measurements for CPC Movement" for more detailed description.

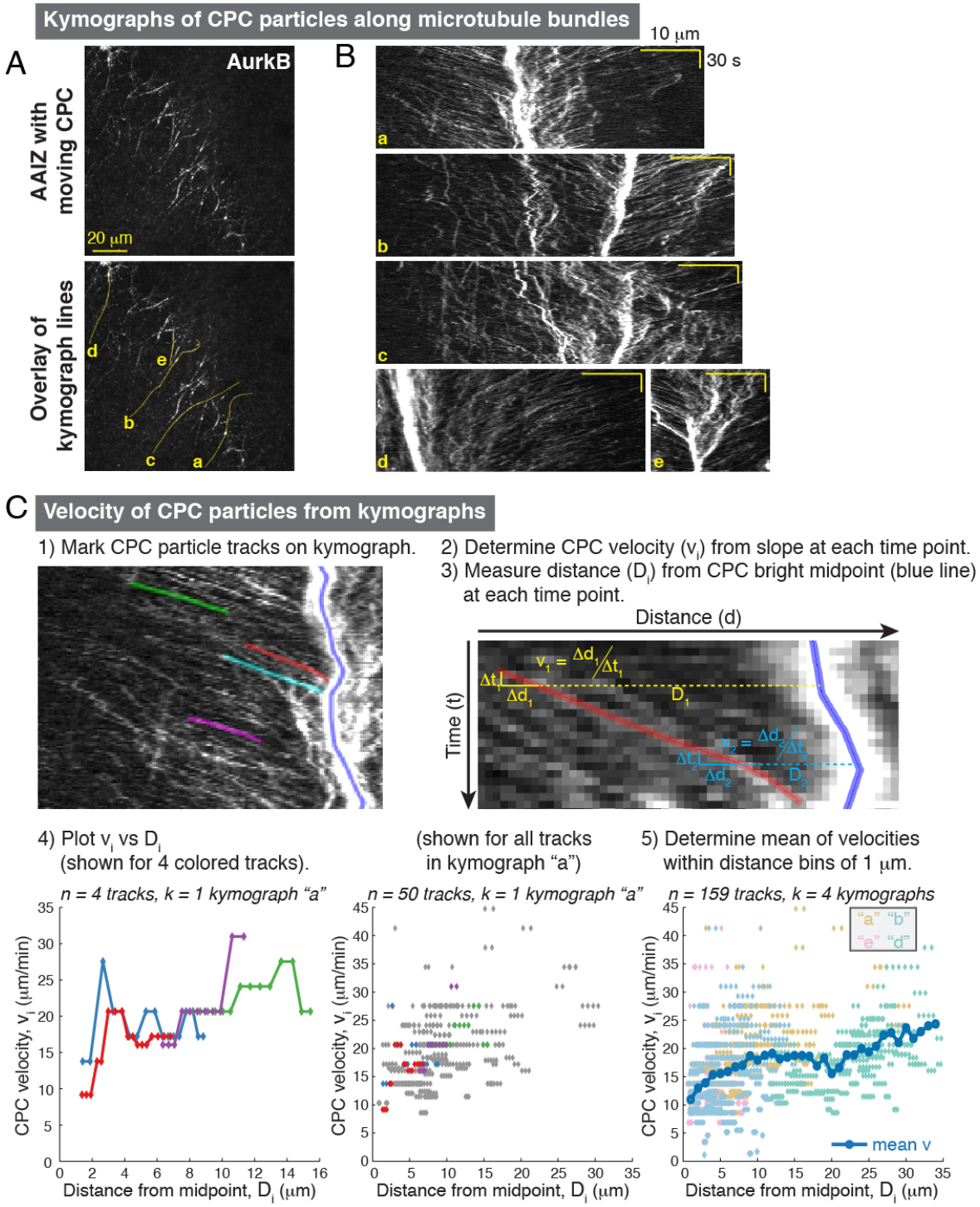

Figure S2.6 (Continued)

Figure S2.7: Tubulin speckle imaging shows antiparallel microtubules sliding outward from overlap center.

(A) Tubulin speckles were formed by uneven incorporation of the relatively hydrophobic X-rhodamine-tubulin into microtubules. The movement of these X-rhodamine tubulin clusters was imaged with time-lapse widefield microscopy at 5 sec intervals (Movie S2.6).

(B) Tubulin speckles were formed by single-molecule level incorporation of Alexa647-tubulin into microtubules. Time-lapse spinning disc confocal images were taken at 4 sec intervals (Movie S2.8).

(C) CPC clusters were visualized using Alexa647-IgG against AurkB and imaged with time-lapse spinning disc confocal microscopy at 1.3 sec intervals (same data as shown in Figure S2.6A, Movie S2.4).

(A-C) Still images from each time-lapse sequence *(top)*. Kymographs along the MT overlap bundles indicated by yellow arrow *(bottom)*. Horizontal scale bars, 20 μm. Vertical scale bars, 1 min. Kymographs show that while microtubules slide slowly outwards from the overlap centers at <5 μm/min, CPC clusters move inwards at 10-25 μm/min towards overlap center. This confirms that the fast inwards movement of the CPC is indeed motor-driven transport along microtubules.

(D) Overlay of EB1-GFP image (magenta) on tubulin image (green) shown in (A); a still image from Movie S2.7 *(left)*. Maximum intensity projection of EB1 images *(middle),* and EB1 tracks colored by their mean direction *(right)* over the first half (2.5 min) of Movie S2.7. Movie S2.7 illustrates the relationship between microtubule plus end growth (i.e. EB1 comet movement) and formation of antiparallel bundles. Horizontal scale bars, 20 μm.

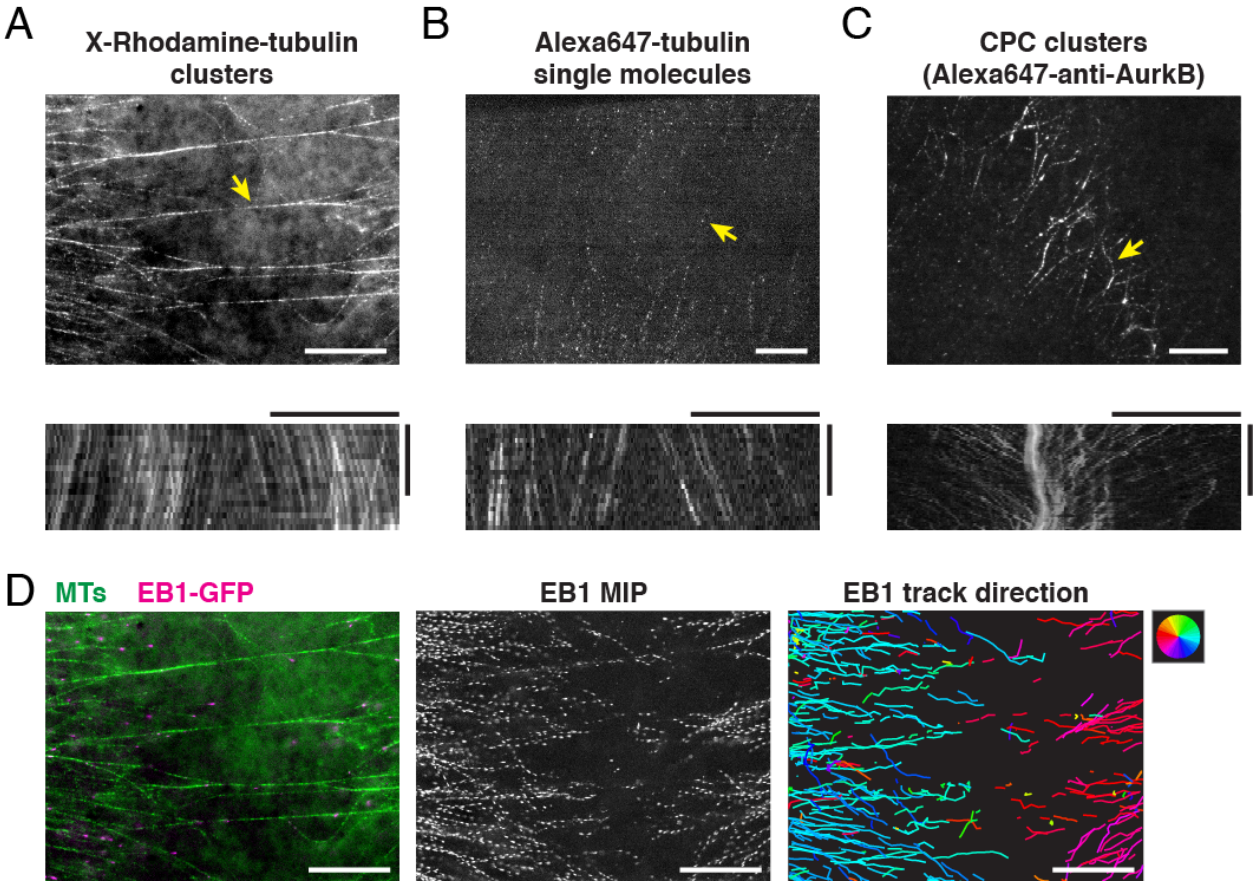

Figure S2.7 (Continued)

Figure S2.8: Related to Figure 2.6F (green line). Measuring the plus-end directed velocity of the kinesin Kif4A.

(A) Expanding aster partially adhered to κ-casein coated coverslip with microtubules (Alexa647-tubulin; red) and Kif4A-GFP (green) visualized. TIRF image from a time-lapse sequence acquired using 2.1sec intervals for a total duration of 7.3min.

(B) Kymographs of a microtubules (red) and Kif4A (green) along a microtubule that had a free plus end but was also part of an anti-parallel overlap (box in A). Scheme *(right)* shows the geometry of microtubules (red lines) before and after the time-lapse (top and bottom panels, respectively), and the inferred plus ends of the anti-parallel microtubules (yellow and blue solid lines); an antiparallel overlap is formed between the solid and dashed yellow lines. Apparent Kif4A velocity (measured from Kif4A kymographs) was corrected by velocity of microtubule sliding (measured from microtubule kymographs).

(C) The velocity distribution of Kif4A moving on microtubules that are not part of AAIZs. Kif4A has a mean velocity of 26.4 ± 4.1 μm/min (mean±SD, n = 34 tracked Kif4A particles), an estimate for maximum velocity in our extract system.

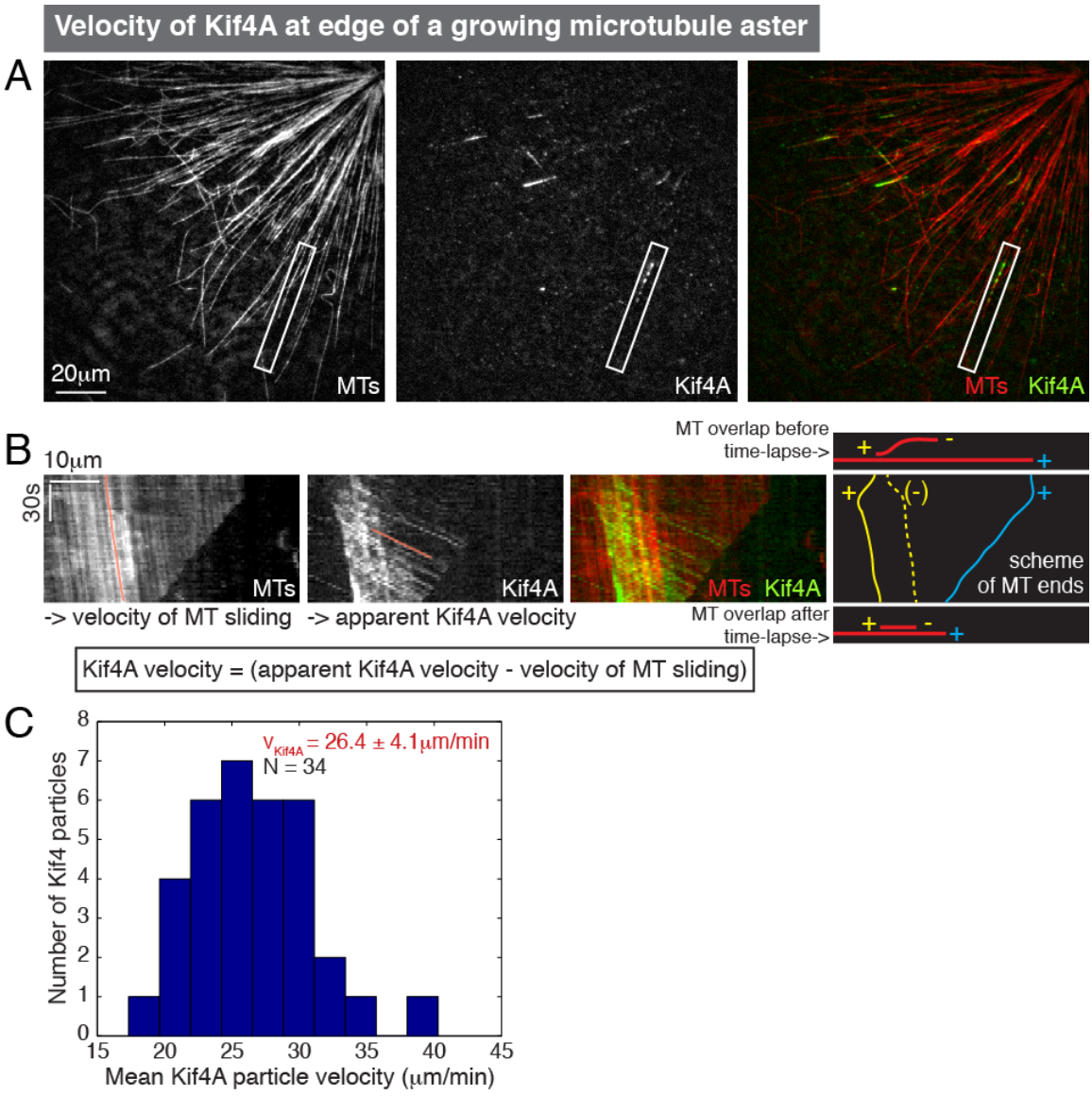

Figure S2.8 (Continued)

Figure S2.9: Related to Figure 2.6, E and F. Directed CPC movement on antiparallel microtubule bundles requires the kinesin Kif4A.

Same analysis of CPC movement as described in Figure S2.6 was performed on extracts where Kif4A was depleted (**A** to **C**) and where Kif4A depletion was followed by addback of purified Kif4A-GFP (**D** to **F**).

(**A**,**D**) Spinning disc confocal image of CPC visualized with Alexa647-labeled antibody against AurkB at an AAIZ at the beginning of a time-lapse sequence *(top)*. Segmented lines for kymographs are overlaid in yellow *(bottom)*.

(**B**,**E**) Kymographs generated from the time-lapse: total duration of 90 sec with 1.29 sec intervals for (**B**) and total duration of 177 sec with 3.94 sec intervals for (**E**).

(**C**,**F**) Instantaneous CPC velocities (v_i) plotted against distance from bright CPC midpoint (D_i) determined from 3 kymographs, with the mean velocity calculated for each 1 μm distance bin.

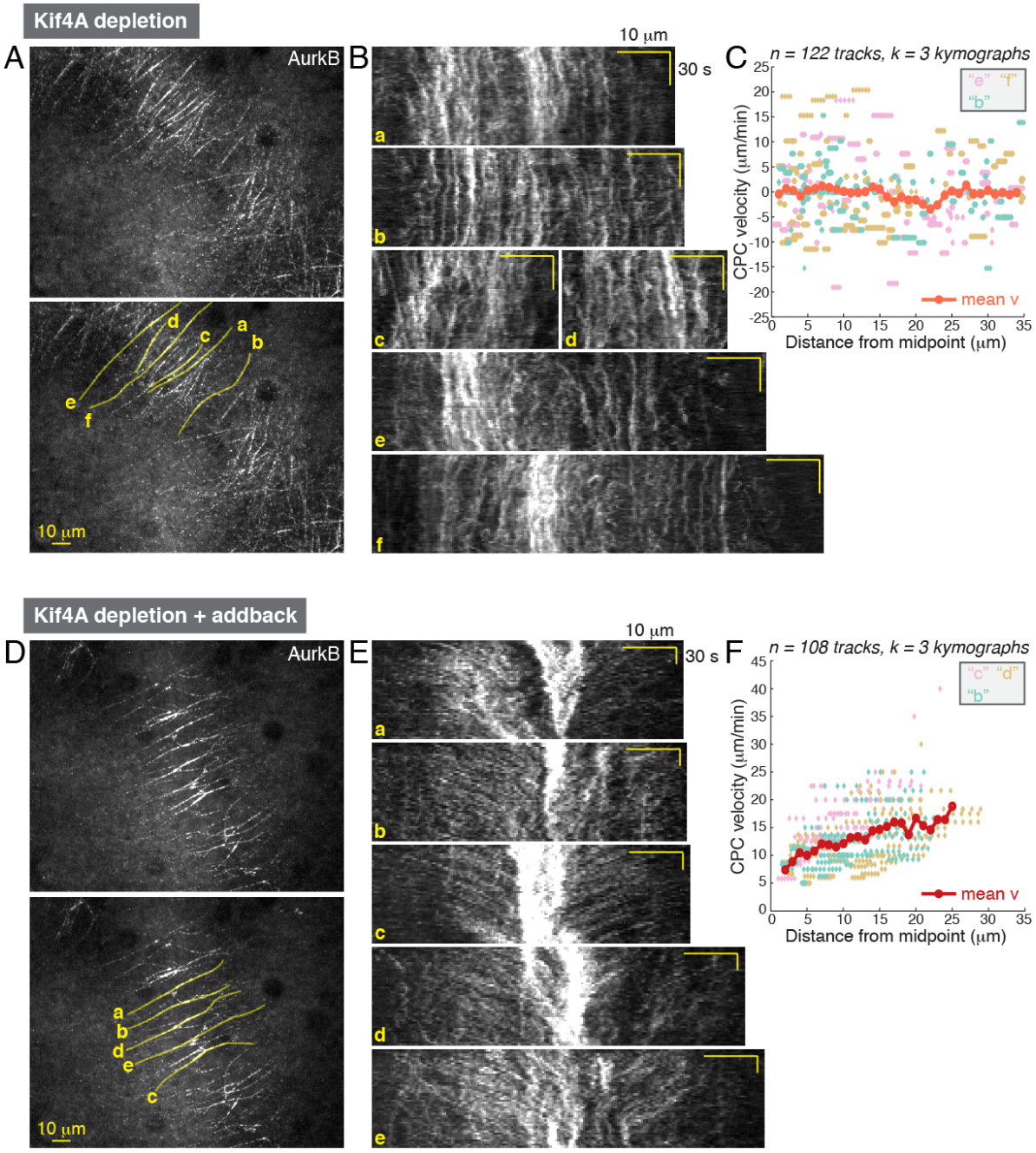

Figure S2.9 (Continued)

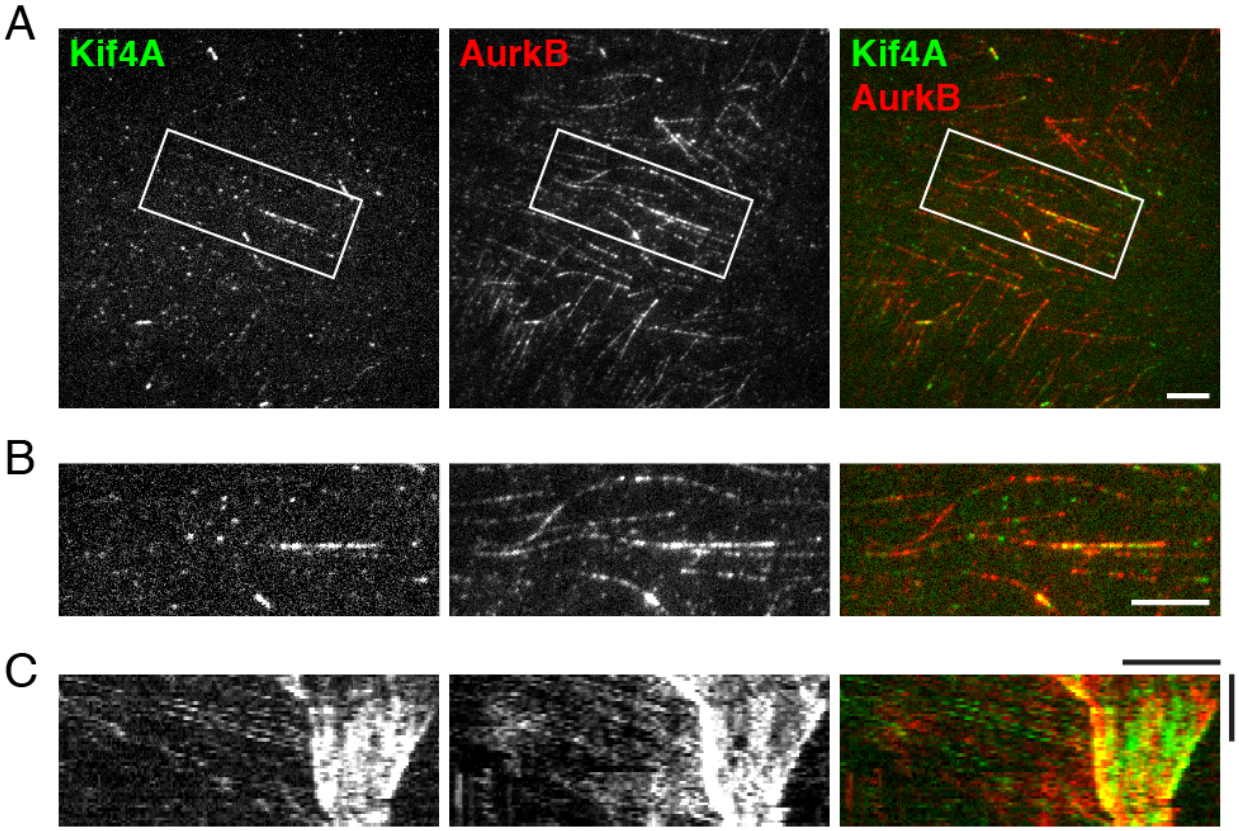

Figure S2.10: Partial co-localization of moving Kif4A and moving CPC clusters at AAIZ.
(**A**) Stills from a time-lapse, two-color TIRF image sequence taken with a 2.73 sec time interval, and a time delay of ~1.36 sec between acquisition in the two channels. Kif4A-GFP was added at 3nM on top of endogenous Kif4A present in extract (left, green). Alexa647-anti-AurkB was added at 0.1µg/mL to probe for endogenous CPC (middle, red). The right shows a merged image. (**B**) 2x zoom-up of rectangle in (**A**) highlighting an antiparallel microtubule overlap and partial co-localization of the two probes.
(**C**) Kymographs along the antiparallel MT overlap shown in (**B**). Note that the two probes move inwards at very similar rates (visualized as parallel lines in the kymographs). The fast-moving clusters localized at the outside of the AAIZ were moving inwards at ~25 µm/min in this example. We noted more co-localization between Kif4A-GFP and CPC clusters in static and slow moving clusters near the center. In fast moving clusters, the lines of Kif4A and CPC were staggered, presumably due to the time delay between acquisition in the green and red channels. Horizontal scale bars, 10 µm. Vertical scale bars, 1 min.

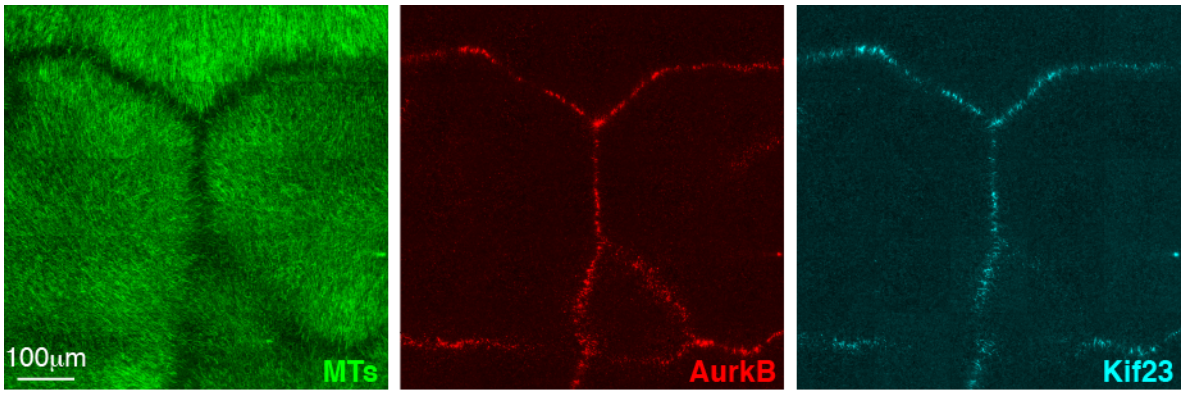

Figure S2.11: Related to Figure 2.7B. The CPC and Centralspindlin complexes co-localize at AAIZs on model plasma membranes. Experimental setup as per Figure 2.7A. TIRF images from 5 × 5 adjacent fields were corrected for uneven illumination and stitched (see Methods). Microtubules (MTs, *green*), CPC (AurkB, *red*), Centralspindlin (Kif23, *cyan*).

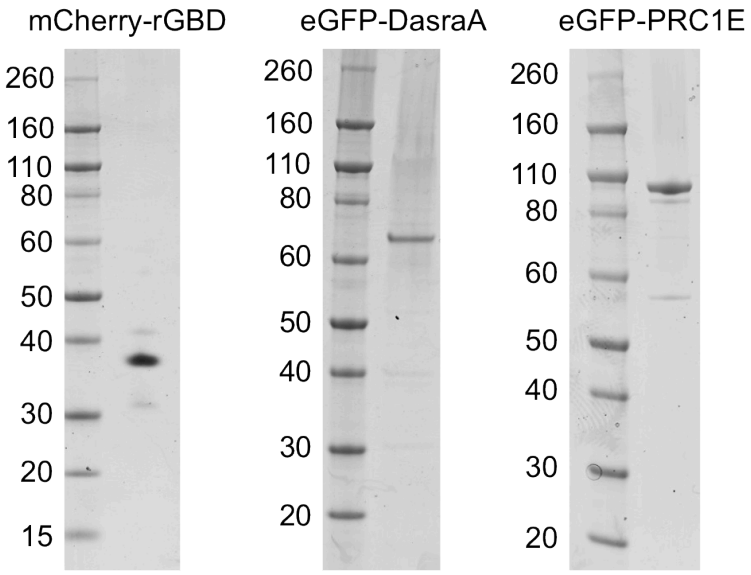

Figure S2.12: Coomassie-stained SDS gels of purified proteins with cloning and purification methods established in this study. Theoretical molecular weights of the protein constructs are: 39 kD (mCherry-rGBD), 61 kD (eGFP-DasraA), and 96 kD (eGFP-PRC1E).

Table S2.1: List of *Xenopus laevis* protein sequences studied in Chapter Two.

Name	**Description/Alternate names**	**NCBI GI number**
AurkA	Aurora kinase A	148236543
AurkB	Aurora kinase B	147899288
DasraA	Borealin-2	148232132
PRC1E	Embryonic paralog of PRC1 (42% identity by sequence)	148231955
Kif4A	Chromokinesin, Xklp1	18202613
Kif20A	Mklp2, Rabkinesin-6	147902220
Kif20AE	Embryonic paralog of Kif20A (41% identity by sequence)	169642006 (starting at "MDSRN")
Kif23	Mklp1, CHO1	148222381

Table S2.2: Parameters for automated detection and tracking of EB1 comets using *plusTipTracker* (Applegate et al., 2011; Matov et al., 2010).

Image sequence calibrations	
Pixel size	0.3284 µm
Frame rate	1.5 s

Detection parameters	
Method	Watershed-based
Sigma 1	1
Sigma 2	7
K	1-2.5

Tracking parameters	
Maximum gap length	2 frames
Minimum sub-track length	3 frames
Minimum search radius	1 pixel
Maximum search radius	3 pixels
Maximum forward angle	30°
Minimum forward angle	10°
Fluctuation radius	1 pixel
Maximum shrinkage factor	1

Supplemental Movie Captions

Movie S2.1: Aster outgrowth and interaction in *Xenopus* egg cytoplasm (related to Figures 2.2B and S2.1A). Asters were nucleated from beads coated with Aurora A kinase antibody on PEG-passivated coverslips. Where neighboring asters met, an aster-aster interaction zone (AAIZ) formed that recruited the chromosomal passenger complex (CPC). Widefield time-lapse sequence was acquired starting at 9 min of aster assembly reaction using a 20X objective, with 1 min intervals. Microtubules (green), CPC (Aurora B kinase subunit, red). Field of view: 277μm x 277μm. Duration: 21 min (420x speed).

Movie S2.2: Block to microtubule interpenetration at an AAIZ (related to Figure 2.4A, top panel, and Figure S2.2). Growth of microtubule plus ends was visualized with EB1-GFP at an AAIZ on PEG-passivated coverslips. Aster #1 at top right corner, aster #2 at bottom left corner, aster #3 at top left corner. Confocal time-lapse sequence was acquired starting at 20 minutes of aster assembly reaction using a 40X oil objective, with 1.5 sec intervals. Field of view: 198μm x 157μm. Duration: 2 min (24x speed).

Movie S2.3: Block to microtubule interpenetration requires Aurora B kinase (related to Figure 2.4A, bottom panel). Growth of microtubule plus ends was visualized with EB1-GFP at an AAIZ in the presence of Aurora B kinase inhibitor (ZM447439) on PEG-passivated coverslips. Aster #1 on the left, aster #2 on the right. Confocal time-lapse sequence was acquired starting at 20 minutes of aster assembly reaction using a 40X oil objective, with 1.5 sec intervals. Field of view: 193μm x 157μm. Duration: 2 min (24x speed).

Movie S2.4: Directed CPC movement on antiparallel microtubule bundles at an AAIZ (related to Figures 2.6E and S2.6). CPC recruitment and movement at the AAIZ was visualized using Aurora B kinase antibody on PEG-passivated coverslips. Aster #1 at top right corner, aster #2 at bottom left corner. Confocal time-lapse sequence was acquired starting at 50 minutes of aster assembly reaction using a 40X oil objective, with 1.44 sec intervals. Field of view: 122μm x 122μm. Duration: 1.5 min (24x speed).

Movie S2.5: Directed CPC motility at an AAIZ requires Kif4A (related to Figure 2.6E and Figure S2.9, A to C). CPC recruitment and movement at the AAIZ in Kif4A depleted cytoplasm was visualized using Aurora B kinase antibody on PEG-passivated coverslips. Aster #1 at top right corner, aster #2 at bottom left corner. Confocal time-lapse sequence was acquired starting at 50 minutes of aster assembly reaction using a 40X oil objective, with 1.31 sec intervals. Field of view: 122μm x 122μm. Duration: 1.5 min (24x speed).

Movie S2.6: Antiparallel sliding of microtubules at AAIZ (widefield) (related to Figure S2.7A). Microtubule sliding was visualized using clusters of unevenly incorporated X-rhodamine-tubulin on PEG-passivated coverslips. Aster #1 on the left, aster #2 on the right. Widefield time-lapse sequence was acquired starting at 50 minutes of aster assembly reaction using a 100X oil objective, with 5 sec intervals. Note slow outwards sliding of microtubules away from center of antiparallel overlap. Field of view: 87.0μm x 66.3μm. Duration: 5 min (40x speed).

Movie S2.7: Antiparallel sliding and plus end growth of microtubules at AAIZ (widefield) (related to Figure S2.7D). Same image sequence as shown in movie S6, but with the EB1 channel added to visualize growing microtubule plus ends. Note the transition from parallel bundles in each aster to antiparallel bundles in the AAIZ. Some EB1 comets entered the antiparallel bundles where they disappeared after tracking along them for a few frames; other EB1 comets disappeared outside of a bundle. X-rhodamine-tubulin (green), EB1-GFP (magenta). Field of view: 87.0μm x 66.3μm. Duration: 5 min (40x speed).

Movie S2.8: Antiparallel sliding of microtubules at AAIZ (confocal) (related to Figure S2.7B). Microtubule sliding was visualized using speckle-level of Alexa647-tubulin on PEG-passivated coverslips. Aster #1 at the top, aster #2 at the bottom. Confocal time-lapse sequence was acquired starting at 50 minutes of aster assembly reaction using a 60X oil objective, with 4 sec intervals. Field of view: 138μm x 105μm. Duration: 5.5 min (60x speed).

Movie S2.9: Organization of F-actin at an AAIZ on a model membrane (related to Figure 2.8D, bottom middle panel). F-actin was visualized using Lifeact-GFP on lipid bilayer-coated coverslip. TIRF time-lapse sequence was acquired starting at 50 minutes of aster assembly reaction using a 60X TIRF objective, with 3 sec intervals. Field of view: 136μm x 136μm. Duration: 4 min (120x speed).

Movie S2.10: Organization of anillin at an AAIZ on a model membrane (related to Figure 2.8E, middle panel). Anillin was visualized using directly labeled antibody on lipid bilayer-coated coverslip. TIRF time-lapse sequence was acquired starting at 50 minutes of aster assembly reaction using a 60X TIRF objective, with 3 sec intervals. Field of view: 136µm x 136µm. Duration: 4 min (120x speed).

References

Applegate, K.T., Besson, S., Matov, A., Bagonis, M.H., Jaqaman, K., and Danuser, G. (2011). plusTipTracker: Quantitative image analysis software for the measurement of microtubule dynamics. J Struct Biol *176*, 168–184.

Becker, B.E., and Gard, D.L. (2006). Visualization of the cytoskeleton in Xenopus oocytes and eggs by confocal immunofluorescence microscopy. Methods Mol Biol *322*, 69–86.

Bement, W.M., Benink, H.A., and von Dassow, G. (2005). A microtubule-dependent zone of active RhoA during cleavage plane specification. J Cell Biol *170*, 91–101.

Benink, H.A., and Bement, W.M. (2005). Concentric zones of active RhoA and Cdc42 around single cell wounds. J Cell Biol *168*, 429–439.

Bieling, P., Telley, I.A., and Surrey, T. (2010). A Minimal Midzone Protein Module Controls Formation and Length of Antiparallel Microtubule Overlaps. Cell *142*, 420–432.

Field, C.M., Nguyen, P.A., Ishihara, K., Groen, A.C., and Mitchison, T.J. (2014). Xenopus egg cytoplasm with intact actin. Meth Enzymol *540*, 399–415.

Groen, A.C., Needleman, D., Brangwynne, C., Gradinaru, C., Fowler, B., Mazitschek, R., and Mitchison, T.J. (2008). A novel small-molecule inhibitor reveals a possible role of kinesin-5 in anastral spindle-pole assembly. J Cell Sci *121*, 2293–2300.

Groen, A.C., Nguyen, P.A., Field, C.M., Ishihara, K., and Mitchison, T.J. (2014). Glycogen-supplemented mitotic cytosol for analyzing Xenopus egg microtubule organization. Meth Enzymol *540*, 417–433.

Gudimchuk, N., Vitre, B., Kim, Y., Kiyatkin, A., Cleveland, D.W., Ataullakhanov, F.I., and Grishchuk, E.L. (2013). Kinetochore kinesin CENP-E is a processive bi-directional tracker of dynamic microtubule tips. Nat Cell Biol *15*, 1079–1088.

Lee, K., Gallop, J.L., Rambani, K., and Kirschner, M.W. (2010). Self-assembly of filopodia-like structures on supported lipid bilayers. Science *329*, 1341–1345.

Loose, M., and Schwille, P. (2009). Biomimetic membrane systems to study cellular organization. J Struct Biol *168*, 143–151.

Loose, M., Fischer-Friedrich, E., Ries, J., Kruse, K., and Schwille, P. (2008). Spatial regulators for bacterial cell division self-organize into surface waves in vitro. Science *320*, 789–792.

Matov, A., Applegate, K., Kumar, P., Thoma, C., Krek, W., Danuser, G., and Wittmann, T. (2010). Analysis of microtubule dynamic instability using a plus-end growth marker. Nat Methods.

Mitchison, T.J., Nguyen, P., Coughlin, M., and Groen, A.C. (2013). Self-organization of stabilized microtubules by both spindle and midzone mechanisms in Xenopus egg cytosol. Mol Biol Cell *24*, 1559–1573.

Oegema, K., Savoian, M.S., Mitchison, T.J., and Field, C.M. (2000). Functional analysis of a human homologue of the Drosophila actin binding protein anillin suggests a role in cytokinesis. J Cell Biol *150*, 539–552.

Petry, S., Groen, A.C., Ishihara, K., Mitchison, T.J., and Vale, R.D. (2013). Branching microtubule nucleation in Xenopus egg extracts mediated by augmin and TPX2. Cell *152*, 768–777.

Riedl, J., Crevenna, A.H., Kessenbrock, K., Yu, J.H., Neukirchen, D., Bista, M., Bradke, F., Jenne, D., Holak, T.A., Werb, Z., et al. (2008). Lifeact: a versatile marker to visualize F-actin. Nat Methods *5*, 605–607.

Sive, H.L., Grainger, R.M., and Harland, R.M. (2010a). Calibration of the injection volume for microinjection of Xenopus oocytes and embryos. Cold Spring Harb Protoc *2010*, pdb.prot5537.

Sive, H.L., Grainger, R.M., and Harland, R.M. (2010b). Microinjection of Xenopus embryos. Cold Spring Harb Protoc *2010*, pdb.ip81.

Straight, A.F., Field, C.M., and Mitchison, T.J. (2005). Anillin binds nonmuscle myosin II and regulates the contractile ring. Mol Biol Cell *16*, 193–201.

Thévenaz, P., Ruttimann, U.E., and Unser, M. (1998). A pyramid approach to subpixel registration based on intensity. IEEE Trans Image Process *7*, 27–41.

Tsai, M.-Y., and Zheng, Y. (2005). Aurora A kinase-coated beads function as microtubule-organizing centers and enhance RanGTP-induced spindle assembly. Curr Biol *15*, 2156–2163.

Wühr, M., Tan, E.S., Parker, S.K., Detrich, H.W., and Mitchison, T.J. (2010). A model for cleavage plane determination in early amphibian and fish embryos. Curr Biol *20*, 2040–2045.

Appendix II

Supplemental Materials for Chapter Three: Cell-Free Reconstitution of Cytokinesis Signaling

Supplementary content includes Materials and Methods, Supplementary Note 3.1, Figures S3.1 to S3.5, Table S3.1, Movies S3.1 to S3.7, and References.

Materials and Methods

Protein expression plasmid constructs

The *X. laevis* Prc1E coding sequence (codon optimized for *E. coli* and insect cell expression; GenScript, NJ) was subcloned into pET-28b bacterial expression vector with an N-terminal Strep-tag (WSHPQFEK), creating Strep-Prc1E. The N-terminal amino acid sequence preceding the Prc1E sequence is: MA-WSHPQFEK-GA. To create the Strep-Prc1 construct, the Prc1E sequence was replaced with the *X. laevis* Prc1 somatic coding sequence from a published construct (Bieling et al., 2010a) kindly provided by Thomas Surrey (London Research Institute, UK). To create the Strep-mCherry-Prc1E construct, a mCherry coding sequence with a C-terminal AAA linker was inserted N-terminal to the Prc1E coding sequence. All subcloning was performed with Gibson cloning.

Proteins and antibodies

X. laevis Kif4A-GFP-His was purified from Sf21 insect cells as described (Bieling et al., 2010a; Nguyen, Groen et al., 2014). *X. laevis* His-GFP-DasraA, human EB1-GFP-His and human EB1-mCherry-His were purified from *E. coli* as described (Nguyen, Groen et al., 2014). *X. laevis* Strep-mCherry-Prc1E, Strep-Prc1E and Strep-Prc1 were purified as previously described for a similar Strep-GFP-Prc1E construct (Nguyen, Groen et al., 2014). Tubulin was purified from bovine brain and labelled with Alexa488, Alexa568, or Alexa647 dyes (Life Technologies, NY) as described (Groen et al., 2014). Protein concentrations were determined by Bradford assay with BSA standards, and refer to dimers for tubulin and monomers for all the other proteins. See Table S3.1 for sequence information on the *Xenopus* proteins studied in this paper.

Affinity purified C-terminal peptide antibodies (rabbit) were produced against *X. laevis* Prc1E (C-FKEEMTKKSSHSEAVFNSTVNENL) (NeoBioLab, MA). Antibodies were raised in rabbits to GST-fused *X. laevis* Prc1 (C-terminal 160 amino acids), and affinity purified using the Prc1 C-terminal tail fused to MBP. Affinity purified antibodies (rabbit) against C-terminal tails of *X. laevis* Kif4A, Kif23, and Aurora kinase A were from a previous study (Nguyen, Groen et al., 2014). Tubulin antibodies (Sigma #T6074) were purchased. Antibodies were labelled on column with Alexa488, Alexa568, or Alexa647 dyes (Life Technologies, NY) as described (Groen et al., 2014).

Passivation of glass coverslips

Partially passivated PEG-coated coverslips were prepared following previous protocols (Field et al., 2014; Portran, 2014) with modifications. Coverslips (18 × 18 mm and 22 × 22 mm, No. 1.5 with 0.16–0.19 mm thickness) were pre-cleaned in 3 M KOH and ethanol as described (Nguyen et al., 2015). Coverslips were blow dried with nitrogen gas and further cleaned with oxygen plasma (Technics plasma etcher 500-II, oxygen gas at 100 mTorr, glow discharge at 200 W for 4 min) as described (Field et al., 2014; Nguyen et al., 2015). Methoxy PEG silane (MW 5000, JenKem Technology USA #A3037) was dissolved at 1 mg/mL in 96% ethanol with 0.1% (v/v) HCl by warming the solution to 50°C. Freshly plasma-cleaned coverslips were incubated in the silane-PEG solution at room temperature for 18 hrs with gentle agitation as described (Portran, 2014). Coverslips were rinsed with 96% and deionized water, and blow dried with nitrogen gas as described (Portran, 2014). Coverslips can be stored in the dark with a desiccant at -20°C for up to one year.

Fully passivated PEG-coated coverslips were prepared either by following previous relatively labour-intensive protocols for covalently coating coverslips with silane-PEG (Bieling et al., 2010b; Field et al., 2014) or by coating partially passivated PEG coverslips with poly-(L-lysine)-PEG (PLL-PEG). For the latter method, partially passivated coverslips were incubated

with 100 µg/mL PLL-PEG {PLL(20)-g[3.5]-PEG(2), SuSoS, Switzerland} dissolved in 10 mM Hepes, pH 7.7, for 10-30 min at room temperature. Coverslips were rinsed in deionized water, blow dried with nitrogen gas, and used within 24 hrs.

Aster assembly assay

Metaphase arrested *Xenopus* egg extracts with intact actin were prepared as described (Field et al., 2014; Nguyen, Groen et al., 2014). Interphase asters were assembled between PEG-passivated coverslips as previously described (Nguyen, Groen et al., 2014) with modifications in the coverslip passivation procedure described below. Briefly, M-phase extract was supplemented with fluorescent probes, treated with 0.4mM $CaCl_2$ to mimic fertilization and induce metaphase-to-interphase transition. Activated extract was supplemented with Protein A Dynabeads (Life Technologies, NY) coupled to Aurora kinase A antibody, which served as artificial centrosomes (Tsai and Zheng, 2005). Extract was then spread between two PEG-passivated glass coverslips. Aster assembly reactions were monitored with a widefield, spinning disc confocal, or TIRF (Total Internal Reflection Fluorescence) microscope at 20°C.

For widefield and confocal imaging, asters were assembled between two fully passivated PEG-coated coverslips. For TIRF imaging, asters were assembled between a fully passivated PEG coverslip (top, 18 × 18 mm) and a partially passivated coverslip (bottom, 22 × 22 mm). Partial passivation allowed microtubules to track along the coated surface, within the TIRF illumination field.

For visualization, fluorescent probes were used at the following concentrations: 250 nM Alexa488-, 568- or 647-tubulin, 40 nM EB1-GFP or EB1-mCherry, 10 nM Kif4-GFP, 20 nM mCherry-Prc1E, 20 nM GFP-DasraA.

Immunodepletions, protein addback, and drug inhibition

Kif4A, Kif23, and Prc1E were depleted using 2 rounds of 20 µg of antibodies conjugated to 50µL Protein A Dynabeads (Life Technologies, NY) for 50 µL of extracts. Depletions using beads coated with random rabbit IgG served as controls. Depletions were confirmed by immunoblots. Kif4A depletion was rescued by adding back ~100 nM Kif4A-GFP, and Prc1E depletion was rescued by adding back ~65 nM purified Prc1E or Prc1. For inhibition of Aurora B kinase, 100 µM ZM447439 (Tocris Bioscience, MN; 10 mM stock solution in 10 mM glycine, pH 7) was added to calcium activated extracts. Aster assembly assays were performed with treated extracts as described above.

All immunodepletion and drug inhibition experiments were performed with $n \geq 3$ biological repeats, using extracts prepared from eggs produced by different female frogs. Ideally, all the treatments ought to be performed on the same extract to reduce extract-to-extract (and frog-to-frog) variability, and the samples from each treatment ought to be imaged at the same time to reduce the variability introduced by the "aging" of extracts while stored on ice. In practice, however, this is impossible due to limitations posed by the amount of extract produced from a single female frog and our ability to handle samples. Therefore, we routinely performed only 3-4 treatments (including control buffer addition or IgG depletion) per experiment. Although we aimed to acquire data for all treatments simultaneously, 1-2 samples out of the 3-4 would often be destroyed via mishandling, thus the data for those treatments had to be acquired in the next round of aster assembly reaction.

Time-lapse fluorescence microscopy

Widefield images were obtained using a 10x Plan Apo 0.45 NA objective lens (Nikon) on an upright Nikon Eclipse 90i microscope equipped with a Prior Lumen 200 metal arc lamp, a Prior ProScan III motorized XY stage, a Hamamatsu ORCA-ER cooled CCD camera, and driven by Metamorph image acquisition software (Molecular Devices, CA).

Spinning disc confocal images were obtained using a 40x oil Plan Apo 1.30 NA objective lens (Nikon) on an upright Nikon Eclipse E800 microscope equipped with a Melles Griot Krypton/Argon ion laser (488nm, 568nm, 647nm), a Yokogawa CSU-10 spinning disc (Perkin Elmer, MA), a Hamamatsu ORCA-ER cooled CCD camera, and driven by Metamorph.

TIRF images were obtained using a 60x Apo TIRF 1.49 NA objective lens (Nikon) on a Nikon Ti-E motorized inverted microscope equipped with a Nikon motorized TIRF illuminator, Perfect focus, a Prior Proscan II motorized stage, Agilent MLC400B laser launch (488nm, 561nm, 647nm), an Andor DU-897 EM-CCD camera driven by NIS-Elements image acquisition software. Two separate TIRF setups were available at the Nikon Imaging Center at Harvard Medical School and the Marine Biological Laboratory.

Immunofluorescence of fixed Xenopus zygotes

Zygotes were fixed and stained 100 min after fertilization as previously described (Nguyen, Groen et al., 2014). Briefly, zygotes were fixed in a methanol/EGTA solution for 24 hrs at room temperature, rehydrated in a series of methanol/TBS mixtures, and then hemisected. Zygotes were bleached overnight in a SSC/formamide/H_2O_2 solution and then incubated with directly labeled antibodies for at least 24 hrs at 4°C. Antibodies were used at approximately the following concentrations: Alexa488-anti-tubulin (1-2µg/mL), Alexa568-anti-Prc1E (1-2µg/mL), Alexa647-anti-Kif4A (1-2µg/mL).

Fixed zygotes were imaged with a laser scanning confocal microscope at the Nikon Imaging Center at Harvard Medical School. A 10x dry objective (Nikon) was used on a Nikon Ti-E inverted microscope with a Nikon A1R point scanning confocal head, driven by NIS-Elements image acquisition software.

Image analysis: microtubule plus end dynamics from EB1 comet tracking (related to Figures 3.3, 3.4 and 3.6)

Time-lapse image sequences of EB1-GFP were acquired, processed, and analyzed as described (Nguyen, Groen et al., 2014). Briefly, extract was supplemented with 40 nM EB1-GFP and 250 nM Alexa647-tubulin. Asters were assembled between fully passivated PEG coverslips as described above. Lower AurkA bead density was used to study isolated asters, and higher bead density to study AAIZs. Multiple isolated asters or AAIZs were imaged between 20 and 50 min of the assembly reaction at 20°C, alternating between control and treatment conditions. A spinning disc confocal microscope with a 40x oil objective (NA = 1.30) was used to acquire images with 2x2 binning. Time-lapse image sequences were acquired of EB1-GFP with 1.5 sec intervals for a total duration of 2 min (81 frames total). Tubulin images were acquired at the beginning and end of each sequence.

EB1 image sequences were registered using the *StackReg* ImageJ plugin with rigid body transformation (Thévenaz et al., 1998). The *plusTipTracker* MATLAB software (Applegate et al., 2011; Matov et al., 2010) was used to perform automated detection and frame-to-frame linking of EB1 comets using the parameters in ref. (Nguyen, Groen et al., 2014). Tracks were filtered out and excluded from analysis based on the criteria listed in ref. (Nguyen, Groen et al., 2014). Remaining tracks were then plotted and colored according to their mean direction (Figure 3.3a) or instantaneous velocity averaged over 3 consecutive frames (Figure 3.3b).

The degree of interpenetration was quantified by dividing all EB1 comets detected in frames 2-81 into two groups based on the direction of their displacement relative to the previous frame (Figure 3.3a', inset showing 'blue' and 'red' directions). Rectangular regions of interests (ROIs; 90 μm x 10 μm) parallel to the bead-bead axis and traversing the interaction zone were overlaid. Each ROI was divided into 9 cells (10 μm x 10 μm each), and the fraction of EB1 comets moving in the 'blue' direction was determined and plotted as grey dots against the distance from the AAIZ midline (see Figure S2.3 in Appendix I). The procedure was repeated for

multiple non-overlapping, neighbouring ROIs within an AAIZ, giving rise to all the grey dot data. The data points were fitted to a sigmoidal distribution (Figure 3.3a', blue curve):

$$f(x) = Y_{min} + \frac{Y_{max} - Y_{min}}{1 + (a/x)^b},$$

where x is distance and $f(x)$ is the fraction of EB1 comets moving in the 'blue' direction. A complementary sigmoidal distribution described the fraction of EB1 comets moving in the other, 'red', direction (Figure 3.3a', red curve). The exact position of the AAIZ 'midline' was defined where the blue and red curves intersected. A 'D60' parameter was defined as the difference between the interpolated distances where the red and blue curves crossed 60%. This parameter served as a measure for the depth of interpenetration.

The instantaneous velocities associated with each EB1 comet detected in frames 2-81 were averaged within each square cell. The total number of EB1 comets was counted, and the comet density determined for each cell. The number of EB1 comets comprising the initiation or the termination of a growth track was counted and expressed as the fraction of total EB1 comets for each cell. EB1 comet speeds, densities, track terminations and initiations were averaged for cells in neighboring ROIs at a given distance from the AAIZ midline. These mean values were plotted in Figures 3.3b' and 3.3c', where the error bars indicate SEMs for EB1 speeds and SDs for densities, track terminations and initiations.

To obtain the % difference in plus end dynamics measurements inside an AAIZ compared to outside, the mean value of each measurement obtained at the exact AAIZ midline (0 μm) was divided by the mean of the mean values obtained at -40, -30, -20, 20, 30, and 40 μm from the AAIZ midline. The mean values obtained at -10 and 10 μm were considered transition values, and thus were omitted from the calculations. The % difference measurements were averaged for multiple ($n \geq 3$) AAIZs per condition; the mean values were plotted with standard deviations as error bars in Figure 3.4h).

All analyses were performed in MATLAB.

Image analysis: kymographs of anti-parallel overlap formation (related to Figure 3.7)

Extract was supplemented with 250 nM Alexa647-tubulin, 10 nM Kif4A-GFP, and 20 nM mCherry-Prc1E. Asters were assembled between a fully and a partially PEG-passivated glass coverslip, which allows microtubules to track along the partially passivated surface. AAIZs were imaged between 20 and 50 min of aster assembly reaction at 20°C. A TIRF microscope with a 60x TIRF objective (NA = 1.49) was used to acquire two- or three-color time-lapse sequences. A segmented line (3 pixels wide) was manually drawn over the Kif4A-positive microtubule bundles in each image frame in ImageJ, and kymographs were generated to show the frame-to-frame fluorescence intensities along these lines.

Image analysis: quantification of radial order within isolated asters

The first approach to quantifying radial order in asters involved tracking EB1 comets over 2 min (81 frames at 1.5 sec intervals) and measuring their directions (angles of frame-to-frame displacement) within a quadrant of an isolated aster. Radial order heat maps were created by dividing the field of view into square cells measuring 5x5 μm^2 (Figure 3.6a'-e'). A radial order parameter (*R*) was calculated from the distribution of angular deviations of EB1 comet directions from the radial direction within each square cell:

$$R = \frac{1}{N}\left|\sum_{n=1}^{N}\left(\cos(\theta_n) + i\sin(\theta_n)\right)\right| = \frac{1}{N}\left|\sum_{n=1}^{N} e^{-i\theta_n}\right|,$$

where $\theta_n = \beta_n - \alpha_n$. The variable α_n is the radial direction of each EB1 comet (i.e. angular coordinate within a polar coordinate system with the aster centre as the pole) and β_n is the angle of displacement of each comet with respect to the previous frame. The variable θ_n ranges from $-\pi$ to $+\pi$ in radians. For the heat maps, all EB1 comets detected from frame 2 to 81 were considered within each square cell.

In directional statistics, circular variance is defined as (*1 - R*), which is a measure of the spread of a population of angles θ_n. *R* is the length of the mean resultant vector of the

population of angles and ranges from 0 to 1. A MATLAB toolbox called 'CircStat' was used to compute the resultant vector length (*R*) (Berens, 2009).

To quantify the dependence of radial order on the distance from the aster centre, the field of view was divided into concentric rings with a width of 5 μm, centring on the AurkA bead. Radial order parameters (*R*) were obtained for each ring area, considering EB1 comets detected within 10 consecutive frames (e.g. frames 2 to 11, 12 to 21, …, 72 to 81). The mean *R* values were obtained from all 8 time ranges and plotted against distance from the bead, along with standard deviations as error bars (Figure 3.6f).

An alternative approach to quantifying radial order in asters involved analysing microtubule morphology from TIRF images of isolated asters (Figure S3.5). TIRF images were acquired with an 60x oil TIRF objective, corrected for uneven illumination and stitched as previously described (Nguyen, Groen et al., 2014). Images were cropped and rotated to position the aster centre at the top left corner. The most prominent microtubule structures (bundles or single microtubules) were detected and their direction determined using a 2-D steerable ridge filter implemented by Francois Aguet (http://www.francoisaguet.net/software.html) based on ref. (Jacob and Unser, 2004). The inputs for the MATLAB function:

```
[res, theta, nms, rotations] = steerableDetector(img, M, sigma)
```

were M = 4 and sigma = 2, and a local threshold filter was further applied to the non-maximum-suppressed response (*nms*) output image. The angular deviations from the radial direction were calculated for each detected pixel as $\theta_n = \beta_n - \alpha_n$, where α_n was the angular coordinate of the pixel in a polar coordinate system with the aster centre as the pole, and β_n was the orientation angle of the pixel determined by the steerable ridge filter (*theta*). The variable θ_n ranged from $-\pi/2$ to $+\pi/2$ in radians. Radial order parameters (*R*) were computed from the distribution of angles (θ_n) within a square cell measuring 51 pixels. Moving this cell as a sliding window generated a heat map of radial order.

All analyses were performed in MATLAB.

Statistics

Related to 2nd paragraphs in Results section titled "Plus end dynamics in AAIZs". To compare the two non-normal distributions of instantaneous plus end growth rates (i.e. frame-to-frame EB1 comet velocities) observed inside vs outside an AAIZ, we used the two-sample Kolmogorov-Smirnov (KS) test. The test was performed using the MATLAB function:
`kstest2(<growth rates inside AAIZ>,<growth rates outside>).`

Related to Figure 3.4g. To evaluate the statistical significance of the difference in the degree of interpenetration between asters observed under various treatment conditions, we used Welch's *t*-test (two-sample, unpaired *t*-test assuming unequal sample sizes and unequal variances) to compare the D60 parameters obtained from treatment conditions to those obtained from IgG control depletion. The test was performed using the MATLAB function:
`ttest2(<IgG data>,<treatment data>,'Vartype','unequal').`

Related to Figure 3.4h. To evaluate the statistical significance of the % difference between the microtubule dynamics measurements inside the AAIZ and those outside, the one-sample *t*-test was used to test against the null hypothesis of no difference (0% difference). The test was performed using the MATLAB function:
`ttest(<data>).`

Supplementary Notes

Supplementary Note 3.1. Correlation between microtubule growth lifetimes and growth rates (related to Figures S3.2 and S3.4).

To better understand why termination events were enriched within AAIZs, we measured the lifetimes of microtubule growth trajectories ending within an AAIZ and compared them to trajectories ending outside (Figure S3.2a, left). Growth lifetimes (the time interval between a nucleation or rescue and a catastrophe or pause) were fit reasonably well by an exponential distribution, as expected for stochastic switching between dynamic states at the plus end in a simple model of dynamic instability (Dogterom and Leibler, 1993; Mitchison and Kirschner, 1984; Verde et al., 1992). We observed a slight shift towards shorter durations within the AAIZ (70% of growth excursions lasting less than the overall mean lifetime [11 sec] inside vs. 63% outside). However, this effect appeared less striking than a shift to slower growth rates within the AAIZ (50% growth excursions slower than the overall average rate [24 μm/min] inside vs. 35% outside) (Figure S3.2a, right). In a simple stochastic model under constant conditions, microtubule growth rates and lifetimes should be uncorrelated. In reality, we observed a slight but statistically significant positive correlation between growth lifetimes and growth rates averaged over the growth lifetime of a single microtubule (Figure S3.2b, control panel). The correlation coefficient (r) was higher inside the AAIZ than outside; this observation was consistent over multiple representative AAIZs analysed (inside $r = 0.24 \pm 0.05$ [SD], outside $r = 0.14 \pm 0.02$ [SD], $n = 4$ AAIZs) (Figure S3.2c). This suggests that some process slows microtubules before a catastrophe or pause is triggered.

We also measured the degree of correlation between growth rates and growth lifetimes inside and outside AAIZs for all these treatments (Figure S3.2b, c). We found a complete loss of correlation when Kif4A or Prc1E was depleted. When AurkB was inhibited, there was a slight but significant correlation, the degree of which was similar to the correlation measured outside

the AAIZ under control conditions. The enhanced correlation observed inside the AAIZ for control aster interactions was eliminated when AurkB was inhibited.

To determine whether the slowdown of microtubule growth inside an AAIZ was affected by the treatments above, we examined the EB1 trajectories rank ordered by their termination velocity (Figure S3.4). AurkB inhibition still led to more microtubules that slowed down before they stopped growing inside an AAIZ than outside, consistent with the decrease in growth rate measured in Figure 3.4h. Depletion of either Kif4A or Prc1E, however, eliminated the preferential slowdown of microtubule growth before termination within an AAIZ. Collectively, these data show that microtubule growth slowdown in AAIZs and the increased rate of catastrophes (or pauses) required Prc1E and Kif4A activities.

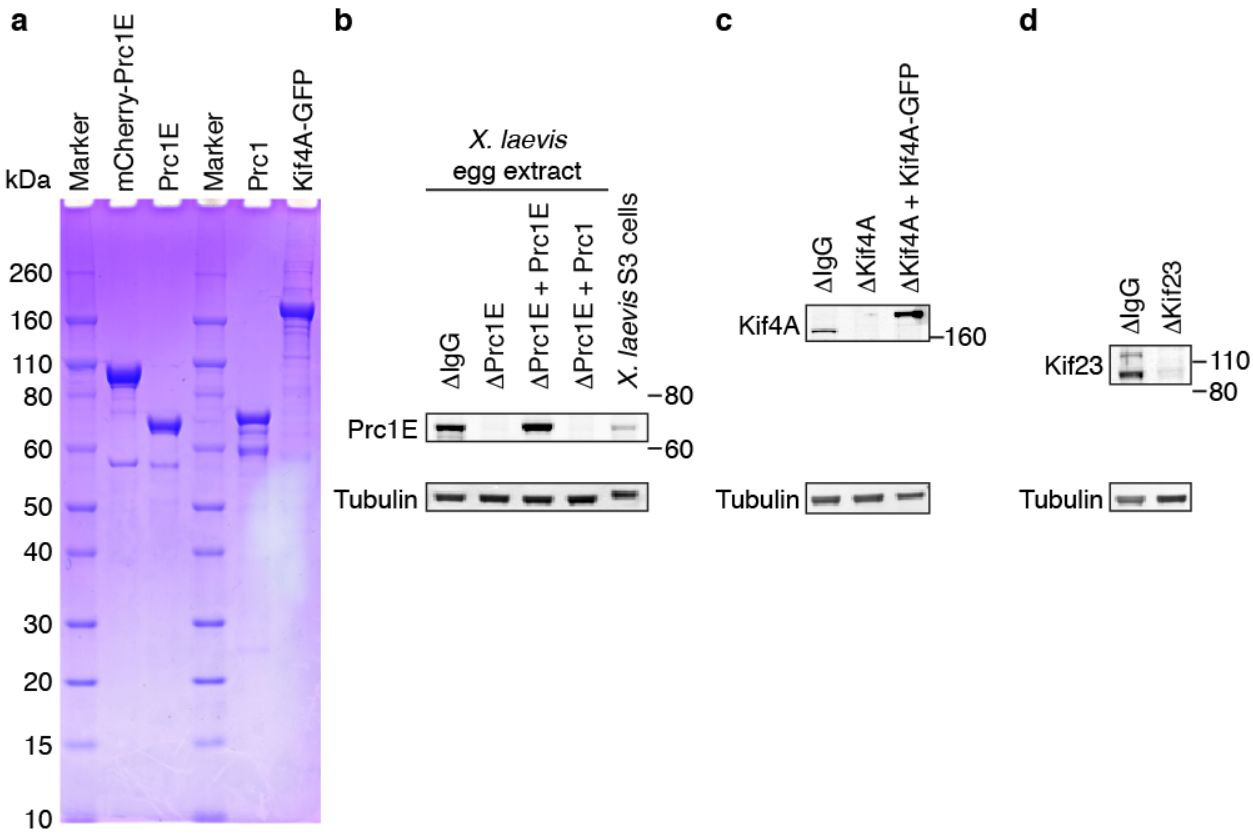

Figure S3.1: Purification, immunodepletion, and addbacks of proteins.

(a) Coomassie-stained SDS gel of proteins used in this study. Theoretical molecular weights of the protein constructs: Strep-mCherry-Prc1E, 96 kD; Strep-Prc1E, 68 kD; Strep-Prc1, 73 kD; Kif4A-GFP-His, 168 kD.

(b-d) Immunoblots showing immunodepletion from *Xenopus* egg extracts and addback of Prc1E **(b)**, Kif4A **(c)**, and Kif23 **(d)**.

(b) Prc1E (~68 kD) depletion was rescued by adding back ~65 nM recombinant Prc1E (~68 kD) or Prc1 (~73 kD). Prc1E was much less abundant in *Xenopus laevis* tissue culture cells (S3 cells).

(c) Kif4A (~139 kD) depletion was rescued by adding back ~100 nM recombinant Kif4A-GFP (~168 kD).

(d) Kif23 (also known as Mklp1, a subunit of the centralspindlin complex, ~90 kD).

Figure S3.2: Correlation between the mean growth rate and growth lifetime of microtubule growth trajectories.

(a) Relative frequencies of growth lifetimes (*left*) and per track average growth rates (*right*) for tracks terminating inside (*red*) vs. outside (*blue*) a control AAIZ.

(b) Representative correlation plots for growth trajectories ending inside an AAIZ (*red*) and outside an AAIZ (*blue*) formed under various conditions, with Pearson correlation coefficients (*r*) and *P*-values displayed. **(c)** Mean Pearson correlation coefficients (±S D) from $n \geq 3$ AAIZs per condition, and the range of *P*-values displayed in parentheses.

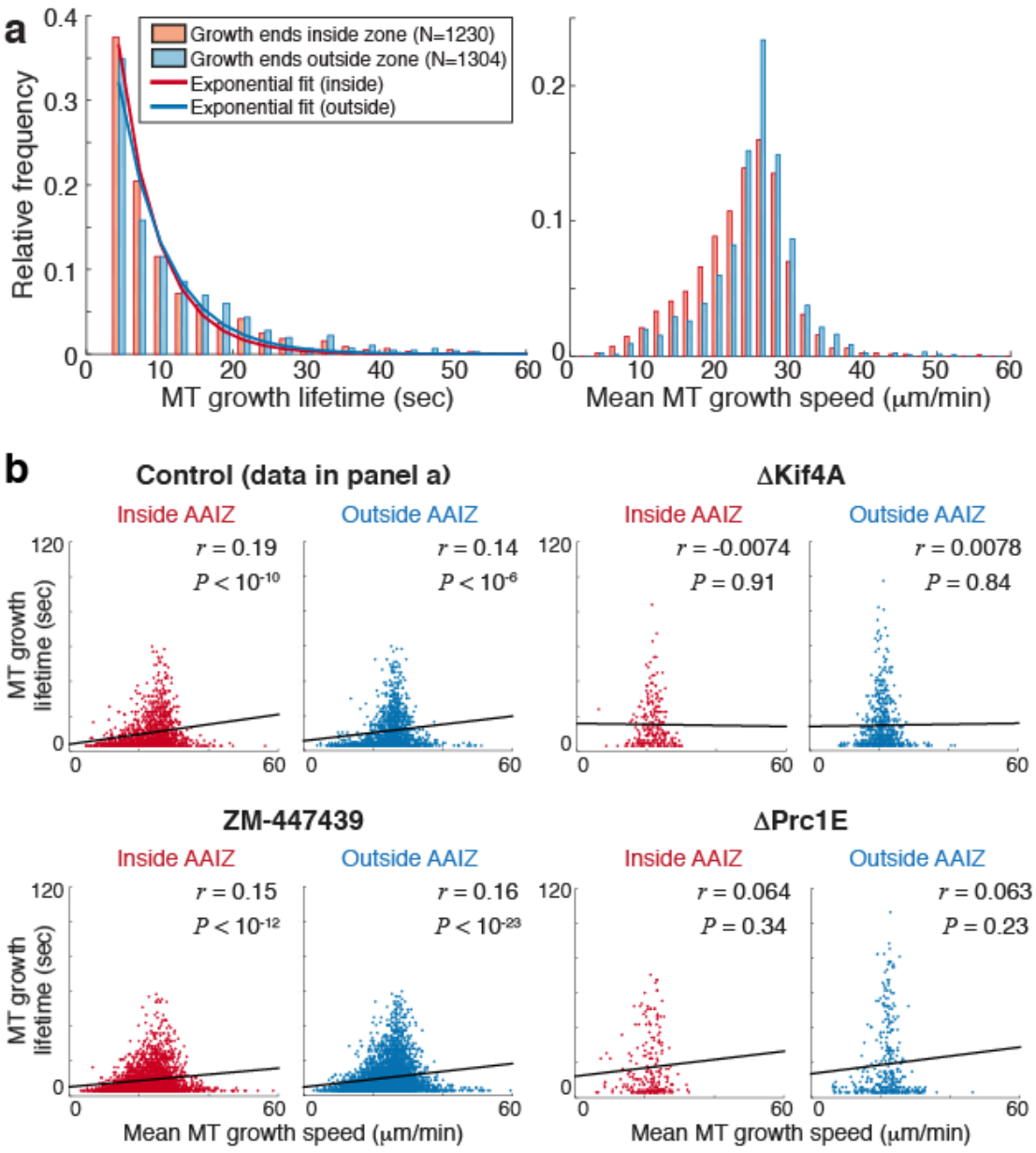

c

	Control	ZM-447439	ΔKif4A	ΔPrc1E	ΔPrc1E addback
r, inside AAIZ (P-values)	0.24 ± 0.05 ($<10^{-6}$–10^{-10})	0.16 ± 0.01 ($<10^{-4}$–10^{-12})	0.03 ± 0.07 (<0.9–0.03)	0.09 ± 0.03 (<0.4–0.1)	0.26 ± 0.10 ($<10^{-4}$–10^{-6})
r, outside AAIZ (P-values)	0.14 ± 0.02 (<0.01–10^{-9})	0.18 ± 0.04 ($<10^{-6}$–10^{-31})	0.00 ± 0.04 (<0.9–0.1)	0.10 ± 0.07 (<0.3–0.001)	0.15 ± 0.12 (<0.06–10^{-4})

Figure S3.2 (Continued)

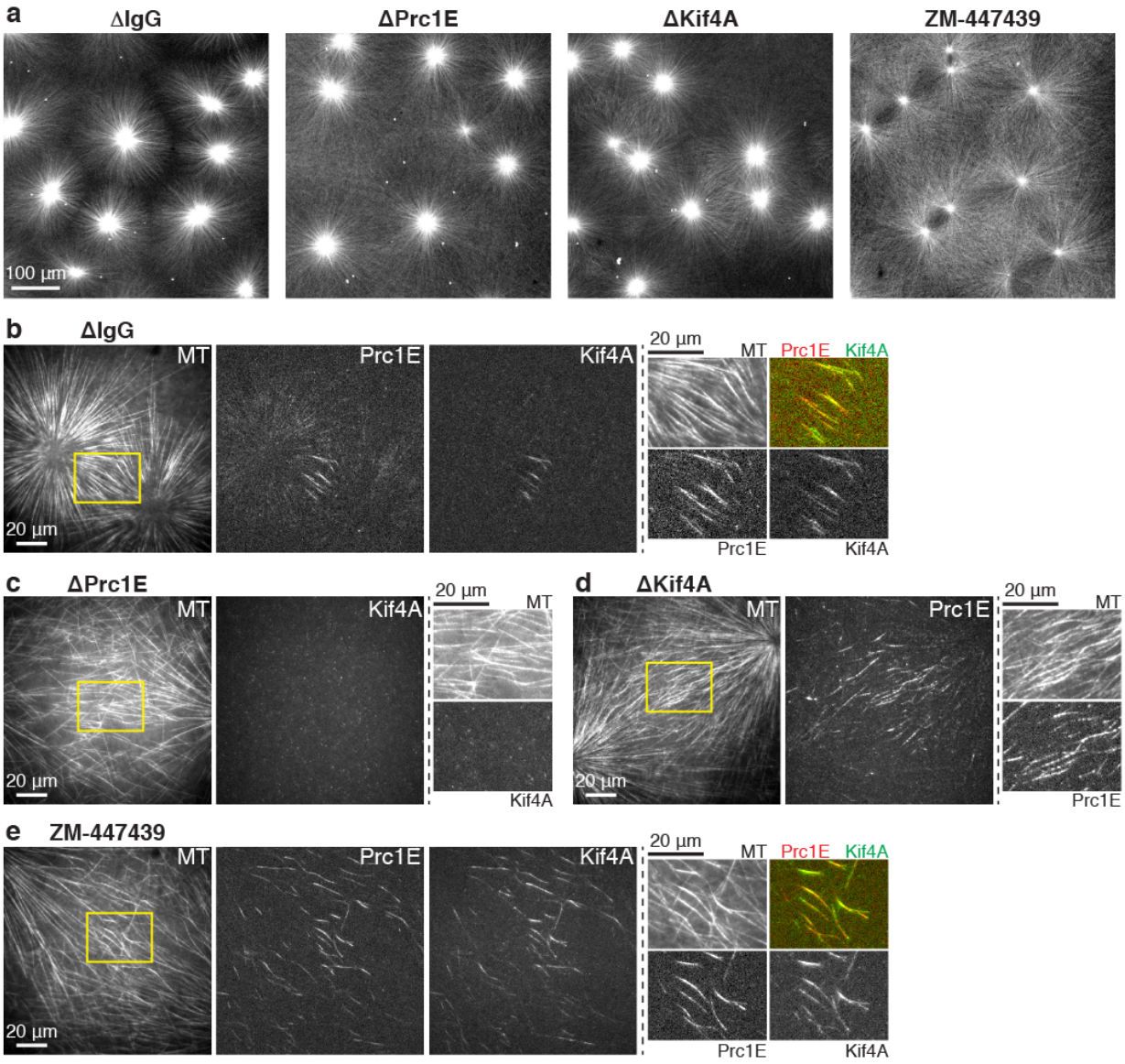

Figure S3.3: Representative images showing microtubule morphology and localization of Prc1E and Kif4A at AAIZs under various conditions.

(**a**) Low-mag widefield tubulin images of interacting asters formed using mock depleted, Prc1E or Kif4A depleted extracts, or extracts treated with 100 µM ZM-447439 (AurkB inhibitor). (**b-d**) High-mag TIRF images showing microtubules (Alexa647-tubulin), mCherry-Prc1E, Kif4A-GFP at AAIZs under the treatments above. Zoom-ups of boxed areas are shown on the right.

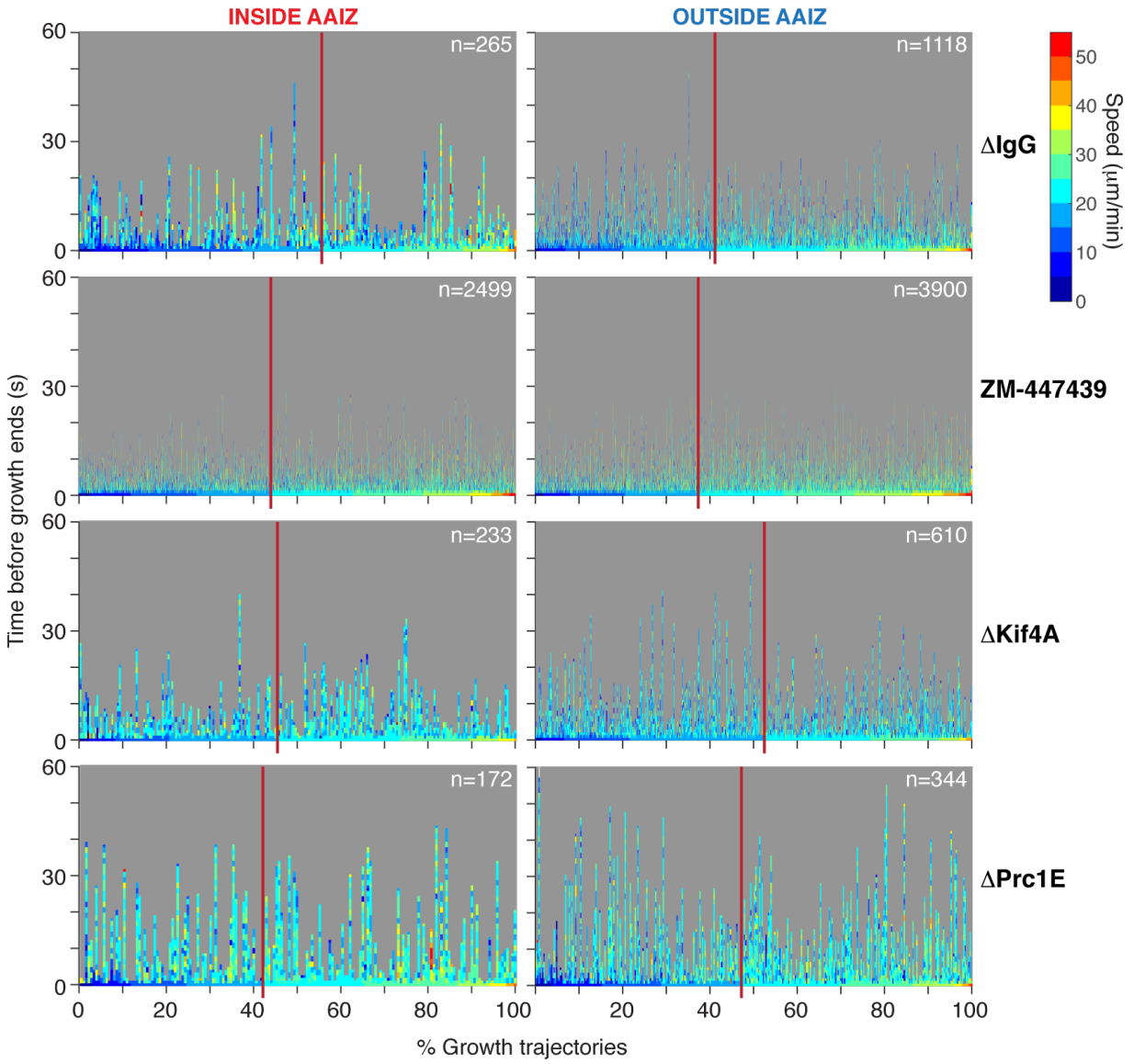

Figure S3.4: Microtubule growth trajectories profiled by growth rates and growth lifetimes under various conditions. Straightened growth tracks colour-coded by instantaneous velocity, and rank ordered by termination velocity measured during the last 3 sec of growth (as per Figure 3.3d). Red line demarcates tracks with termination velocity less than 20 μm/min from those with higher termination velocity. Conditions as labelled on the right: mock depletion, AurkB inhibition with 100 μM ZM-447439, Kif4A and Prc1E depletions.

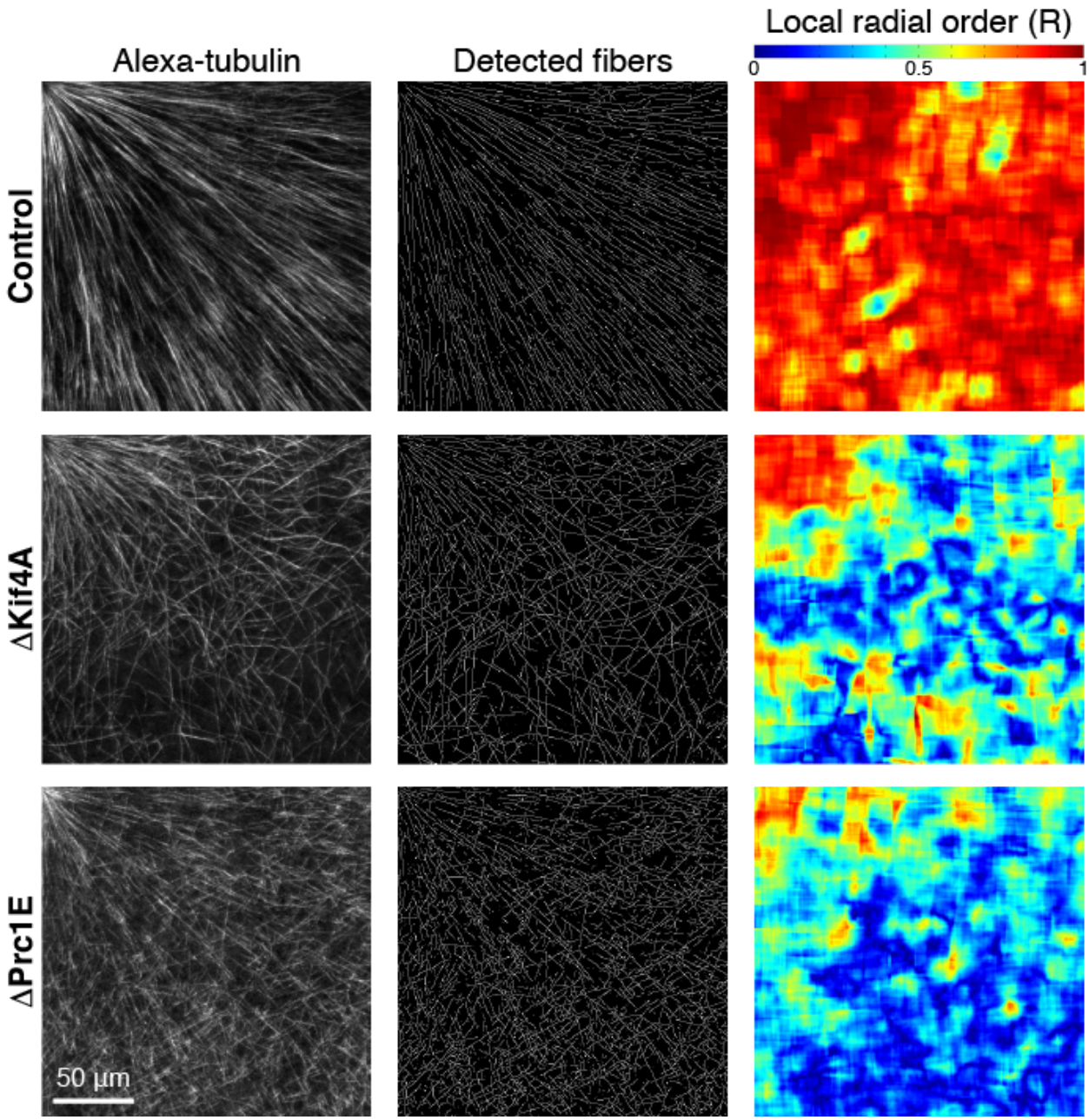

Figure S3.5: Alternative radial order measurement from microtubule morphology.
Microtubules within isolated asters imaged with TIRF microscopy under mock, Kif4A, or Prc1E depletion conditions (1st column). The most prominent microtubule structures (bundles or single microtubules) were detected and their direction determined using a steerable ridge filter (2nd column). The angular deviations of microtubules from the radial direction were calculated and radial order parameters (*R*) were computed from the distribution of angles within a square cell. Moving this cell as a sliding window generated a heat map of radial order, where warmer colours represent higher radial order (3rd column; see Methods).

Table S3.1: List of *Xenopus laevis* protein sequences studied in Chapter Three.

Name	**Description/Alternate names**	**NCBI GI number**
AurkA	Aurora kinase A	148236543
AurkB	Aurora kinase B	147899288
DasraA	Borealin-2	148232132
Kif4A	Chromokinesin, Xklp1	18202613
Kif23	Mklp1, CHO1	148222381
Prc1	Protein regulator of cytokinesis 1	148236333
Prc1E	Embryonic paralog of PRC1 (42% identity by sequence)	148231955

Supplemental Movie Captions

Movie S3.1: Related to Figure 3.1a

Confocal movie of aster growth and interaction with Prc1E and Kif4A visualized.

Movie S3.2: Related to Figure 3.1b

Widefield movie of aster growth and interaction with Prc1E and CPC visualized.

Movie S3.3: Related to Figure 3.3a

EB1 tracking in control AAIZ imaged with confocal microscope.

Movie S3.4: Related to Figure 3.5a

EB1 tracks overlaid on Prc1E images in control AAIZ imaged with TIRF microscope.

Movie S3.5: Related to Figure 3.5b

EB1 tracks overlaid on Prc1E images in Kif4A-depleted AAIZ imaged with TIRF microscope.

Movie S3.6: Related to Figure 3.7a

Overlap formation at aster edge with tubulin and Kif4A visualized with TIRF microscope.

Movie S3.7: Related to Figure 3.7b

Overlap formation at aster edge with tubulin, Kif4A, and Prc1E visualized with TIRF microscope.

References

Applegate, K.T., Besson, S., Matov, A., Bagonis, M.H., Jaqaman, K., and Danuser, G. (2011). plusTipTracker: Quantitative image analysis software for the measurement of microtubule dynamics. J Struct Biol *176*, 168–184.

Berens, P. (2009). CircStat: a MATLAB toolbox for circular statistics. J Stat Softw.

Bieling, P., Telley, I.A., and Surrey, T. (2010a). A Minimal Midzone Protein Module Controls Formation and Length of Antiparallel Microtubule Overlaps. Cell *142*, 420–432.

Bieling, P., Telley, I.A., Hentrich, C., Piehler, J., and Surrey, T. (2010b). Fluorescence microscopy assays on chemically functionalized surfaces for quantitative imaging of microtubule, motor, and +TIP dynamics. Methods Cell Biol *95*, 555–580.

Dogterom, M., and Leibler, S. (1993). Physical aspects of the growth and regulation of microtubule structures. Phys Rev Lett *70*, 1347–1350.

Field, C.M., Nguyen, P.A., Ishihara, K., Groen, A.C., and Mitchison, T.J. (2014). Xenopus egg cytoplasm with intact actin. Meth Enzymol *540*, 399–415.

Groen, A.C., Nguyen, P.A., Field, C.M., Ishihara, K., and Mitchison, T.J. (2014). Glycogen-supplemented mitotic cytosol for analyzing Xenopus egg microtubule organization. Meth Enzymol *540*, 417–433.

Jacob, M., and Unser, M. (2004). Design of steerable filters for feature detection using canny-like criteria. IEEE Trans Pattern Anal Mach Intell *26*, 1007–1019.

Matov, A., Applegate, K., Kumar, P., Thoma, C., Krek, W., Danuser, G., and Wittmann, T. (2010). Analysis of microtubule dynamic instability using a plus-end growth marker. Nat Methods.

Mitchison, T., and Kirschner, M. (1984). Dynamic instability of microtubule growth. Nature *312*, 237–242.

Nguyen, P.A., Field, C.M., Groen, A.C., Mitchison, T.J., and Loose, M. (2015). Using supported bilayers to study the spatiotemporal organization of membrane-bound proteins. Methods Cell Biol *128*, 223–241.

Nguyen, P.A., Groen, A.C., Loose, M., Ishihara, K., Wühr, M., Field, C.M., and Mitchison, T.J. (2014). Spatial organization of cytokinesis signaling reconstituted in a cell-free system. Science *346*, 244–247.

Portran, D. (2014). Micropatterning microtubules. Methods Cell Biol *120*, 39–51.

Thévenaz, P., Ruttimann, U.E., and Unser, M. (1998). A pyramid approach to subpixel registration based on intensity. IEEE Trans Image Process *7*, 27–41.

Tsai, M.-Y., and Zheng, Y. (2005). Aurora A kinase-coated beads function as microtubule-organizing centers and enhance RanGTP-induced spindle assembly. Curr Biol *15*, 2156–2163.

Verde, F., Dogterom, M., Stelzer, E., Karsenti, E., and Leibler, S. (1992). Control of microtubule dynamics and length by cyclin A- and cyclin B-dependent kinases in Xenopus egg extracts. J Cell Biol *118*, 1097–1108.